Terms and Conditions of Use of Digitised Theses from Trinity College Library Dublin

Copyright statement

All material supplied by Trinity College Library is protected by copyright (under the Copyright and Related Rights Act, 2000 as amended) and other relevant Intellectual Property Rights. By accessing and using a Digitised Thesis from Trinity College Library you acknowledge that all Intellectual Property Rights in any Works supplied are the sole and exclusive property of the copyright and/or other IPR holder. Specific copyright holders may not be explicitly identified. Use of materials from other sources within a thesis should not be construed as a claim over them.

A non-exclusive, non-transferable licence is hereby granted to those using or reproducing, in whole or in part, the material for valid purposes, providing the copyright owners are acknowledged using the normal conventions. Where specific permission to use material is required, this is identified and such permission must be sought from the copyright holder or agency cited.

Liability statement

By using a Digitised Thesis, I accept that Trinity College Dublin bears no legal responsibility for the accuracy, legality or comprehensiveness of materials contained within the thesis, and that Trinity College Dublin accepts no liability for indirect, consequential, or incidental, damages or losses arising from use of the thesis for whatever reason. Information located in a thesis may be subject to specific use constraints, details of which may not be explicitly described. It is the responsibility of potential and actual users to be aware of such constraints and to abide by them. By making use of material from a digitised thesis, you accept these copyright and disclaimer provisions. Where it is brought to the attention of Trinity College Library that there may be a breach of copyright or other restraint, it is the policy to withdraw or take down access to a thesis while the issue is being resolved.

Access Agreement

By using a Digitised Thesis from Trinity College Library you are bound by the following Terms & Conditions. Please read them carefully.

I have read and I understand the following statement: All material supplied via a Digitised Thesis from Trinity College Library is protected by copyright and other intellectual property rights, and duplication or sale of all or part of any of a thesis is not permitted, except that material may be duplicated by you for your research use or for educational purposes in electronic or print form providing the copyright owners are acknowledged using the normal conventions. You must obtain permission for any other use. Electronic or print copies may not be offered, whether for sale or otherwise to anyone. This copy has been supplied on the understanding that it is copyright material and that no quotation from the thesis may be published without proper acknowledgement.

Magmatic differentiation and bimodality in oceanic island settings - implications for the petrogenesis of magma in Tenerife, Spain

---

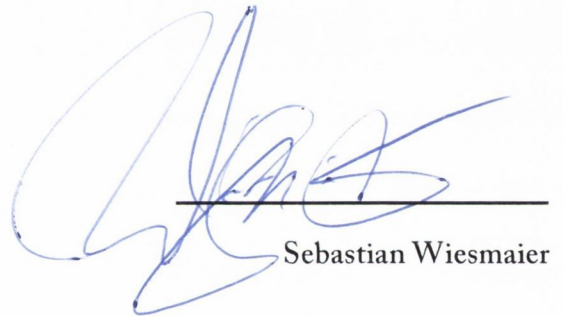Thesis for the obtainment of a doctoral degree (Ph.D.)

2010

Sebastian Wiesmaier

I, Sebastian Wiesmaier, hereby declare that:

- my thesis has not previously been submitted as an exercise for a degree at this or any other University,
- it is entirely my own work, apart from the sections indicated in the text,
- I agree that the Library may lend or copy the thesis upon request.

Sebastian Wiesmaier

Summary

The Tenerife post-Icod-collapse succession, comprised of the Teide-Pico Viejo central complex and its adjacent rift zones, marks the latest eruptive cycle on Tenerife (200-0 ka) that broadly evolved from primitive lavas to differentiated and partly explosive volcanism. At the same time, primitive lavas continued to erupt from dyke complexes in the rift zones, while intermediate lavas effused in the geographical transition from rift zone to central complex. To constrain the magmatic processes, that gave rise to the observed temporal and spatial patterns, several types of geochemical analyses of these rocks were applied and results embedded into a detailed, pre-existing framework of radiometric ages and whole-rock data.

A case study of the composite lava flow of Montaña Reventada allowed to investigate magma mixing as one potential mechanism to generate intermediate magma on Tenerife. The two end-members were a basanite and a phonolite, which erupted one after another, the basanite before the phonolite. The phonolite carries a considerable amount of mafic enclaves. Based on field evidence, the magma mixing event was constrained to a short interval before the eruption. A detailed geochemical dataset was used to confirm the mixed nature of the inclusions and to determine mixing ratios. Not all elements and oxides could be modelled, which is explained by observed crystal exchange between basanite and phonolite and by interdiffusion of trace elements between enclaves and phonolite. It thus appears that intermediate magma may form by magma mixing on Tenerife.

Mafic magmas, in turn, appear to experience a main phase of crystallisation at upper mantle/lower crustal levels on Tenerife. Microanalysis of feldspar crystals for major- and trace elements and $^{87}Sr/^{86}Sr$ ratios was therefore conducted to reconstruct magmatic processes that these phenocrysts witnessed at depth. A set of empirical equations helped to calculate the composition of the host melts to these crystals. This information was then implemented into an energy-constrained numerical model of recharge, assimilation and fractional crystallisation (EC-RAχFC). As a result, two distinct compositions of primitive lava that have erupted in Tenerife - one with high-Sr/high-Zr, the other with low-Sr/low-Zr concentrations - were constrained to follow distinct paths of assimilation

and fractional crystallisation at depth. The high-Sr/high-Zr group appears to originate in upper mantle/lower crustal magma chambers. In this environment of constant replenishment and expulsion of magma, simultaneous crystallisation and remelting of cumulate slowly enriches the resident magma in trace elements, while the non-enriched magma (low-Sr/low-Zr) appears to have largely escaped this evolutionary stage or was subjected to it very briefly only.

Finally, the analysis of groundmass of samples from 58 out of 64 known lava deposits for their Sr, Nd and Pb isotopic composition indicates a large influence of re-melted country rock for the two most evolved lavas (phonolites) within this succession. The Sr and Pb isotopes allow to exclude sediment assimilation for the observed increase in $^{87}Sr/^{86}Sr$ ratios in some of the phonolites, but nevertheless indicate an open system for the recent Tenerife plumbing system. After investigating all available data on potential end-members for elevated $^{87}Sr/^{86}Sr$ ratios, a hypothetical contaminant is constrained to explain the observed increase in phonolite $^{87}Sr/^{86}Sr$ ratios. Low Sr/Nd ratios indicate a highly differentiated rock was the contaminant, similar to the Granadilla ignimbrite or the Diego Hernández Formation, both from the pre-Teide/Pico Viejo succession. Major and trace element and $\delta^{18}O$ data are consistent with this type of highly differentiated rock being the contaminant to the Teide phonolites. AFC modelling shows that fractional crystallisation plays a strong role throughout the differentiation sequence, whereas for the most evolved lavas crustal melting might dominate.

Contents

CHAPTER 3

MICROANALYSIS OF FELDSPAR PHENOCRYSTS FROM TEIDE-PICO VIEJO COMPLEX AND ITS ASSOCIATED RIFT ZONES: CONSTRAINING THE LOWER CRUSTAL MAGMATIC PLUMBING SYSTEM BY MELT- AND EC-RAχFC-MODELLING

CHAPTER 4

BIMODALITY OF LAVAS IN THE POST-ICOD-COLLAPSE SUCCESSION IN TENERIFE - A CRUSTAL MELTING ORIGIN FOR THE TEIDE-PICO VIEJO PHONOLITES?

INTRODUCTION

The presented study deals with the petrogenetical constraints on the evolution of an oceanic island, using the example of Tenerife. Extensive geochemical analyses were conducted on the most recent eruptions of this island. These date back to 200ka overall and define the last major eruptive cycle on Tenerife, which shows continuous activity until the present day (Carracedo et al., 2007). The obtained geochemical results are embedded into a well-defined stratigraphic framework, which allows to characterise a dynamic plumbing system through time and space over this eruptive interval.

1.1. The Canary Islands

The Canary Islands are a 450km long volcanic belt that is located about 115km off West-Africa (Fig. 1.1). The archipelago comprises a chain of seven major volcanic islands that get progressively younger from East to West (e.g. Carracedo, 1999). This has been ascribed to the surface expression of a mantle plume or hotspot (Hoernle et al. 1993; Carracedo, 1994, 1996). Activity persists on even the oldest islands (except for La Gomera), which may be attributed to either an elongation of the plume head in direction of plate motion and therefore underneath the oldest islands (Zhang & Tanimoto, 1992) or to edge-driven convection (King & Anderson, 1998; King & Ritsema, 2000). A submarine seamount, called "Las Hijas" ("The Daughters") is located 70 km Southwest of El Hierro, and is possibly the next island to emerge above sea level (Rihm et al., 1998).

The Canary hotspot may originate from a plume from the Core-Mantle-Boundary to account for the increased magmatic productivity (Davies & Davies, 2009 and references therein). Davaille et al. (2005) observed seismically that the plume splits below 1400km depth to feed the Azores, the Canaries and the Cape Verdes. The overall melt production for the Canary Island hotspot has been determined by Sleep (1990) at ~1 Mg/s (=1000 kg/s). The overriding African plate shows relatively slow motion at ~10 mm/a, compared

to the oceanic crust in the Pacific (Duncan, 1981; Morgan, 1983).

The Canary Islands are situated above Mesozoic tholeiitic oeanic crust (Schmincke & Rihm, 1994; Hoernle, 1998; Schmincke et al., 1998; Neumann et al., 2000). A sharp transition between oceanic and continental crust was postulated by Neumann et al. (2005). They located the transition East from the Canary Islands with the lower slopes of the continental rise underlying Fuerteventura and Lanzarote. Magnetic chron S1 indicates an age of igneous oceanic crust west of Fuerteventura of ~175 Ma, while chron M25 implies an age of ~156 Ma for the oceanic crust below the easternmost Canary Islands (El Hierro and La Palma) (Klitgorg & Schouten 1986; Verhoef et al., 1991; Roest et al., 1992).
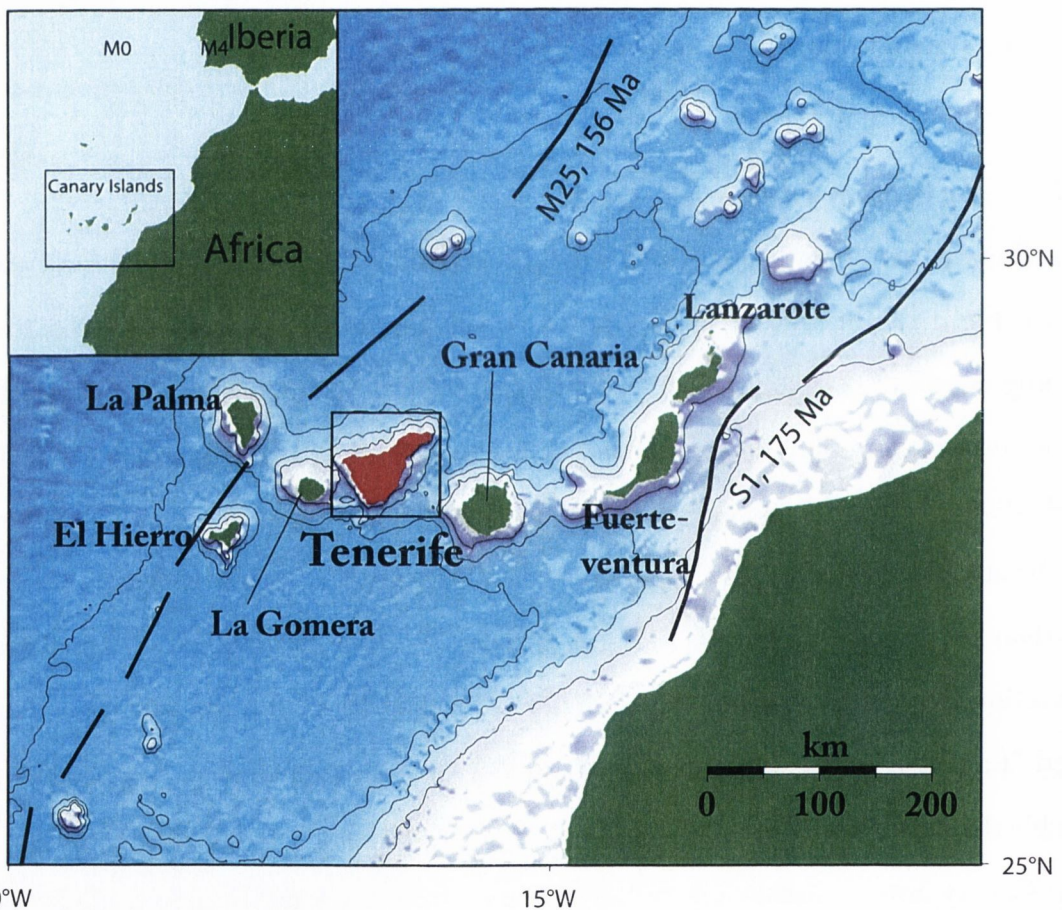
Fig. 1.1: Overview of the Canary Islands. Black lines indicate age constraints of underlying igneous oceanic crust based on magnetic anomalies (Roeser, 1982; Klitgord & Schouten, 1986; Roest et al., 1992).

The lithosphere was invoked Ranero et al. (1995) to thin out from about 100km thickness below the western Canary Islands to about 80km below Fuerteventura and Lanzarote. The oceanic crust has been found N and NE of Gran Canaria to be overlain

by of ~4km sediments above a ~7km thick igneous sequence (Ye et al., 1999). This 11km thick sequence of crust may be compacted underneath an island to about 3km of sediment (layer 3) and 2-4 km of igneous material (layer 1 & 2), with the Moho at ~15km depth, as suggested by Krastel et al. (2002) on the example of Gran Canaria.

1.2. Geology of Tenerife

Tenerife, as part of the Canary Island archipelago, is the fourth of the seven islands to have emerged and is located between Gran Canaria (older) and La Gomera (younger) (Abdel-Monem, 1971, 1972; Ancochea et al., 1990; Guillou et al., 2004b; Paris et al., 2005). Its oldest exposed deposits are outcrops of the largely covered central Miocene basaltic shield, which are named Roque Del Conde, and have been dated at 11.9 Ma (Guillou et al., 2004b). This central Miocene shield has been traced to continue towards the North East (Ancochea et al., 1990, Carracedo et al., 2009) and field and age data seem to suggest that it underlies the younger peripheral shield volcanoes of Anaga in the Northeast (Carracedo, 1979; Thirlwall et al., 2000; Guillou et al., 2004b; Walter et al., 2005; Carracedo et al., 2009) and Teno in the Northwest (Carracedo, 1979). These peripheral shields show mainly primitive volcanism although up-section they also contain trachytic and phonolitic dykes, plugs and lavas. Deeply eroded now, the main construction phases of Teno and Anaga ended 5 and 4 Ma ago respectively (Guillou et al., 2004b; Walter et al., 2005), but Teno showed renewed basaltic eruptions in the last 250 ka.
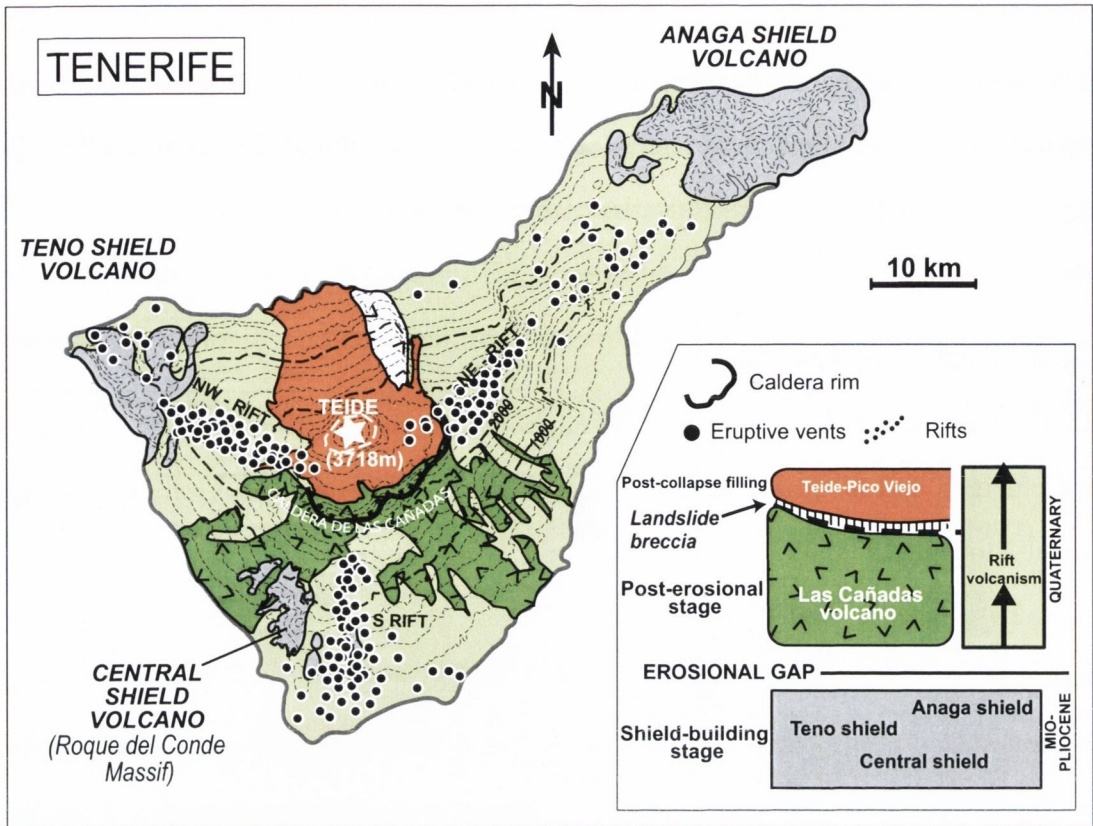
Fig. 1.2: Simplified geological map of Tenerife (modified after Carracedo et al. (2007); original file: courtesy of J. C. Carracedo). Note the distribution of monogenetic vents that indicate the three rift zones to the South, the Northeast and the Northwest.

The overall structure of the island was and is controlled by three rift zones, one to the South, one to the Northwest and another one to the Northeast (Fig. 1.2). The two latter of these three are currently active (Carracedo, 1994, 1996; Walter & Troll, 2003) and extend into Anaga and Teno (Carracedo et al., 2007). Principally showing mafic volcanism, some differentiated lavas occured in the Pleistocene as landslide fills on the North East rift (Carracedo et al., 2009). In more recent times, mafic eruptions form single or multiple (and then usually aligned) monogenetic cones only, which characterises the typical activity on the rift zones.

Coinciding with the cessation of volcanism on the peripheral shields, Tenerife's central part resumed erupting at around 3.5 Ma to build the central Las Cañadas Volcano. It consists of a complex Lower Group formation that comprised multiple eruptive centres and is separated from the Upper Group by a major unconformity. This Upper Group shows three cycles of activity, each from subordinate and primitive to large phonolitic explosive eruptions (Martí et al., 1994; Ancochea et al., 1999), culminated in a series of

caldera-forming ignimbrite eruptions from 1 Ma to 0.2 Ma (e.g. Wolff, 1983; Martí et al., 1994, 1997; Martí & Gudmundsson, 2000; Bryan et al., 2000; Brown et al., 2003; Brown & Branney, 2004; Edgar et al., 2007). The central Las Cañadas volcano collapsed laterally at around 200-180 ka (Watts & Masson, 1995; Carracedo, 1999, 2007) to leave behind the Icod landslide scar. Buried by subsequent eruptions, it still is morphologically recognisable as today's Valle de Icod (Valley of Icod). Márquez et al. (2008) extrapolated the layer of the now buried landslide debris that they found in watertunnels in the Valle de Icod to a height of 1000 masl to the South of Teide. Pre-existing vertical collapse structures may have initially aided lateral instability (e.g. Troll et al., 2002), but may have been largely destroyed by this event and the present day Las Cañadas Caldera may represent retrograde-erosive remains of a landslide headscarp (cf. Carracedo, 1999, 2007).
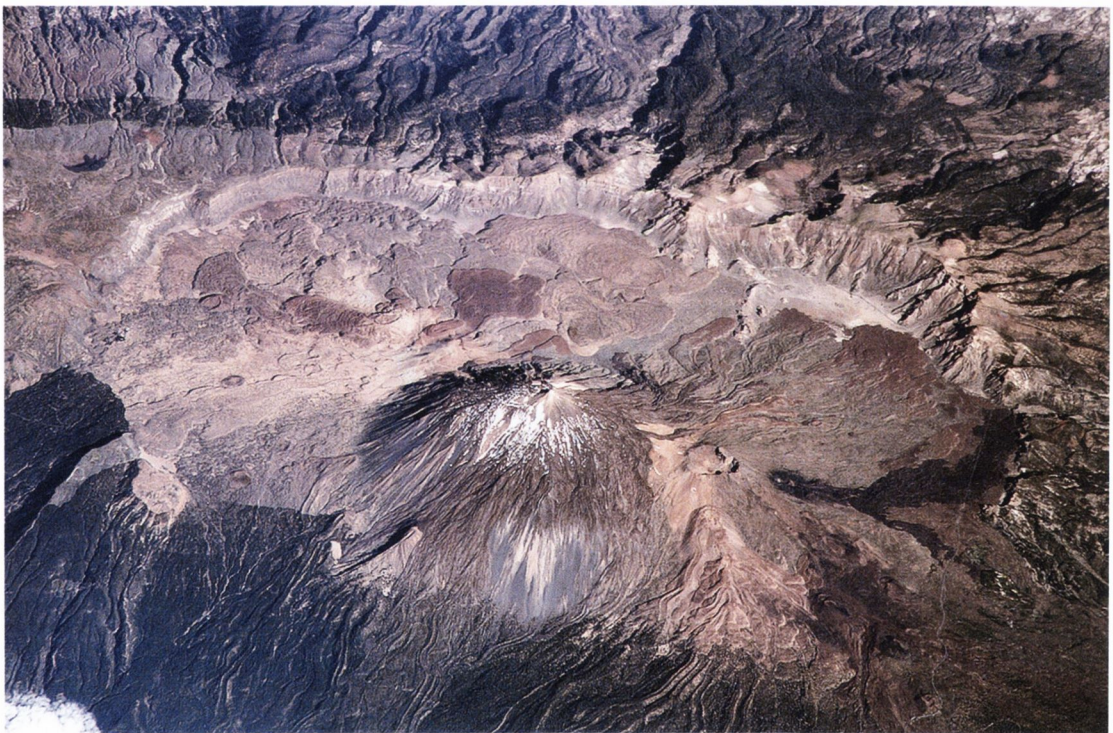
Fig. 1.3: Aerial view of the Las Cañadas Caldera with the nested complex of Teide-Pico Viejo. View towards South-South-East. Image courtesy: NASA.

The recent Teide-Pico Viejo central stratovolcano complex formed inside the Las Cañadas collapse scar after this collapse (<200 ka, Fig. 1.3) which, by now, has almost completely been filled by Teide-Pico Viejo's sequence of initial basanite to more recent phonolite lavas, with the Las Cañadas Caldera as a remnant surface expression of the pre-collapse

architecture. Activity has been initially exclusively mafic with the first appearance of intermediate lavas at around 14 ka BP and that of phonolites at around 9 ka BP (Carracedo et al., 2007). The sub-plinian Montaña Blanca eruption, located on the eastern flank of Teide, was probably the most violent eruption after the Icod collapse and occurred at around 2 ka BP (Ablay et al., 1995).

This succession of nested activity within the Cañadas Caldera has been complemented by exclusively monogenetic, basanite cones on the Northwest rift and scarcer but similar activity on the Northeast rift zone (Carracedo et al., 2007).

This most recent succession, the central Teide-Pico Viejo complex and its perimetre in the Las Cañadas Caldera and, in addition, the activity on the NW and NE rifts (after ~200 ka) represent the combined activity on the island after the Icod landslide. They are therefore termed post-Icod-collapse lavas herein and are the focus of this PhD thesis.
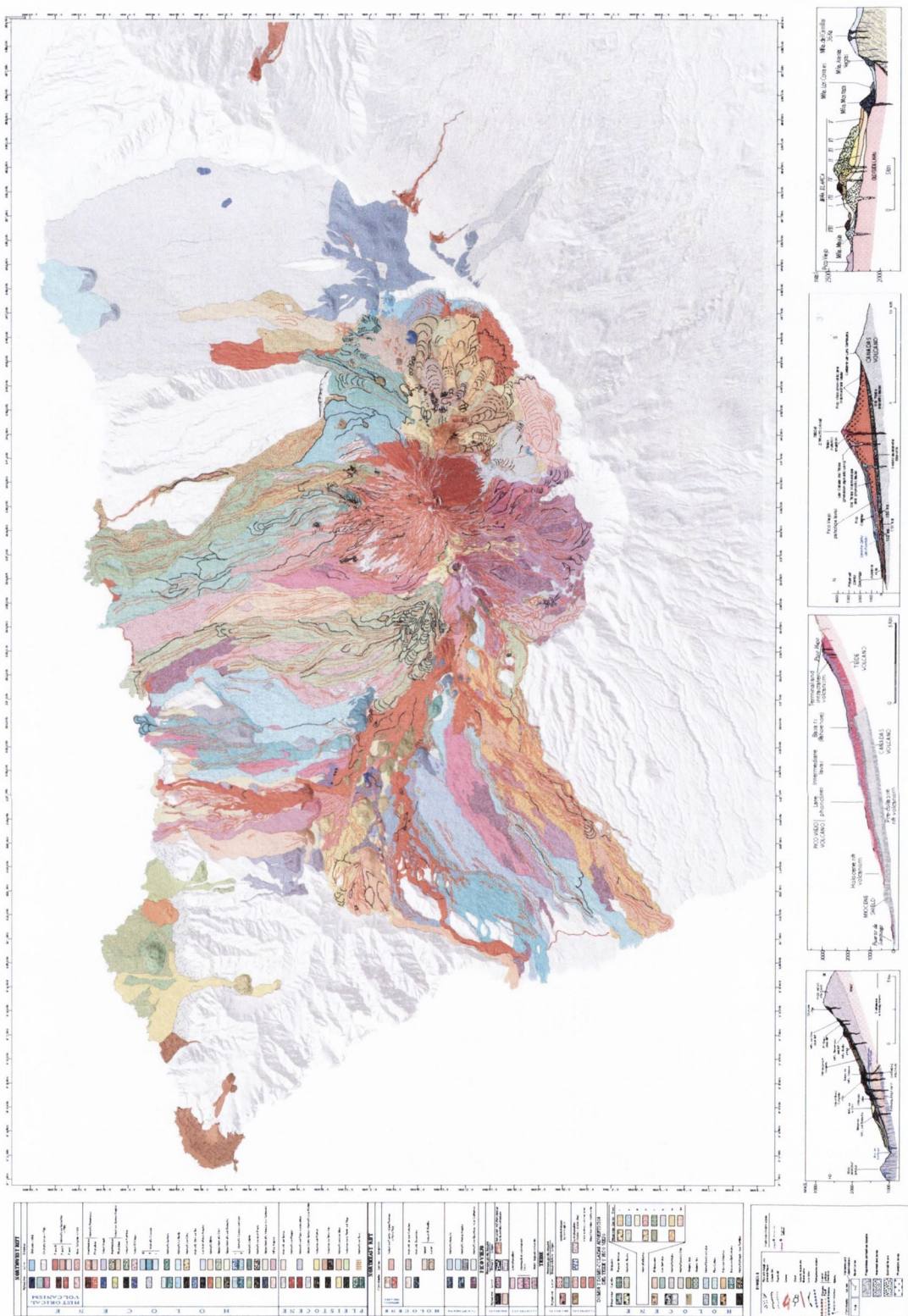
Fig. 1.4: Map of the recent post-collapse succession on Tenerife (Carracedo et al. (2007), printed with permission).

7

1.3. *Previous work and sample set*

The present work focusses on radiogenic isotope characteristics of the post-Icod-collapse lavas in Tenerife. The foundation of this study has been laid by three publications: Carracedo et al. (2007) made detailed age and stratigraphical constraints available, along with the map that is being printed here with permission (Fig. 1.4), Rodríguez-Badiola et al. (2008) provided a whole-rock major and trace element dataset on 100 representative samples and Carracedo et al. (2008) provided volume constraints for individual eruptions. The sampleset that these workers used, has been made available to us to proceed on geochemical analyses and interpretation of the post-collapse succession. Initially being used for mapping purposes, the sampleset comprised almost 600 samples, of which we selected a representative set of 229 samples to cover 58 of 64 known eruptions within this succession. Note, some eruptions comprise multiple phases. Six eruptions of the 64 known eruptions were only discovered after this project had commenced and, hence, are not included. However, all but two eruptions are present in the whole-rock dataset of Rodríguez-Badiola et al. (2008). This allows us to define three broad compositional groups of lavas (primitive, transitional and evolved) that underly the subsequent interpretation of isotope data (Table 1.1).

The rift zone lavas are exclusively basanites, aphyric or containing ol ± cpx ± plag. Phonotephrites and tephri-phonolites are grouped around the wider perimetre or form part of the central complex Teide-Pico Viejo. These rocks are either aphyric or contain cpx ± plag ± amp ± mt/il. Phonolites are geographically restricted to the central complex and radial vents of this edifice and contain afp ± cpx ± amp ± bt ± mt/il.

Table 1.1: Eruptions from Teide-Pico Viejo complex and the rift zones and the type of analyses performed on the sample suite

Eruption	Eruption phases	Samples	TAS	Groundmass analyses	Suite
Abejera Alta		ABA-21, ABA-22, ABA-36*	Pho	Pb	Evolved
Abejera Baja		ABB-19, ABB-20	Pho	Pb	Evolved
Montaña Abeque		ABQ-47*	Fo	Sr	Primitive
Volcán de Arafo		ARA-01*	Bas	Pb, Sr, Nd	Primitive
Montaña Arenas Negras		ARE-13	Bas	Pb, Sr, Nd	Primitive
Montaña del Banco		BAN-53	Bas	Pb, Sr, Nd	Primitive
Montaña Bilma		BIL-34*, BIL-36	Bas	Pb, Sr, Nd	Primitive
El Boquerón		BOQ-13, BOQ-14	Pho	Pb	Evolved
Montaña Botija		BOT-28*	Bas	Pb, Sr, Nd	Primitive
Montaña Cascajo	Phase 1	CA1-21, CA1-23*, CA1-75	Bas	Pb, Sr, Nd, O	Primitive
	Phase 2	CA2-20*	Bas	Pb, Sr, Nd	Primitive
	Phase 3	CA3-22, CA3-24*	Bas	Pb, Sr, Nd	Primitive
Pico Cabras		CAB-27	Pho	Pb, Sr, Nd	Evolved
Volcán de Boca Cangrejo		CAN-05, CAN-06*	Bas	Pb, Sr, Nd	Primitive
Chahorra		CHA-03*	PTe	Pb, Sr, Nd	Primitive
Chinyero		CHI-01*	Bas	Pb, Sr, Nd	Primitive
Volcan El Ciego		CIE-18, CIE-19*	TPh	Pb, Sr	Transitional
Montaña de Chío		CIO-32, CIO-77, CIO-81, CIO-82, CIO-83	BTa	Pb, Sr, Nd, O	Primitive
Montaña de Las Colmenas		COL-15*	TBa	Pb	Primitive
Montaña de Los Corrales		COR-04*, COR-05	Tan	Pb, Sr, Nd	Transitional
Montaña Cruz		CRU-39*	Bas	Pb, Sr, Nd	Primitive
Volcán Cuevas Negras		CUE-14*	Bas	Pb, Sr, Nd, O	Primitive
Montaña de La Cruz		DLC-18*	Tra		Evolved
Montaña Estrecho		EST-40*, EST-41	Bas	Pb, Sr, Nd	Primitive
Fasnia - Siete Fuentes		FAS-02*	Bas	Pb, Sr	Primitive
Montaña Garachico		GAR-04*	Bas	Pb, Sr	Primitive
Galería Rio de Guia (PV-EVO)		GRG-1300, GRG-2800, GRG-2850			
Montaña Guamasa		GUA-17	Bas	Pb, Sr	Primitive
Volcán Los Hornitos		HOR-17	Bas	Pb, Sr	Primitive
Montaña Juan Évora		JEV-03*	Bas	Pb, Sr	Primitive
Montaña Las Lajas		LAJ-23, LAJ-24*	TPh	O	Transitional
Las Lenguas		LEN-15*	Tra	Pb, Sr, O	Transitional
Montaña Majúa		MAJ-16, MAJ-17*	Pho	Pb, Sr, O	Evolved
Bocas de Doña María		MAR-31, MAR-37	BTa	Pb, Sr, O	Primitive
Montaña Blanca	Phase 1	MB1-34	Pho		Evolved
	Phase 3	MB3-11*	Pho		Evolved
	Phase 4	MB4-10*	Pho		Evolved
	Phase 5	MB5-04*, MB5-05	Pho	Pb	Evolved
	Phase 6	MB6-12*	Pho		Evolved
	Phase 7	MB7-08*	Pho	Pb, Sr	Evolved
	Phase 8	MB8-06, MB8-09*	Pho	Pb, Nd	Evolved
Montañetas Negras		MNE-33*	Bas	Pb, Sr	Primitive
Montaña Negra (Lavas Bco. de Vergara)		VER-32	Tra	Pb, Sr	Transitional

Table 1.1 continued: Eruptions from Teide-Pico Viejo complex and the rift zones and the type of analyses performed on the sample suite

Eruption	Eruption phases	Samples	TAS	Groundmass analyses	Suite
Montaña Mostaza		MOS-11*	TBa	Pb, Sr	Primitive
Montañas Negras		NEG-50, NEG-51	Bas	Pb, Sr, O	Primitive
Volcán del Palmar		PAL-56, PAL-57*	Bas	Pb, Sr	Primitive
Volcán Portillo	Lower unit	PO1-06*	Tan	Pb, Sr	Transitional
	Upper unit	PO2-07, PO2-09	Tan	Pb, Sr	Transitional
Pico Teide - Lavas Antiguos (Playa Sto. Domingo)		PT-ANT-16	Bas	Pb, Sr	Primitive
Pico Teide - Lavas Antiguos (Playa San Marcos)		PT-EAR-15	Bas	Pb	Primitive
Pico Teide - Intermediate Lavas		PT-INE-07, PT-INE-11, PT-INE-17	TPh	Pb, Sr, O	Transitional
Pico Teide - Lavas Negras		PT-LAE-02*, PT-LAE-03, PT-LAE-04, PT-LAE-05, PT-SUM-01	Pho	Pb, Sr, O	Evolved
Pico Viejo - Pa'hoe'hoe Lavas		PV-EAR-13, PV-EAR-15, PV-EAR-16, PV-EAR-17	PTe	Pb, Sr, O	Primitive
Pico Viejo - Evolved Lavas		PV-EVO-05*, PV-EVO-06, PV-EVO-07, PV-EVO-21, PV-EVO-28	Bas	Pb, Sr, O	Primitive
Pico Viejo - Intermediate Lavas		PV-INT-08, PV-INT-09, PV-INT-18, PV-INT-29	PTe	Pb, Sr, O	Primitive
Pico Viejo - Lavas De La Orotava		PV-LAT-01	Pho	Pb, Sr	Transitional
Pico Viejo - Phonolite I		PV-LAT-02, PV-LAT-03*, PV-LAT-04, PV-LAT-61, PV-LAT-66	Pho	O	Transitional
Cuevas del Ratón		RAT-44, RAT-84	PTe	Pb, Sr, O	Primitive
Roques Blancos		RBL-01, RBL-02*, RBL-03	Pho	Pb, Sr, O	Evolved
Montaña Reventada	Basanite	REV-87	Bas	Pb, Sr	Primitive
	Phonolite	REV-10, REV-64*, REV-71, REV-85	Pho	Pb, Sr	Transitional
	Enclaves	REV-09, REV-63*	PTe		Primitive
Montaña Samara		SAM-26, SAM-27	PTe	Pb, Sr	Primitive
Montaña de Los Silos		SIL-60	Bas	Pb, Sr	Primitive
Montaña de Taco		TAC-58	BTa	Pb	Primitive
Montaña de los Tomillos		TOM-14	PTe	Pb	Primitive
Montaña del Topo		TOP-55	Bas	Pb	Primitive
Volcán Tierra del Trigo		TRI-61	Bas	Pb, Sr	Primitive
Volcán Negro		VON-12, VON-13	PTe	Pb	Primitive

Eruptions and phases not represented in this study:

Montaña Blanca Phase 2 (phonolitic)			Pho		
*La Mancha Ruana (phonolitic, between Teide and Pico Viejo)			Pho		
*Hoya del Abrunco (trachytic, below Abejera Baja and Pico Cabras)			Tra		
*PT-CALV (primitive phreatomagmatic eruption Teide)			Bas		
PV-PHR (phreatomagmatic eruption PV)					
Los Gemelos (small phonolitic eruption between PT and PV)			Pho		
*Montaña Liferfe (phonotephritic NW rift zone eruption)			PTe		

Table 1.1.: List of lava flows covered in this work. Details on sample location, age, dating method and vent locations can be found in the electronic appendix and stem from Carracedo et al. (2007). Some eruptions comprise multiple phases of close temporal relation. The WR column marks units that have been analysed on wholerock major and trace elements by Rodríguez-Badióla et al. (2008), asterisks * denote samples that are present in both their and our dataset. Types of analysis: Pb = Pb isotopes, Sr = $^{87}Sr/^{86}Sr$, Nd = $^{143}Nd/^{144}Nd$, O = $\delta^{18}O$. All samples with groundmass data were principally attempted on three radiogenic isotopes Pb, Sr, Nd. In this, we did not always succeed, hence, there are a number of samples with one or two isotopic systems only. A selection of samples was chosen for $\delta^{18}O$ stable isotope analysis. Rocktypes: Bas = basanite; PTe = phonotephrite; TPh = tephriphonolite; Pho = phonolite; TBa = trachybasalt; BTa = basaltic trachyandesite; Tan = trachyandesite; Tra = trachyte. Suite indicates the classification of the lava according to its trace element fingerprint.

1.4. Classification of samples

In a TAS diagram (LeBas et al., 1986), following the flow chart of LeBas & Streckeisen (1991, Fig. 8 therein), rocks from the post-Icod-collapse succession plot as an alkaline trend from basanites to phonolites with a few excursions into the trachytic series. The bimodality of the composition of the lava flows is evident, as 97% of the known eruptions of the last 200 ka have been sampled, with only one sample per unit present in the dataset to avoid overrepresentation (Fig. 1.5).
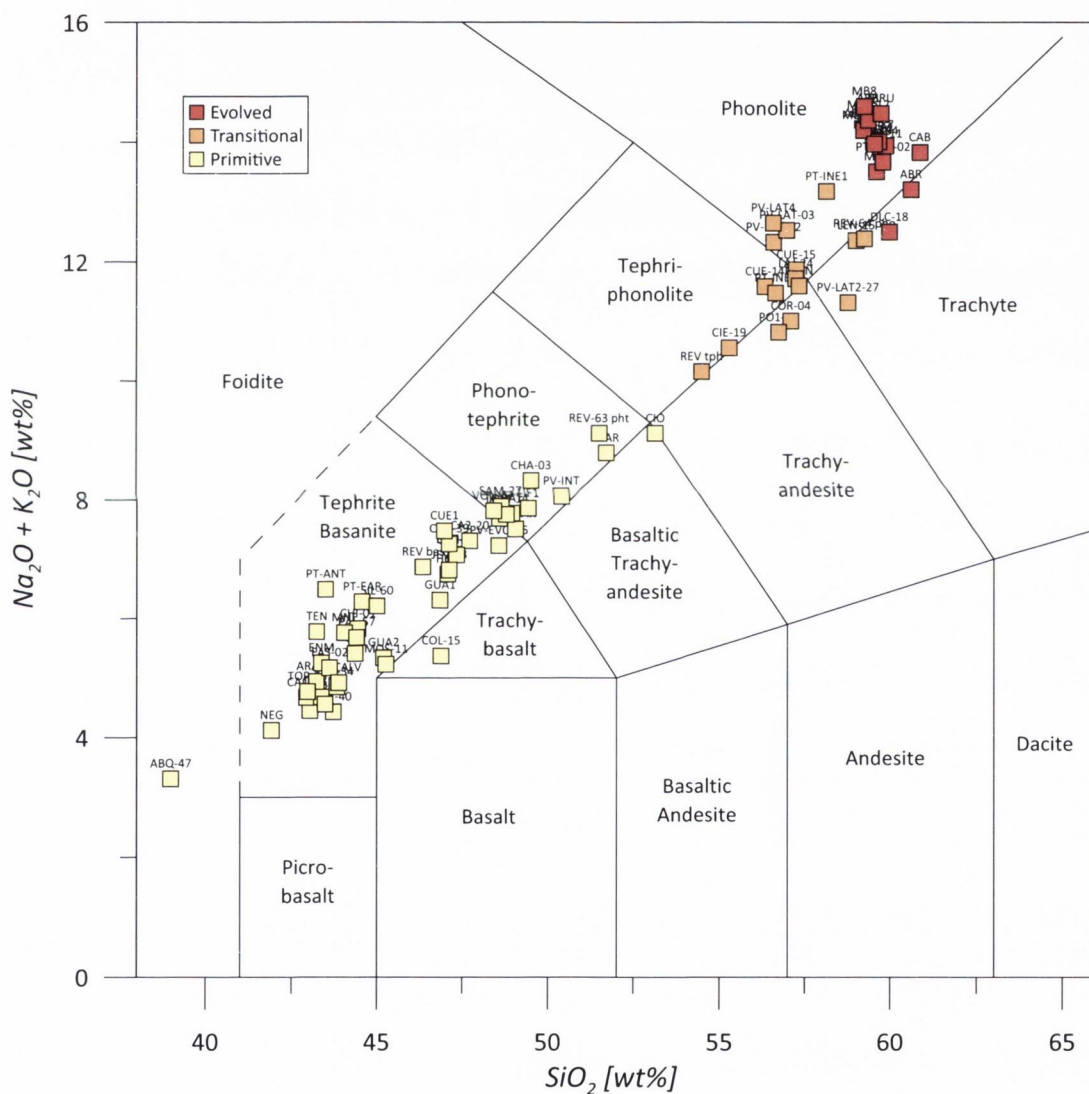
Fig. 1.5: Total alkali silica diagram after LeBas et al. (1986). Note loose clustering of transitional lavas and the steep trend defined by the evolved group. Data from Rodríguez-Badiola et al. (2008).

Primitive lavas range from foiditic compositions of up to 53 wt.% SiO_2 (basaltic trachyandesite). Transitional lavas span from 55 to 60 wt.% SiO_2, but are not very abundant up to 57 wt.% SiO_2, and mainly occur as loosely grouped tephriphonolites, phonolites and

trachytes. Evolved lavas tightly cluster around 60 wt.% SiO_2 and define a semi-vertical trend that is at a steep angle to the classic differentiation trend established by all three groups.

The post-Icod-collapse lavas (<200ka) can be categorised from their whole-rock trace element patterns into three groups. Rodríguez-Badiola et al. (2008) analysed 99 samples by XRF for major and trace element concentrations. Their samples cover all analysed units in this study and in many cases the same sample was analysed here. The lavas are arranged by parallel trends in their trace element patterns on a multi-element variation ("spider") diagram, i.e. trends that do not cross-cut each other. This defines groups of lavas that probably share a very similar geochemical history, which are further characterised by the presence of positive or negative anomalies in the elements Pb, Ba and Sr.

This approach is preferred over using conventional TAS diagrams, as major element concentrations may mask combinations of various petrogenetic processes. In turn, the concentrations of trace elements relative to each other are probably a better reflection of the underlying differentiation processes that gave rise to them. Trace element patterns of samples indicate, within certain limits, similar or distinct trace element ratios and are thus useful for discriminating overall magmatic histories.

Among the samples from this study, an overall enrichment of most trace elements can be observed with increasing degree of differentiation. The elements Ba and Sr deviate from this general pattern and show negative spikes in the evolved group. Also, the mid-REE (Nd, Sm, Eu, Gd, Tb and Dy) tend to get depleted with increasing differentiation by factors of 2 to 3. The elements Pr and Y remain largely unchanged by differentiation (Fig. 1.6).

Wolff & Palazc (1989) find similar elemental patterns in the Quarternary ignimbrite succession of Tenerife and attribute this to fractionation of feldspar and titanite. On Gran Canaria, Troll et al. (2003) also found titanite to be the controlling mineral for MREE depletion of the intermediate to evolved magmas of the Miocene Mogan Group volcanics.
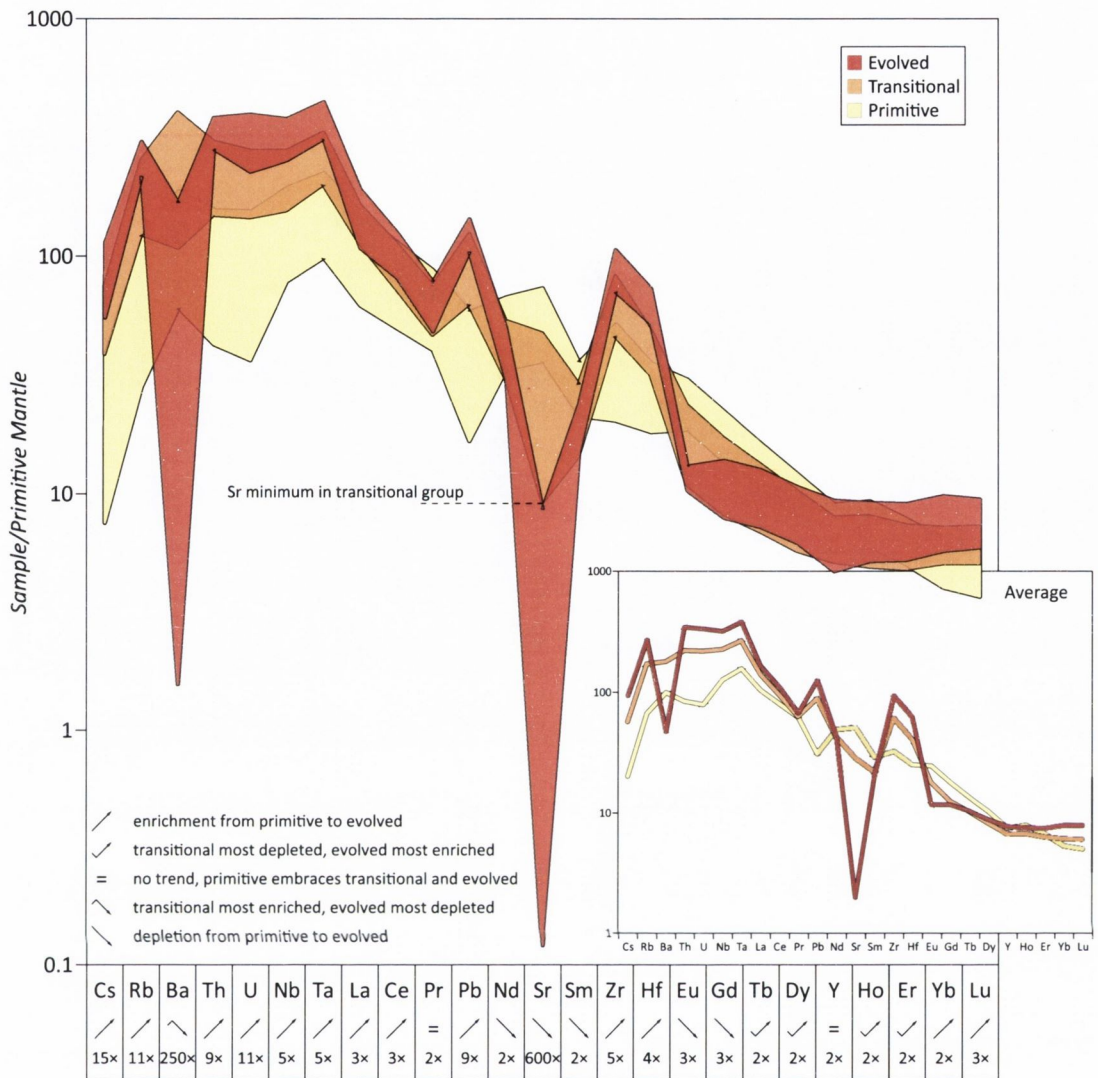
Fig. 1.6: Multi-element variation diagram for post-collapse lavas from Tenerife, normalised to primitive mantle after McDonough & Sun (1995). Inset shows averages of each group. Bottom bar shows trend for indiviual elements with increasing differentiation for total range of elements. For example, an upwards pointing arrow indicates an overall enrichment of that element from the primitive to the evolved group. A bent arrow indicates a depletion in transitional, followed by an enrichment in evolved lavas (or vice versa).

Three groups of lava rock are thus identified from the data of Rodríguez-Badiola et al.

(2008):

1.4.1. The primitive lavas (yellow)

The primitive lavas comprise all basanites and tephrites from the rift zones, one foidite, one basaltic trachyandesite and several intra-caldera and Teide-Pico Viejo phonotephrites and trachybasalts. They possess a negative Pb anomaly relative to the neighbouring elements on a multi-element variation diagram (Fig. 1.6). The primitive lavas are the most abundant in this study (n=40) and will be colour-coded in yellow throughout the rest of this work.

1.4.2. The transitional lavas (orange)

The transitional samples range from basaltic trachyandesites to trachyte and trachydacites and from tephriphonolites to phonolites. These samples show positive Pb anomalies, negative Sr anomalies and a small to absent negative Ba anomaly (Fig. 1.6). Sample REV-64 (Montaña Reventada trachyte) has a slightly lower Sr anomaly, but is, on grounds of its negative Ba anomaly, still grouped with the transitional lavas.

The transitional lavas erupted from either Teide and Pico Viejo or other vents inside the Las Cañadas Caldera. There is no clear structural boundary between the rift zones and central complex, as a result the transitional lavas can be assigned to the wider perimeter of the Teide-Pico Viejo twin stratocone system. Ten transitional units were analysed and will be colour-coded in orange.

1.4.3. The evolved lavas (red)

The third group is comprised of phonolites erupted from Teide-Pico Viejo or the flank vents of this central volcano. The evolved lavas include Montaña Blanca, Roques Blancos and the last eruption from Teide's central vent (Lavas Negras, 1150 ± 140 a BP, Carracedo et al., 2007). They are defined by strongly negative anomalies in both, Sr and Ba, with Sr being lower than a normalised value of 10 (Fig. 1.6). The evolved group (n=12) will be colour-coded in red. The range of yellow-orange-red is thus thought to indicate an increasing degree of differentiation (broadly basanite/phonotephrite - tephriphonolite -

phonolite).

Geographically, the vents of the three compositional groups display a crude concentric arrangement around the central vent of Teide (Fig. 1.7).
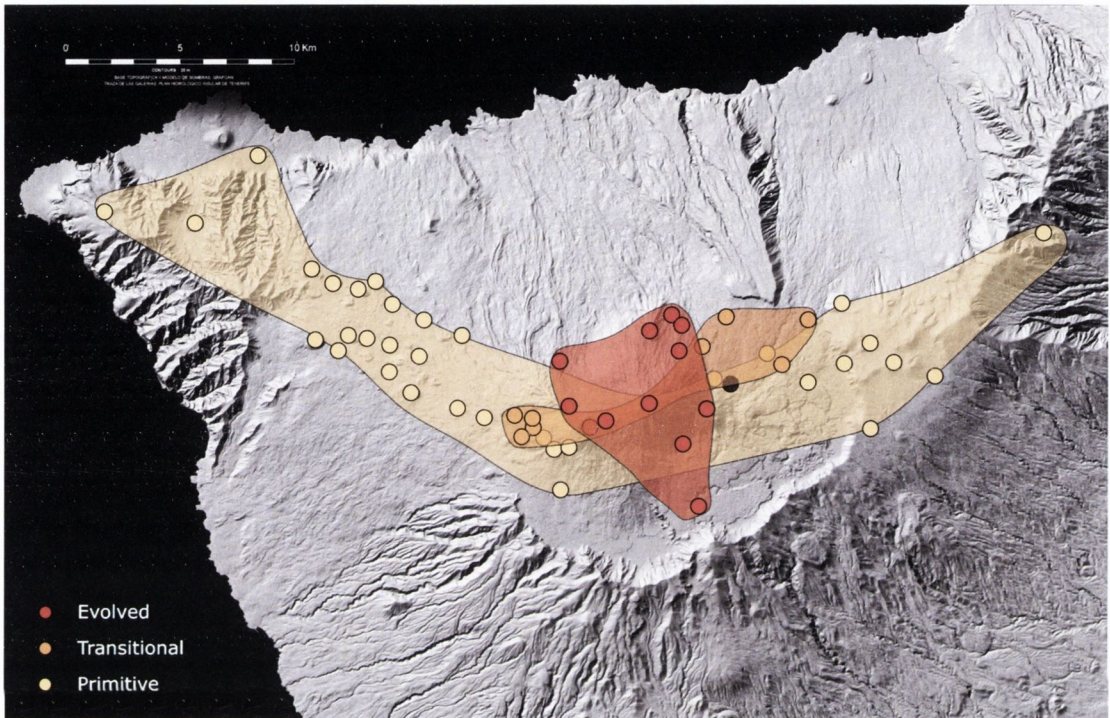
Fig. 1.7: Distribution of post-collapse vents on Tenerife. In red, evolved lavas, in orange, transitional lavas with primitive lavas in yellow. The black circle indicates Montaña de los Conejos for which whole-rock data was not available from Rodríguez-Badiola et al., 2008. This lava flow was not included in our study. Note the clustering of evolved lavas in and around the central complex, with the transitional lavas falling into the geographical and chemical transition between the two end-member compositions. The primitive lavas define the rift zones, but also occur in the older products of the central complex.

1.5. Overview of chapters

This most recent succession on Tenerife has been investigated, targeting three broad but distinct compositional groups of lava rocks that have been ientified (Fig. 1.4). This distinction had been made on grounds of trace element fingerprints, which provides a robust characterisation of lava rocks based on 25 trace elements and divides them into primitive, intermediate and evolved. The processes that were controlling the formation of these three compositional groups have a dedicated chapter each:

- First, a detailed case study of a composite lava flow provides a first-order example of the formation of intermediate or mixed rocks in this succession. This was achieved by combining major-/trace element and $^{87}Sr/^{86}Sr$, $^{143}N/^{144}Nd$, Pb-Pb and $\delta^{18}O$ data with detailed field evidence.

- Microanalysis of individual zones of feldspar phenocrysts for their major and trace element concentrations along with their $^{87}Sr/^{86}Sr$ ratios helped to reconstruct and model magmatic differentiation at lower crustal/upper mantle levels.

- Finally, we addressed the formation of felsic rocks in this succession (evolved group). The analysis of the groundmass of these lavas for three radiogenic isotope systems $^{87}Sr/^{86}Sr$, $^{143}N/^{144}Nd$ and Pb-Pb allows to constrain the formation of felsic melts. Furthermore, $\delta^{18}O$ ratios in selected feldspar and groundmass samples constrained potential effects of assimilation.

The 1100 AD Montaña Reventada composite eruption: interaction of genetically distinct magmas on ocean islands, Tenerife, Spain

1. INTRODUCTION

The combined recent succession of lavas in Tenerife comprises the Teide-Pico Viejo central complex and the adjacent rift zones that are a fundamental feature to the evolution of the structure of this ocean island edifice (Carracedo, 1994, 1996; Carracedo et al., 2007). Within this overall bimodal succession of mainly basanite and phonolite, lavas of intermediate composition occur, albeit of subordinate volumetric significance. The most conspicuous way of producing a hybrid magma is simple mixing of two compositionally distinct magmas (i.e. a mafic and a felsic one). In the majority of cases this manifests in a direct contact between mafic and felsic magma and often incomplete mixing that are observable in outcrop and on hand-specimen scale. In a review of this concept, Wilcox (1999) found some 650 publications that deal in some form with magma mixing, starting with Bunsen in 1851.

One of the key issues for understanding magma mixing in a given deposit is whether or not the distinct magmas co-existed for any appreciable amount of time in a stratified magma chamber prior to eruption and if they are co-genetic. Co-genetic, stratified magma chambers have frequently been hypothesised and the majority of mixed magma occurrences are explained this way (e.g. Sparks et al., 1977; Blake, 1981a; Huppert et al., 1982; Wolff and Storey, 1984; Blake and Ivey, 1986; Freundt and Schmincke, 1992; Araña et al., 1994; Kuritani, 2001; Troll and Schmincke, 2002). In addition, the intrusion of a genetically distinct magma into another has also been proposed to address the origin of mixed magmas, whereby the newly arriving magma triggers an eruption due to super-

heating and re-mobilisation (e.g. Turner, 1980; Turner and Campbell, 1986; Eichelberger et al., 2000; Izbekov et al., 2004; Troll et al., 2004). For example, Izbekov et al. (2004) suggested that a mafic dyke had dissected a resident andesitic magma chamber to give rise to the 1996-1999 eruption at Karymsky volcano, Kamchatka that erupted a range of mixed products.

As a case study of how intermediate magma may form in Tenerife, we focus on one particular example where two distinct magmas, basanite and phonolite, interacted to result in the apparent formation of a hybrid magma. Montaña Reventada is one of the most recent lava flows within the post-collapse succession in Tenerife. It erupted around 900 years ago from the wider perimeter of Pico Viejo as part of the Northwest rift zone (Carracedo et al., 2007), and emplaced a thin layer of basanite followed by a thick layer of phonolite that contains abundant dark inclusions. Araña et al. (1989, 1994) delivered a detailed description of this flow, along with a geochemical dataset that constrained the origin of the enclaves as being controlled by mixing and diffusional processes. Several discrepancies remain, however, partly due to inconsistencies between their major-/trace element and their isotopic datasets and partly due to a lack of geological background information available at the time. The present work overcomes these problems through a reliable, geochemically coherent dataset that rectifies the contradictions presented in this previous study. Furthermore, the detailed field and age constraints of Carracedo et al. (2007) allow a substantial revision of the magmatic processes and consequent dynamics envisaged for the Montaña Reventada eruption and place them into a meaningful geological context.

1.1. *Description of the Montaña Reventada lava flow and sampled outcrops*

Montaña Reventada consists of a group of vents located within the Northwest rift zone of the <200ka post-collapse series of Tenerife (Carracedo et al., 2007) (Fig. 2.1). Successive eruptions of basanitic and phonolitic lava make for a "composite" character of this monogenetic event. In contrast to the majority of composite eruptions, where a more felsic magma is followed by a more mafic one (e.g. Sparks et al., 1977; Blake, 1981;

Eichelberger et al., 2000; Troll & Schmincke, 2002; Troll et al., 2004), the initial pulse at Montaña Reventada consisted of a mafic component that was followed by a phonolitic phase.
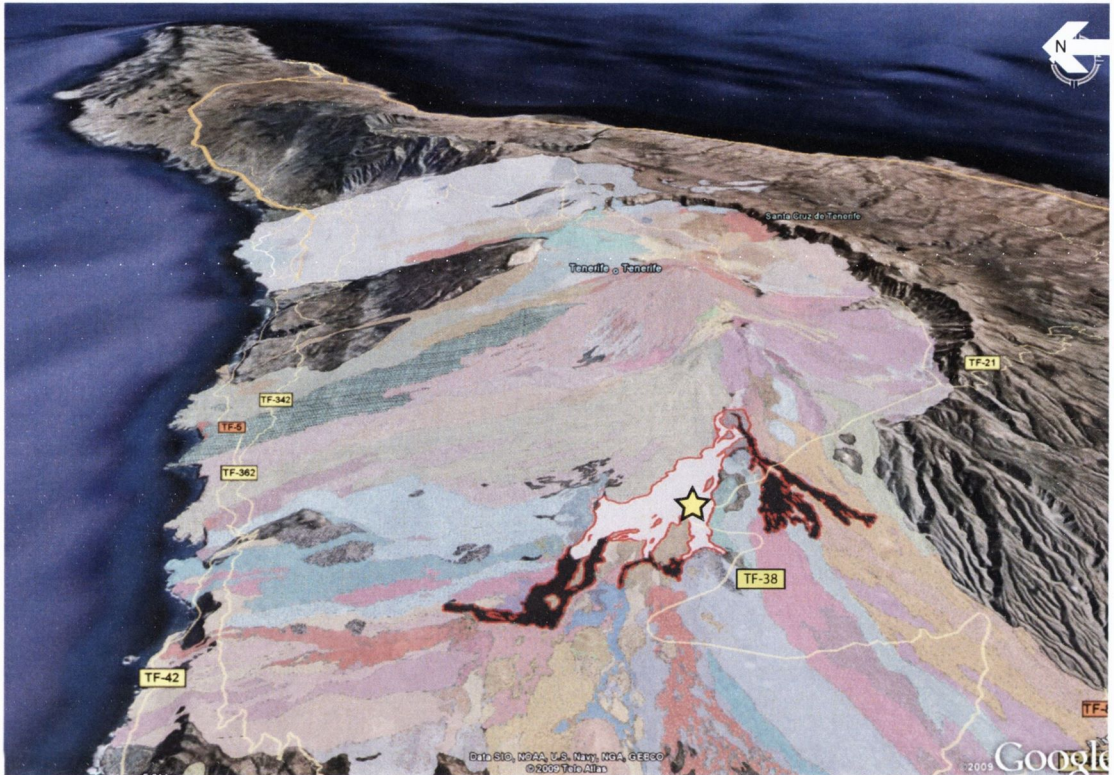
Fig. 2.1: Aerial view of the 900 BP Montaña Reventada lava, light grey field denotes the extent of phonolite lavas, dark grey the underlying basanite lavas (Google Earth, coloured fields are the geological map of the post-collapse succession on Tenerife after Carracedo et al., 2008). The star indicates the location of the sampled outcrop.

Two exceptional roadcut outcrops at 330437/3128642 (UTM 28R ±15 m) at either side of the road provide a view through the complete stratigraphy of this eruption, including the bottom contact with older lavas. This roadcut on TF-38 (also referred to as "Carretera Boca Tauce"), downhill from the Las Cañadas Caldera, has been previously described by Araña et al. (1994). After passing Montaña Samara, the road leads into a wide, sweeping left turn through the Montaña Reventada lava rocks. From bottom to top, the stratigraphy comprises:

- Red bottom breccia: about 10 to 20 cm thick. It is comprised of scoriaceous basanite, scarcely phyric and some parts show flow banding.

- Lower layer basanite: Massive, dark and mostly aphyric lava of variable thickness (20 - 200cm), that shows flow banding (overturned in places). Typical vertical cooling cracks are abundant. In places, the massive parts grade into welded scoria, where the

scoria clasts are of variable vesicularity.

- Upper layer phonolite: Massive, light-coloured and porphyritic lava of 10 - 12 m thickness. It contains about 10% alkali feldspar and scarce clinopyroxene. Scarce amphibole features opaque dehydration rims. Cooling fractures are less pronounced than in basanite. The lava contains melanocratic enclaves that range in size from few cm to up to 50 cm and appear to gradually decrease in abundance up-section. The contact between the basanite and the overlying phonolite is smooth and undulating, lacking any type of top or basal brecciation. In places, the phonolite intrudes the lower basanite or appears to lift out basanite blocks (<50cm). In one case, a cooling fracture of the underlying basanite appears to have been opened and filled with phonolite (see inset in Fig. 2.2). Here, the basanite shows a chilled margin against the intruded phonolite and, hence, was still hot when being intruded. In the first metre above the basanite-phonolite contact, vesicles between 2 mm and several cm are abundant. These are elongate and parallel to the contact and grade into equant shape at about 40cm above the contact. The phonolite becomes pink in the uppermost half metre (oxidies top) and mafic enclaves are almost completely absent near the top.

- The mafic enclaves that are contained within the phonolite are up to 50 cm across. There are two types of enclaves distinghuishable on a hand-specimen scale (four using petrography). One fraction (up to 10 cm) are angular, vesicular and scarcely porphyritic and have clearly been broken as solids, while another fraction (5 - 50 cm) is porphyritic and non-vesicular and has lobate outlines that have been deformed in a ductile fashion (blob-like). Chilled margins on the crystal-rich blob enclaves indicate a considerable temperature contrast between enclaves and host lava. The vesicular, scarcely phyric enclaves may indicate stronger undercooling (quenching), where instantaneous freezing caused volatiles to exsolve to form vesicles, thus aiding brittle fragmentation to make angular fragments (cf. Eichelberger, 1980; Troll et al., 2004).

- A top breccia that is up to 1.5m in thickness consists of large clinker and glassy blocks.
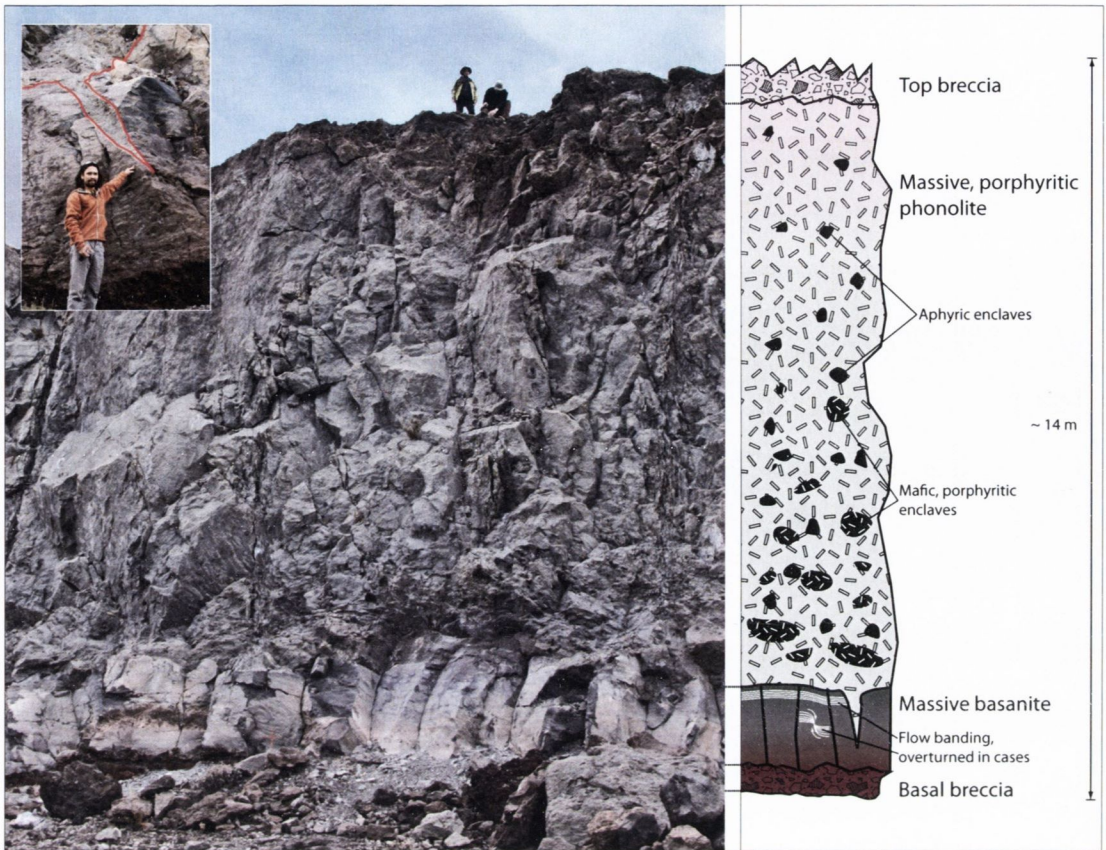
Fig. 2.2: Main outcrop of the Montaña Reventada composite flow. Note the volume relations of the basanite to the phonolite. The inset shows an opened fracture within the basanite that has been filled with phonolite.

Previous work

The Montaña Reventada eruption had been previously investigated by Araña et al. (1989 & 1994). Those two are essentially the same publication, one being in Spanish (1989) and one in English (1994), on the latter of which we focus here. In the present study, we are merging our dataset with that of Araña et al. (1994) and are adding solid isotopic evidence to advance understanding of the ongoing processes within a revised geological context. Araña et al. (1994) constrained the diffusional hybridisation of the enclaves that resulted from the interaction of the two distinct magmas. However, without detailed knowledge on the overall geological regime at the time, they presented a model that is in part incoherent with the present geological understanding of the recent magmatic plumbing system of Tenerife (e.g. Carracedo et al., 2007). Araña et al. (1994) argued in favour of diffusional processes acting at the interface between the basanite and the trachyte on grounds of major and trace element data. As a consequence, their mass balance calculations, combined with mineral abundances, allowed them to exclude a continuous differentiation series as an

origin for the hybrid enclaves. Furthermore, they found that the unequal distribution of mineral phases between two magmas can account for deviations of principal mixing trends in the resulting hybrid.

Although they were able to conclusively explain the hybridisation by mass balance calculations of major and trace elements, their Pb isotope data contradict this conclusion. Uncertainties also persist with their interpretation of the basanitic magma being erupted before the trachytic one (reclassified in this study as phonolite). They suggested that the basanite pooled below the trachyte in the magma chamber to create a diffusional interface. Subsequently, a temperature and density equilibrium between the two magmas was achieved that reduced the basanite's density below the one of the phonolite, in order for the basanite to erupt before the phonolite. This has been suggested in case of rapidly quenched enclaves that develop a foamy texture (e.g. Eichelberger, 1980; Coombs et al., 2003) and, hence, have a reduced density. However, for dense mafic inclusions, as found in Montaña Reventada, this remains unsubstantiated.

2. METHODOLOGY

To define the lithological units in more detail and constrain the formation of this composite eruption, samples were analysed for their major- and trace element concentrations as well as for their radiogenic and stable isotope systematics (Sr, Nd, Pb and O). This dataset is complemented by field and petrographical evidence, along with microanalytical data on Reventada feldspars from Chapter 3.

2.1. Samples and sample selection

The sample set consisted of 14 stratigraphically constrained whole-rock and six groundmass samples. For whole-rock analyses, three basanites, seven phonolites and four mafic enclaves were selected. Groundmass measurements encompassed two basanites and four phonolites. All samples are from the road section on TF-38 described above.

Unweathered pieces of sample were cut and selected for whole-rock and groundmass

analysis. The samples are generally fresh as they are of young age (900 BP). Nevertheless, cracks and rims affected by weathering were avoided. Samples for whole-rock and groundmass analyses were crushed in a jaw crusher and then hand-picked to separate enclave material from whole-rock samples and enclave material and crystal matter were also separated from groundmass samples. Approximately 30g of fresh, pristine chips were hand-picked and pulverised in a WC TEMA mill.

2.2. *Major and trace element analyses (X-ray Fluorescence)*

Samples were sent for XRF analysis to IFM-GEOMAR, Kiel, Germany. Samples were dried at 110°C before analysis. The major and trace element dataset was produced on fused beads using an automated Philips PW1480 x-ray spectrometer. Trace elements measured were Co, Cr, Ni, V, Zn, Ga, Rb, Ba, Th, Nb, La, Ce, Pr, Pb, Sr, Zr and Y. Among these Cr and Ni gave no useful results. All analyses were performed with a Rh tube; calibration was performed using international geological reference samples (cf. Abratis et al., 2002; Troll & Schmincke, 2002). Lithium tetraborate glass fusion beads were prepared following the methods of Norrish and Hutton (1969), with modifications after Harvey et al. (1973) and Brian et al. (1980). H_2O and CO_2 were determined by infra-red photometry (Rosemount CSA 5003) after heating the rock powder to 960 °C. Analyses listed in Table 2.3 are presented as hydrous.

2.3. *Trace element analyses (ICP-MS)*

Trace element analysis by ICP-MS was conducted by Frances Deegan at the Department of Petrology (FALW), Vrjie Universiteit, Amsterdam, Netherlands. Samples were prepared using a modified version of the method described by Turner et al. (1999). Samples and geochemical reference materials (~100mg) were dissolved using concentrated HF-HNO_3 in a ratio of 3:1 for in 30ml Savillex screw-top Teflon beakers. After digestion, the samples were dried down and refluxed with concentrated HNO_3. After digesting and nitrating the samples, they were re-dissolved in concentrated HNO_3. Aliquots of 1ml were taken for ICP-MS measurements and dried down. Samples were then diluted to make a 1:5000

3% HNO_3 measuring solution for the ICP-MS. All reagents were prepared using double-distilled concentrated acids and ultra pure water (>18 MΩ).

Table 2.1: Instrument settings and data acquisition parameters for trace element analyses (ICP-MS)

Instrument	Quadrupole Thermo X-Series II ICP-MS
Forward power (W)	1300
Reflected power (W)	< 3
Nebuliser	Meinhardt
Nebuliser gas flow rate (l/min)	0.85
Coolant gas flow rate (l/min)	14
Auxiliary gas flow rate (l/min)	1
Spray chamber	Scott double-pass water cooled (~1 °C)
Detector	ETP Dinode operating in PC and Analogue
Sensitivity	(2-5) × 10^7 counts per second / ppm ^{115}In and ^{238}U
Ion collection	Peak hopping
Dwell time* and points / peak	2.56-20.48 ms, 3 points / peak separated by 5 DAC units
Analysis time	90-s acquisitions (~60 sweeps), 4 repeats

Table 2.1.: Instrument settings and parameters for ICP-MS trace element analysis. *Dwell times were adjusted to minimise counting statistic errors, depending on individual isotope abundances and element response factors.

The samples were analysed using a Quadrupole Thermo X-Series II ICP-MS for trace and rare earth elements. Detection limits and analytical precision ranged from <100 ppb to <1 ppt, and relative analytical precision was typically ~2 to 5% (one standard deviation). See Table 2.1 for a summary of instrument settings and Eggins et al. (1997) for an in-depth description of the applied method.

2.4. *Radiogenic isotopic analyses*

All radiogenic isotopic analyses were conducted by Frances Deegan at the Department of Petrology (FALW), Vrjie Universiteit, Amsterdam, Netherlands.

300mg of homogenised sample powder was digested in a mixture of 6ml concentrated HF and 2ml concentrated HNO_3 at 150°C for about 3 days. The samples were then nitrated twice before beginning chemical separation procedures for Sr, Nd, and Pb. All samples for Sr, Nd and Pb isotopic analysis and standards and blanks were treated in the same manner. All errors are reported as 2 SD (Table 2.5).

2.4.1. *Sr isotope analysis*

Strontium extraction was performed using 0.075ml volume columns filled with Eichrom Sr spec resin. Columns were cleaned three times prior to separation with 3N HNO_3 and

ultra-pure water. Cleaning was repeated 3 times. The columns were then conditioned with 0.4ml of 3N HNO_3. The samples were re-dissolved in 6ml 3N HNO_3, of which 0.5ml was loaded onto the columns after centrifuging. The remaining sample solution was dried and re-dissolved in 6ml 2N HNO_3 for later Nd extraction. The prefraction was washed out with 3N HNO_3. Strontium was then collected by passing ultra-pure water through the columns. Samples were dried and nitrated twice before running on the TIMS.

In preparation for mass spectrometry, Sr samples were loaded onto single Re filaments with a mixture of TaCl and 1N phosphoric acid. Strontium isotope ratios were measured by thermal ionization mass spectrometry (TIMS) at the Department of Earth Sciences, Vrije Universiteit Amsterdam, Netherlands using a multicollector ThermoFinnigan MAT 262 system operating in static mode. Analyses were typically carried out at 3-4V, for 15 blocks (10 scans per block) per sample. Average multiple analyses of NBS 987-S = (0.710230) (n=77). Whole-procedural blanks were below 0.5 ng for Sr.

2.4.2. Nd isotope analysis

The samples were passed through TRU-spec resin columns to collect the REE fraction. Columns were washed three times with 2N HNO_3 and ultra-pure water and then conditioned with 2N HNO_3. The sample was dissolved in 6ml 2N HNO_3 prior to loading. The prefraction was washed out with 2N HNO_3. The REE were collected in ultra-pure water which was then evaporated and the sample re-dissolved in 0.165N HCl.

The resulting solution of REE was then passed through LN columns to collect Nd. Columns were washed three times with 6-7N HCl and 2N HF and then conditioned with ultra-pure water followed by 0.165N HCl. Samples were sonicated for 30 mins and centrifuged before loading onto the LN columns. The prefraction was washed out with 9ml 0.165N HCl. Neodymium was collected in 0.25N HCl. Samples were dried, nitrated, and diluted to produce a measuring solution of 800ng Nd in 4ml 1% HNO_3 for the Finnigan Neptune MC-ICP-MS.

Samples were analysed following the routine of Luais et al. (1997). The procedure yielded a typical Nd beam intensity of 10-12 V, occasionally up to 20 V have been recorded. A typical run lasted 18 min and consumed 300 ng of solution. Between samples

or standards, the Teflon tubing and glassware were cleaned with 3% distilled HNO_3 and 0.05N distilled HNO_3. The standard solution BHVO2 yielded 0.51298(5). Internal standard CIGO values during this study (n=9) were 0.51134(4) and the total procedural blank was < 200pg.

2.4.3. Pb–Pb isotope analysis

Samples were dissolved in 0.7N HBr, dried down and re-dissolved in 0.7N HBr. Columns were loaded with AGIx8 resin and washed twice with 6N HCl and ultra-pure water. Columns were conditioned with 0.7N HBr before loading the sample solution onto the columns. The prefraction was washed out with 0.7N HBr followed by 3N HCl. The Pb fraction was collected in 6N HCl, dried down, nitrated and diluted to produce a measuring solution of 400ng Pb in 4ml 1% HNO_3 for the Finnigan Neptune ICP-MS.

Pb isotopes were analysed by standard–sample bracketing using a Thermo Finnigan Neptune multi-collector ICP-MS. All analyses were conducted using a Cetac AX-100 autosampler, in combination with a Cetac Aridus desolvating nebuliser to introduce samples into the MC-ICP-MS. The wash-out time between analyses was 3 min, and uptake time 2 min. A total of 5 blocks of 20 cycles was measured, with integration times of 4 s per cycle. Levels of ^{201}Hg were always less than 0.05mV. See Table 2.2 for instrument settings.

Table 2.2: Pb isotope settings and data acquisition parameters

Instrument settings	
Sample uptake rate (Al/min)	50
Guard electrode	On
Rf power (W)	1200
Plasma gas flow rate (l/min)	15
Auxiliary gas flow rate (l/min)	0.7
Nebuliser gas flow rate (l/min)	0.9
Aridus gas flow rate Ar (l/min)	4.2-4.8
Aridus gas flow rate N_2 (l/min)	0.04-0.08
Sampling cone	Ni, 1.1 mm aperture
Skimmer cone	Ni, 0.8 mm aperture
Lens settings	Optimised for analyte signal intensity and stability
Data acquisition parameters	
Scan type	Static multi-collection
Cup configuration	L4: ^{201}Hg; L2: ^{204}Pb+Hg; C: ^{206}Pb; H1: ^{207}Pb; H2: ^{208}Pb; H3: ^{209}PbH
Sensitivity (V/ppm 208Pb) 200	200
Sampling time	5 blocks of 20 measurements of 4 s integration time

Table 2.2.: Instrument settings and parameters for MC-ICP-MS Pb isotope analysis.

For each measurement, the average of the two bracketing machine blanks was subtracted before calculation of the Pb isotopic ratios. The blank levels varied between sessions with intensities of 1.5–3.0 mV on ^{208}Pb. Variable blank correction always introduced less uncertainties than the error from counting statistics in the concentration range of our solutions.

A 100 ppb solution of NIST SRM-981 standard gave 16.9435(7), 15.5017(10) and 36.7297(15) for ^{206}Pb/^{204}Pb, ^{207}Pb/^{204}Pb and ^{208}Pb/^{204}Pb, respectively (n=2). The values of Baker et al. (2004) were used for normalisation. For the BHVO standard, these ratios yielded 18.6252(8), 15.5392(10) and 38.2269(17) for ^{206}Pb/^{204}Pb, ^{207}Pb/^{204}Pb and ^{208}Pb/^{204}Pb, respectively (n=2). Full procedure Pb blank solutions were in the order of 0.05 ppb, corresponding to 150 pg Pb. Data reduction was done offline, following the formula for sample–standard bracketing (Albarède et al., 2004). The error propagation was performed using relative errors (%). All errors given on Pb isotopic ratios are 2 standard deviations (absolute). A more detailed description of the method applied can be found in Elburg et al. (2005).

2.5. Oxygen isotope analysis

Oxygen isotope data were obtained on a subset of 13 samples at the University of Cape Town. Approximately 10 mg of whole-rock powder were analysed using conventional Ni reaction vessels. Ten samples were loaded in each sample run, of which two were the NBS28 quartz standard. Oxygen was produced by reaction with ClF_3 at 550 °C for at least three hours. The isotope ratios were measured using a gas-source Finnegan Mat DeltaXP mass spectrometer in dual inlet mode, and the results are reported in standard δ-notation relative to V-SMOW. The average value obtained for the NBS28 samples was used to normalize the raw data in each run to the SMOW scale assuming a value of NBS28 of 9.64 ‰. In practise, the difference between the raw and normalised data was < ~0.5 ‰. During the analysis of oxygen isotopes in this study, averaging the difference between duplicate NBS28 analyses gave an error of ±0.10 ‰ (cf. Fagereng et al., 2008 for

analytical details). A standard analytical uncertainty of 0.1 ‰ was applied (see Harris et al., 2000) (Table 2.5).

Table 2.3: *Montaña Reventada major and trace element data (XRF)*

	Top of phonolite:					Bottom of phonolite:						Basanite:					Enclaves in phonolite:			
Sample	207_4	207_5	207_6	207_4 GM	207_6 GM	206_2	206_3	206_5	206_2 GM	206_5 GM	206 Cont	205_1	205_2	205_3	205_1 GM	205_2 GM	E 206A	E 206B	E 206D	E 204F
[wt.%]																				
SiO_2	58.88	58.17	58.75	59.16	58.86	58.68	59.12	57.65	59.31	57.82	57.46	46.63	46.2	46.19	46.86	46.71	50.08	50.12	50.44	48.4
TiO_2	1.1	1.21	1.12	1.08	1.11	1.08	1.03	1.28	1.06	1.28	1.35	3.31	3.35	3.33	3.32	3.36	2.62	2.64	2.6	2.92
Al_2O_3	18.58	18.5	18.51	18.55	18.47	18.53	18.61	18.58	18.63	18.52	18.49	17.16	17.13	17.14	17.18	17.17	17.65	17.68	17.74	17.65
Fe_2O_3	4.54	4.99	4.57	4.53	4.76	4.56	4.41	5.09	4.54	5.09	5.3	11.13	11.22	11.21	11.09	11.19	9.04	9.04	9.02	9.84
MnO	0.17	0.16	0.16	0.17	0.17	0.16	0.16	0.17	0.16	0.17	0.17	0.18	0.18	0.18	0.18	0.18	0.18	0.18	0.18	0.21
MgO	1.09	1.28	1.12	1.06	1.12	1.05	1	1.33	1.04	1.35	1.46	4.42	4.53	4.55	4.48	4.58	3.35	3.44	3.39	3.75
CaO	1.98	2.35	2.1	1.96	2.08	1.99	1.87	2.65	1.97	2.63	2.89	9	9.15	9.12	9.06	9.14	6.91	7.01	6.89	7.72
Na_2O	7.67	7.67	7.81	7.73	7.88	7.91	7.85	7.7	7.9	7.64	7.59	4.94	4.97	4.93	4.83	4.86	6.3	6.05	6.07	5.67
K_2O	4.73	4.57	4.66	4.83	4.74	4.75	4.81	4.42	4.82	4.52	4.32	1.92	1.85	1.88	1.91	1.91	2.46	2.62	2.66	1.75
P_2O_5	0.29	0.35	0.31	0.29	0.32	0.29	0.28	0.37	0.29	0.38	0.4	1.26	1.29	1.3	1.29	1.29	0.99	1	1	1.17
H_2O	0.16	0.26	0.2			0.09	0.1	0.09			0.17	0.08	0.09	0.09			0.12	0.14	0.08	0.24
CO_2	0.02	0.01	0.02			0	0	0.01			0.04	0.02	0.02	0.02			0.02	0.02	0.01	0
Sum	99.29	99.52	99.37	99.6	99.76	99.24	99.4	99.5	99.98	99.67	99.69	100.28	100.17	100.13	100.51	100.7	99.91	100.1	100.29	99.45
[ppm]																				
Co	30	10	8	-	-	9	9	13	-	-	32	55	57	49	29	27	46	48	32	46
V	46	48	46	44	52	35	38	56	44	56	59	217	215	219	220	215	151	165	154	174
Zn	108	105	105	106	108	102	103	106	105	107	105	119	117	114	118	117	113	117	115	126
Ga	27	26	27	27	27	26	23	27	27	25	26	24	25	25	26	23	25	24	26	25
Rb	112	105	108	114	113	114	114	106	112	107	100	48	44	46	46	48	64	67	68	34
Ba	983	941	995	884	847	951	977	954	885	839	968	687	632	670	666	643	796	732	778	1148
Th	36	40	34	38	35	38	34	28	39	38	35	20	31	30	30	34	28	34	32	28
Nb	144	144	143	150	153	149	149	144	153	146	139	94	92	93	92	94	116	115	115	108
La	70	62	73	73	60	59	78	62	67	73	70	59	72	46	52	68	79	61	57	84
Ce	129	181	128	181	145	173	166	148	189	162	154	125	134	128	123	144	187	140	155	165
Pr	12	15	13	14	12	12	14	15	12	18	10	13	13	11	12	12	15	15	13	16
Pb	27	24	22	31	23	22	22	15	26	17	17	13	13	7	16	17	13	15	11	10
Sr	191	238	214	182	202	200	177	321	190	304	360	1125	1134	1133	1132	1135	953	966	950	1189
Zr	589	584	588	605	607	600	602	580	617	593	570	384	372	379	377	377	456	455	461	381
Y	17	20	18	19	18	19	20	21	19	20	20	29	29	32	28	29	27	27	28	34

Table 2.3.: Major and trace element data, analysed by XRF, from the Montaña Reventada composite eruption. Note that data are in stratigraphical order: 207 is the top of the phonolite, 206 is the bottom of the phonolite and 205 is the underlying basanite. No significant difference between the top and bottom phonolite was detected and both are not distinguished in more detail thereafter. GM in a sample name denotes a groundmass sample, "Cont" is the phonolite sample from just above the contact between the basanite and the phonolite.

Table 2.4: Montaña Reventada trace element data (ICP-MS)

Sample	Top of phonolite:					Bottom of phonolite:						Basanite:					Enclaves in phonolite:			
	207_4	207_5	207_6	207_4 GM	207_6 GM	206_2	206_3	206_5	206_2 GM	206_5 GM	206 Cont	205_1	205_2	205_3	205_1 GM	205_2 GM	E 206A	E 206B	E 206D	E 204F
Li	17.11	18.71	16.34	16.68	13.52	16.42	20.49	14.76	14.05	14.03	11.90	5.71	10.81	8.26	5.94	9.33	6.79	11.76	12.70	7.18
Be	4.51	4.57	3.41	5.19	3.04	5.44	6.72	4.28	4.81	4.74	3.45	2.72	3.33	2.30	2.42	2.74	3.34	2.69	3.42	2.56
Sc	1.68	2.89	2.11	1.72	1.72	1.65	2.18	2.23	1.59	2.20	1.91	8.79	12.69	9.47	8.57	10.71	7.91	6.17	7.19	7.40
Ti	6315	7718	7163	6811	5777	6450	7910	6852	6374	8129	6185	18475	24698	16337	17612	20208	15208	12766	15444	16220
V	31.9	44.4	33.1	34.8	26.7	33.4	38.2	42.5	32.5	49.6	37.5	207.4	274.5	177.1	198.9	218.4	144.5	120.93	151.68	153.98
Cr	0.50	0.73	0.15	0.54	0.25	0.53	0.75	1.03	0.53	0.58	0.61	0.78	0.46	1.18	0.42	0.36	0.50	0.70	0.66	0.86
Co	50.50	25.42	4.05	3.03	2.85	21.99	24.51	20.09	2.76	4.65	39.22	52.95	77.46	46.02	24.00	26.27	57.14	44.29	36.30	41.29
Ni	0.37	0.35	0.41	0.30	0.11	0.24	0.27	0.55	0.29	0.35	0.41	1.13	1.60	1.35	1.09	1.17	0.91	0.83	0.82	0.54
Cu	3.82	5.28	4.08	3.90	3.22	3.25	4.13	4.56	3.74	4.76	4.47	16.96	22.03	15.34	17.14	17.69	9.19	9.99	11.62	11.07
Zn	126.3	150.6	153.6	127.6	106.3	131.2	164.7	123.3	122.4	131.0	103.7	136.3	168.8	126.9	129.3	140.0	140.9	118.4	142.9	150.6
Ga	22.31	24.21	21.68	24.74	16.22	23.88	30.56	21.17	23.43	24.56	17.66	21.65	28.84	19.23	20.28	22.97	23.43	18.98	24.15	21.41
Rb	90.05	97.71	86.14	91.28	62.88	101.62	116.55	79.90	91.25	95.38	64.70	39.50	36.31	29.89	36.00	33.18	58.16	47.98	53.57	25.93
Sr	171.3	244.7	203.0	159.1	155.6	186.7	218.4	274.0	154.2	270.4	239.6	982.1	1327.3	936.7	910.3	1068.2	968.5	767.4	885.2	1075.5
Y	25.48	30.18	20.05	26.46	16.55	26.74	36.18	24.68	22.63	25.67	18.63	28.90	44.43	31.47	28.20	35.58	38.41	27.72	33.46	36.16
Zr	572.9	610.3	602.8	651.4	466.6	620.5	774.4	538.1	626.2	631.3	445.1	366.5	447.4	306.0	340.9	375.8	448.6	370.4	471.8	355.3
Nb	146.6	157.8	162.0	165.1	121.8	157.8	192.1	134.4	157.3	164.4	113.8	82.3	115.3	77.5	81.3	99.8	113.4	93.3	110.3	110.8
Mo	1.49	1.66	1.33	1.69	0.89	1.56	1.89	1.04	1.59	1.23	0.89	0.75	0.97	0.66	0.67	0.75	1.04	0.91	1.15	0.60
Rh	0.00	0.00	0.00	0.00	0.00	0.00	0.00	0.00	0.00	0.00	0.00	0.00	0.00	0.00	0.00	0.00	0.00	0.00	0.00	0.00
Cd	0.06	0.09	0.07	0.06	0.07	0.13	0.13	0.08	0.09	0.08	0.06	0.07	0.10	0.08	0.06	0.10	0.11	0.08	0.10	0.12
In	0.10	0.08	0.08	0.10	0.07	0.11	0.14	0.10	0.11	0.12	0.09	0.20	0.25	0.16	0.19	0.19	0.16	0.13	0.17	0.18
Sn	2.27	2.41	2.08	2.56	1.66	2.38	2.93	2.08	2.23	2.46	1.76	1.45	2.26	1.46	1.39	1.81	1.92	1.55	1.82	1.87
Sb	0.48	0.50	0.48	0.54	0.39	0.46	0.57	0.36	0.55	0.44	0.36	0.15	0.20	0.13	0.15	0.17	0.27	0.23	0.36	0.19
Cs	1.07	1.08	0.79	1.00	0.61	1.06	1.34	0.80	0.89	0.77	0.61	0.32	0.32	0.33	0.38	0.40	0.72	0.51	0.54	0.25
Ba	975.8	1055.4	1032.9	839.8	694.3	996.9	1289.7	881.1	789.1	796.4	668.5	581.9	728.4	528.8	526.1	616.2	780.3	594.6	708.7	1053.7
La	78.72	89.22	56.45	78.08	45.89	82.42	111.49	72.12	69.20	74.16	54.85	59.52	86.93	60.33	58.41	70.91	84.60	61.32	71.91	85.79
Ce	136.4	156.3	97.9	138.0	82.0	146.6	194.9	130.3	121.8	133.0	103.4	140.9	185.7	125.2	128.1	149.0	166.6	125.3	155.0	176.7
Pr	13.35	15.22	8.90	13.38	7.55	14.23	18.99	12.78	11.76	12.91	9.80	13.61	19.97	14.04	13.14	16.28	18.02	13.01	15.24	17.63
Nd	44.58	51.74	29.37	44.87	25.04	47.57	62.85	43.64	39.16	44.05	33.88	53.70	79.41	55.84	51.46	64.77	67.83	48.97	57.66	65.57
Sm	6.93	8.08	4.61	7.03	4.05	7.48	9.95	6.97	6.04	7.12	5.46	9.76	14.72	10.46	9.35	11.87	12.07	8.86	10.30	11.44
Eu	2.18	2.59	1.92	2.20	1.56	2.28	3.06	2.17	1.91	2.25	1.72	3.13	4.71	3.32	2.97	3.81	3.87	2.79	3.31	3.91
Tb	0.83	0.97	0.60	0.84	0.50	0.88	1.17	0.83	0.71	0.81	0.65	1.14	1.68	1.19	1.07	1.38	1.41	1.02	1.21	1.33

Table 2.4 continued: Montaña Reventada trace element data (ICP-MS)

Sample	Top of phonolite:					Bottom of phonolite:						Basanite:					Enclaves in phonolite:			
	207_4	207_5	207_6	207_4 GM	207_6 GM	206_2	206_3	206_5	206_2 GM	206_5 GM	206 Cont	205_1	205_2	205_3	205_1 GM	205_2 GM	E 206A	E 206B	E 206D	E 204F
Gd	5.41	6.46	3.75	5.49	3.16	5.74	7.50	5.46	4.84	5.57	4.19	8.46	12.74	9.12	8.10	10.35	10.22	7.48	8.83	9.63
Dy	4.54	5.31	3.31	4.73	2.81	4.84	6.32	4.50	4.02	4.52	3.53	5.83	8.73	6.25	5.64	7.27	7.54	5.51	6.59	7.06
Ho	0.84	0.95	0.62	0.89	0.54	0.88	1.17	0.81	0.75	0.84	0.63	1.05	1.54	1.10	0.98	1.27	1.32	0.96	1.15	1.24
Er	2.38	2.72	1.82	2.51	1.60	2.51	3.28	2.30	2.12	2.30	1.76	2.61	3.81	2.70	2.45	3.15	3.44	2.45	3.03	3.16
Tm	0.35	0.40	0.27	0.38	0.24	0.38	0.50	0.35	0.31	0.34	0.25	0.35	0.50	0.36	0.31	0.42	0.46	0.33	0.42	0.42
Yb	2.29	2.59	1.76	2.45	1.53	2.33	3.20	2.20	2.10	2.24	1.65	2.11	2.99	2.15	1.97	2.47	2.87	2.04	2.56	2.49
Lu	0.32	0.36	0.25	0.34	0.21	0.34	0.45	0.31	0.28	0.30	0.23	0.28	0.39	0.28	0.25	0.32	0.38	0.27	0.33	0.33
Hf	9.59	10.07	9.31	11.10	7.83	10.86	13.18	9.35	10.79	10.71	7.68	7.04	8.53	5.95	6.29	7.32	8.28	6.65	8.43	6.53
Ta	8.28	8.17	7.85	8.43	6.01	8.75	10.39	7.51	8.14	8.20	6.41	5.75	7.20	4.63	4.87	5.54	7.07	5.64	6.74	6.05
W	154.2	79.6	34.2	2.9	1.8	108.9	117.8	73.4	2.3	1.8	129.0	145.1	240.7	109.0	0.8	0.9	271.3	171.6	112.7	136.7
Re	0.00	0.00	0.00	0.00	0.00	0.00	0.00	0.00	0.00	0.00	0.00	0.00	0.00	0.00	0.00	0.00	0.00	0.00	0.00	0.00
Pb	7.10	7.44	6.04	7.65	4.64	8.52	10.04	6.28	7.28	6.59	4.81	3.18	3.75	2.60	2.92	3.11	5.26	4.11	4.99	3.26
Tl	0.19	0.12	0.10	0.18	0.06	0.27	0.32	0.18	0.24	0.16	0.14	0.06	0.12	0.08	0.05	0.11	0.16	0.14	0.19	0.09
Pb	8.27	8.57	6.75	8.67	5.25	8.91	10.93	7.34	8.18	7.93	5.53	3.52	4.09	2.88	3.18	3.62	5.43	4.12	5.32	3.53
Bi	0.01	0.01	0.04	0.06	0.02	0.02	0.03	0.01	0.36	0.06	0.01	0.02	0.02	0.01	0.14	0.05	0.02	0.02	0.02	0.01
Th	13.99	15.06	11.83	14.87	10.63	14.90	19.87	12.27	12.45	12.57	8.97	6.48	8.59	6.32	5.59	7.21	11.07	7.68	11.09	6.36
U	3.58	3.73	2.75	3.75	2.33	3.71	4.68	3.28	3.29	3.49	2.79	1.90	2.19	1.55	1.68	1.86	2.43	2.00	2.49	1.59

Table 2.4.: Trace element data (ICP-MS) from the Montaña Reventada composite eruption. All data are given in ppm. Note that data are in stratigraphical order: 207 is the top of the phonolite, 206 is the bottom of the phonolite and 205 is the underlying basanite. GM in a sample name denotes a groundmass sample. GM in a sample name denotes a groundmass sample, "Cont" is the phonolite sample from just above the contact between basanite and phonolite.

Table 2.5: Montaña Reventada isotope data

Sample	$^{87}Sr/^{86}Sr$ (2σ)	$^{143}Nd/^{144}Nd$ (2σ)	$^{206}Pb/^{204}Pb$ (2σ)	$^{207}Pb/^{204}Pb$ (2σ)	$^{208}Pb/^{204}Pb$ (2σ)	$\delta^{18}O$ [‰, SMOW]	$\delta^{18}O$ 2σ [‰, SMOW]
Top of phonolite:							
207_4	0.703049 (11)	0.512900 (46)	19.7767 (8)	15.6219 (10)	39.5980 (18)	6.84	0.1
207_5	0.703045 (17)	0.512865 (43)	19.7761 (7)	15.6210 (9)	39.5929 (14)		
207_6	0.703049 (10)	0.512910 (46)	19.7802 (7)	15.6210 (9)	39.5983 (15)	6.81	0.1
207_4GM	0.703077 (7)	0.512863 (46)	19.7723 (10)	15.6203 (16)	39.5873 (22)	6.70	0.1
207_6GM	0.703032 (9)	0.512870 (37)	19.7750 (12)	15.6209 (17)	39.5931 (25)	6.89	0.1
Bottom of phonolite:							
206_2	0.703032 (7)	0.512900 (43)	19.7807 (11)	15.6232 (14)	39.5997 (23)	6.60	0.1
206_3	0.703046 (7)	0.512848 (42)	19.7762 (6)	15.6175 (9)	39.5845 (14)		
206_5	0.703056 (9)	0.512879 (38)	19.7746 (6)	15.6189 (8)	39.5882 (13)	6.83	0.1
206Cont	0.703062 (9)	0.512875 (34)	19.7723 (6)	15.6178 (8)	39.5835 (14)		
206_2GM	0.703055 (8)	0.512882 (37)	19.7708 (10)	15.6195 (15)	39.5843 (22)	6.22	0.1
206_2GM rep	0.703066 (7)						
206_5GM		0.512883 (39)	19.7671 (9)	15.6168 (15)	39.5769 (19)	6.53	0.1
Basanite:							
205_1	0.703040 (7)	0.512896 (46)	19.7418 (16)	15.6122 (17)	39.5607 (31)	7.90	0.1
205_2	0.703040 (7)	0.512867 (39)	19.7401 (10)	15.6163 (9)	39.5673 (20)	6.83	0.1
205_3	0.703032 (9)	0.512877 (35)	19.7355 (7)	15.6213 (9)	39.5720 (14)		
205_1GM	0.703046 (9)	0.512862 (36)	19.7377 (9)	15.6173 (16)	39.5638 (18)	6.00	0.1
205_2GM	0.703024 (10)	0.512855 (38)	19.7193 (10)	15.6146 (17)	39.5423 (22)	6.04	0.1
Enclaves in phonolite:							
E 206A	0.703036 (8)	0.512899 (42)	19.7641 (12)	15.6196 (15)	39.5858 (23)	6.68	0.1
E 206B	0.703059 (9)	0.512871 (46)	19.7528 (7)	15.6117 (8)	39.5603 (15)		
E 206D	0.703032 (7)	0.512875 (40)	19.7594 (7)	15.6175 (8)	39.5786 (14)		
E 204F	0.703039 (6)	0.512875 (38)	19.7660 (8)	15.6142 (9)	39.5701 (16)	6.16	0.1

Table 2.5.: Isotopic data (Sr: TIMS, Pb and Nd: MC-ICPMS, Oxygen: stable isotope mass spectrometry) from the Montaña Reventada composite eruption. All errors are 2 SD. Note that data possesses a stratigraphical order: 207 is the top of the phonolite, 206 is the bottom of the phonolite and 205 is the underlying baanite. No significant difference between the top and bottom phonolite was detected. GM in a sample name denotes a groundmass sample.

3. RESULTS

3.1. Petrography and feldspar compositions

Reventada basanite is essentially aphyric with scarce feldspar phenocrysts being occasionally present. The rock is vesicle-free in hand-specimen. The microcrystalline, melanocratic groundmass consists of lath-shaped feldspar, mafic microlites with high birefringence colours and opaque minerals, probably magnetite and ilmenite. The groundmass shows abundant lamination, which in places is folded and overturned. Micro-vesicles are few, but when found they are equant-shaped or slightly elongate (Fig. 2.3).
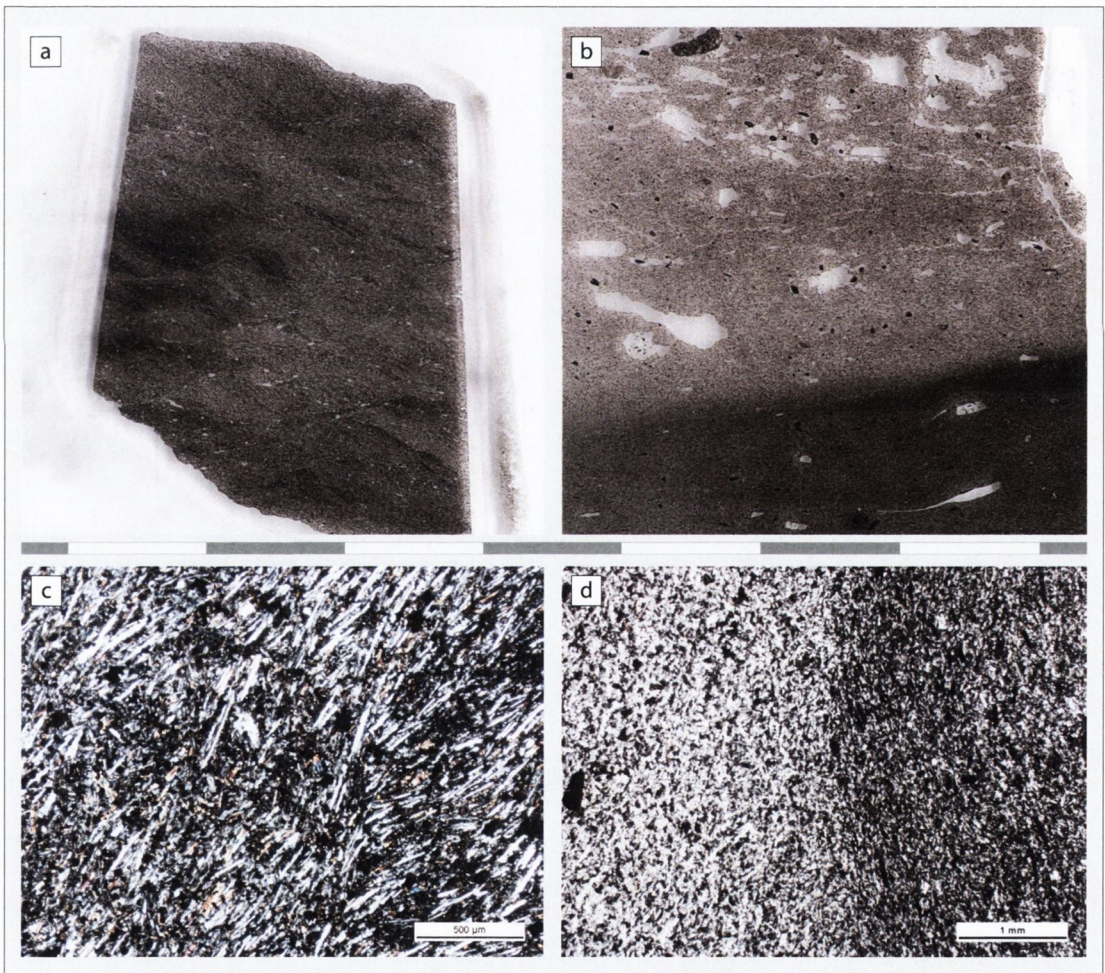
Fig. 2.3: Thin-sections of the Montaña Reventada basanite. a) aphyric, flow-banded texture, b) diffuse contact to phonolite above. Pictures c) and d) are microscopic close-ups of both a) and b). Scalebar is in cm divisions and applies for upper row. In the bottom two panels, scale as indicated. Note the diffuse contact between the two principal lava types.

The overlying phonolite is porphyritic, containing less than 10% feldspar phenocrysts, 3% opaque minerals, along with rare clinopyroxene and amphibole. Sometimes, feldspar

is intergrown with opaque minerals and less often with pyroxene and opaque minerals. Feldspars are usually single, euhedral crystals with slightly rounded corners. Larger crystals tend to have a sieved texture. Few glomerocrysts are present. Microcrystalline, leucocratic phonolite groundmass is holocrystalline and consists mainly of feldspar and opaque minerals. Vesicles are abundant and make up ~10 vol.% of the total rock close to the lower contact, but get gradually less within one metre up-section from the contact to the basanite (Fig. 2.4).
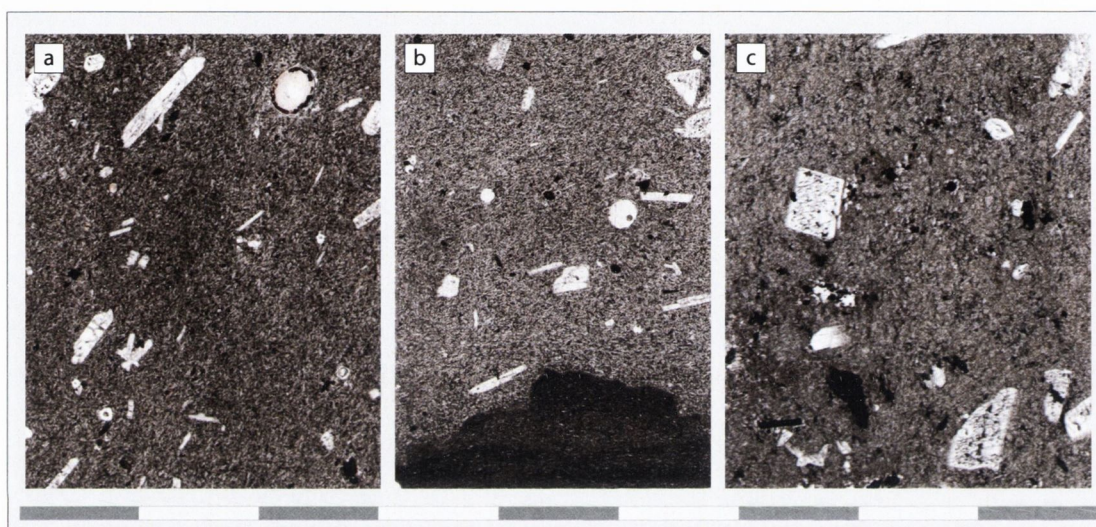
Fig. 2.4: Thin-sections of the Montaña Reventada phonolite. a) flow-aligned crystals, b) diffuse contact to the lower basanite and c) lack of vesicles. Scale bar is 9 cm long. Sieve-textured feldspar occurs in all samples.

Enclaves are very variable in texture and range from frothy and vesicle-rich to scarcely phyric and banded to phyric and patchy. Four major types are distinguished: **a)** scarcely feldspar bearing and strongly vesicular with a cryptocrystalline groundmass. They correspond to the foamy type of enclave in hand-specimen (Fig. 2.5 a). The feldspars within this type of enclave is alkaline and of anhedral, relictic appearance, the majority being contained within vesicles, probably a result of rapid exsolution of volatiles **b)** scarcely feldspar-bearing, dense enclaves that show flow-banding. Phenocryst orientations roughly follow this lamination (Fig. 2.5 b), **c)** dark-coloured, feldspar-bearing enclaves with a "blobby" texture, may or may not show a chilled margin and contain many nodules of darker material (Fig. 2.5 c) and **d)** less dark, feldspar-bearing enclaves that show a relatively coarser-grained groundmass of microlites that appears to consist of feldspars and amphiboles. They have a patchy appearance of lighter- and darker-coloured groundmass

mingled with each other. Glomerocrysts of feldspar intergrown with opaque oxides clinopyroxene and amphibole may occur in this type (Fig. 2.5 d-e).
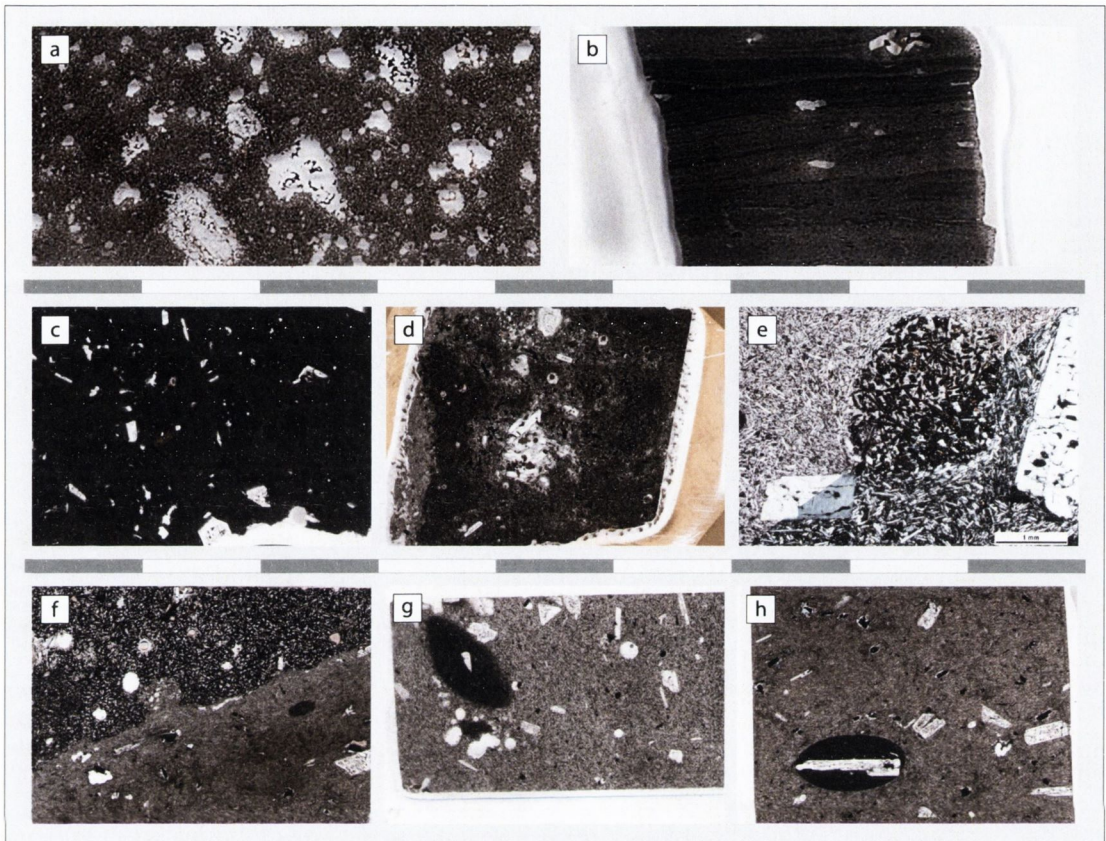

Fig. 2.5: Thin-sections of representative enclaves contained within the Montaña Reventada phonolite. Note the variety of textures: a) scarcely phyric and vesicle-rich, b) flow-banded, scarcely phyric, c) massive, crystal-rich, mingled, d) and e) frothy enclaves that show a coarse-grained texture in thin-section and intergrowth clusters (fsp + amp + cpx + mt). Thin-sections f), g) and h) show contact relationships between enclaves and the phonolite: f) phonolite intruding enclave, g) diffuse and h) sharp contact of small enclave to phonolite. Scale bars are 9cm long and applies for all pictures, except where otherwise indicated.

Contact relationships between enclaves and the host phonolite range from well-defined and angular to diffuse. Foamy, vesicular enclaves usually display an angular outline while large, blob-like enclaves have a chilled margin. Coarse-grained, light-coloured enclaves are intruded by phonolite in cases and, thus, appear to have stood competent against the liquid phonolite groundmass (Fig. 2.5 f). Enclaves of about 1 cm or less in size may show a sharp, well-defined contact, or a diffuse transition from enclave to phonolitic material (Fig. 2.5 g-h).
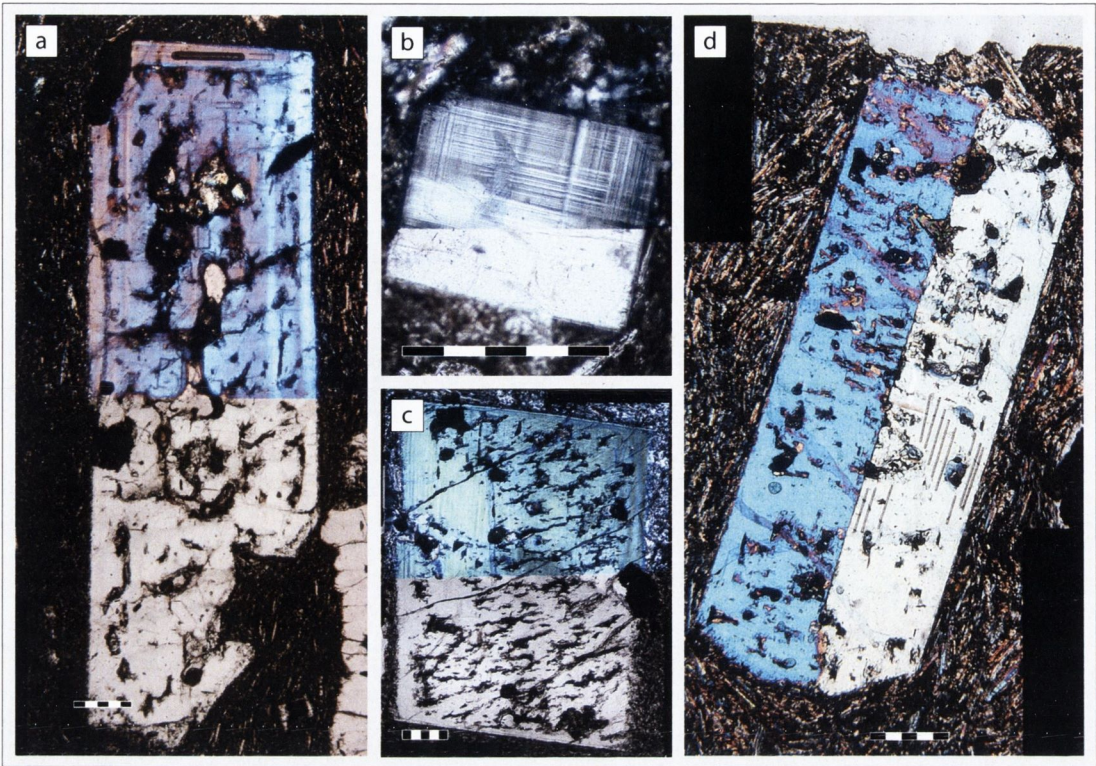
Fig. 2.6: Photomicrographs of feldspars contained in the Montaña Reventada phonolite. Sections are 150µm thick, hence, the high interference colours. a), c) and d) euhedral anorthoclases with sieve textures, probably from reheating, all three crystals are present in the microprobe dataset b) late-stage euhedral microcline. Scale bars represent 500µm in all four panels.

Montaña Reventada phonolite shows exclusively anorthoclase in measured feldspar compositions (see Fig. 2.11). The crystals reach several mm in size and are usually euhedral with only slightly rounded edges. Carlsbad twinning in these alkali feldspars is abundant (Fig. 2.6).

Enclaves show similar anorthoclases, but also include a range of plagioclase crystals from labradorite to oligoclase. The plagioclases tend to have stronger resorbed rims than the anorthoclases. Sieve textured plagioclase occurs, but is less abundant (Fig. 2.7).
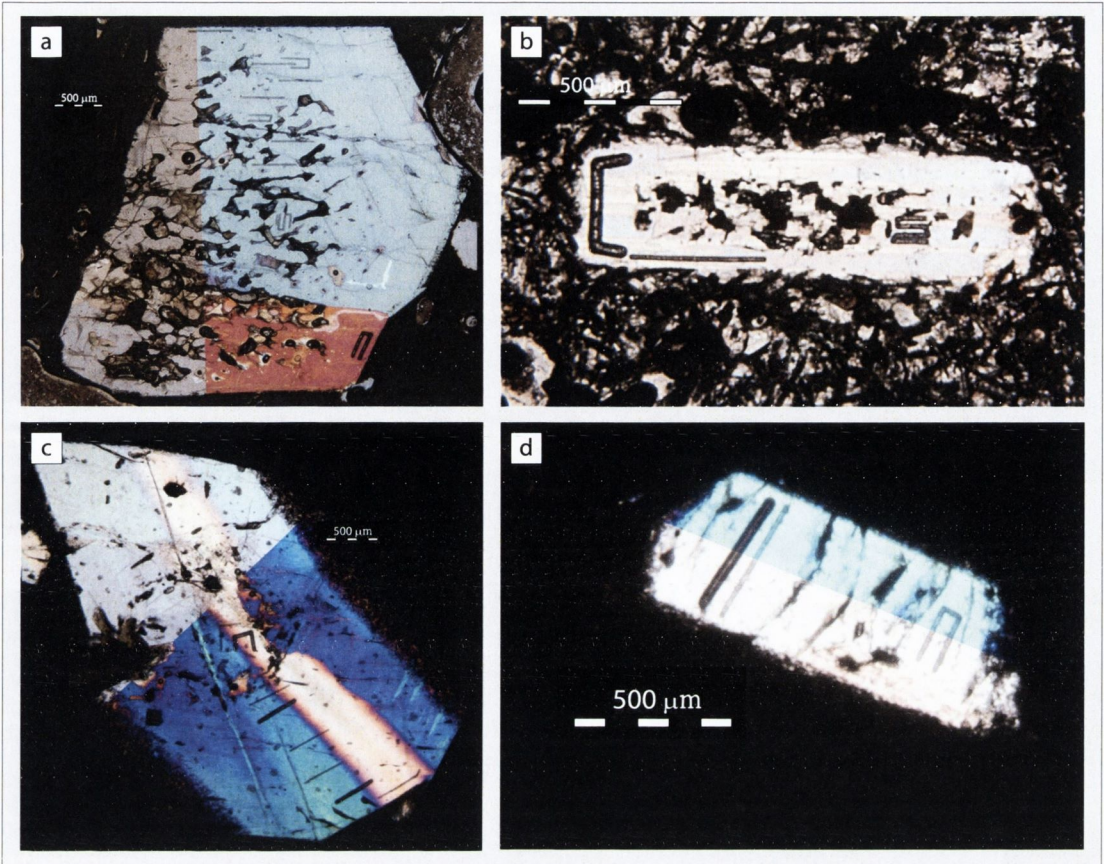
Fig. 2.7: Photomicrographs of feldspars contained in enclaves found within the Montaña Reventada phonolite. Sections are 150μm thick, hence, the high interference colours. Scale bars are 500μm. A variety of feldspar compositions was found: a) anorthoclase, b) labradorite c) oligoclase and d) anorthoclase (compositional data from chapter 3). Depending on crystal size, they show different degrees of resorption and sieving. Note laser trenches in all four crystals.

3.2. Whole-rock composition

3.2.1. Major elements

We used the Total Alkali versus Silica diagram (TAS, LeBas et al., 1986) to distinguish the constituents of the Montaña Reventada lava flow. The lower lava layer classifies as a basanite and the upper as a phonolite, while enclaves contained within the phonolite occupy the gap between the two as either basanites or phonotephrites. Enclave data from Araña et al. (1994) plot on the same linear whole-rock alkali sequence between basanites and phonolites. These authors classified the upper layer of Montaña Reventada as trachyte without further specifying the classification scheme employed. Within the TAS pattern that was applied here, their samples plot as phonolites (Fig. 2.8).
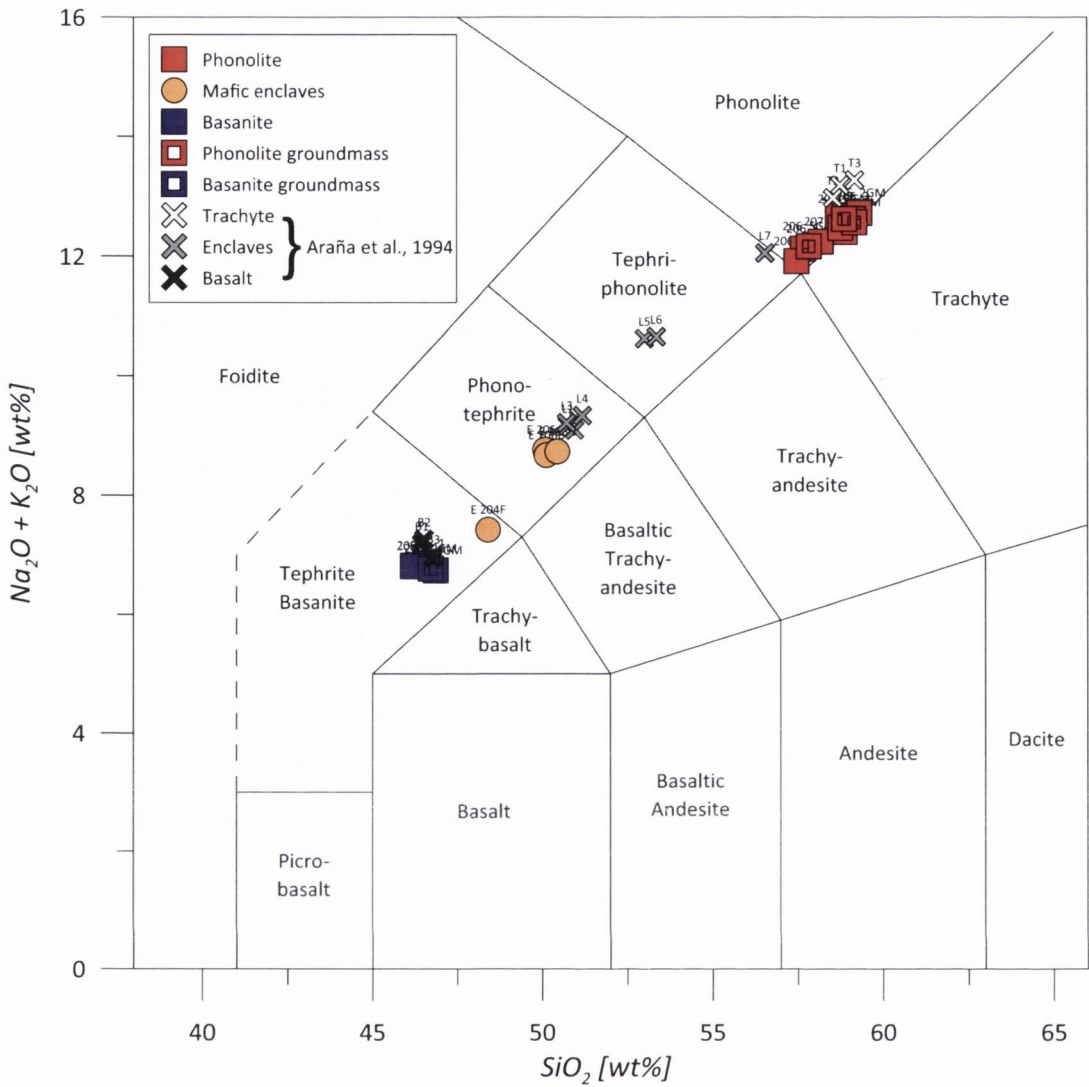
Fig. 2.8: Total alkali versus silica diagram after LeBas et al. (1986). The two principal lava types, basanite and phonolite, appear as endmembers while the enclaves are of intermediate composition. The Araña et al. (1994) dataset (crosses) plots on the same linear trend as our samples, between the two principal types of lava.

Major element data from the present study are broadly consistent with the data from Araña et al. (1994), when plotted in Harker diagrams (see Fig. 2.15). All major elements form straight trends between basanite and phonolite (iron oxides have been recalculated to FeO_{tot} using the formula $FeO_{tot} = FeO + 0.899\ Fe_2O_3$, Bence & Albee, 1968). The gap between the two principal lava types is always bridged by enclaves of intermediate composition.

3.2.2. Trace elements

In a multi-element variation diagram, basanites and enclaves show very similar characteristics, however, enclaves appear more enriched in the lithophile elements Cs, Rb, Ba, Th and U. Basanite and enclaves are similar to the primitive lavas defined in Chapter 4. Phonolites are more enriched overall, but display a negative Sr and a positive Zr anomaly and an overall depletion in HREE (Fig. 2.9). The phonolite data, too, are consistent with the results from Chapter 4. Although being phonolites from a TAS perspective, they still have to be regarded transitional lavas as they do not possess the extreme negative Sr and Ba anomalies observed in fully evolved Tenerife lavas (after the classification in Chapter 4).
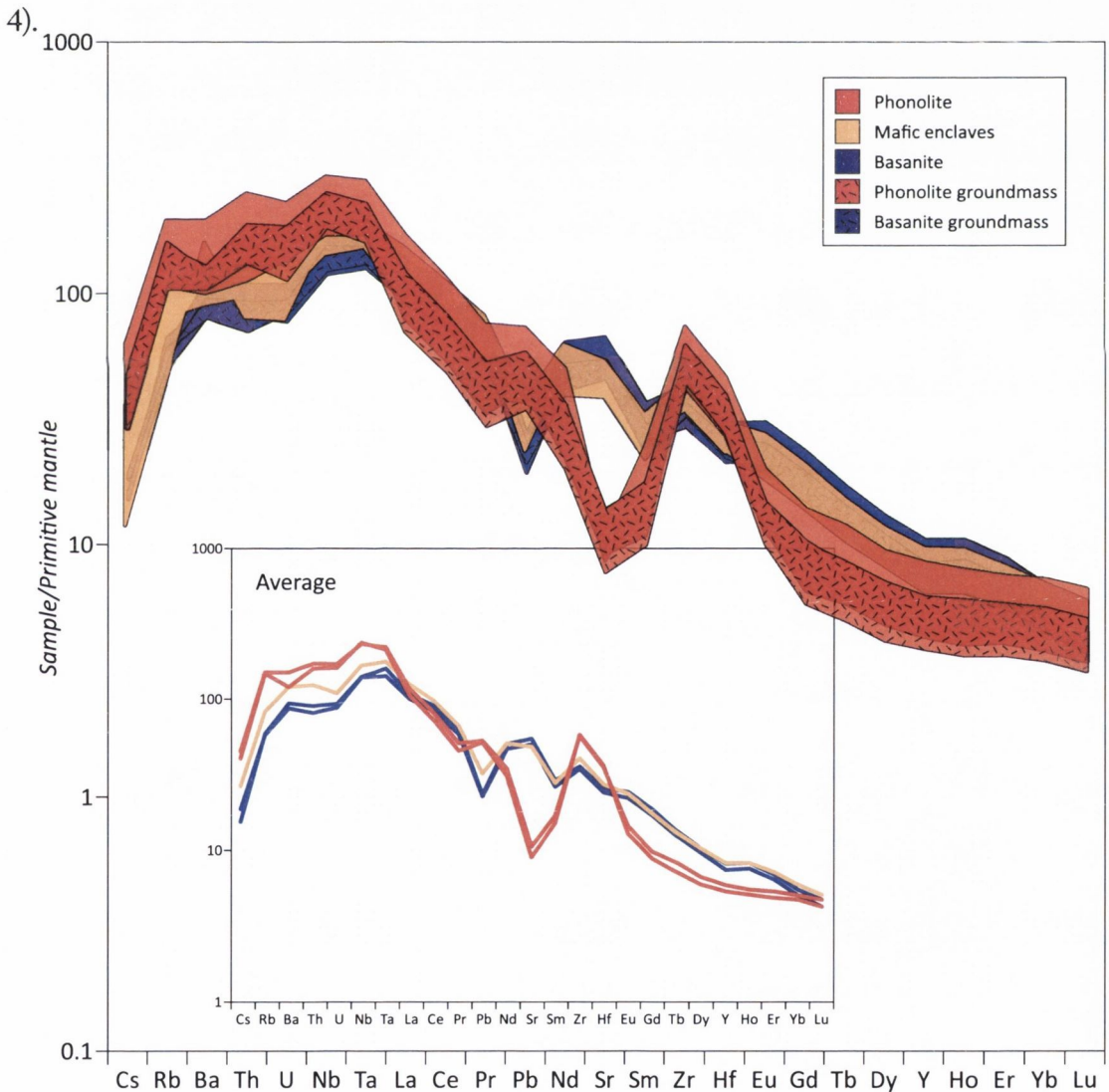

Fig. 2.9: Multi-element variation diagram of the components of the Montaña Reventada eruption. Samples normalised to primitive mantle (McDonough & Sun, 1995). Groundmass and whole-rock samples of each group are similar. Enclaves are similar to the basanites except for increased Cs, Rb, Ba, Th and Pb. Phonolites are further enriched in these elements and, moreover, have a marked negative Sr anomaly and positive Zr anomaly.

When whole-rock data are plotted against Zr concentration (used as an index of differentiation, cf. Wolff et al., 2000), basanites and phonolites plot as end-members. Enclaves generally fill the gap between those two end-members with the exception of one basanitic enclave that shows similar zirconium concentrations to the massive basanite. In the case of Ba, Sr, La and Y, this enclave appears more enriched with respect to the basanite (Fig. 2.10).
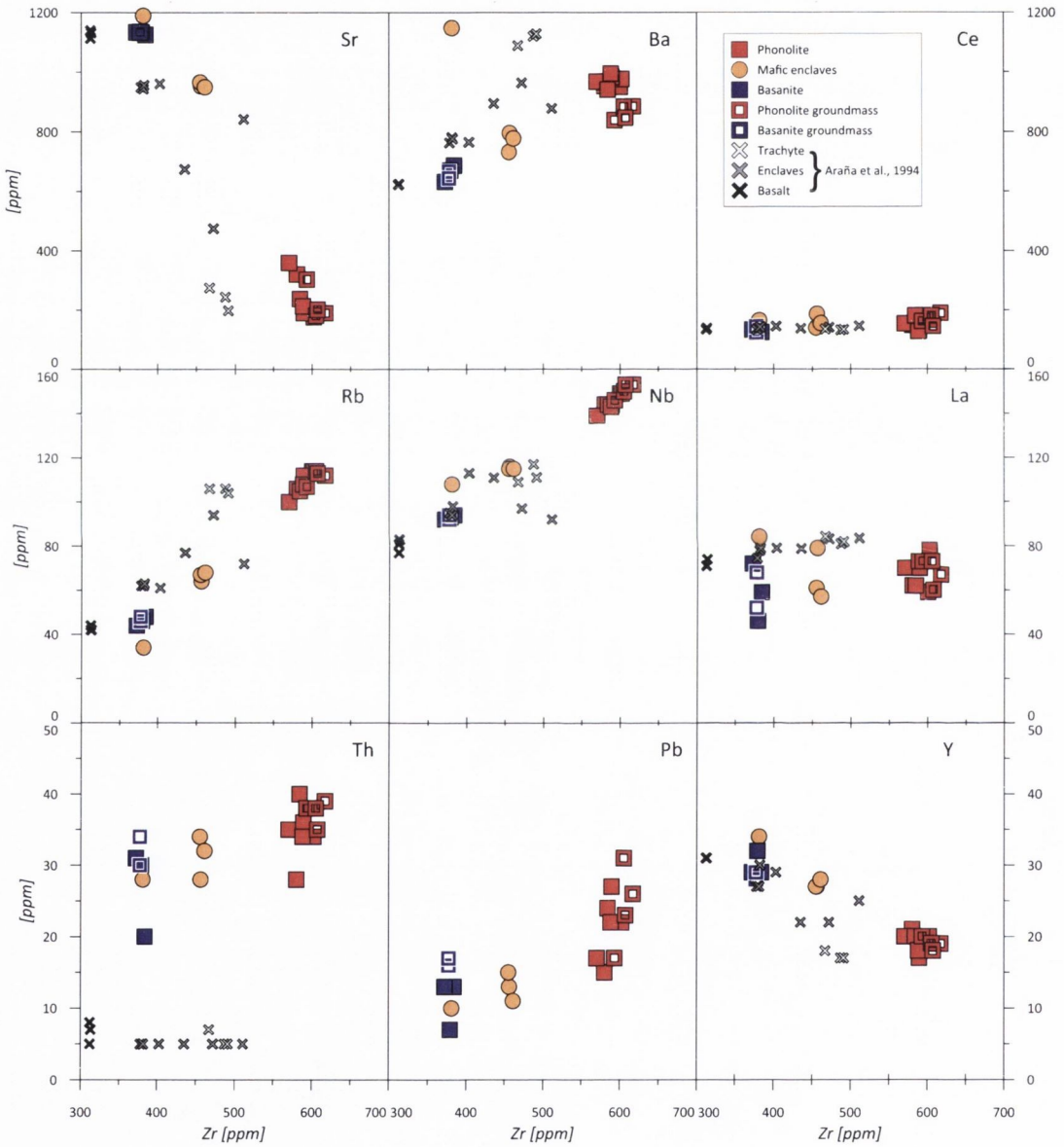

Fig. 2.10: Selected trace elements versus Zr concentration from Montaña Reventada. Data from XRF dataset. The crosses denote data from Araña et al. (1994) for comparison. Their data span a smaller range in Zr, Nb, Th and La, and are of lower resolution.

3.3. Major element composition of feldspar phenocrysts

Using the data of Araña et al. (1994), their results scatter widely around our data and, on the plagioclase end of the series An-Ab-Or, extend to more mafic compositions. Despite this scatter, the range of feldspar compositions they found within enclaves and phonolites, are broadly consistent with our bimodal pattern (data from Chapter 3, see electronic appendix for full data of feldspar analyses). Several of the plagioclase crystals, however, are normally or reversely zoned (Fig. 2.11).
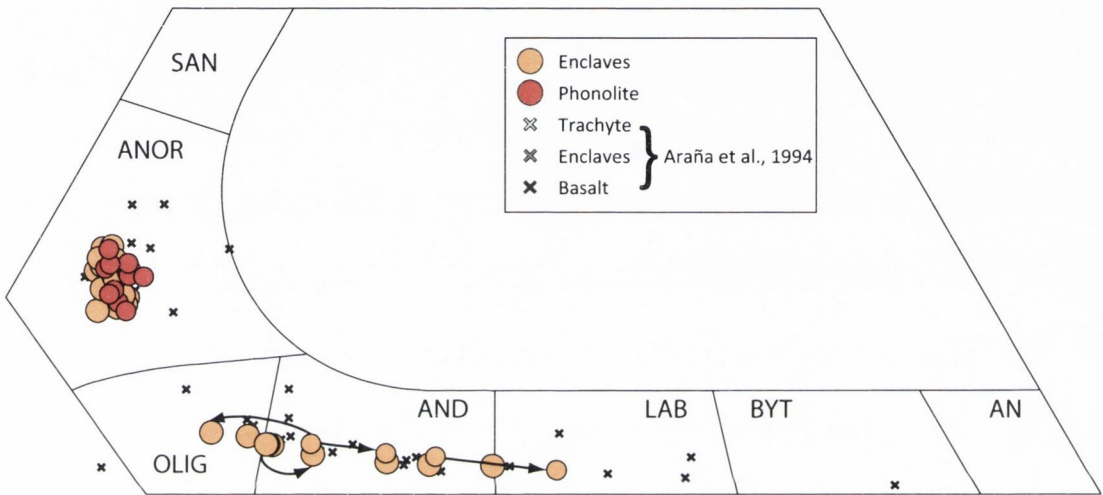

Fig. 2.11: Ternary diagram of feldspar compositions found in the Montaña Reventada lava flow. Circles represent our data (chapter 3) and crosses data from Araña et al. (1994). Arrows indicate variations in enclave plagioclase from core to rim. Plagioclase may be normally or reversely zoned. Bimodal distribution of feldspar compositions is found in enclaves that probably took up anorthoclase from the phonolite.

3.4. Isotope systematics

3.4.1. Strontium and Neodymium

The Sr ratios of Montaña Reventada samples are overall similar to the post-Icod-collapse succession (Chapter 4) and, moreover, agree with the systematics of the primitive, transitional and evolved lava groupings that was created in that chapter. Basanite whole-rocks have $^{87}Sr/^{86}Sr$ values of between 0.0703032(9) and 0.703040(7). This is similar to the phonolite whole-rocks that range from 0.703032(7) to 0.703062(9), but with the basanites possessing higher Sr concentrations. The groundmasses of basanites range from 0.0703024(10) to 0.703046(9), with similar to slightly higher values for phonolite

groundmass of 0.703032(9) to 0.703077(7). However, the two principal lava types have effectively the same Sr ratios. The enclaves form no exception, displaying 0.703032(7) to 0.703059(9), with Sr concentrations being lower or slightly higher than found in the basanite.

In turn, changing whole-rock Nd concentrations leave $^{143}Nd/^{144}Nd$ ratios largely unaffected, yielding ratios between 0.512848(42) to 0.512910(46). Basanites show 0.512855(38) to 0.512896(46) and phonolites 0.512848(42) to 0.512910(46). Enclaves show a range in Nd ratios between 0.512871(46) and 0.512899(42), i.e. intermediate between basanites and phonolites. All ratios, however, are within error of each other (Fig. 2.12).
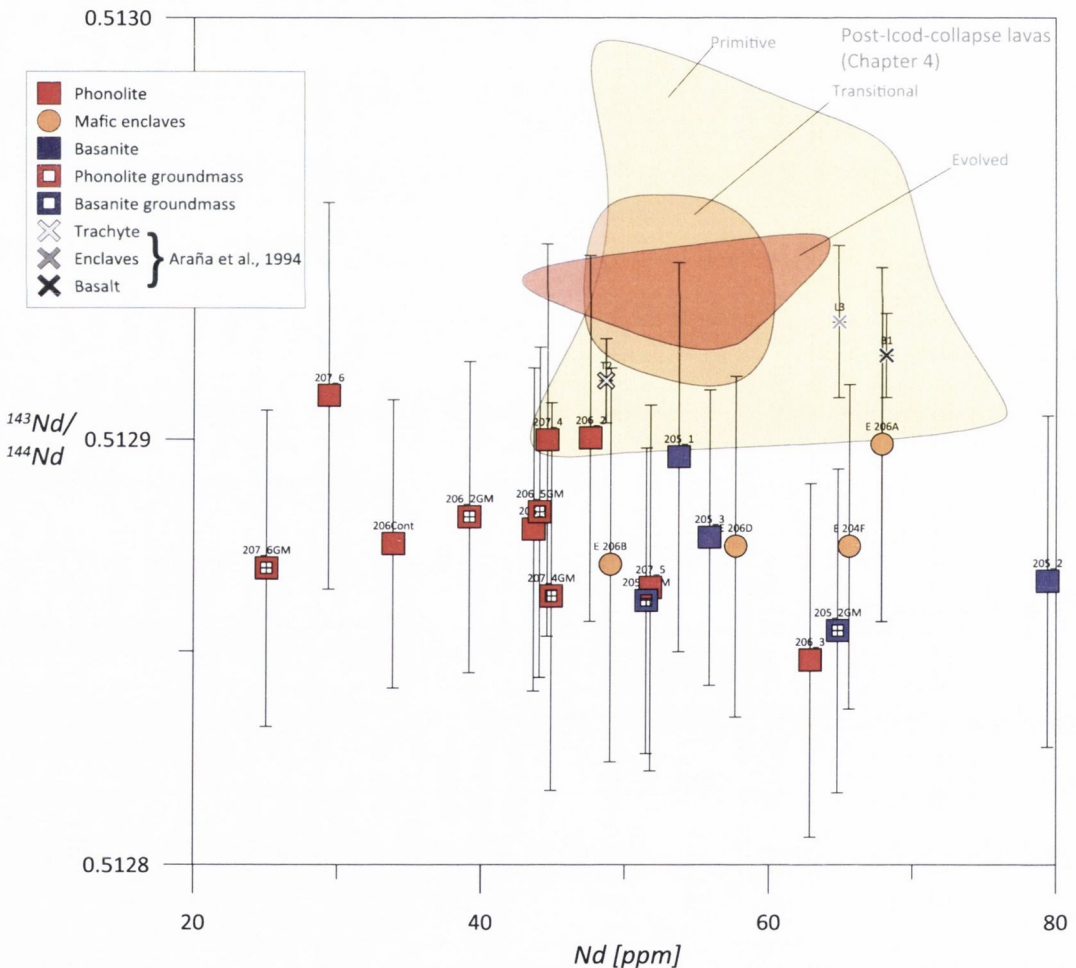

Fig. 2.12: Neodymium isotope ratios versus Nd concentration of Montaña Reventada rocks. For reference, Nd isotope data from chapter 2 (post-collapse lavas). All samples are within error of each other.

3.4.2. Pb–Pb systematics

Analysis of Montaña Reventada rocks on Pb isotope composition yielded the following ratios (reported with 2× standard deviation in brackets). Basanites: Whole-rock $^{206}Pb/^{204}Pb$ ratios range from 19.7355(13) to 19.7418(31), groundmass: 19.7193(21) to 19.7377(18); whole-rock $^{207}Pb/^{204}Pb$ ratios from 15.6122(34) to 15.6213(17), groundmass: 15.6146(34) to 15.6173(32); whole-rock $^{208}Pb/^{204}Pb$ ratios from 39.5607(61) to 39.5720(29), groundmass: 39.5423(43) to 39.5638(37). Phonolites: Whole-rock $^{206}Pb/^{204}Pb$ ratios range from 19.7723(12) to 19.7807(23), groundmass: 19.7671(18) to 19.7750(25); whole-rock $^{207}Pb/^{204}Pb$ ratios from 15.6175(17) to 15.6232(28), groundmass: 15.6168(30) to 15.6209(34); whole-rock $^{208}Pb/^{204}Pb$ ratios from 39.5835(27) to 39.5997(45), groundmass: 39.5769(39) to 39.5931(51). Enclaves (all whole-rock): $^{206}Pb/^{204}Pb$ ratios range from 19.7528(14) to 19.7660(16); $^{207}Pb/^{204}Pb$ ratios from 15.6117(17) to 15.6196(29); $^{208}Pb/^{204}Pb$ ratios from 39.5603(29) to 39.5858(46).
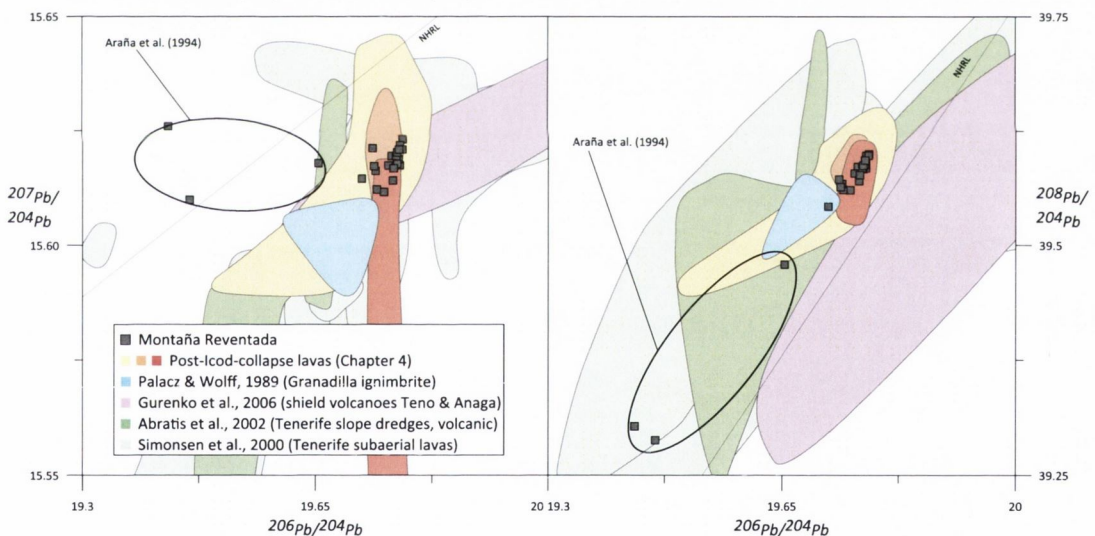

Fig. 2.13: Pb isotope analysis of the Montaña Reventada eruption in black compared to Tenerife post-collapse lavas (chapter 2) and literature data (fields). Northern Hemisphere Reference Line (NHRL) after Hart (1984). Note deviation of data from Araña et al. (1994), which do not agree with the data from the post-collapse lavas in general and also not with the data from this work.

The results agree well with literature data (Tenerife data: Palacz & Wolff, 1989; Simonsen et al., 2000; Abratis et al., 2002; Gurenko et al., 2006) and with data on the Post-Icod-collapse succession from Chapter 4 (see Fig. 2.18). As Montaña Reventada is part of this post-Icod-collapse succession, the similarity of the two Pb datasets in Chapter 4 and this chapter, aquired in two different laboratories, is likely to indicate reproducible and reliable results.

3.5. Oxygen isotopes

Basanites, phonolites and enclaves have been analysed for their whole-rock oxygen composition. Moreover, basanites and phonolites have been measured for their groundmass oxygen ratio to assess the effects of crystal matter within many of the whole-rock samples on the oxygen isotope composition.

Phonolite whole-rocks group within 6.6 and 6.81 ‰, with the phonolitic groundmass exhibiting a larger range between 6.22 and 6.89 ‰. Mafic enclaves are slightly lower overall, ranging from 6.16 to 6.68 ‰. Basanite whole-rock samples range widely from 6.83 to 7.90 ‰, while the basanite groundmass is tightly confined to significantly lower values of between 6.00 to 6.04 ‰ (Fig. 2.14).
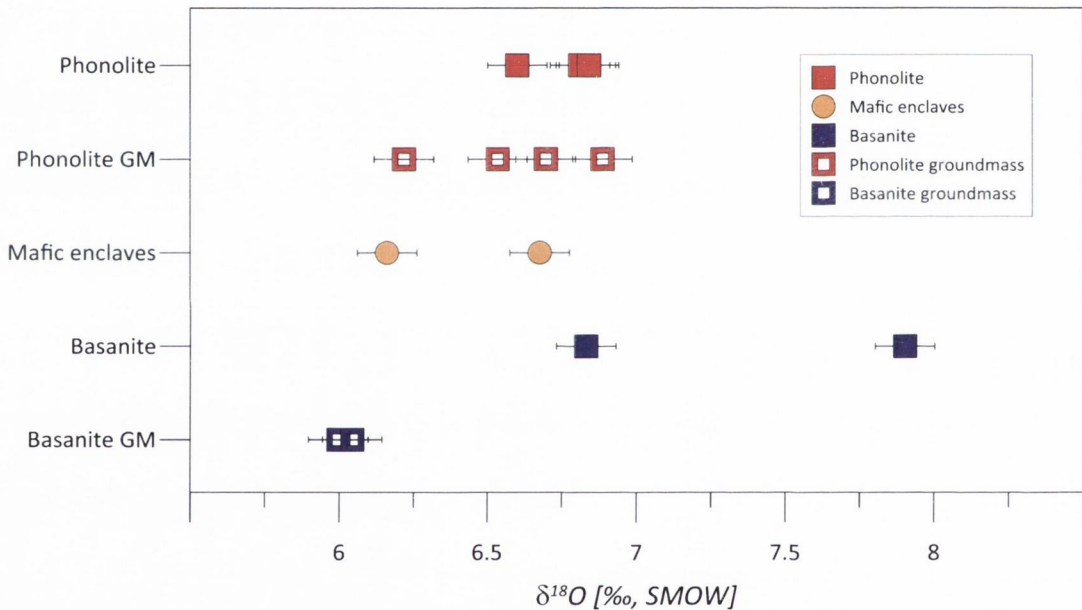

Fig. 2.14: Montaña Reventada $\delta^{18}O$ value ranges for the various components, groundmass data: speckled ornament.

4. DISCUSSION

4.1. Major and trace element constraints

Whole-rock major element trends are remarkably linear for all oxides and allow two principal end-members, basanite and phonolite, to be defined, with the enclaves plotting at intermediate concentrations between the end-members (see Fig. 2.8 and Fig. 2.15). Trace element data from the basanite whole-rock and groundmass samples are similar, which is consistent with the scarcely phyric nature of this part of the lava pile (see Fig. 2.9). To check for interface processes, the phonolite was sampled just above the contact to the basanite (sample 206cont). However, the data from this sample consistently cluster with the phonolite data from up-section (for both major and trace elements), suggestive of the phonolite having been too cool to trigger significant diffusional hybridisation during flow and emplacement. Therefore, interaction between the two magmas occurred prior to subaerial emplacement, when individual small blobs of mafic magma were entrained in the phonolite (cf. Araña et al., 1994).
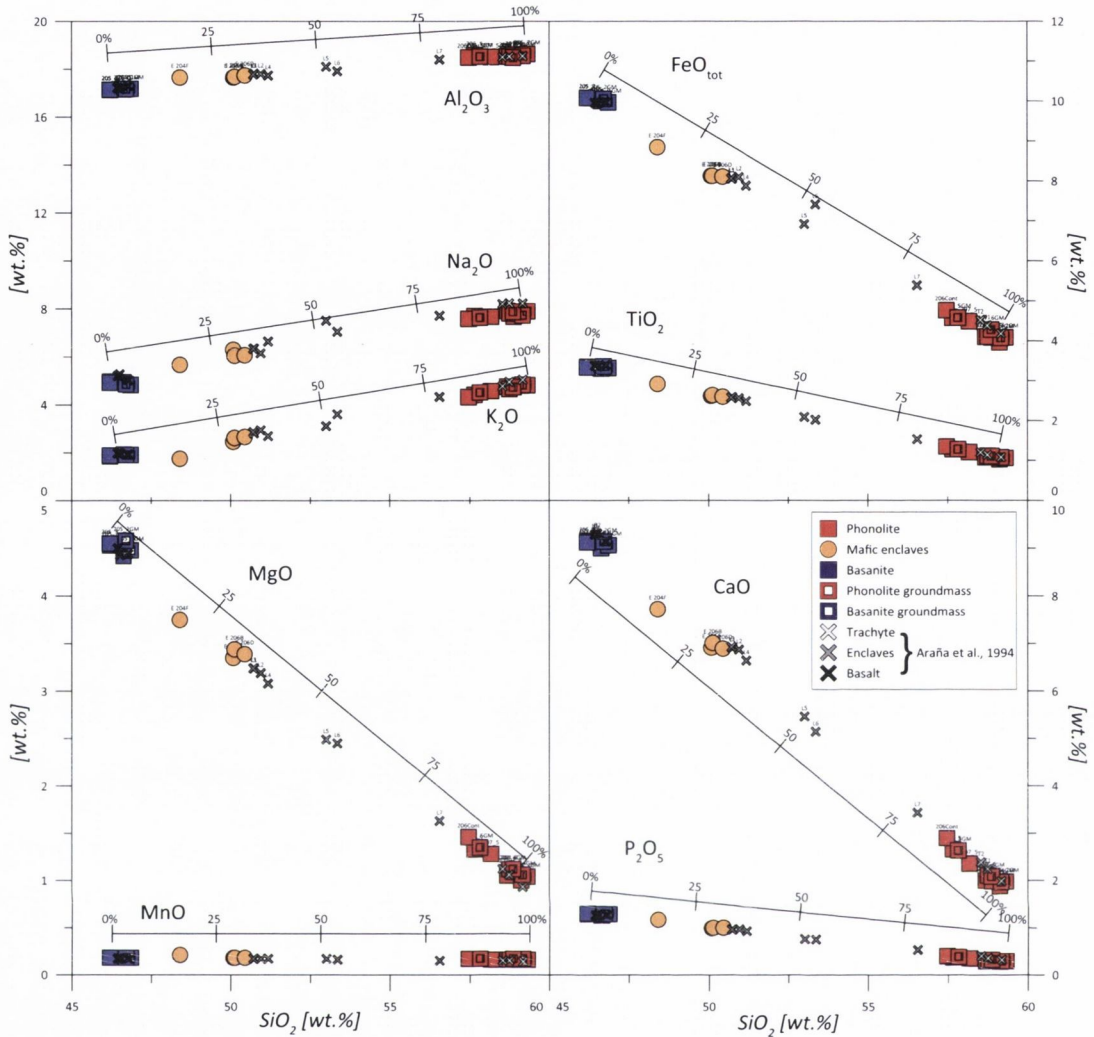
Fig. 2.15: Wholerock major element composition of the Montaña Reventada eruption. Red: upper layer phonolite, blue: lower layer basanite, orange: enclaves contained in phonolite, crosses: Reventada data from Araña et al. (1994). Fe data recalculated to FeO_{tot}. All major elements define straight trends when correlated to SiO_2, which indicates an origin of enclaves by mixing of the two principal components basanite and phonolite, rather than by fractional crystallisation. Note graphical mixing lines that indicate the percentage of phonolitic material for intermediate compositions.

Bounded by the basanite and phonolite lava end-member, the samples form an apparently continuous series of differentiation. However, none of these trends resemble classic liquid line of descent patterns. Doglegs in typical trends of co-genetic suites are, for example, often interpreted as the onset of the fractionation of a certain phase. Instead, the patterns observed here are completely straight and indicate that hybridisation was the dominant factor, i.e. physical and chemical mingling and mixing (cf. Geldmacher et al., 1998).

The strong compositional gradient that persists between a basanite and a phonolite magma has been shown to trigger considerable amounts of diffusive equilibration

(Koyaguchi, 1989). Furthermore, a thermal gradient needs to have existed between enclaves and phonolite to produce the observed chilled margins present in a lot of enclaves (cf. Sparks et al., 1977; Eichelberger et al., 1980). Lastly, the high surface-volume ratio of the enclaves enhances their diffusional equilibration. These factors are highly suggestive of diffusion governing the enclaves' hybridisation. Araña et al. (1994) suggested that diffusion controlled the Na and K concentration patterns in enclaves and phonolite (that deviate from simple mixing), which is in line with the enhanced diffusivities of these elements compared to the lower diffusion coefficients of SiO_2 and CaO, TiO_2, MgO and FeO which depend on SiO_2 (Walker et al., 1981; Watson, 1982; Walker & DeLong, 1982; Lesher, 1986; Lesher & Walker, 1986). As an additional, non-diffusional process, migration of crystal matter from phonolite to enclave may have introduced compositional complexities, which in this study mainly shows in the trace element concentrations (e.g. Ba) as major element trends are effectively straight.

Mass balance constraints

As basanite and phonolite samples are not compositionally uniform, we used the respective maximum and minimum major and trace element concentrations from basanites and phonolites to calculate a mass balance for the enclaves. When calculating for a given mixture of basanite and phonolite (e.g. 20 and 80%), this yielded maximum and minimum boundaries for each element or oxide. Trace element and oxide concentrations in one enclave were modelled to fall into the interval of calculated maximum and minimum of each sample. The elements that fell out of this mass balance range are interpreted to have been influenced by either diffusion or addition of crystal matter. Please consult the electronic appendix for a spreadsheet of the mass balance calculation.

The enclaves from our dataset are computed to represent mixtures of between 66:34 basanite to phonolite (E206A, E206B and E206D) and 80:20 basanite to phonolite (E204F). This is consistent with the graphical mixing solution, where the former three enclaves cluster together and the latter shows a more mafic composition (Fig. 2.15). Simple mixing of basanite and phonolite explains all major elements, except for Al_2O_3, MnO, Na_2O, K_2O and P_2O_5. However, the two less abundant major element oxides MnO

and P_2O_5 fell within one hundreth of one weight percent of the model limits, which we deemed insignificant. In turn, the overabundance in all enclaves in Al_2O_3 and Na_2O is suggestive of added anorthoclase in noticable fractions. The lack of K_2O in enclaves, in turn, can be explained by uphill diffusion of K_2O towards the potassium-rich side of the diffusional interface, i.e. towards the phonolite, which consequently depletes the enclave in this oxide (e.g. Watson & Baker, 1991; Bindeman & Perchuk, 1993; Bindeman et al., 1999).

Table 2.6: Modelling of enclave compositions

| Enclave | Basanite [%] | Phonolite [%] | Compared with calculated mixture | |
			enriched in:	depleted in:
E206A	66	34	W	Li, Cu
E206B	66	34	-	Sc, Cu
E206D	66	34	-	-
E204F	80.4	19.6	Ba	Ni, Cu, Cs, Rb, U

Table 2.6.: **Percentages of mixtures between basanite and phonolite that reproduce enclave compositions are given above. Several trace elements were enriched or depleted in the real samples, compared to the theoretical mixture, but variations remain unique to each samples. The enrichment of W most likely stems from the use of a tungsten-carbide mill during sample preparation.**

The majority of trace elements can successfully be modelled by simple mixing, with only a few exceptions. When filtered for elements that deviate more than 10% from the expected mixing interval, lithophile elements Li, Sc, Cs, Rb and U were depleted, while W and Ba were enriched. Thw enrichment of W most likely stems from the use of a tungsten-carbide mill during sample preparatio. The siderophile element Ni and the chalcophile element Cu were depleted in the enclaves with respect to the mixing calculation (Table 2.6). With the exception of copper, all enclaves seem to behave differently in terms of trace element deviations, which hampers general conclusions on diffusional processes. However, Bindeman et al. (1999) constrained up-hill diffusion for Li, Cs and Rb from basaltic to rhyolitic melts, and the enrichment of Ba in one sample may be explained by the uptake of anorthoclase that may contain up to 8000 ppm in Montaña Reventada rocks (data from Chapter 3).

Enclaves always plot on potential mixing lines between basanite and phonolite (see Fig. 2.8, Fig. 2.10 and Fig. 2.15). Enclave E204F, an aphyric, vesicle-rich angular fragment of basanite from within the phonolite, deviates in Sr, Ba, Rb, La and Y concentrations by possessing either the highest (Sr, Ba, La, Y) or lowest (Rb) concentration of all samples.

As it has not taken up crystal matter from the phonolite, it serves as the best sample to constrain the diffusional process of the mentioned elements, for the observed deviations likely stem from diffusion only. The trace element fingerprint of the phonolite indicates that either it was formed as a result of an earlier phase of mixing and homogenisation of two magmas (one more evolved and one more primitive) or the country rock, it was derived from, was of less mafic composition than phonolites that show an evolved signature. Regarding the homogenous crystal populations that show no signs of a mixing event, we suggest the latter.

4.2. Petrography and feldspar composition

Petrographical evidence is consistent with a continuous eruption of first basanite and then phonolite. Flow-banded enclaves closely resemble the laminated texture of the underlying basanite. They may therefore represent clasts that have been picked up by the phonolite while it was overriding the basanite. The lack of a basanite top breccia and a phonolite bottom breccia is suggestive of that, too, i.e. the sharp interface between the two layers indicates a close temporal relationship.

Overturned flow-banding in the basanite indicates that a shearing component was present at the time this lava was still plastic. We interpret this type of small-scale folding to stem from the push of the advancing flow front of the overriding phonolite. It follows that the basanite must have been ductile at the time of phonolite emplacement.

Furthermore, on microscopic scale, the diffuse contact between basanite and phonolite indicates that they approached a similar temperature upon emplacement, i.e. the basanite was still hot at the time the phonolite arrived. It thus appears likely that the basanite and the upper phonolite are contemporaries.

Frothy vesicle-rich enclaves, in turn, may be first-contact-quenched fragments that reflect a magmatic history (e.g. Eichelberger, 1980). Large temperature contrast between a hot mafic magma and a cooler silicic one hereby initiates rapid quenching of the fraction of mafic magma that initially touches the felsic one during e.g. magma chamber replenishment. This solidification simultaneously oversaturates volatiles in the rest melt,

which consequently exsolve and produce a foamy, vesiculate texture which shortly after freezes completely. Exsolution of volatiles may further enhance crystallisation (cf. Sparks, 1997; Hammer et al., 2000) and form a positive feedback together with concurrent solidification. This would ultimately speed up this process considerably. Considering the angular (i.e. fragmented) nature of these enclaves, it appears likely that they represent fragments of this inital, rapidly quenched contact zone between basanite and phonolite.

Sieve textures in anorthoclases indicate an increase in temperature within the phonolite (cf. Nelson, 1992; Hibbard, 1995; Stewart & Pearce, 2004). Indeed, the petrography conducted shows that strongly sieved anorthoclase crystals are not found in other phonolites from the post-collapse succession (e.g. Abejera Alta, Abejera Baja, El Boquerón, Pico Cabras, Montaña Majua, Montaña Blanca, Roques Blancos), which complies with the lack of extensive mixing textures in these lavas.

Compositional zoning in feldspars in the enclaves, in turn, may reflect either earlier histories experienced by the mafic magma (reverse zoning) or hybridisation of the enclaves' groundmass, which may be recorded in the normally zoned plagioclase feldspar. Potential xenocrysts cannot be excluded in these, however.

Petrography allows to considerably confine the geological interpretation. Basanite and phonolite must have followed in close succession, probably right after each other. Furthermore, they need to have been in contact with each other prior to eruption, as shown by both angular and ameboidal enclaves and reheating of phonolite. Variations in feldspar compositions (normally zoned plagioclase) and the presence of sieved anorthoclase crystals in enclaves reflect their transfer from phonolite to basanite.

4.3. Sr and Nd isotope systematics

The Montaña Reventada Sr isotope data are consistent with an origin of enclaves by mixing. Nd isotope ratios fall within error of each other and, hence, do not allow advanced interpretations. However, the obtained $^{143}Nd/^{144}Nd$ ratios are very similar for all samples and thus do not preclude a mixing origin of the hybrid enclaves. Equally, the similarity of $^{87}Sr/^{86}Sr$ ratio in basanite, phonolite and enclaves inhibits distinguishing

between chemical and physical mixing. In the same way, the combined Sr and Nd data of Araña et al. (1994) forbids discrimination between the basanite and the enclave (only one enclave was measured) due to their large errors. Mixing relationships are therefore obscured on a plot of $^{143}Nd/^{144}Nd$ versus $^{87}Sr/^{86}Sr$. However, the essentially constant Sr ratios follow the mixing systematics of the post-Icod-collapse succession (Chapter 4)and can be discriminated by correlating them with their respective Sr concentration. Data from Chapter 4 resemble a hyperbolic mixing curve and the new data from this chapter follow this pattern in the bottom leg of the curve (Fig. 2.16).

The compositions of enclaves group close to the basanite due to similar levels in Sr concentrations. One enclave (E204F) that is higher in Sr concentration differs in other trace elements, too, but is consistent with the multi-element patterns of basanite. It could be that hybridisation was less effective in this sample. Diffusion, which is thought to be the main process of hybridisation in this case (Araña et al., 1994), is greatly hindered in solids compared to silicate liquids (Watson & Baxter, 2007 and references therein). Indeed, enclave E204F is an angular fragment of what we interpret to have resulted from the initial quenching of mafic magma upon contact with the phonolite (cf. Eichelberger et al., 1980; Troll et al., 2004). Hence, this sample was probably solid when it was entrained in the phonolitic magma and may not have experienced the degree of hybridisation that is found in ameboidal enclaves that were ductile in comparison.
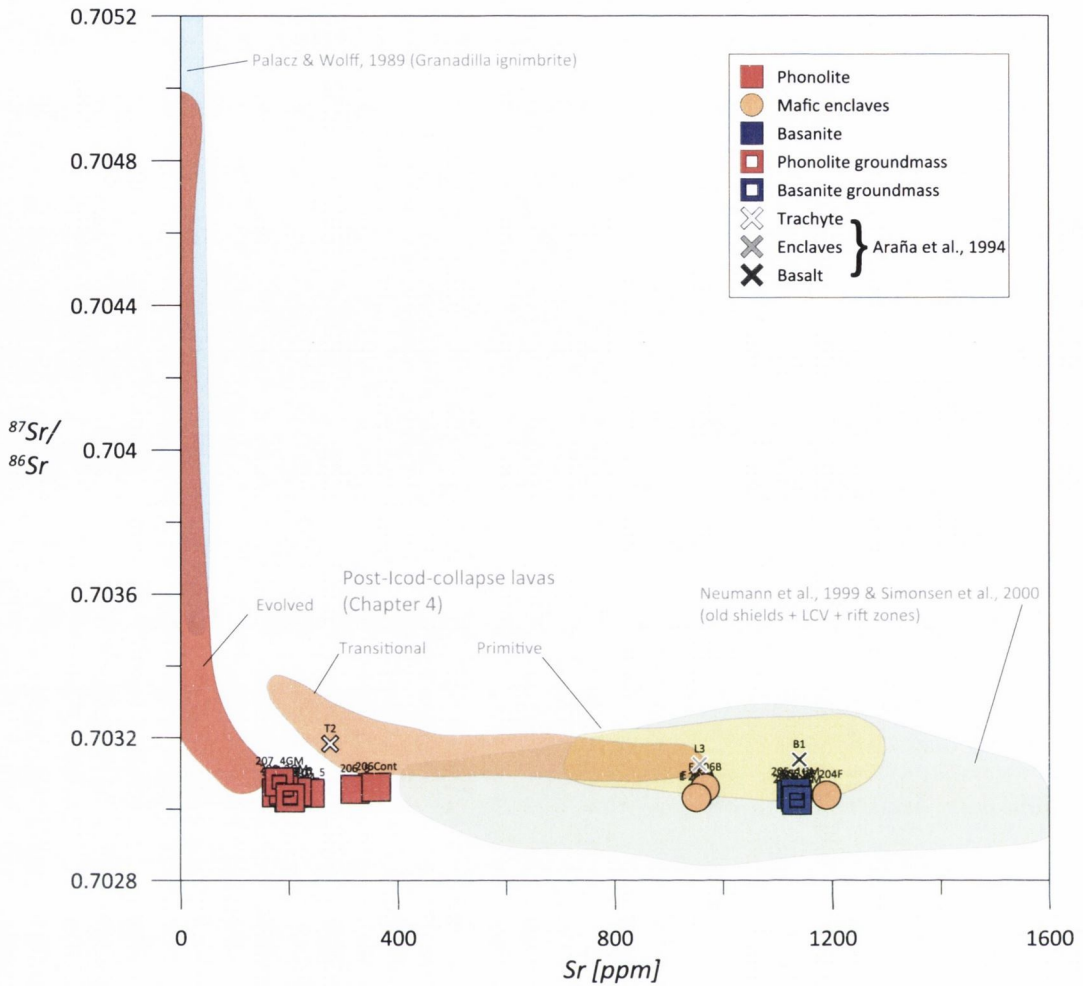
Fig. 2.16: Sr isotope compositions versus wholerock Sr concentrations. All errors are 2σ and contained within symbols. Data from Neumann et al. (1999) (trace elements) and Simonsen et al. (2000) (isotopes) were from the same sample set and correlated by us on grounds of sample name, unfortunately their highest radiogenic samples of up to 0.7042 were not matched with trace element analyses. Data from the Granadilla ignimbrite (Palacz & Wolff, 1989) are also shown.

4.4. Oxygen isotopes

Phonolite samples are systematically higher in oxygen isotope composition than phonolitic groundmass, which indicates a higher $\delta^{18}O$ value for crystal matter contained within the rock. Enclaves possess a similar range of $\delta^{18}O$ values as the host phonolite, but their values are at the same time encompassed by the range of basanitic $\delta^{18}O$. Oxygen isotope data from enclaves are consistent with a hybridisation origin as they plot between the basanitic and phonolitic data (Fig. 2.17). In the case of enclave E204F, the basanitic groundmass is a valid end-member as the enclave sample is scarcely phyric, only. This is consistent with a

mixing process where the relatively small size of the enclaves (high surface-volume ratio) allows for rapid exchange of isotopes by diffusion.
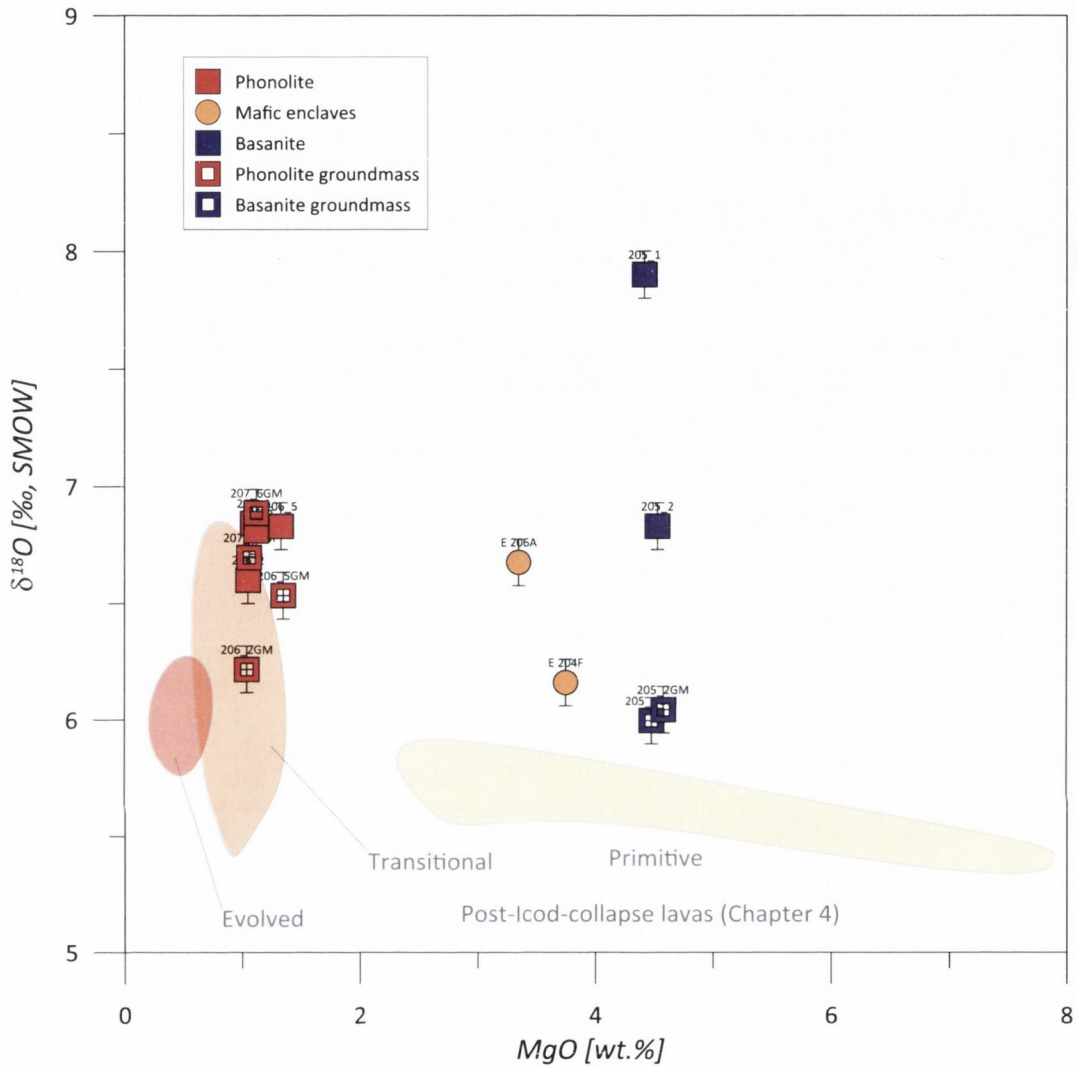

Fig. 2.17: Montaña Reventada oxygen isotope ratios versus wholerock MgO. The data from transitional lavas overlap at 2σ level with the analysed phonolites that belong to this group. In contrast, basanite whole-rock samples are much higher than the primitive eruptions and show very variable whole-rock values. Mafic enclaves plot as intermediate between phonolite and basanite, owing to their hybrid nature.

The basanite whole-rock samples show high values of up to 7.9 ‰ compared to groundmass of around 6 ‰. The only difference between whole-rock and groundmass samples are the scarce removed feldspar phenocrysts in the groundmass. Moreover, the two measured basanite whole-rock samples differ strongly between each other, while groundmass samples are similar in $\delta^{18}O$. It appears therefore most likely that high $\delta^{18}O$ crystal matter or high $\delta^{18}O$ xenoliths (cf. Donoghue et al., 2008) are responsible for the strongly deviating oxygen isotope signal in the whole-rock basanite samples. However,

currently there is more basanite samples being analysed on their $\delta^{18}O$ composition to base future interpretations on more data.

4.5. Pb–Pb systematics

Pb isotope measurements from Araña et al. (1994) scatter widely and do not overlap at all with the 20 analyses of this study, which cluster much tighter within the post-collapse data fields. Furthermore, proposed mixing relationships between the phonolite and basanite to produce intermediate enclave compositions are contradicted by their Pb data that oppose any mathematically possible mixing relationship (Fig. 2.18). We will therefore ignore these data for interpretation.
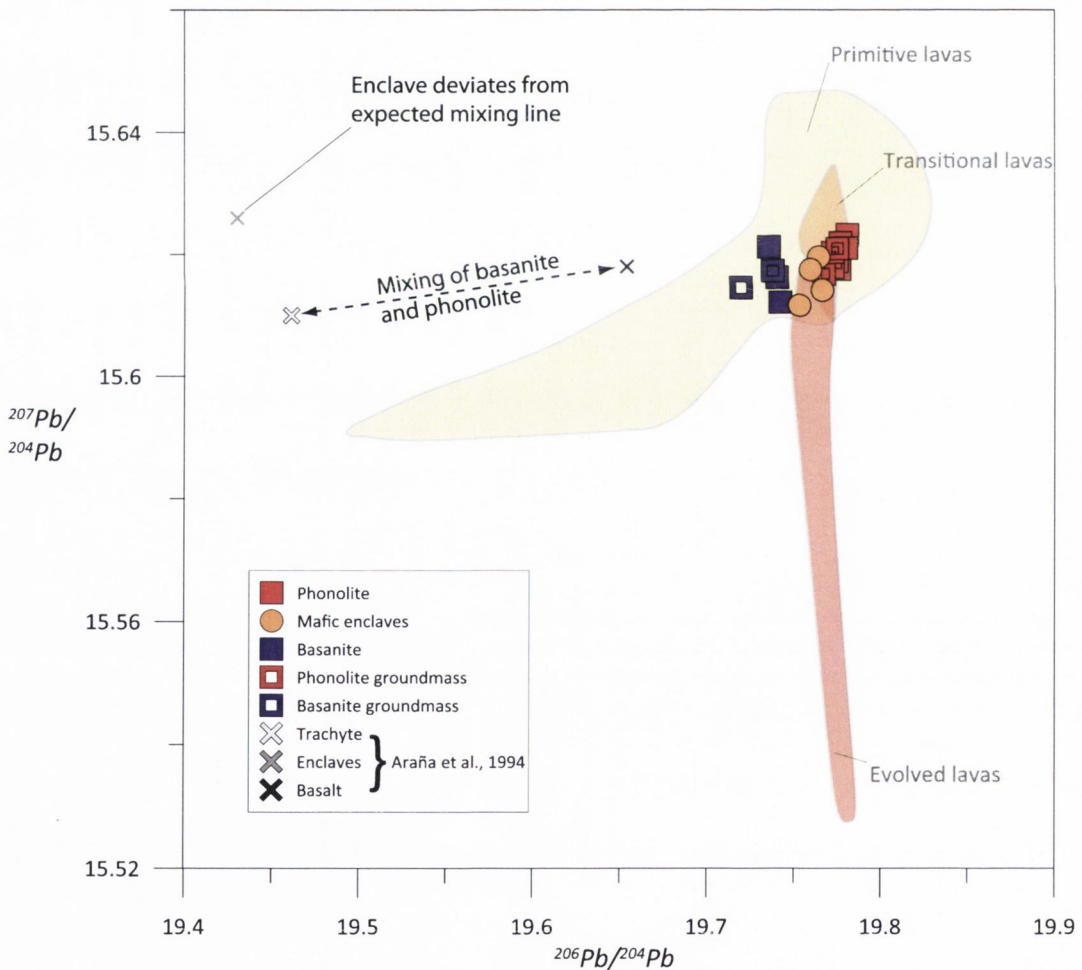

Fig. 2.18: Montaña Reventada Pb isotopic composition in comparison with the post-collapse lava framework from chapter 2 (coloured fields). In line with the previous classification, the Reventada phonolite plots as transitional, whereas the basanite is primitive. Pb data from Araña et al. (1994) appears to be fallible.

All enclave samples can be explained as a mixture between the basanitic and phonolitic end-members. The basanites, phonolites and enclaves show similar $^{207}Pb/^{204}Pb$ ratios, insufficient to constrain mixing. The $^{206}Pb/^{204}Pb$ values, however, divide the components of Montaña Reventada into three distinct groups, with the enclaves placed in-between the basanite and phonolite. Enclaves have thus been produced through mixing of the two main components, basanite and phonolite.
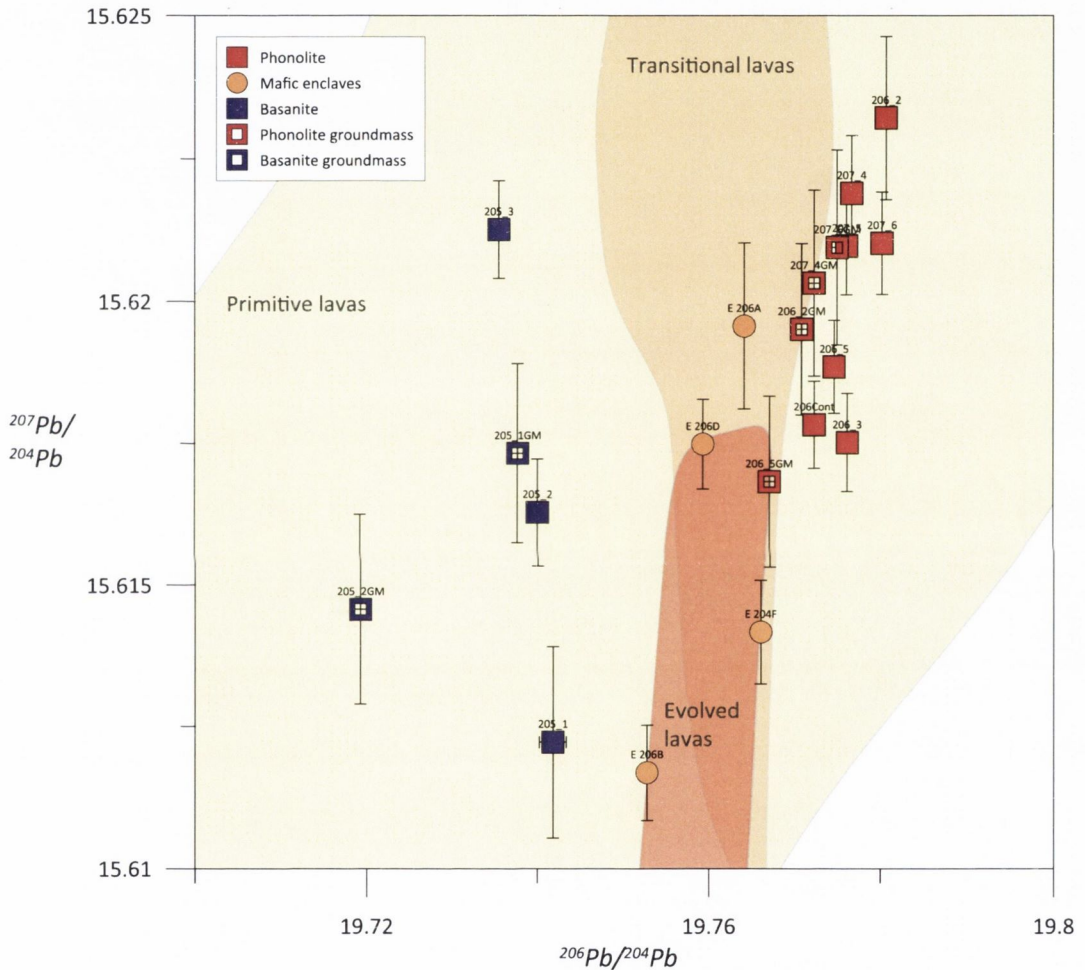
Fig. 2.19: Pb-Pb isotope systematics of the Montaña Reventada eruption. Errors are 2σ and are included in the data symbol when not visible. Basanite and phonolite define independent sub-vertical trends. Enclaves that are found in the phonolites show a similar range in $^{207}Pb/^{204}Pb$ but bridge the gap in $^{206}Pb/^{204}Pb$ between the basanite and phonolite.

The wide range of $^{207}Pb/^{204}Pb$ ratios in enclaves suggests that self-diffusion was a subordinate factor in this case (cf. Watson & Baxter, 2007), as otherwise the $^{207}Pb/^{204}Pb$ would need to be more similar among the enclave samples. Instead, chemical diffusion was likely responsible for the $^{207}Pb/^{204}Pb$ systematics, and, hence, also for the observed

^{206}Pb/^{204}Pb.

It thus appears that a certain degree of heterogeneity in whole-rock samples has to be expected, possibly due to slightly varying contents of crystal matter in each sample. Groundmass samples principally overlap in error, in turn. Hybrid enclaves may even be more irregular as amounts of anorthoclase crystals entrained into each batch of mafic magma likely varies from enclave to enclave. Moreover, enclave volume will vary, too, resulting in an accelerated homogenisation and increased significance of crystal uptake for smaller ones.

5. MODEL

Subaerial emplacement

The areal extent that the basanite flow covers is much larger than that of the phonolite, even though the phonolite is much thicker. Hence, it appears likely that the basanite was much less viscous. Considering a normal "caterpillar-like" emplacement of a lava flow on the surface, we suggest that the basanite erupted first and spread quickly due to its low viscosity (Cas & Wright, 1987) (because the surface it covers is about twice as large as that of the phonolite, the thickness of both units divided by two serves as good approximation of eruption volume). When the eruption of primitive magma waned, pressure dropped within the conduit. This mobilised the heated up phonolite magma, which used the existing basanite conduit. There is no *a priori* reason why it should remain steady for a period of time after the basanite ceased erupting. The lack of signs for explosive activity related to the phonolite and the still higher viscosity of the phonolitic lava, in comparsion to the basanite, imply, however, a considerably slower eruption rate and low volatile content. Given similar conduit geometry, this may have caused the lava "caterpillar" to have been temporarily interrupted as the eruption waned when the phonolite started effusing at a much slower rate than the basanite. While the basanite still kept flowing away from the vent, phonolite was beginning to cover the deposited basanite in the proximal facies. This resulted in a physical separation of both lava types, with the phonolite being emplaced

on top of the basanite as a new layer. The gradational vesiculation of the phonolite away from the contact with the basanite, up to one metre above the contact, indicates that either the heat coming from the freshly emplaced basanite led to exsolution of volatiles from decomposing mineral phases within the phonolite, or gas migrated upwards from the basanite into the phonolite. Furthermore, scoriaceous and deformed banded mafic enclaves contained within the phonolite indicate that the phonolite acted as an erosive agent and removed the top layer of basanite. The lack of breccia in-between the two distinct layers of lava is suggestive of a close temporal relationship between the two lavas. The internal shearing visible within the basanite displays folded and overturned flow-banding and corroborates this view.

Evidence for direct magmatic contact

The enclaves within the phonolite that exhibit textural and compositional mixing relationships between the two lavas, suggest an interval of direct magmatic interaction. Angular and vesicular enclaves within the phonolite are interpreted to stem from the quenching of mafic magma at the initial contact with the phonolite. This implies that the temperature difference between the two bodies of magma must have been very pronounced for these textures to occur (Sparks et al., 1977; Eichelberger, 1980). Upon contact, exchange of thermal energy created a steep temperature gradient which cooled the basanite and heated the phonolite and gave rise to quenched enclave textures. The subsequent movement of the superheated phonolitic body triggered internal shearing, thus disrupting these solids and their vesicular boundary zone, creating angular fragments. Enclaves that feature a chilled margin are also indicative of a strong temperature contrast. The temperature gradient was apparently inadequate to produce a mafic foam similar to the angular enclaves but still large enough to form a chilled margin at the contact of the enclaves with the phonolitic magma. We interpret these as resulting from entrainment of mafic magma in an already "heated-up" phonolite. This is corroborated by the smooth and undulate contacts of these enclaves that appear as if a liquid had frozen.

Furthermore, exchange of crystal matter across the boundary between two magmas is indicative of mechanical interaction and has been documented for over 150 years (e.g.

Bunsen, 1851; Gamble et al., 1979; Tepley et al., 1999; Troll & Schmincke, 2002; Troll et al., 2004; Browne et al., 2006; Meade et al., in press). In the case of the Montaña Reventada eruption, the mafic end-member was almost aphyric, implying that crystal exchange was a one-way route, i.e. from the phonolite into the enclaves. In particular, this process may account for disparities between distinct enclaves, in that different amounts of crystals may have entered individual enclaves. The presence of up to 10% of anorthoclase feldspar in enclaves that shows similar composition and texture to the feldspar found in the phonolite that should be almost aphyric by default, thus suggests direct mechanical interaction.

Timing constraints

Blake (1981) modelled flow fields that occur when a vertically extensive magma chamber is drained (i.e. erupts) and concluded that, at any given time during eruption, all layers of a potentially zoned magma chamber would be sampled and erupted. From that, a mingled deposit would result that shows a crude inverse stratigraphy of all types of magma present in the chamber and increasingly contains lower residing magma up-section in the resulting deposit. With respect to the stratigraphy of Montaña Reventada, this would imply a magma chamber in which the basanite had overlain the phonolite. This, however, has to be considered an instable configuration as the mafic magma is denser relative to the felsic one (e.g. Turner, 1980; Sparks & Huppert, 1984; Turner & Campbell, 1986).

By using the MELTS algorithm, Coombs et al. (2003) constrained enclaves and chilled margins that form between an andesite and a dacite on the order of hours. Prolonged contact would thereafter lead to solidification of the undercooled andesite. This means for Montaña Reventada that timescales of interaction were probably on the same order of magnitude and a contact between basanite and phonolite of more than a few hours to perhaps days appears unlikely. An eruption from a well-established, zoned magma chamber, as postulated by Araña et al. (1994), therefore appears unlikely, too.

Moreover, in several studies, mixing of two such compositionally distinct magmas has proved to require thorough mingling before diffusion evens out the remaining chemical and textural heterogeneities (e.g. Kouchi & Sunagawa, 1995). The Reventada enclaves, in

contrast, are texturally and lithologically discrete entities. Thus the timescales required for thorough mingling within a comparatively viscous phonolitic magma are not consistent with these enclaves being a mere physical mixture of two magmas. Rather, a diffusional hybridisation appears more likely, as has been postulated by Araña et al. (1994), to explain the variable character of the enclaves. This, in turn, indicates rather short time-scales of interaction, again, indicating that a long-lived stratified magma chamber is unlikely to have existed.

Thermal constraints

The Montaña Reventada basanite is a typical example of a rift zone eruption. It is a principally aphyric, low volume lava of basanitic composition that probably ascended quickly through a dyke system without prolonged residence in crustal magma chambers (cf.Hansteen et al., 1998; Klügel et al., 2000, 2005; Galipp et al., 2006; Longpré et al., 2008; Stroncik et al., 2009). Geochemically, the Montaña Reventada basanite is equivalent to other mafic Tenerife rift zone eruptions, not only in major and trace elements but also in its isotopic composition. But, it is also very similar to other rift zone eruptions in terms of volume (low) and crystal content (low). Several studies suggested that, for lavas, the two factors of eruption volume and amount of transported crystals are a proxy for the strength of an eruption (Murata & Richter, 1966; Marsh, 2004; Kinman et al., 2009). This implies that these small, primitive rift zone eruptions may closely represent the background signal of melt production in Tenerife.

In contrast, the phonolitic part of Montaña Reventada may be more likely derived from recycling of country rock. Assimilation and fractional crystallisation may account for variations within the most recent Tenerife phonolites, yet, to a good degree, they may consist of re-melted country rock (see Chapter 4). This means that primitive magma supplied sufficient heat to trigger the formation of the phonolite, but need not directly have interacted with the resulting phonolite itself (e.g. Annen & Sparks, 2002).

On the other hand, the phonolite's much larger volume, 5-10× that of the basanite, implies that it is difficult, if not impossible, to reconcile a direct genetic link with the simultaneously erupted basanite. Neither was the low volume of the co-eruptive basanite

sufficent to produce the observed quantity of phonolite by fractional crystallisation, nor was the thermal energy of this amount of basanite adequate to melt country rock to the extent inferred by the volume of phonolite (cf. Sparks et al., 1977). Moreover, a co-genetic suite from fractional crystallisation is excluded by the straight-lined major element trends. We consider it thus more likely that a basanitic dyke encountered the phonolite magma after the phonolite had been formed by previous processes that are unrelated to the basanite. This basanite dyke was therefore co-eruptive, but not co-genetic, with the phonolite.

We envisage an already emplaced phonolite magma chamber that was cut sideways by an ascending mafic dyke (cf. Izbekov et al., 2004). When the basanite dyke intruded the phonolitic magma chamber, it quenched against it, leaving behind solidified mafic material within the phonolite as well as still liquid magma. The resulting liquid mafic enclaves were prone to mineral and molecular exchange due to their small size and direct contact with the phonolite. In principle, however, the bulk of the two magmas were never adjacent to each other for any extended period of time. Both end-members thus remained mechanically and chemically distinct and bear no direct genetic relationship. This is in agreement with the results of Chapter 4, where phonolitic magma from the post-collapse succession was found to be derived to a large degree from re-melting of country rock at shallow depths and, hence, is compositionally distinct from the underlying mantle melts. In contrast, basanitic magma ascends mainly in dykes from deeper levels and does reflect a compositional connection with the mantle (e.g. Carracedo, 1994, 1996).
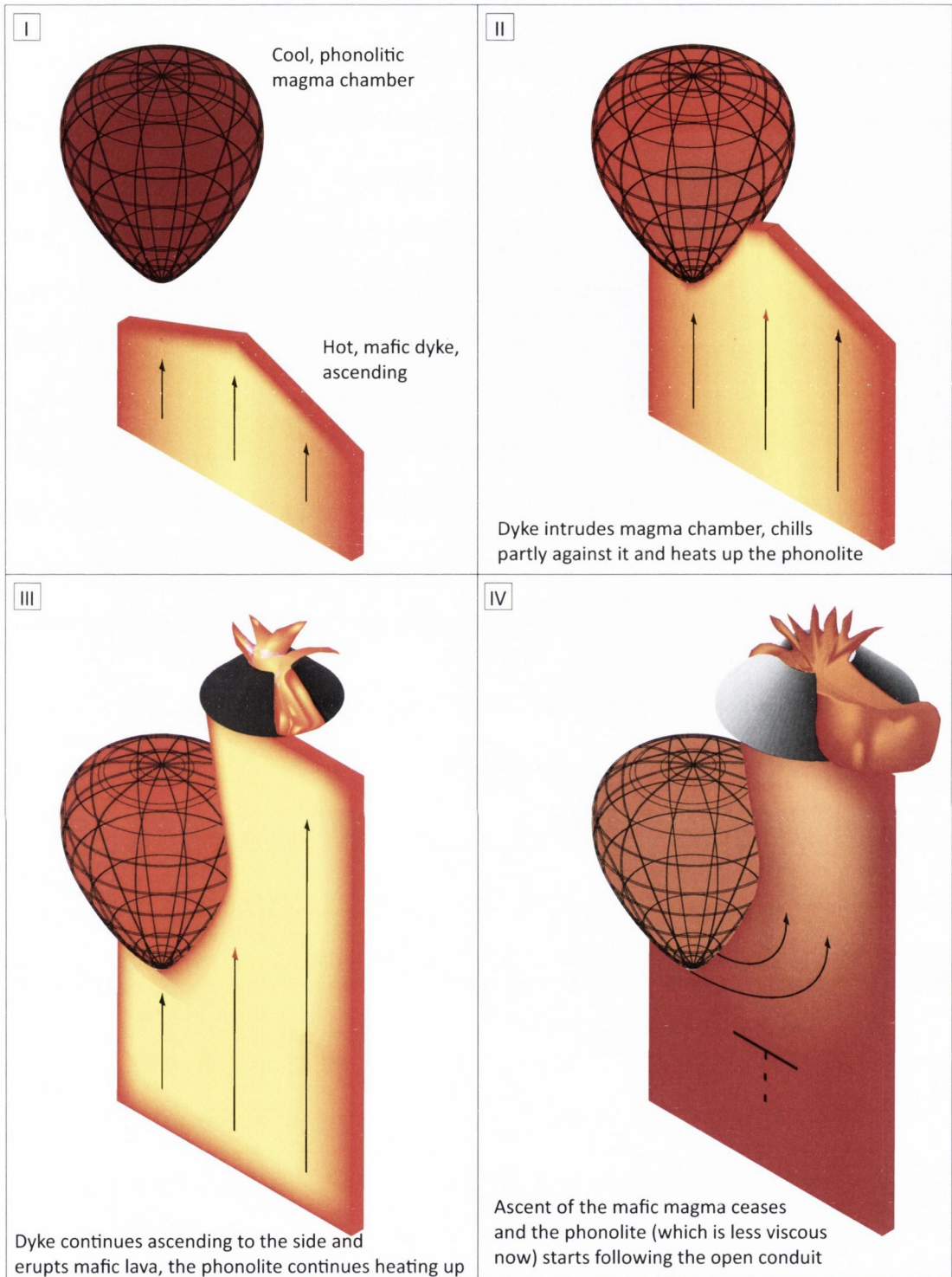
Fig. 2.20: Idealised model of magma body relationships during the Montaña Reventada eruption in four phases from I to IV. Colors follow temperature estimates, from yellow = hot (mafic material) to burgundy = cool (phonolitic magma). Not to scale. Initially, the mafic dyke exhibits a normal temperature gradient towards the country rock (I and II) which diminishes on its sides as long as it keeps ascending and being replenished from below (III). The dyke erupts, but cools rapidly after magma supply ceases (IV). The phonolite, in contrast, remains steady throughout phase I to III as evidenced by the lack of phonolitic material within in the basanite lava. It will, however, have gradually heated up during these stages, becoming less viscous. The arrest of the dyke finally permits the phonolite to ascend through the pre-existing conduit, facilitated by its now reduced viscosity (IV).

The Montaña Reventada composite flow is therefore a direct manifestation of the petrogenetical bimodality in recent Tenerife activity. It is located exactly above the

assumed boundary of phonolite production, where interaction of mafic dykes and active phonolitic magma chambers have to be expected (Carracedo et al., 2007). Described by Izbekov et al. (2004), a basaltic dyke intercepted an andesite magma chamber in the 1996 eruption of Karymsky, Kamchatka and erupted before the bulk of the andesite. A similar case in Tenerife was made by Martí et al. (2008) who found that the Abrigo ignimbrite was shallowly emplaced but too volatile-poor to erupt by itself. Instead, abundant mafic enclaves and mingling textures within the pumices showed an interaction with mafic magma that may have triggered the eruption. Apart from explosivity and erpution volume, the Montaña Reventada eruption is different only in geometrical terms, where the mafic dyke may have arrived sideways to allow the basanite to erupt before the phonolite (Fig. 2.20). This is consistent with the typical lateral extent of dykes of a few metres width by many kilometres length and, in this case, a comparatively small phonolitic magma pocket (total eruption volume approx. 0.13 km^3, Carracedo et al., 2008).

6. CONCLUSIONS

Intermediate magmas in Tenerife may form through direct interaction of two end-member-type magmas: basanite and phonolite. At Montaña Reventada, thorough mixing has been interrupted by eruption, so that enclaves reflect short-term interaction between basanite and phonolite. Prolonged interaction of basanite and phonolite within the same magma chamber likely leads to homogenisation of the whole magmatic body and may be one of the processes responsible to produce intermediate magmas on the Canary archipelago. We furthermore provide a geologically feasible model of eruption, where a dyke of large lateral extent encountered an already emplaced phonolite pocket. As the dyke eruption waned, the decrease in pressure allowed the heated-up and less viscous phonolite to follow the basanite in its conduit.

MICROANALYSIS OF FELDSPAR PHENOCRYSTS FROM TEIDE-PICO VIEJO COMPLEX AND ITS ASSOCIATED RIFT ZONES: CONSTRAINING THE LOWER CRUSTAL MAGMATIC PLUMBING SYSTEM BY MELT- AND EC-RAχFC-MODELLING

1. INTRODUCTION

In the previous chapter, the petrogenesis of recent intermediate lavaswithin the post-collapse succession in Tenerife (<200ka) was addressed on the example of the Montaña Reventada eruption. In that case, magma mixing between a mafic and a felsic magma just prior to eruption yielded significant volumes of various hybrid composition enclaves. However, the mafic lavas from this succession show a certain variability, too (see section 1.5). This study therefore aims to constrain the differentiation processes that are at work to form mafic lavas in the recent post-Icod-collapse succession in Tenerife.

Mafic magma may pool at deeper levels in typical oceanic island settings (Hawaii being an extreme case). Several thermobarometry studies on the Canary Islands have attributed the crystallisation of the assemblages in primitive eruptions to upper mantle or lower crustal storage (Hansteen et al., 1998; Klügel et al., 2000, 2005; Galipp et al., 2006; Longpré et al., 2008; Stroncik et al., 2009), where they may stall for a period after primary melt formation within the mantle. When considering a swift ascent through a sheeted dyke complex without interposed magma chambers (typical for rift zone eruptions on ocean islands), the bulk of the crystal cargo that the primitive magma carries is likely to have crystallised at these levels, recording the processes that influence magmatic variability at the crust-mantle interface (e.g. Longpré et al., 2008).

When investigating phenocryst assemblages, feldspar has proven to be useful in elucidating the magmatic histories of igneous rocks. Apart from being the most abundant rock-forming mineral in the crust, its wide stability field (~ <25km, e.g. Borghini et al.,

2009 and references therein), crystallisation from a wide variety of melt compositions and its sustained "resistance" to diffusional reequilibration of major elements (plagioclase; Morse, 1984) make it an ideal candidate to determine the evolution of magma. Metaphors like "tree-rings" are widely used in the literature and describe the layer-by-layer addition of new feldspar material onto a pre-existing crystal, thereby recording the ambient melt composition.

In recent studies, Sr isotope compositions of individual zones in feldspar crystals has been undertaken by carving out small portions of feldspar with a microdrill for subsequent analysis by TIMS after chemical purification (Charlier et al., 2006). Correlation of this "crystal isotope stratigraphy" with major and trace element profiles and petrographical features of the individual zones has yielded complex histories of mafic recharge, hybridisation, homogenisation, wall crystallisation and assimilation (e.g. Davidson & Tepley, 1997; Knesel & Davidson, 1999; Tepley et al., 1999; Tepley et al., 2000; Tepley & Davidson, 2003; Chadwick et al., 2007; Gagnevin et al., 2007). Gagnevin et al. (2005) cored alkali feldspar megacrysts instead of conventional drilling to improve sample yield and quality.

The TIMS strategy, while providing high-quality, high-precision analyses, is extremely time-consuming which has led to the advent of studies based on laser ablation multi-collector ICPMS. Davidson et al. (2001) repeated a previous microdrilling study (Davidson & Tepley, 1997), but instead used laser ablation coupled to a multi-collector mass spectrometer. They were able to replicate the earlier results with the trade-off of larger analytical uncertainties. However, the new method was significantly less time-consuming and allowed for a substantially greater volume of analyses. Ramos et al. (2004) provided a methodology for LA-MC-ICPMS studies on geologic materials by extensively testing the method on various natural specimen (carbonate, plagioclase, clinopyroxene and low Rb/Sr fine-grained basaltic groundmass) and scrutinising for potential isobaric interferences. This methodology has been applied by several subsequent studies (e.g. Ramos et al., 2005, Salisbury et al., 2008).

Another set of studies concentrates on non-isotopic methods of microanalysis. For

example, Ginibre et al. (2002 a&b) used back-scattered electron images (BSE) and trace element zoning to distinguish types of oscillatory zoning in plagioclase and two distinct episodes of magma recharge at Parinacota volcano, Chile. On the Canary Islands, Troll & Schmincke (2002) found a complex interplay of fractional crystallisation, convection, magma mixing and assimilation recorded by the major element micro-stratigraphy of feldspars in the rhyolitic/trachytic ignimbrite 'A' in Gran Canaria. Triebold et al. (2006) constrained mafic recharge and magma mingling events for individual eruptions of the Teide-Pico Viejo complex in Tenerife by using back-scattered electron images (BSE) and detailed trace element profiles from plagioclase crystals.

Common to all of these studies is that they identified distinct isotopic and trace element signatures of the interacting components. Isotopic studies on Tenerife have shown that the isotopic composition of Sr is rather homogeneous in the majority of whole-rock analyses (Palacz & Wolff, 1989; Simonsen et al., 2000; Abratis et al., 2002; Gurenko et al., 2006). Even if scarce, $^{87}Sr/^{86}Sr$ ratios that exceed this general Tenerife signal have nevertheless been reported (Palacz & Wolff, 1989; Simonsen et al., 2000) for Tenerife. Furthermore, whole-rock data are commonly known to represent an average and mask small-scale heterogeneities. The microanalytical data available from the ERUPT project (Chertkoff et al., 2005 a&b) were too few to discard isotopic heterogeneity on a single-crystal scale for Tenerife, especially as high $^{87}Sr/^{86}Sr$ ratios have been found in the work presented in Chapter 4. We therefore adopted a regional-scale approach by covering as many eruptions of the stratigraphically well-constrained post-collapse succession in Tenerife. This succession consists of the central complex Teide-Pico Viejo, monogenetic vents located in the surrounding Las Cañadas Caldera and on the Northwest and the Northeast rift zone.

The aim of this study is to constrain the overall dynamics present within a magmatic system by investigating a large number of feldspar crystals. To achieve this, the selected phenocrysts are from lavas that a) span the whole range of compositional variability witnessed in Tenerife and b) cover a well-constrained period of time (200 ka to present). Individual zones in feldspar phenocrysts within the post-collapse lavas of Tenerife were

analysed for their major and trace element and Sr isotope composition. The results from this work are embedded into a framework of pre-existing stratigraphical and wholerock major and trace element data (Carracedo et al., 2007; Rodríguez-Badiola et al., 2008). The classification of primitive, transitional and evolved lavas based on their trace element patterns is shown in section 1.5. This is used to colour-code the feldspar data after the composition of the lava they were found in (primitive - yellow, transitional - orange, evolved - red).

Table 3.1: *Samples for feldspar microanalysis of lavas from Teide-Pico Viejo complex and rift zones*

Eruption	Eruption phases	Samples	Rock	Feldspar types	Analyses performed		
					Major elements EMP	Trace elements LA-ICPMS	$^{87}Sr/^{86}Sr$ LA-MC-ICPMS
Abejera Alta		ABA-21, ABA-22, ABA-36*	Pho	Anorthoclase	•	•	-
Abejera Baja		ABB-19, ABB-20	Pho	Anorthoclase	•	•	-
El Boquerón		BOQ-13, BOQ-14	Pho	Anorthoclase	•	•	-
Montaña Cascajo	Phase 1	CA1-75	Bas	Bytownite	•	•	•
	Phase 2	CA2-20*	Bas	Labradorite	•	•	•
	Phase 3	CA3-22	Bas	Bytownite	•	-	•
Pico Cabras		CAB-27	Pho	Sanidine	•	•	
Volcan El Ciego		CIE-18	TPh	Anorthoclase	•	•	att.
Montaña de Chío		CIO-32, CIO-77, CIO-81, CIO-82, CIO-83	BTa	Andesine, Oligoclase	•	•	•
Volcán Cuevas Negras		CUE-14*	TPh	Andesine	•	•	•
Galería Rio de Guia (PV-EVO)		GRG-1300, GRG-2800, GRG-2850	n/a	Andesine	•	•	•
Montaña Las Lajas		LAJ-23	TPh	Andesine, Oligoclase	•	•	•
Las Lenguas		LEN-15*	Tra	Oligoclase, Anorthoclase	•	•	•
Montaña Majúa		MAJ-16, MAJ-17*	Pho	Andesine, Anorthoclase	•	•	•
Bocas de Doña María		MAR-37	PTe	Andesine	•	•	•
Montaña Blanca	Phase 1	MB1-34	Pho	Anorthoclase	•	•	-
	Phase 4	MB4-10*	Pho	Anorthoclase	•	•	att.
	Phase 5	MB5-04*, MB5-05	Pho	Anorthoclase, Sanidine	•	•	att.
	Phase 7	MB7-08*	Pho	Anorthoclase	•	•	-
Montañas Negras		NEG-50	Bas	Bytownite	•	•	•
Volcán Portillo	Upper unit	PO2-07	Tan	Labradorite	•	•	•
Pico Teide - Lavas Antiguos (Playa Sto. Domingo)		PT-ANT-16	Bas	Anorthoclase	•	•	att.
Pico Teide - Lavas Antiguos (Playa San Marcos)		PT-EAR-15	Bas	Labradorite	•	•	att.
Pico Teide - Intermediate Lavas		PT-INE-07, PT-INE-11, PT-INE-17	TPh	Oligoclase	•	•	•
Pico Teide - Lavas Negras		PT-LAE-03, PT-LAE-05, PT-SUM-01	Pho	Anorthoclase	•	•	att.
Pico Viejo - Pa'hoe'hoe Lavas		PV-EAR-15, PV-EAR-16, PV-EAR-17	PTe	Labradorite, Andesine	•	•	•
Pico Viejo - Evolved Lavas		PV-EVO-07, PV-EVO-21, PV-EVO-28	Bas	Andesine	•	•	•
Pico Viejo - Intermediate Lavas		PV-INT-08, PV-INT-18, PV-INT-29	PTe	Andesine	•	•	•
Pico Viejo - Phonolite I		PV-LAT-02, PV-LAT-04, PV-LAT-61, PV-LAT-66	Pho	Oligoclase, Anorthoclase	•	•	•
Cuevas del Ratón		RAT-84	PTe	Oligoclase	•	•	•
Roques Blancos		RBL-02*, RBL-03	Pho	Oligoclase, Anorthoclase	•	•	•
Montaña Reventada	Enclaves	REV-09, REV-63, REV-85a	Enclave	Andesine, Oligoclase, Anorthoclase	•	•	•
	Phonolite	REV-10, REV-70, REV-71, REV-85b	Pho	Labradorite, Andesine, Oligoclase, Anorthoclase	•	•	•
Montaña Samara		SAM-26	PTe	Labradorite	•	•	-
Volcán Negro		VON-12	PTe	Labradorite	•	•	•

Table 3.1.: List of samples and the types of analyses performed on feldspars from the Montaña Reventada eruption. Rocktypes: Bas = basanite; PTe = phonotephrite; TPh = tephriphonolite; Pho = phonolite; BTa = basaltic trachyandesite; Tan = trachyandesite, Tra = trachyte. Performed analyses are marked with •, "att." stands for attempted but failed and "-" equals not performed. More information and details on sample location can be found in the appendix.

2. METHODOLOGY

2.1. *Sample selection*

Microanalysis was conducted on whole-rock samples that contained at least 2-3% feldspar by volume. The set of specimens covered 66 samples from 29 eruptions (altogether 34 eruption phases) from the post-collapse succession (Table 3.1).

2.2. *Microanalysis*

The following microanalytical techniques were performed at the GeoAnalytical Lab at Washington State University, Pullman, WA, USA: a) Electron Microprobe (EMP) for analyses of major elements, b) Laser Ablation - Inductively Coupled Plasma-Mass Spectrometry (LA-ICPMS) for trace element analyses and c) Laser Ablation - Multi Collector-Inductively Coupled Plasma - Mass Spectrometry (LA-MC-ICPMS) for $^{87}Sr/^{86}Sr$ analyses.

2.2.1. *Rock cutting and thin section preparation*

Samples with flow alignment of crystals were preferentially selected and cut parallel to the flow plane. Units that did not display such alignment or flow lamination were cut depending on texture. All microanalyses were conducted on 150μm thin sections and sample sites were controlled with petrographical microscopes that were built into the EMP and the laser ablation unit. 99 thin sections of 46 × 26 mm size were prepared to fit the brackets of the EMP and laser ablation unit.

Sections had to be of 150 μm thickness for the destructive laser ablation process that generally carves tens of microns into the sample during analysis.

2.2.2. *Electron Microprobe (EMP) Analysis*

Major element analysis of feldspar was performed at Washington State University on a Cameca SX-50 on carbon coated thin sections. Analytical conditions included an electron beam acceleration of 15 kV, a beam current of 15 nA, beam size of 10μm^2 and counting

times of 10 - 30s on peaks. Low beam current and short on-peak-time of 10s compensated for potential Na loss. Relative analytical precision [(standard deviation/mean) × 100] was <1 % for Si and Al, <3 % for Na, <5 % for Ca and K and <20 % for Fe. Ba analysis failed for most attempts with errors exceeding 2500 % in cases. BaO data plotted generally on the higher side when compared to laser ablation measurements.

Crystals that were free from inclusions were analysed with programmed traverses of varying distances and continuous manual refocussing. Phenocrysts with a large amount of inclusions or 'untidy' textures were analysed spot-by-spot. We excluded measurements with a total outside 100 ± 2 wt.%.

2.2.3. Laser ablation

For trace element and Sr isotope analyses, we used a New Wave™ UP-213 Nd:YAG laser ablation unit (213 nm wavelength; Jackson, 2001; Roy and Neufeld, 2004) coupled to single and multi-collector mass spectrometers (see Table 3.2 for respective operating parameters). Laser ablation was conducted in dynamic mode which allows continuous monitoring of the elemental signals over the duration of one analysis. Laser troughs were preferred over points in order to maximize isotopic signals while minimizing the depth of the laser pit. A continuous flow of Ar gas carried the resulting aerosol to the mass spectrometer. Mass fractionation is generally increased by greater pit/trough depths, utilising 150μm thick sections provided a maximum excavation depth below which there was no discernible laser induced fractionation (Ramos et al., 2004).

Table 3.2: Instrument parameters of the New Wave™ UP-213 laser ablation unit

	Trace element analysis	$^{87}Sr/^{86}Sr$	Units
Spot size	20	40	[μm]
Trough length	500	500	[μm]
Scan speed	16	50	[μm/s]
Fluence	~12	12	[J/cm²]
Repetition rate	20	20	[Hz]
Duration	~30	~180	[s]
Passes	1	40	-
Depth/pass	10	2	[μm]
Rate of auxiliary gas flow (He)	-	0.85 to 0.95	[l/min]

2.2.4. *Trace element analysis: Laser Ablation – Inductively Coupled Plasma – Mass Spectrometry (LA-ICPMS)*

Feldspar zonation patterns and inclusions were investigated by transmitted light petrography prior to LA-ICP-MS analysis and whenever possible they were texturally correlated with previously measured EMP data points. Individual zones of feldspar were analysed for 14 trace elements (Rb, Ba, La, Ce, Pr, Nd, Sm, Eu, Gd, Y, Pb, Mg, Sr and Ti) and two major elements (Ca and Si).

Analyses were performed using a ThermoFinnigan Element2™ Inductively Coupled Plasma-Mass Spectrometer (ICP-MS). The ICP-MS was set to start capturing simultaneously with laser ablation. Each analysis was therefore preceded by 10-15 seconds of 'empty' Ar flow that served to monitor instrument blank levels throughout the session.

Calibration was performed using the National Institute of Standards (NIST) 612 glass standard. Silica, previously determined by electron microprobe analysis, was used as an internal standard. The detection limit for the LA-ICP-MS was below 0.1 ppm for most elements, and in-run precision was <10%. Sm and Gd were excluded from the dataset as their intensities were low and exhibited fluctuation (cf. Fig. 3.1 and Fig. 3.2).
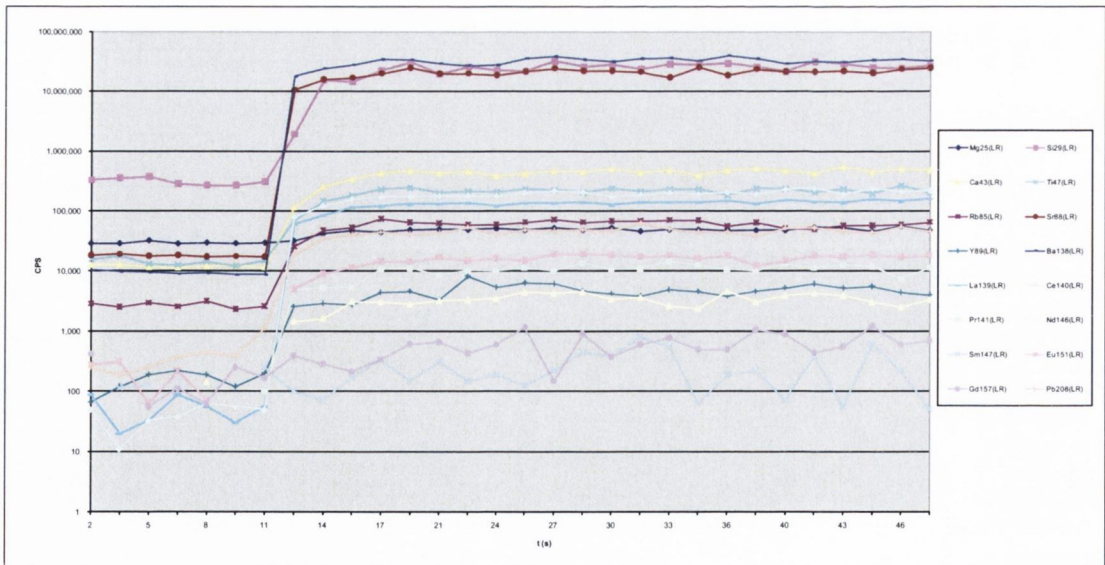

Fig. 3.1: Graph of a typical flawless trace element analysis in a feldspar (copied from the original spreadsheet). X-axis is time of analysis, y-axis the recorded beam intensity. Fluctuations are averaged out, this provides a robust signal of trace element contents in the feldspar zone. Note the more variable behaviour of Sm and Gd intensities due to low concentrations. These two elements were therefore not included in the results.
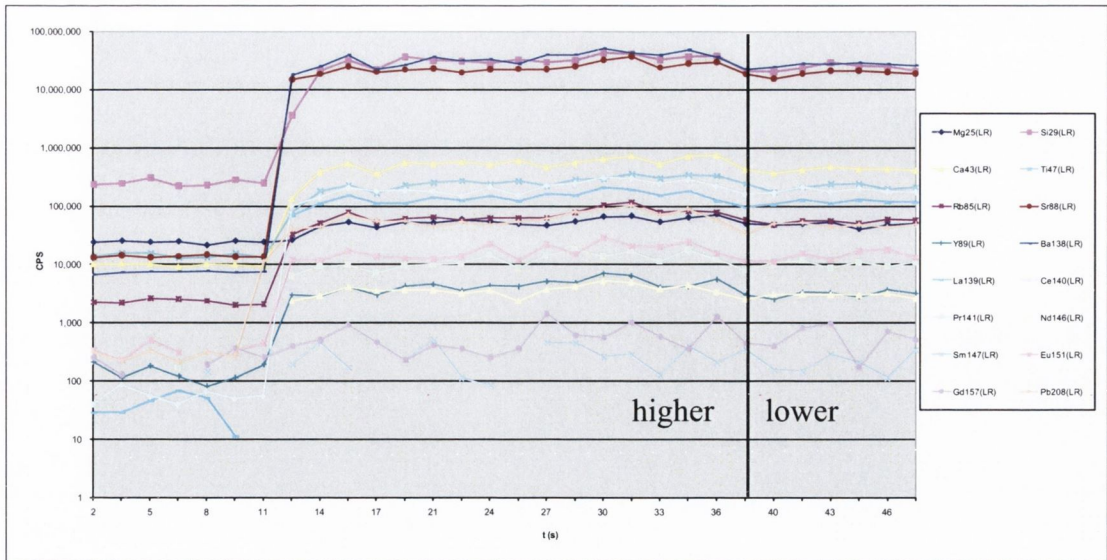
Fig. 3.2: Example of a graph of an analysis where two different compositional zones during one run had been encountered in a feldspar (copied from the original spreadsheet). X-axis is time of analysis, y-axis the recorded beam intensity. Note the decrease in intensities towards the end of the run and the parallel fashion in which they decrease. In this case, data interpretation is limited to the interval between 20 and 35 seconds to yield a meaningful average of intensities.

Continuous recording of intensity levels allowed the data to be scrutinised for unseen compositional boundaries within the feldspar. Parallel signals at nearly constant intensity levels implied compositional homogeneity in those elements (Fig. 3.1). Parallel, but step-like patterns indicated that two compositionally distinct zones had been analysed (Fig. 3.2).

2.2.5. Laser Ablation – Multi Collector – Inductively Coupled Plasma – Mass Spectrometry (LA-MC-ICPMS)

Analysis of Sr isotopic ratios in feldspar zones was performed at the GeoAnalytical Lab, Washington State University, WA by laser ablation multi collector ICP-MS, following the method of Ramos et al. (2004). Ramos et al. (2004) used the same laboratory and analytical setup. All samples were polished to a 1 µm finish and cleaned in alcohol prior to analysis. For a typical Tenerife post-collapse plagioclase (~2000 ppm Sr), a 40×500×100 µm trough yielded ~11 ng of Sr. Laser parameters are outlined in Table 3.2. The laser ablation sample cell was flushed with He carrier gas to pick up the ablated sample. A gas flow of ~0.7 l/min of argon was added to this gas/sample mixture prior to introduction of sample into the plasma.

71

Analyses of laser-ablated samples consisted of 100 ratios, with each ratio measured in 1 s integrations. Method and intrument parameters were optimised to obtain ^{88}Sr beam intensities between 2 and 4 V (Table 3.3). Baselines for analyses were measured on-peak for ~60 s while flushing the sample chamber with He mixed with Ar. This is comparable to a normal analysis, but without activating the laser. Typical baselines were ≤0.2 mV (^{88}Sr) depending on the length of the analytical session. Analyses of unknowns were bracketed by three sets of three analyses of an external standard. The standard was a large plagioclase from the Imnaha member in the Columbia River basalts. This feldspar shows a homogenous composition with respect to its ^{86}Sr/^{88}Sr ratio and its Sr concentration (0.70405 and 700ppm, respectively).

Table 3.3: Instrument parameters of the ThermoFinnigan Neptune MC-ICPMS

		Units
RF power	1200	[W]
Argon cooling gas flow rate	15	[l/min]
Auxiliary gas flow rate	0.8	[l/min]
Interface cones	Nickel	
Acceleration voltage	10	[kV]
Ion-lens settings	Optimized for maximum sensitivity and optimal peak shape	
Mass resolution	400	
Mass analyzer pressure	$5–8×10^{-9}$	[mbar]
Detection system	Nine Faraday collectors	
Sampling mode	3 or 10 blocks of 10×8 s integrations for laser and solution analysis, respectively	
Background/baseline determination	3 min on peak in 2.0% HNO_3	
Nebuliser	Glass cyclonic spray chamber fitted with a Micromist PFA nebuliser	
Uptake mode	Free aspiration	
Sample uptake rate	50	[µl/min]
Typical sensitivity on 88Sr	55–60 (10^{-11} Ω resistors)	[V/ppm]
Ar sample gas flow rate	0.60–1.05, optimized to maximize ^{88}Sr signal	[l/min]
Beam dispersion (Dispersion Quad)	-25	

We monitored ^{85}Rb and ^{83}Kr to account for isobaric interferences of ^{87}Rb, ^{84}Kr and ^{86}Kr. For the Rb interefrence correction, a natural ^{87}Rb/^{85}Rb ratio of 0.3855 was used (corrected for mass bias by the measured ^{86}Sr/^{88}Sr ratio), which is applicable for unspiked or low Rb concentration samples (Waight et al., 2002). See Ramos et al. (2004) for an overview of potential interferences and correction procedures (their Table 3).

2.2.6. Calibration of feldspar isotope data using microdrill/TIMS

Strontium isotope analysis by LA-MC-ICP-MS initially yielded demonstrably offset $^{87}Sr/^{86}Sr$ ratios with a need for external calibration. Initial ratios produced were between 0.702089(84) and 0.703340(151), which are lower than assumed mantle values and lower than most published Tenerife $^{87}Sr/^{86}Sr$ data. We therefore applied a combination of microdrilling and TIMS analysis to measure individual feldspar zones. Furthermore, the whole range of trace element concentrations and $^{87}Sr/^{86}Sr$ ratios that were obtained from laser ablation analysis was covered in these measurements to achieve a robust external calibration.

Material was excavated from individual feldspar zones with a Merchantek Microdrill following the drilling procedure of Charlier et al. (2006). Drilling was conducted at Washington State University. A minimum amount of 100ng Sr was aimed for to achieve a concentration of 100ppb in 1ml liquid for subsequent MC-ICPMS analysis. The real concentration in each feldspar zone was known from previous LA-ICPMS analyses, which enabled calculation of the necessary volume for each drill site.

The drill volume was calculated as product of the section of our drillbit (a cut-off isosceles triangle of variable size with depth) and drill length. The drillbit possessed an opening angle of $\alpha=30°$ measured with the turning stage of a petrographic microscope (error $\pm1°$). The drill depth was then adjusted according to the total necessary volume for each individual zone of feldspar. The drilling procedure was conducted in a continuous air flow unit to reduce the amount of air-suspended particles. Prior to drilling, a drop of ultrapure water was placed on the thin section to capture the drill flakes. We drilled in five passes each corresponding to 20% of the total drill depth.

The combination of drill volume and ICPMS requirements dictated a wider and deeper drill pit than the laser had excavated before. This involved drilling across several zones to obtain the analyte volume. Therefore, only adjacent zones that were known from previous analyses to be homogenous in both Sr concentration and $^{87}Sr/^{86}Sr$ isotopic ratio were drilled, so as not to yield an average of two compositionally different zones.

Samples were then digested in HF and HNO_3 and Sr was separated using Eichrom Sr-

Spec resin in the clean laboratory at Washington State University. Typical blanks were less than 10pg Sr, following the method outlined in Wolff et al. (1999).

Samples were tested for intensity (proportional to concentration of Sr) on the MC-ICPMS at Washington State University. The first drill session yielded samples with a concentration of only 10ng Sr. As a result, the columns were recalibrated and gave acceptable results when tested with other samples of similar concentration. However, a repeat drill session on our samples yielded equally low concentrations in the pre-screening. The reason for this remains unclear. A new strategy was adopted which involved analysing the low Sr samples by TIMS at the Isotope Geoscience Unit, SUERC, East Kilbride, Scotland in collaboration with Prof. Rob Ellam.

Samples were loaded on single Re filaments together with a Ta emitter solution. Measurements were conducted on a VG Sector 54-30 with a dynamic multi-collector routine and a $^{86}Sr/^{88}Sr$ fractionation control (normalised values). Samples were run manually at 0.5V to prevent excessive loss of the small samples at an early stage of the analysis.
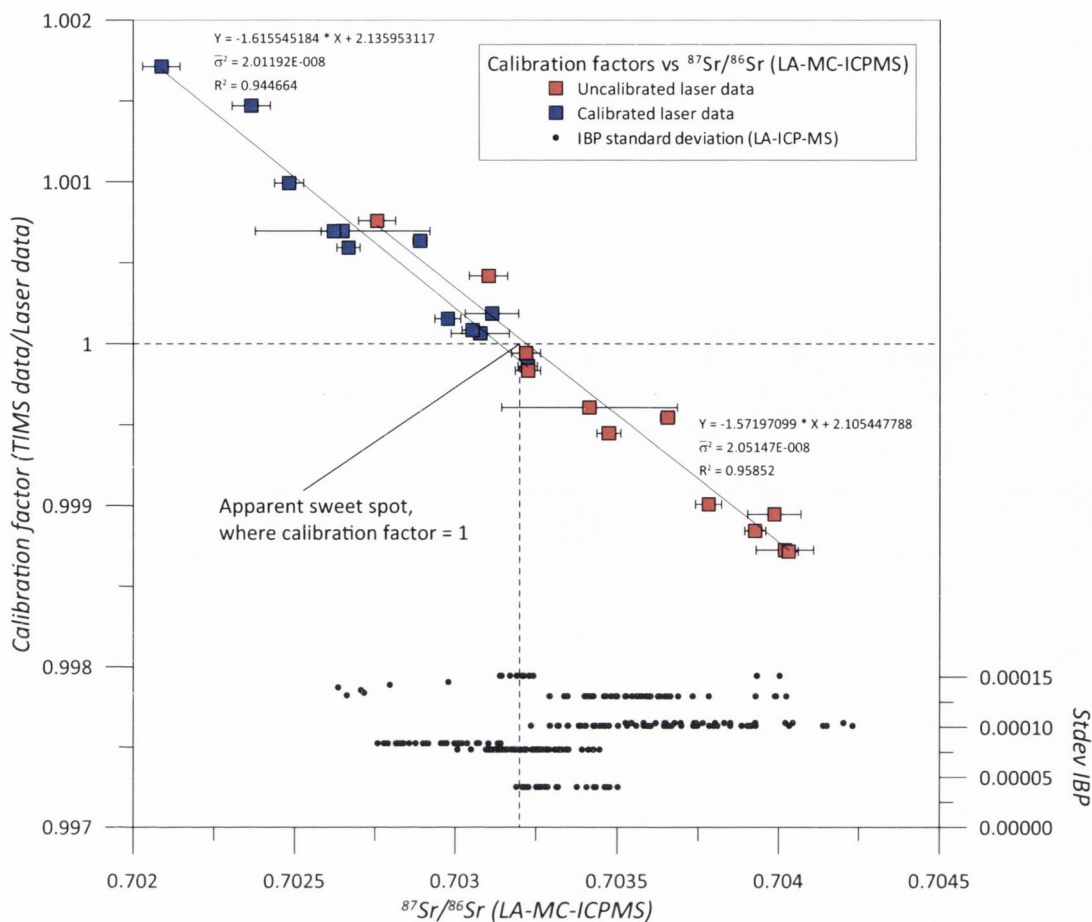
Fig. 3.3: Calibration factors (TIMS data divided by laser data) versus the original laser data. Blue squares are raw laser data, red squares are calibrated laser data. Errors contained within symbol when not visible. Laser data are unrealistically low in $^{87}Sr/^{86}Sr$ (>0.702089) and had to be calibrated by analysing the same feldspars by a microdrill/TIMS approach. Note the $^{87}Sr/^{86}Sr$ ratios from TIMS analysis correlate with the laser data (R^2=0.95), i.e. the error in the laser data is systematic (the higher the farther away the ratio is from an apparent sweetspot at ~0.70304). The calibration factors (y-axis) were used to recalculate the $^{87}Sr/^{86}Sr$ ratios from feldspar analysis. Lower part: black dots are error values yielded from LA-MC-ICPMS analysis; no correlation with $^{87}Sr/^{86}Sr$ ratio could be detected.

Uncalibrated laser data were divided by the corresponding microdrill/TIMS data to obtain a calibration factor for each point. Uncalibrated laser data correlate strongly with the obtained calibration factors (Fig. 3.3, R^2 > 0.95) and allows a linear regression equation to be devised. The calibration factors for the remaining analyses without directly comparable microdrill/TIMS data were then calculated from this regression equation ($y = A * x + B$), with x being the uncalibrated $^{87}Sr/^{86}Sr$ ratio, obtained from LA-MC-ICPMS analysis.

This meant an overall "levelling" of ratios from this calibration. The initial range of externally calibrated LA-MC-ICPMS ratios was 0.702089 to 0.703398, while after the calibration this range was reduced to 0.7031 to 0.7033 for the bulk of the analyses (235 out of 242). Seven analyses yielded ratios of up to 0.7034 (Fig. 3.6). The calibrated ratios

are slightly higher than previously reported wholerock ^{87}Sr/^{86}Sr data from Tenerife (e.g. Simonsen et al., 2000; Gurenko et al., 2006) but are in agreement with Sr ratios from previous ^{87}Sr/^{86}Sr data on Tenerife feldspars (Palazc & Wolff, 1989; Chertkoff et al., 2005a, b).

2.3. *Modelling of melt composition and crystallisation temperature*

Several studies have defined a set of equations on plagioclase-melt trace element partitioning based on synthetic and natural examples (e.g. Blundy & Wood, 1991; Bindeman et al., 1998). These empirical relationships allow calculation of the distribution coefficients (D_i) for various elements, and yield, for example, the compositional dependence of D_{Sr} on anorthite content in plagioclase. Bédard (2006) added several empirical equations that relate the anorthite composition of plagioclase to various chemical and physical parameters of the melt that the plagioclase crystallised from, again based on pre-existing natural and experimental data.

We used the data from this study to model the MgO, Sr and Ba concentrations in the melt from which a given plagioclase composition crystallised from. Furthermore, the temperature at which a given zone of feldspar crystallised from the melt was calculated.

The following equations describe the modelling approach. The parameters and sources used for each step are given in Table 3.4.

- Eq. 3.1: Melt MgO concentration

$$lnMgO = \frac{X_{An} - (b \pm \Delta b)}{a \pm \Delta a}$$

- Eq. 3.2: Crystallisation temperature of plagioclase

$$\frac{10000}{T} = a * lnMgO + b$$

- Eq. 3.3: Plagioclase-melt distribution coefficient for Sr and Ba

$$lnD_i = \frac{a * X_{An} + b}{R * T}$$

- Eq. 3.4: Melt Sr and Ba concentrations

$$C_{melt}(i) = \frac{C_{plag}(i)}{D_i}$$

Table 3.4: Parameters for melt modelling equations

	Y	X	a	±a	b	±b	Comment	Reference	Their equation
Melt MgO [wt.%]									
	lnMgO	X_{An}	0.04448	±0.00158	0.42132	±0.07065	for dry melts, MgO >1wt.%	Bédard, 2006	3a
	lnMgO	X_{An}	0.50206	±0.09061	0.10090	±0.10362	for dry melts, MgO >1wt.%	Bédard, 2006	3b
	lnMgO	X_{An}	0.10639	±0.00444	0.57229	±0.13285	wet melts	Bédard, 2006	3c
Crystallisation temperature [°C]									
	10000/T	*lnMgO*	-0.95668	±0.01728	10.3758	±0.0232		Bédard, 2006	5a
	1/T	*lnMgO*	-2.04×10^{-4}		7.92×10^{-4}			Bindeman et al., 1998	3
Distribution coefficients plagioclase-melt									
	$RTlnD_{Sr}$	X_{An}	-26700	±1900	26800	±1200		Blundy & Wood, 1991	
	$RTlnD_{Ba}$	X_{An}	-38200	±3200	10200	±1800		Blundy & Wood, 1991	
	$RTlnD_{Sr}$	X_{An}	-30400	±1100	28500	±700		Bindeman et al., 1998	2
	$RTlnD_{Ba}$	X_{An}	-55000	±2400	19100	±1300		Bindeman et al., 1998	2
	$RTlnD_{Sr}$	X_{An}	-20710	±1772.3	23856	±3581.5		Bédard, 2006	19a
	$RTlnD_{Ba}$	X_{An}	-35204	±2797.5	10146	±5590.4		Bédard, 2006	18a

Table 3.4.: All calculations follow the equation $Y = a * X + b$.

Table 3.5: Representative feldspar analyses for Teide-Pico Viejo complex and rift zone eruptions

Sample	CIO-77-1-01-r	CIO-77-1-16	CIO-83-1-01-r	CIO-83-1-14	CUE-14-2-01-r	CUE-14-2-10-c	MAJ-16-1-08-c
Distance from core [μm]	2120	197	1624	168	562	0	0
EMP [wt.%]							
SiO_2	60.75	55.34	58.41	58.18	59.22	57.95	56.77
Al_2O_3	23.41	26.58	26.20	26.38	25.32	25.74	26.29
Fe_2O_3	0.57	0.46	0.34	0.46	0.46	0.51	0.52
K_2O	1.04	0.53	0.94	0.84	0.73	0.67	0.54
Na_2O	7.76	5.97	6.68	6.58	7.35	6.63	6.27
CaO	5.06	8.71	7.52	7.72	6.76	7.45	8.41
BaO	0.37	0.02	0.26	0.19	0.24	0.16	0.17
Total	98.96	97.62	100.35	100.34	100.07	99.11	98.96
An [mol%]	24.88	43.23	36.28	37.40	32.29	36.79	41.20
Ab	69.03	53.63	58.34	57.73	63.54	59.25	55.64
Or	6.10	3.14	5.38	4.87	4.17	3.95	3.16
LA-MC-ICPMS							
$^{87}Sr/^{86}Sr$	0.703220(78)	0.703231(78)	0.703225(78)	0.703218(78)	0.703234(84)	0.703247(84)	0.703195(40)
LA-ICPMS [ppm]							
Rb	1.3	1.8	3.7		1.8	1.6	1.4
Ba	850.5	1019.3	1226.5		1165.6	850.8	634.2
La	13.0	10.0	18.4		14.3	12.4	11.9
Ce	18.3	13.4	23.3		17.4	17.7	18.4
Pr	1.1	0.8	1.4		1.1	1.0	1.2
Nd	2.8	2.0	3.7		2.8	2.3	3.7
Eu	1.3	1.2	1.7		1.7	1.3	1.1
Y	0.3	0.4	0.5		0.4	0.3	0.6
Pb	2.7	2.7	3.4		3.2	3.0	2.2
Sr	3348.9	3050.7	2212.3		3341.4	2840.3	2135.0
Ti	679.9	500.2	967.8		641.7	564.7	602.6
Mg	241.6	246.6	223.5		192.6	193.6	298.9

Table 3.5 continued: Representative feldspar analyses for Teide-Pico Viejo complex and rift zone eruptions

Sample	MAR-37-1-02	MAR-37-1-07-c	PT-INE-17-1-01-r	PT-INE-17-1-10	PV-EAR-16-1-02	PV-EAR-16-1-13	VON-12-1-01-c
Distance from core [μm]	1216	0	371	140	1814	336	0
EMP [wt.%]							
SiO_2	56.64	56.90	60.29	60.10	55.27	53.55	51.32
Al_2O_3	26.67	26.49	24.63	24.24	28.29	28.46	29.69
Fe_2O_3	0.33	0.38	0.38	0.40	0.50	0.48	0.51
K_2O	0.86	0.84	1.19	1.34	0.72	0.83	0.29
Na_2O	6.15	6.24	7.80	7.81	5.30	4.59	4.55
CaO	8.39	8.05	5.44	4.94	10.39	11.33	11.76
BaO	0.13	0.10	0.26	0.26	0.10	0.06	0.00
Total	99.16	99.01	99.99	99.09	100.56	99.32	98.12
An [mol%]	40.83	39.58	25.96	23.91	49.88	54.92	57.85
Ab	54.18	55.49	67.26	68.39	45.99	40.26	40.47
Or	4.99	4.93	6.78	7.70	4.14	4.82	1.68
LA-MC-ICPMS							
$^{87}Sr/^{86}Sr$	0.703214(40)	0.703202(40)	0.703192(104)	0.703176(104)	0.703131(101)	0.703150(101)	0.703223(151)
LA-ICPMS [ppm]							
Rb	3.3	2.7	5.1	4.5	1.8	1.7	0.6
Ba	944.3	787.9	1950.7	1879.2	425.7	395.5	282.3
La	18.1	14.8	16.9	16.3	5.2	5.4	5.1
Ce	23.4	19.6	18.6	17.9	9.1	9.4	9.0
Pr	1.5	1.2	1.0	0.9	0.7	0.7	0.6
Nd	4.3	3.0	2.2	1.9	2.0	2.1	1.9
Eu	1.4	1.2	1.2	1.3	0.9	1.0	0.6
Y	0.6	0.4	0.7	0.6	0.2	0.2	0.2
Pb	3.1	2.8	3.8	3.7	1.0	0.9	0.8
Sr	2362.8	2259.9	1890.2	1994.8	1546.1	1586.6	1949.6
Ti	838.4	767.1	701.9	613.8	998.5	741.4	690.9
Mg	217.0	-	111.6	109.2	510.5	508.0	537.9

Table 3.5.: Representative feldspar analyses from the Tenerife post-collapse succession. In sample names, "-c" stands for core and "-r" for rim. The distance from the crystal core region was calculated from x- and y-stage coordinates that were obtained during EMP analysis.

3. RESULTS

3.1. Feldspar major elements

Feldspar compositions range from bytownite to sanidine. Primitive lavas mainly contain plagioclase with some anorthoclase, transitional lavas are restricted to andesine, oligoclase and anorthoclase, and evolved lavas contain mainly anorthoclase and sanidine with some plagioclase crystals present (oligoclase, andesine and labradorite). Compositions are distributed bimodally with peaks at An_{40} and An_0 (Fig. 3.9), where the peak at An_0 represents the alkali feldspar group, comprising anorthoclase and sanidine. Representative results of feldspar analyses can be found in Table 3.5. The range of major element compositions of feldspar is consistent with the data from Bryan et al. (2002). For the complete EMP dataset, please consult the electronic appendix.

3.2. Trace element analysis of feldspar

Trace elements in feldspar zones show the following ranges of concentration: Sr 6 - 3932 ppm, Rb 0 - 90 ppm, Pb 0 - 10 ppm, Ba 0 - 13179 ppm, Mg 3 - 989 ppm, Ti 233 - 1283 ppm, La 1 - 32 ppm, Ce 1 - 46 ppm, Pr 0 - 4 ppm, Eu 0 - 5 ppm, Nd 0 - 17 ppm, Y 0 - 8 ppm (Fig. 3.4). Gd and Sm analyses were also performed, but varied in their intensities during one single run. Averaging out the intensities over the duration of the analysis could therefore not be applied and, hence, Gd and Sm data were not included in the results of this study.
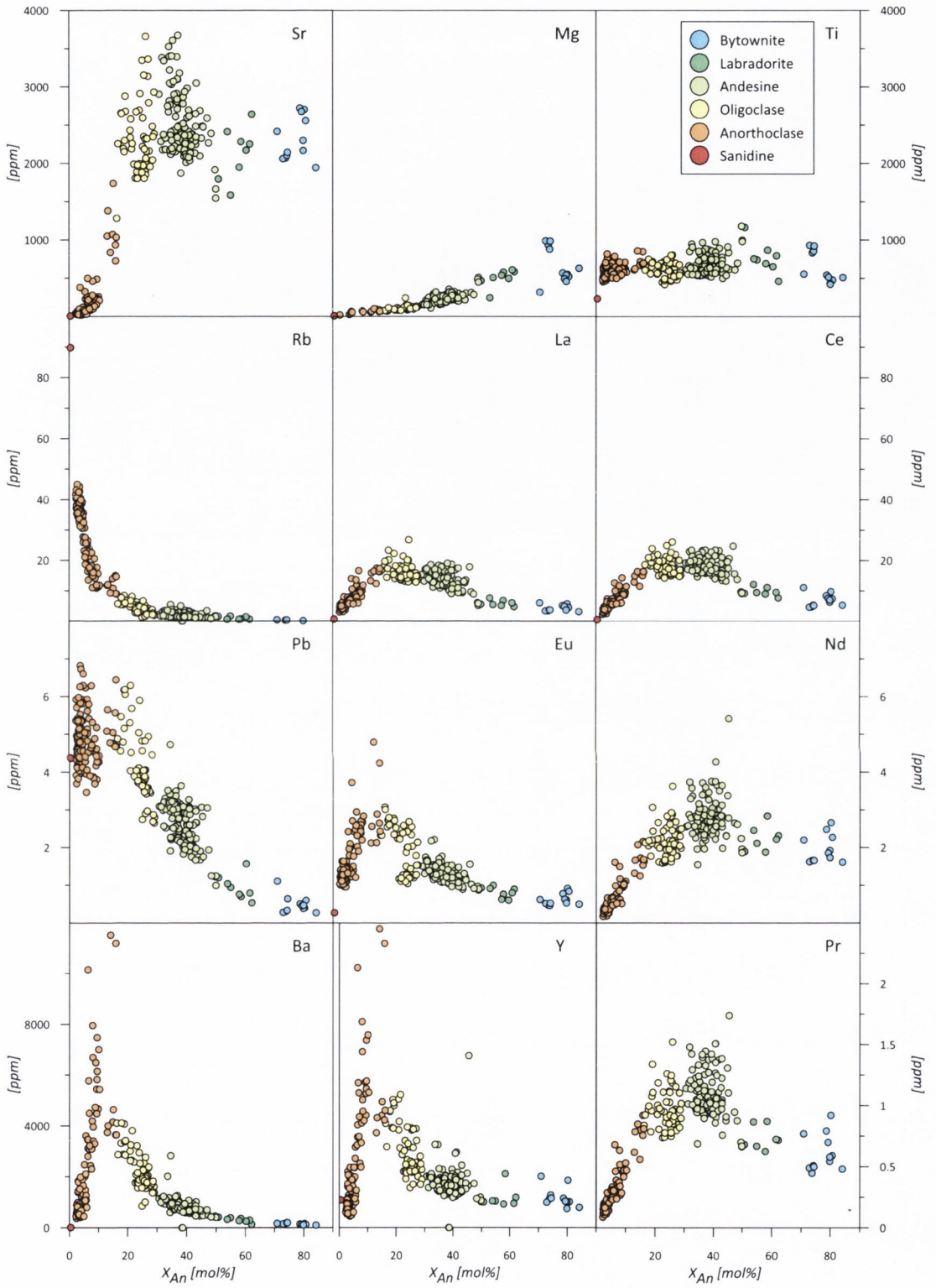
Fig. 3.4: Trace element analyses on individual zones of feldspar crystals compared to respective X_{An} content. Colours indicate feldspar composition (see key).
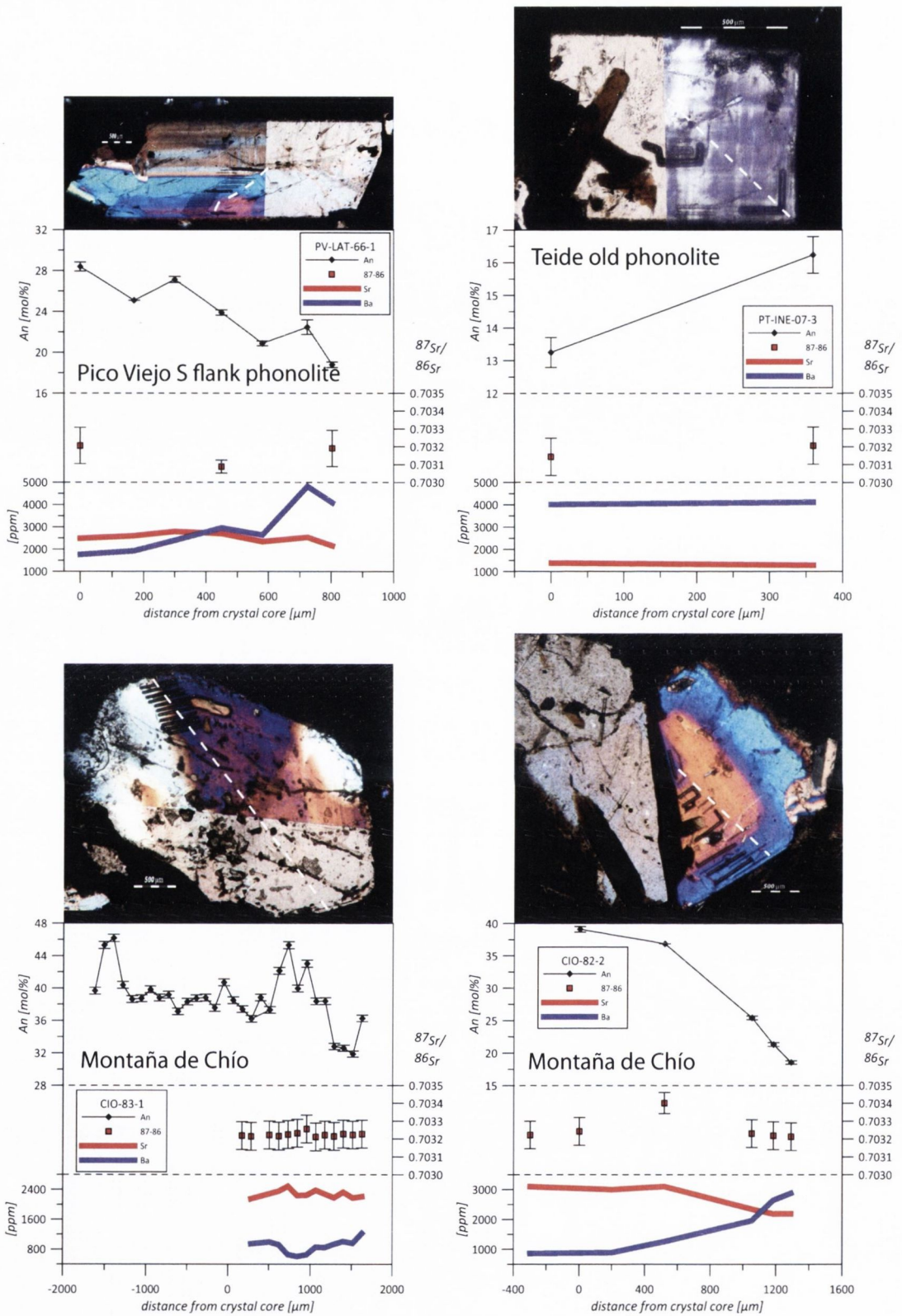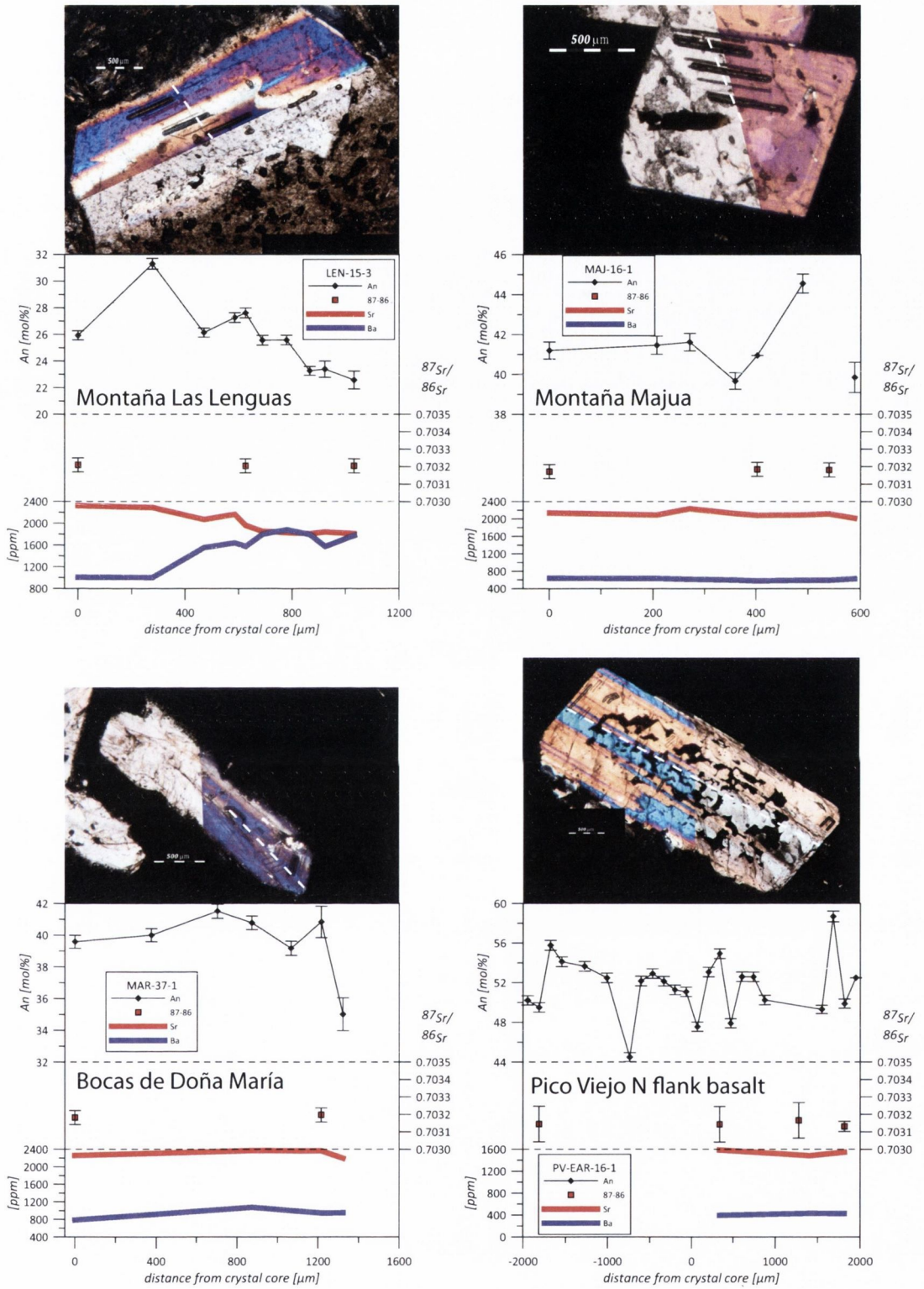
Fig. 3.5: Representative photomicrographs of feldspar microanalyses and corresponding data. White dashed lines indicate the EMP analytical traverses, thin dark lines in crystals are the troughs from LA-ICP-MS trace element analyses, and thick dark lines are troughs from LA-MC-ICP-MS Sr isotope analysis. Note the $^{87}Sr/^{86}Sr$ ratio usually stays within a narrow interval. Montaña de Chío (CIO-83-2) shows one significantly higher ratio of 0.7034 and may have experienced assimilation of a higher radiogenic component. Other crystals from Montaña de Chío (e.g. CIO-83-1) show a similar peak, but within error.

Fig. 3.5 continued: Representative photomicrographs of feldspar microanalyses and corresponding data. White dashed lines indicate the EMP analytical traverses, thin dark lines in crystals are the troughs from LA-ICP-MS trace element analyses, and thick dark lines are troughs from LA-MC-ICP-MS Sr isotope analysis. Note the $^{87}Sr/^{86}Sr$ ratio usually stays within a narrow interval.

3.3. *Strontium isotope composition in feldspar*

Altogether 242 ^{87}Sr/^{86}Sr ratios were obtained on feldspars of bytownite to anorthoclase composition. After external calibration of Sr isotope ratios by microdrill/TIMS data, feldspar zones range in ^{87}Sr/^{86}Sr between 0.703088(41) and 0.703399(59) and cluster mainly around values of 0.7032. Analytical uncertainties that were obtained during LA-MC-ICPMS analysis range between 0.000041 to 0.000151. Hence, the majority of ^{87}Sr/^{86}Sr ratios are similar and no correlation with anorthite content could be detected (Fig. 3.6).
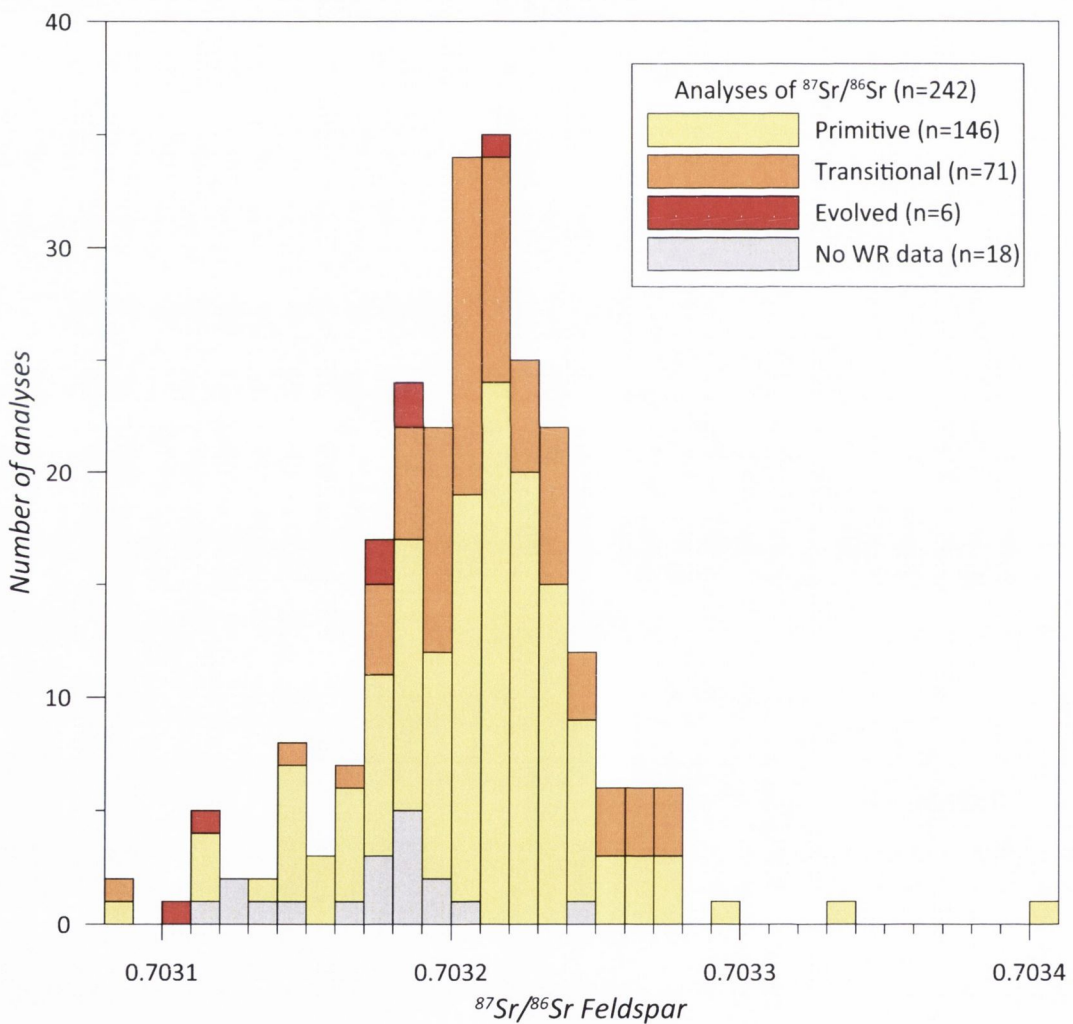

Fig. 3.6: Histogram of measured ^{87}Sr/^{86}Sr ratios in individual zones of Tenerife post-collapse plagioclase and anorthoclase. Data are colour-coded after the composition of the host whole-rock sample.

3.4. Calculation of crystallisation temperature and melt Sr concentration

The modelling of melt composition, using the equations from Blundy & Wood (1991) and Bédard (2006) yielded a temperature interval of 645 (-45, +50) to 1257 (-170, +255) °C (Fig. 3.7).
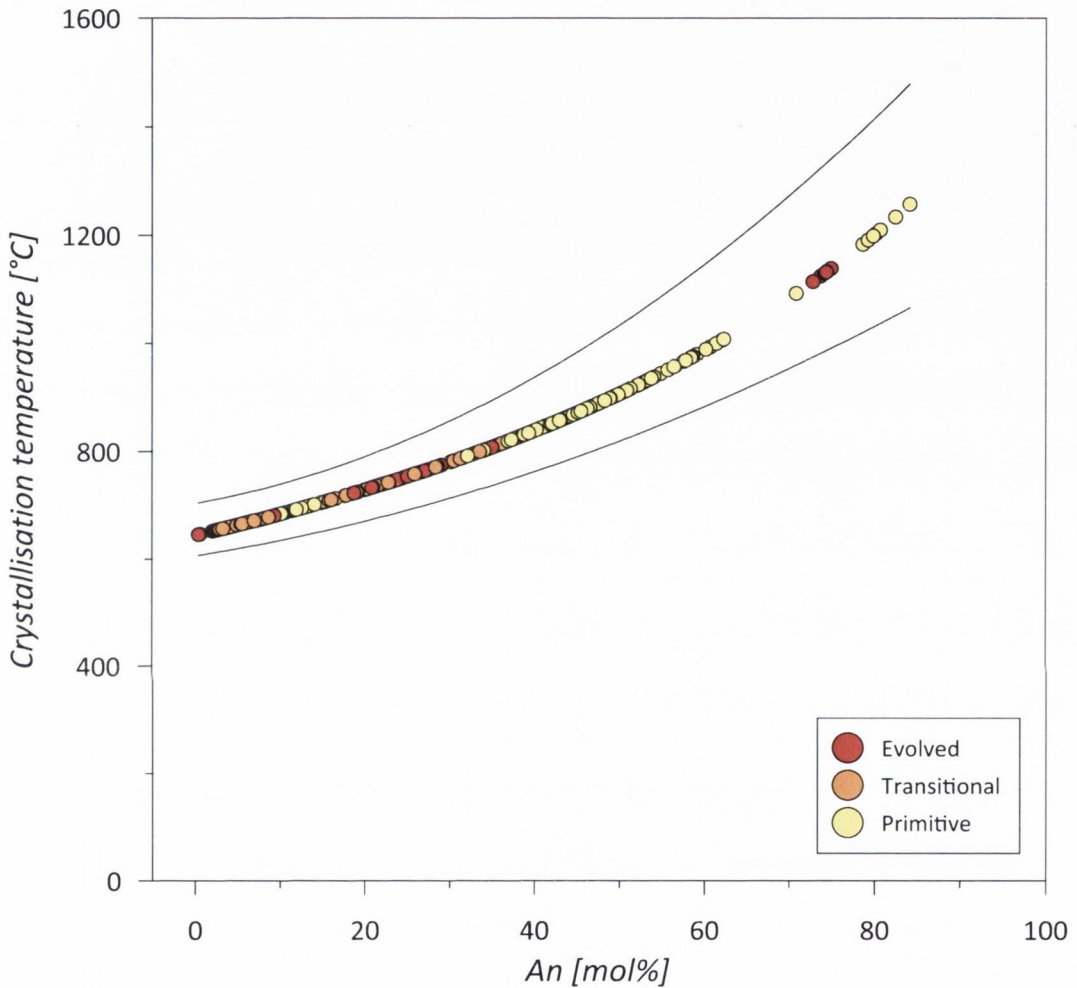

Fig. 3.7: Crystallisation temperature of individual zones of feldspar versus their anorthite content, calculated from equation 3c and 5a in Bédard (2006). Data are colour coded after the composition of the host whole-rock sample. Plagioclases from phonolites show too high a crystallisation temperature to have precipitated from evolved phonolite melts and are likely to be xenocrystic instead.

For the calculation of melt MgO, the equations for both wet and dry melts of Bédard (2006) were tested. The results for dry melt MgO are inconsistent with our natural data (their equation 3b, Table 3.4). However, the equation for wet melts reproduces the natural data very well, particularly between 1 and 6 wt.% of MgO (Fig. 3.8). Below 1 wt.% MgO in natural samples, the calculation slightly underestimates the MgO concentration of the most evolved lavas. This may be an artefact as these values are computed from the anorthite content of anorthoclase crystals.

Feldspar possesses high melt-mineral partition coefficients for Ba and Sr. These elements are incompatible in olivine and considerably less compatible in the other main basaltic phases like amphibole or clinopyroxene. They are thus ideal elements to monitor magmatic processes that occur within the feldspar stability field. Several studies have used high-spatial resolution SIMS analysis of Sr and Ba in plagioclase to either trace back recycling of crystal matter in plutonic suites (e.g. Blundy & Shimizu, 1991), mafic recharge (e.g. Browne et al., 2006) or melt migration of single eruptions (e.g. Berlo et al., 2007). Furthermore, their partition coefficients for plagioclase-melt are dependent on the anorthite content in the plagioclase, so their concentrations in the melt should be able to be modelled via the equations of Blundy & Wood (1991), Bindeman et al. (1998) and Bédard (2006).

Modelled melt Ba concentrations using the above equations exceed natural data ten-fold (up to 22360 ppm of Ba in melt) and were thus not used. In turn, the range of natural Sr concentrations is reproduced convincingly. Hence, modelled Sr data may serve as an estimate for the Sr melt compositions for the natural high-Sr plagioclases (Fig. 3.8).
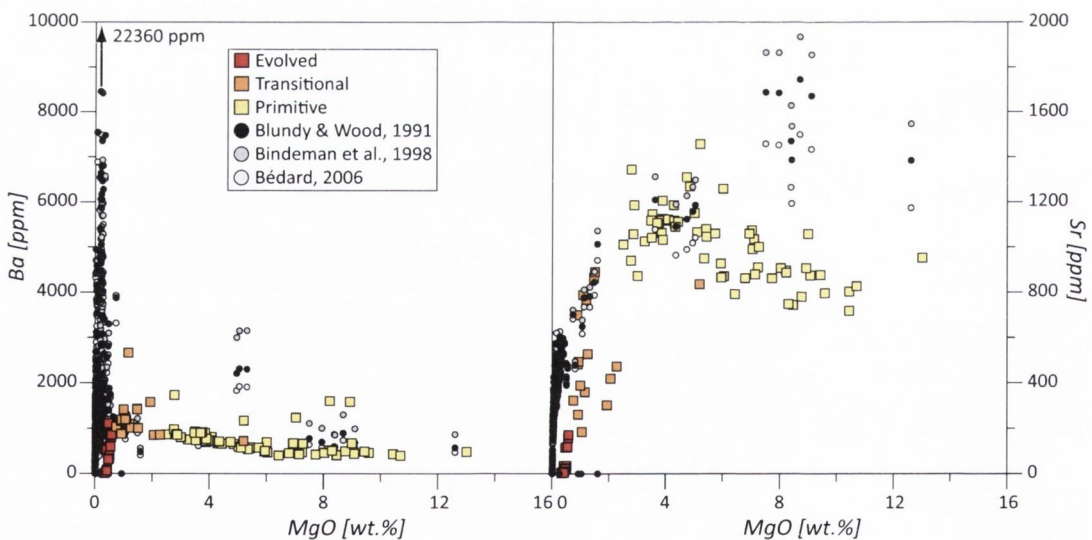

Fig. 3.8: Modelled melt compositions in comparison with existing whole-rock data from Rodríguez-Badiola et al. (2008). The melt MgO concentrations were calculated using the equations of Bédard (2006). In colour, natural data; in shades of grey, modelled data. Modelled Ba data reach a maximum of 22360 ppm and are not used further. Modelling melt Sr compositions with the equation parameters of Blundy & Wood (1991) replicates the natural data best between MgO of 1 and 6 wt.% (black points).

4. DISCUSSION

4.1. Feldspar major elements

The feldspar compositions display two pronounced peaks in their distribution, one at An_0 and another at An_{40} (Fig. 3.9). Assemblages that crystallise two co-existing types of feldspar are usually not present in ocean islands (e.g. Nekvasil et al., 2000; Troll & Schmincke, 2002). In the sample set studied here, the group of An_0 feldspars consists mainly of anorthoclase and sanidine which are found in hybrid or phonolitic lavas within the post-collapse succession. Several studies have constrained the crystallisation depth of phase assemblages of phonolitic or syenitic magma in Tenerife to be at 4km, at sea level or slightly below (Wellman, 1970; Wolff, 1987; Ablay et al., 1998; Andújar et al., 2008).

In contrast, primitive magma is widely found to have pooled at lower crustal or upper mantle levels in the Canaries, i.e. depths of around ≥15 km with higher intermediate levels, but not as shallow as evolved magmas (Hansteen et al., 1998; Klügel et al., 2000, 2005; Galipp et al., 2006; Longpré et al., 2008; Stroncik et al., 2009). Combined with a relatively rapid ascent through the abundant dyke complexes in rifts (Stillman et al., 1975; Carracedo, 1994, 1996), which precludes significant amounts of storage and crystallisation. In the post-Icod-collapse succession, it therefore seems reasonable to attribute plagioclase formation to deeper levels than what can be inferred for alkali feldspar in phonolites, i.e. to lower crustal/upper mantle levels. Hence, this bimodality of feldspar compositions might be a result of these two main levels of crystallisation in the recent Tenerife plumbing system.

Other effects, in turn, may level out this bimodality. Hybrid lavas in many cases represent mixtures of deep-level and shallow-level magma (Chapter 2) that, hence, may precipitate intermediate feldspar, resulting from their intermediate melt composition. Decompression crystallisation of microlites (Hammer et al., 2000) may obscure this bimodality of feldspar compositions, however, this type of crystals was excluded from the analysis in this study and the effects of decompression on crystallisation are therefore expected to be subordinate in the present dataset.
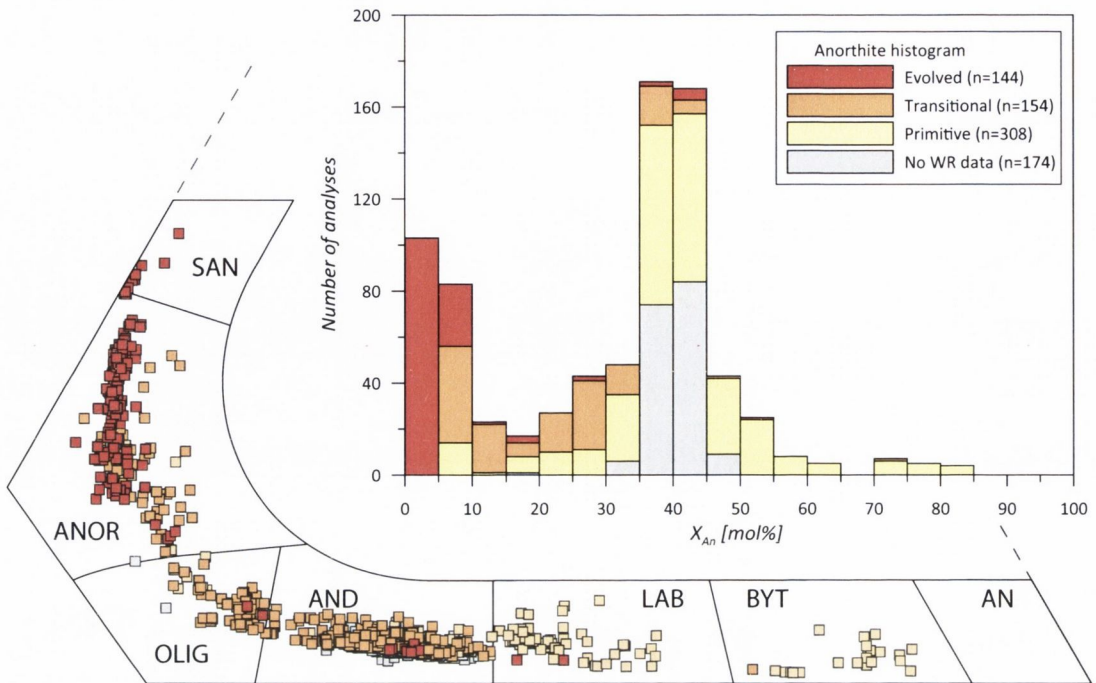
Fig. 3.9: EMP analyses of 780 individual feldspar zones and cores. Grey symbols are samples without corresponding whole-rock analysis. Histogram shows bimodality of feldspar compositions that crystallise in the post-collapse plumbing system.

4.2. Partition coefficients

Trace element partition coefficients have been calculated using the available whole-rock data (Rodríguez-Badiola et al., 2008) and microanalytical data on feldspar rims obtained in this study (Table 3.6). Only data from crystals with equilibrium textures were used.

Partitioning into plagioclase of An_{80} to An_{40} is not altered by varying concentrations of other elements (Bindeman et al., 2000a), confirming the suggestion of Blundy & Wood (1994) that elastic moduli are the controlling factor of trace element partitioning into plagioclase.

Table 3.6: Whole-rock - feldspar partition coefficients

Plagioclase

	Primitive			Transitional			Evolved		
	Min	Max	Average	Min	Max	Average	Min	Max	Average
Mg	0.003	0.051	0.016	0.007	0.033	0.015	-	-	-
Ca	0.00009	0.00029	0.00016	0.00014	0.00041	0.00030	-	-	-
Ti	0.022	0.077	0.047	0.070	0.124	0.094	-	-	-
Rb	0.012	0.155	0.049	0.018	0.098	0.057	-	-	-
Sr	0.000	3.441	2.299	1.989	8.493	4.613	-	-	-
Y	0.005	0.036	0.013	0.014	0.075	0.032	-	-	-
Ba	0.237	6.683	1.470	1.061	4.587	2.811	-	-	-
La	0.055	0.270	0.152	0.141	0.229	0.180	-	-	-
Ce	0.052	0.157	0.103	0.083	0.152	0.112	-	-	-
Pr	0.032	0.090	0.057	0.041	0.098	0.060	-	-	-
Nd	0.022	0.068	0.039	0.027	0.076	0.041	-	-	-
Sm	0.006	0.052	0.021	0.011	0.041	0.021	-	-	-
Eu	0.146	0.856	0.381	0.473	1.285	0.904	-	-	-
Gd	0.010	0.150	0.033	0.033	0.950	0.227	-	-	-
Pb	0.088	0.980	0.395	0.201	0.421	0.324	-	-	-

Alkali feldspar

	Primitive			Transitional			Evolved		
	Min	Max	Average	Min	Max	Average	Min	Max	Average
Mg	0.003	0.003	0.003	-	-	-	0.001	0.017	0.007
Ca	0.00006	0.00006	0.00006	0.00007	0.00014	0.00010	0.00006	0.00014	0.00009
Ti	0.036	0.036	0.036	0.085	0.110	0.098	0.104	0.177	0.132
Rb	0.206	0.206	0.206	0.112	0.172	0.142	0.159	0.291	0.225
Sr	0.914	0.914	0.914	0.000	1.507	0.754	1.915	15.320	6.160
Y	0.017	0.017	0.017	0.036	0.067	0.052	0.003	0.021	0.008
Ba	2.527	2.527	2.527	2.793	6.671	4.732	2.473	45.569	11.532
La	0.178	0.178	0.178	0.084	0.159	0.122	0.026	0.082	0.046
Ce	0.086	0.086	0.086	0.049	0.082	0.065	0.012	0.045	0.024
Pr	0.040	0.040	0.040	0.019	0.044	0.031	0.005	0.021	0.011
Nd	0.020	0.020	0.020	0.014	0.031	0.023	0.003	0.014	0.007
Sm	0.012	0.012	0.012	0.020	0.020	0.020	0.004	0.029	0.012
Eu	0.582	0.582	0.582	0.790	1.137	0.964	0.527	0.892	0.700
Gd	0.021	0.021	0.021	0.091	1.249	0.670	0.010	0.413	0.082
Pb	0.733	0.733	0.733	0.301	0.317	0.309	0.186	0.353	0.264

Table 3.6.: Feldspar partition coefficients, calculated using whole-rock data of Rodríguez-Badiola et al. (2008) and compositions of equilibrium feldspar rims from this study. Upper table for plagioclase, lower for alkali feldspar. Partition coefficients have been grouped after the composition of the whole-rock the feldspars were contained in. No feldspar rims of plagioclase composition are found in evolved lavas, hence, partition coefficients cannot be calculated for this group.

In plots of partition coefficient versus the anorthite composition of the corresponding feldspar rim mostly systematic variations occur. Compatible trace elements are Sr, Ba and partly Eu. Several Sr partition coefficients yielded values of up to 500 and as low as 0.1.

These data were discarded as xenocrysts. The remaining partition coefficients for Sr range between 1 and 10, increasing with decreasing An content. Ba ranges from incompatible in the feldspars with very high An concentration to highly compatible in alkali feldspar. Ultimately, feldspar fractionation may thus be responsible for the observed negative Sr and Ba anomalies in the post-Icod-collapse succession (see section 1.4). Pb and Eu are in the 0.1 to 1 range, nearing compatibility at some intermediate plagioclase compositions, but largely remaining incompatible. Rubidium partition coefficients increase in value with increasing An content, allowing for high Rb/Sr ratios in alkali feldspar. LREE partition coefficients peak at intermediate plagioclase composition, while Nd and Sm prefer more anorthite-rich feldspar compositions. The Gd partition coefficients show a wide spread and a badly defined trend, deviating from well-defined correlations in the other REE measured. Our trace element data have been analysed using the same analytical procedure as Olin & Wolff (2010), who deem their Gd data in pyroxenes unreliable for analytical reasons. The data on Gd partition may thus be unreliable. Yttrium partitioning decreases strongly in alkali feldspar. Partitioning behaviour of Y was traditionally used as a proxy for HREE partitioning (e.g. Thompson et al., 1984), which has been refuted by several newer studies (Olin & Wolff, 2010 and references therein). However, Y is very incompatible in feldspar, and albeit not exactly similar, HREE likely are incompatible, too.
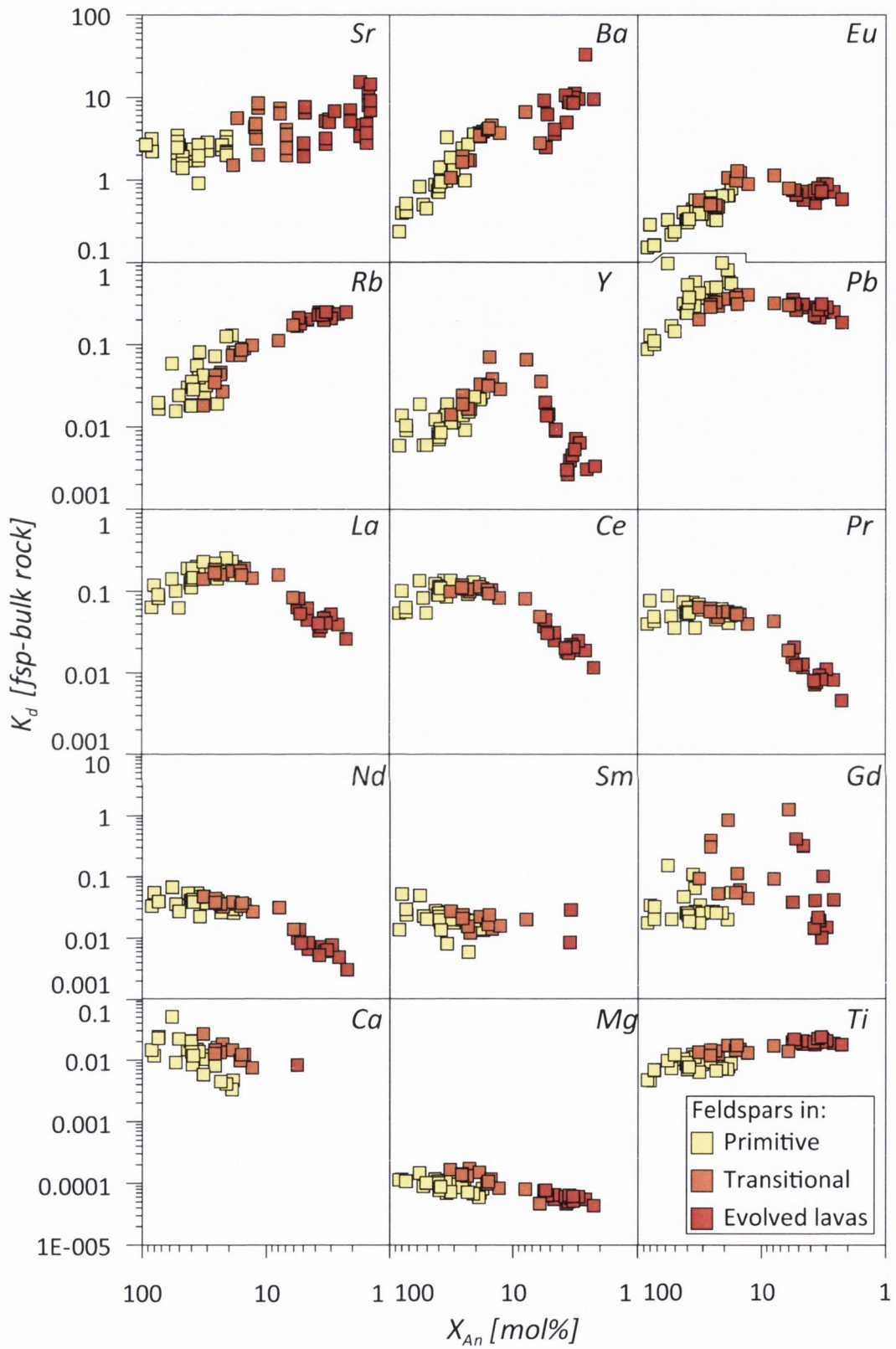
Fig. 3.10: Partition coefficients versus corresponding feldspar anorthite composition. The whole-rock composition has been assumed to be the melt composition (data of Rodríguez-Badiola et al., 2008). Compatible elements are Sr, Ba and Eu.

4.3. Strontium isotope composition in individual zones of feldspar

As noted by Wolff & Palazc (1989), Sr isotope ratios are believed to be rather homogenous in Tenerife. The majority of $^{87}Sr/^{86}Sr$ whole-rock compositions fall into a range between 0.7028 and 0.7032 with only a few examples of evolved deposits being higher at up to 0.7057 (Palacz & Wolff, 1989; Simonsen et al., 2000; Abratis et al., 2002; Gurenko et al., 2006). Earlier studies measured Sr isotopes on bulk feldspar separates or *in situ* in plagioclase, which reflects this narrow range of $^{87}Sr/^{86}Sr$ (Palacz & Wolff, 1989; Chertkoff et al., 2005 a&b). Consistent with these previous studies, the bulk of the $^{87}Sr/^{86}Sr$ analyses of Tenerife post-collapse feldspars in this study fall in a range between 0.70315 and 0.70328 (n=227 of 242, 93.8 %). The presented dataset modifies this interval upwards to 0.7034. Anorthite content and $^{87}Sr/^{86}Sr$ ratio do not correlate in this sample set (Fig. 3.11).

On the other hand, the alkali feldspar that crystallised from the phonolites is very difficult to analyse for its $^{87}Sr/^{86}Sr$ ratio. Equilibrium textures of anorthoclase in high-$^{87}Sr/^{86}Sr$ phonolites indicate that high-$^{87}Sr/^{86}Sr$ anorthoclase may potentially be found in these phonolites. The high Rb/Sr found in these feldspars induces large isobaric interferences in a MC-ICPMS which preclude laser ablation microanalysis. In turn, their low Sr concentrations would require large, whole epoxy-mounted crystals to yield enough Sr for a successful microdrill/TIMS strategy (cf. Knesel & Davidson, 1999). However, with the exception of the feldspars found in the hybrid phonolites (e.g. Roques Blancos, Montaña Reventada), these crystals show pronounced equilibrium textures and a general lack of resorption features. We speculate therefore that a careful bulk separate of alkali feldspar from the highest radiogenic phonolites may yield a higher $^{87}Sr/^{86}Sr$ than previously found in the Tenerife feldspar dataset and, thus, clarify the discrepancies between the whole-rock and microanalytical datasets.
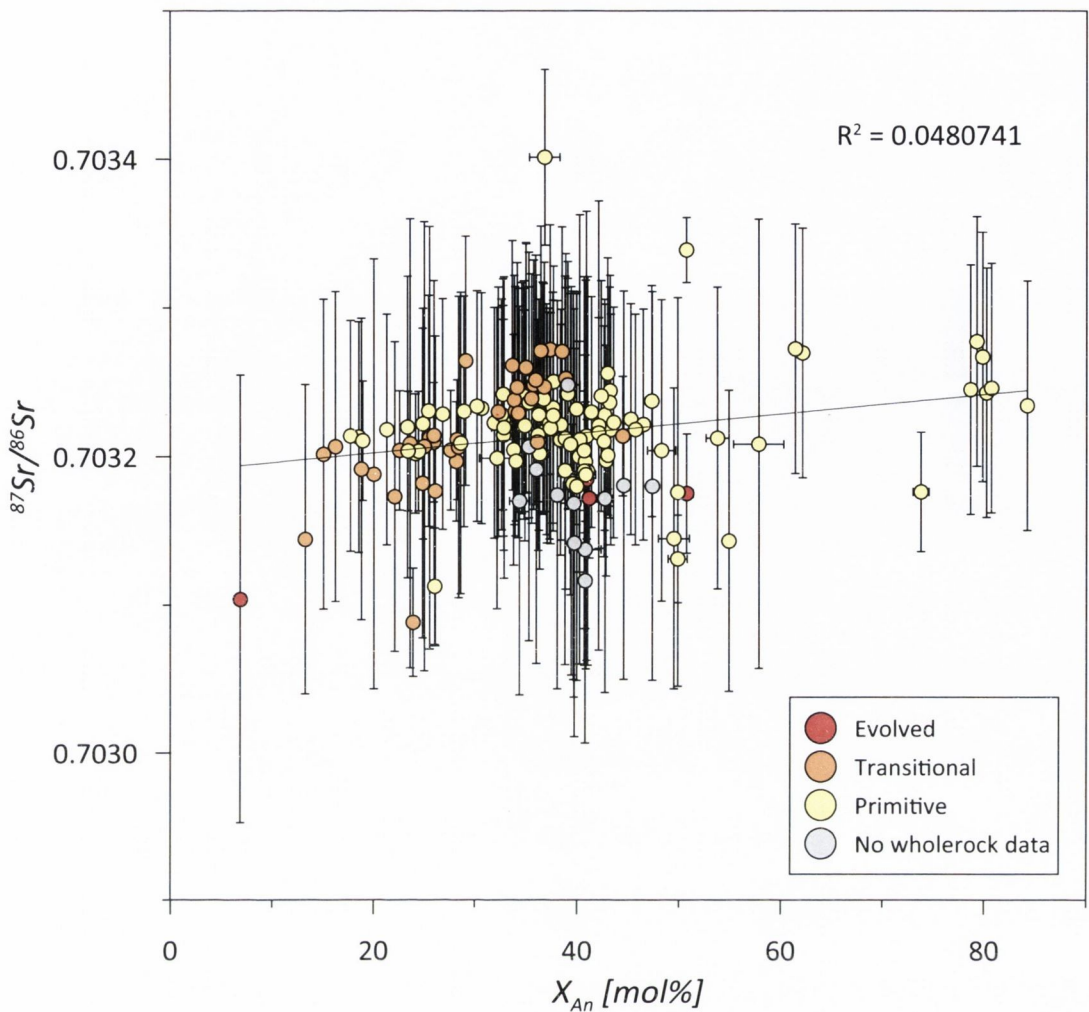
Fig. 3.11: Anorthite content versus its respective $^{87}Sr/^{86}Sr$ composition in individual zones of feldspars from Tenerife post-collapse lavas. Note that the correlation of anorthite content and $^{87}Sr/^{86}Sr$ appears to be absent.

4.4. Calculation of melt parameters and the EC-RAχFC model

Calculated melt compositions allow correlation of melt Sr content with the Sr ratios measured within feldspar. The slight decrease in $^{87}Sr/^{86}Sr$ ratios at low melt Sr concentration may be an artefact of the uncertainties that pertain within the applied equations for the modelled Sr concentrations. The anorthite data from this study plot well into the alkali feldspar fields, which is beyond the calibration limits of the equations. Bindeman et al. (1998) constrained their set of equations to a range of anorthite content between 40 and 80 %. In this range of anorthite compositions, natural data show linear relationships and allow these empirical equations to best approximate D_{Sr}. To yield applicable results, the conclusions were limited to data in the range $0.4 < X_{An} < 0.8$ (Fig. 3.12). All other data are presented in the graphs, but are shaded grey to denote their limited applicability.
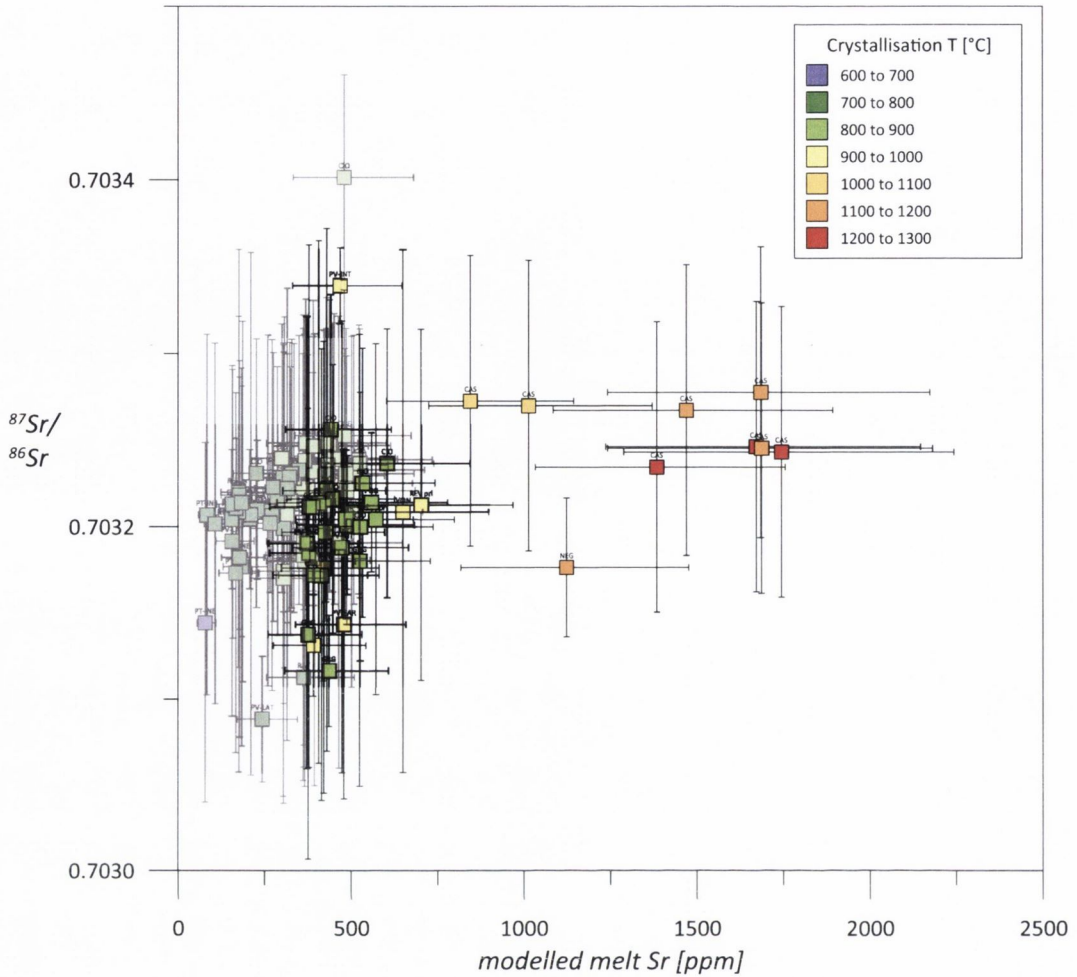
Fig. 3.12: $^{87}Sr/^{86}Sr$ of individual feldspar zones versus their respective Sr concentrations in the melt modelled using the empirical equations of Blundy & Wood (1991) and Bédard (2006). Bindeman et al. (1998) constrained the relationship of anorthite content and D_{Sr} to be linear and most robust for the $0.4 < X_{An} < 0.8$ range. Data outside this range of anorthite content is "greyed out". The downward trend in $^{87}Sr/^{86}Sr$ for these lavas is probably an artefact of this uncertainty.

There are two groups of primitive lavas, one that possesses low Zr and low Sr concentrations (<350 and <1000ppm, respectively) and another that shows higher Zr and higher Sr concentrations (>300 and >1000ppm, respectively, see Fig. 3.14). Unfortunately, both groups are too similar to be distinguished by their incompatible trace element ratios. However, high-Sr/high-Zr lavas appear to be of slightly higher degree of differentiation throughout. We therefore distinguish these two groups by their composition of compatible Sr and incompatible Zr.

Modelled crystallisation temperatures indicate that the low-Sr/low-Zr group may have been hotter when initially crystallising feldspar. The hottest temperatures of up to 1300 °C are yielded by lavas that only contain rare, small plagioclases (Montaña Cascajo

CA3 and CA1, Montaña Negra NEG). Samples with significant amounts of feldspar have crystallised these phenocrysts at temperatures below 1000 °C (Fig. 3.13). As the feldspars in these lavas are much more abundant than in the "hotter" group and possess Sr concentrations between 2000 and 4000 ppm, it seems viable that fractional crystallisation is responsible for the decreased Sr concentration in the "hotter" low-Sr lavas. However, this neither explains their lower Zr concentration (it should be *higher* after a phase was fractionated due to the incompatibility of Zr), nor does it account for the high-Sr lavas that lack plagioclase in their phase assemblage. However, aphyric lavas represent the majority in both the hot and cool primitive lavas. It thus seems more likely that magma from the low-Sr/low-Zr group evolved towards the high-Sr/high-Zr spectrum which started crystallising feldspar after becoming enriched in Sr.
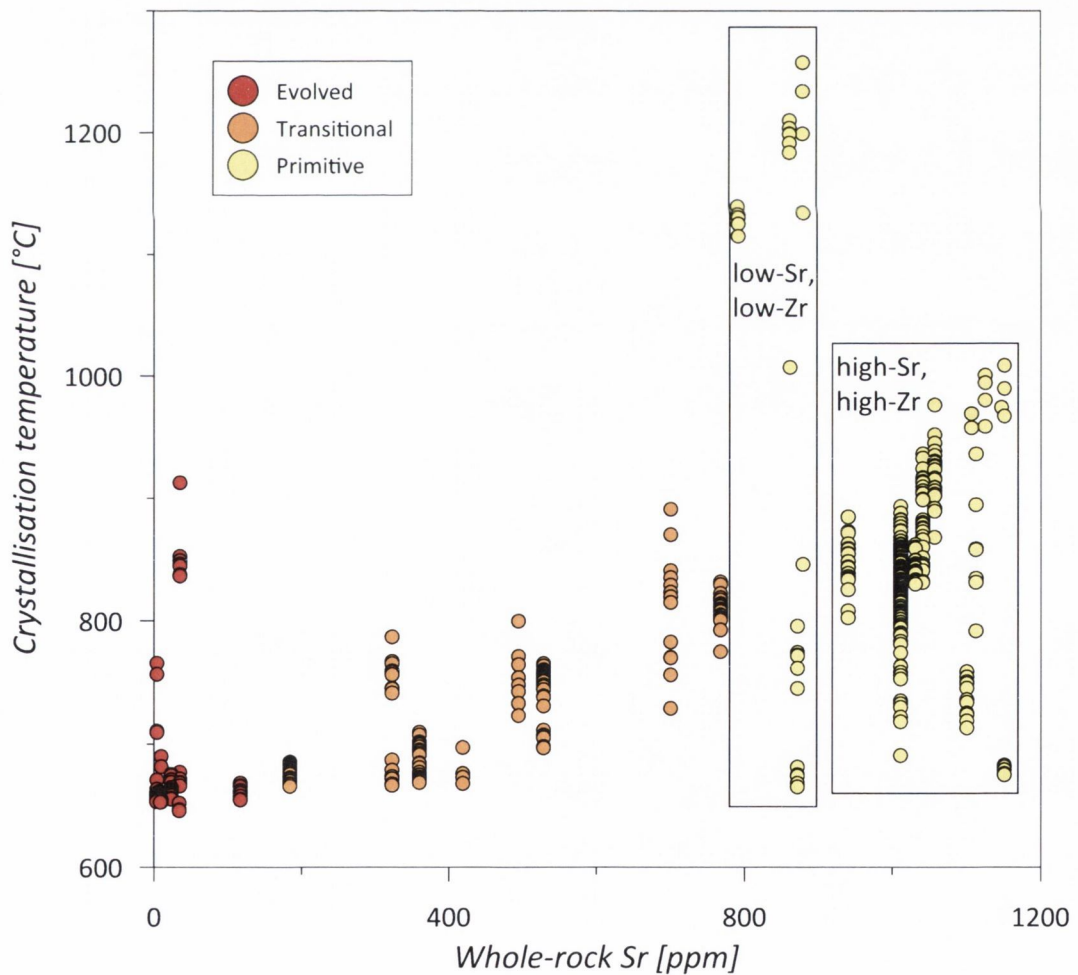

Fig. 3.13: Whole-rock Sr data versus the modelled crystallisation temperature of feldspars in the Tenerife post-collapse lavas. Primitive lavas show a pronounced high at the lower end of the range of Sr concentrations.

There are two possible mechanisms for the evolution of a low-Sr/low-Zr magma to a magma more enriched in these two trace elements. These are closed-system fractional crystallisation and open-system assimilation/fractional crystallisation (AFC). Major element mass balance calculations using cumulate xenoliths with less than 1000 ppm Sr as precipitate show that the latter is technically feasible (Fig. 3.14). However, this does not account for the second group of cumulate xenoliths that possess much higher Sr which indicates that assimilation is an important process for the observed magmatic variability as well (cf. DePaolo, 1981).
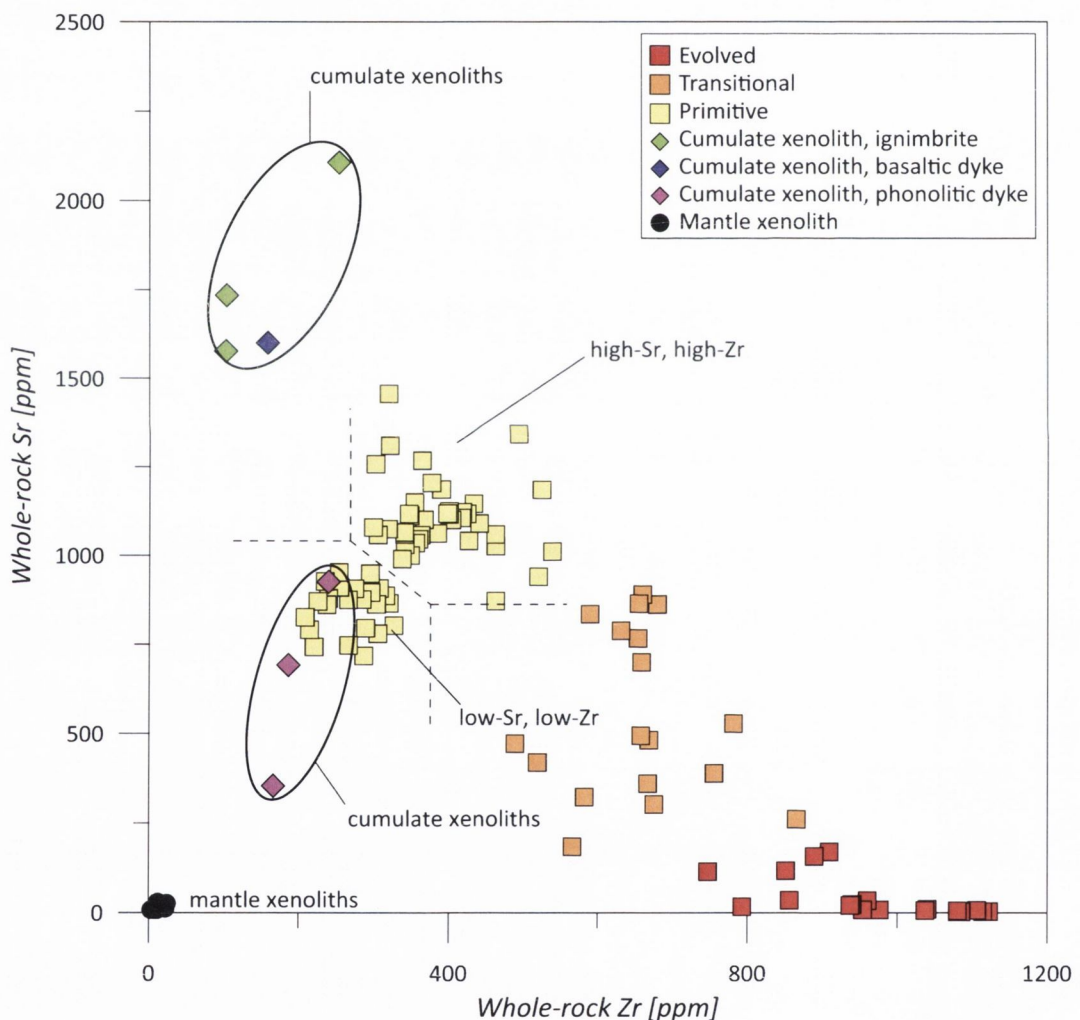

Fig. 3.14: Whole-rock Sr data versus Zr concentrations of the Tenerife post-collapse lavas. Cumulate xenolith data from Neumann et al. (2000), mantle xenolith data from Neumann et al. (2002). Primitive lavas cluster in two groups, one high-Sr/high-Zr, the other low-Sr/low-Zr.

In contrast to pure fractional crystallisation, **E**nergy-**C**onstrained modelling of **R**echarge, **A**ssimilation and **F**ractional **C**rystallisation (EC-RAχFC) incorporates various compositional end-members along with first-order magma chamber phenomena that

account for the bulk of variations expected to occur in natural systems. The theoretical background of EC-RAχFC has been laid out by the studies of Spera & Bohrson (2001, 2002, 2004). Additionally, the modelling of natural systems was presented in Bohrson & Spera (2001, 2003) and Fowler et al. (2004). Results that are consistent with the observed complex compositional variations in nature indicate a high degree of reliability when using parameters that reflect natural conditions. EC-RAχFC thus provides a reliable tool to constrain the processes at work in magma chambers.

The scenario modelled here is of a magma of low-Sr/low-Zr composition that arrives in a upper mantle/lower crustal magma chamber (called 'pristine magma' following the nomenclature of Spera & Bohrson, 2004). There it crystallises and fractionates an amount of cumulate rock, while the magma chamber is being replenished with a new batch of magma of similar low-Sr/low-Zr composition (thereafter refered to as 'recharge magma'). The system is heated up by this new batch of magma and thermal re-equilibration generates anatectic melt from the cumulate, while ongoing fractionation produces fresh cumulate contemporaneously.

Conceptually, the EC-RAχFC model applied here breaks down the continuous process of replenishment, assimilation and fractional crystallisation and expulsion into the smallest possible increment that is feasible to model with the existing code. Because eruption is not incorporated in the code, this model represents the input of magma and subsequent thermal equilibration. If this "primitive cell" was to be repeated over and over again, the thermal history of the magma chamber would resemble a "saw-tooth" profile, heating up from replenishment and cooling down again, something that may or may not be realised in nature. As such, the model remains an approximation, albeit the best possible to constrain magma chamber processes at present, given the plethora of factors it incorporates. Because all end-members are natural data and were left unchanged throughout the modelling process, the thermal parameters were the only way to influence the model and therefore represent results that need to be discussed.

Constraints on the **thermal parameters** for the EC-RAχFC model (see Table 3.7 for definition of parameters):

- Annen & Sparks (2002) constrained the effects of repetitive basaltic intrusion on the thermal conditions of the crustal region where the basalt is emplaced. Eruptions in Tenerife have occurred more or less every hundred years over the past 30 - 200 ka (Carracedo et al., 2007). Hence, continuous basaltic injections at lower crustal levels are a geologically realistic feature. As a result, a much steeper geothermal gradient may be expected and lower crustal material will be kept constantly at near solidus levels. It will thus be remelted rather easily within the extent of the horizontal thermal gradient. As a consequence, we therefore assume relatively narrow temperature intervals in which the EC-RAχFC scenario takes place.

- As the cumulate in our model co-exists with the melt in the magma chamber, the solidus of the cumulate must be higher than the prevailing temperature in the magma chamber, i.e. the melt temperature. However, as the model only accepts one common solidus for all components, the magma temperature needs to be set higher than the solidus, in order to achieve an operational model (in this particular case, other applications usually assume solidi that are significantly lower for all components).

- The initial temperature of the recharge magma will be the highest modelled crystallisation temperature of plagioclase, 1300 °C. These occurred in the low-Sr/low-Zr group of primitive lavas. This temperature also consitutes its liquidus, hence: $T_{l,r} = T_r^o$.

- The initial temperature of the pristine magma will be slightly lower than the recharge magma, to account for earlier heat loss and potential small amounts of fractionation that may have occurred. As fractionation goes on, this initial temperature also constitutes its (slightly lower) liquidus, hence: $T_{l,m} = T_m^o$.

- The assimilant in this model is the gabbroic cumulate that has been fractionated from earlier pristine melt. Its liquidus is the same as the magma, but the initial temperature needs to fall below the solidus.

- The solidus in this case only describes the solidus of the cumulate, as the phase

assemblage needs to be stable at the ambient temperature that is defined by the 'pristine' magma. The melt has a lower solidus than the cumulate, otherwise it would be frozen at the temperatures where the cumulate is stable.

- To model a case in which the amount of liquid melt stays high during the process, lower cumulate temperatures are required. In reality, pristine magma, recharge magma and cumulate should be thermally very close, but because the code does not allow independent solidi to be defined, they need to be artificially separated in order to keep the magma liquid.

- Long-term continuous replenishment should balance with intermittent expulsion of magma. Hence, the thermal parameters were fine-tuned to even out the mass of anatectic melt and cumulate that are produced (in order not to clog the magma chamber or reduce the amount of cumulate to zero). The relative mass of recharge M_r^0 is kept at 0.5 to account for the probable subordinate volume of a batch of replenishing magma in comparison to the total volume of the magma chamber. Expulsed material can be defined as equal to the relative mass of recharge, again to balance out volumetric constraints, but plays no role in the code.

- Specific heat capacities and crystallisation/fusion enthalpies were calculated from the oxide and mineral values given by Spera & Bohrson (2001) using the average compositions of the high-Sr/high-Zr, low-Sr/low-Zr group and Tenerife cumulate xenoliths (Neumann et al., 2000).

- The normalised fraction of anatectic melt from the assimilant that enters the magma body (χ) was assumed to be 0.95. In mantle and cumulate xenoliths, interstitial melt is commonly found, i.e. melt extraction is not 100%.

Table 3.7: Parameters for EC-RAχFC modelling

Thermal parameters

Pristine magma liquidus temperature, $T_{l,m}$	1290 °C	Crystallization enthalpy, Δh_m (J/kg)	398300
Pristine magma initial temperature, T_m°	1290 °C	Isobaric specific heat of magma, $C_{p,m}$ (J/kg K)	1479
Recharge magma liquidus temperature, $T_{l,m}$	1300 °C	Crystallization enthalpy, Δh_r (J/kg)	398300
Recharge magma initial temperature, T_m°	1300 °C	Isobaric specific heat of magma, $C_{p,m}$ (J/kg K)	1479
Assimilant liquidus temperature, $T_{l,a}$	1300 °C	Fusion enthalpy, Δh_a (J/kg)	364000
Assimilant initial temperature, T_a°	1210 °C	Isobaric specific heat of assimilant, $C_{p,a}$ (J/kg K)	1307
Solidus temperature, T_s	1250 °C		
Equilibration temperature, T_{eq}	1277 °C		
Recharge M_r°	0.5		

Compositional parameters

	Sr	Nd	Zr	Ni
Pristine magma initial concentration (ppm), C_m°	858	67	288	150
Pristine magma isotope ratio, ε_m	0.703108	0.512927		
Pristine magma trace element distribution coefficient, D_m	0.86	0.5	0.5	1.1
Recharge magma initial concentration (ppm), C°	858	67	288	147
Recharge magma isotope ratio, ε_r	0.703120	0.512927		
Recharge magma trace element distribution coefficient, D_r	0.86	0.5	0.5	1.1
Assimilant initial concentration (ppm), C°	1754	87	154	150
Assimilant isotope ratio, ε_a	0.703009	0.512885		
Assimilant trace element distribution coefficient, D_a	0.86	0.5	0.5	1.1

Table 3.7.: Melt functions were non-linear and non-linear logistical parameters were a=450, b=-11 for pristine and recharge magma, and a=400, b=-11 for the assimilant.

Compositional parameters:

• An approximation for the pristine and recharge magma in this model are the lavas from the low-Sr/low-Zr group. Gabbroic and hornblendite xenoliths from Tenerife served as the cumulate rock assimilant (Neumann et al., 2000). According to the authors, the cumulates have formed from fractional crystallisation of mafic alkaline magmas. The leucogabbros of Neumann et al. (2000) are described as medium to coarse grained, with interlocking grain boundaries and and consist of aug + plag + ox ± hbl ± afp ± ol ± ap ± bt ± sphene ± haüyne.

• Partition coefficients for melt-mineral distribution of Sr and Zr were obtained online from the GERM database (http://earthref.org). From phenocryst-matrix determinations, Zr shows D values of 0.13 - 0.27 for plagioclase (Villemant et al., 1981), 0.1088 - 0.27 for clinopyroxene (Villemant et al., 1981; Fujimaki et al., 1984; Zack & Brumm, 1998) and 0.29 for ilmenite (ilmenite is used as a proxy for oxides, Zack & Brumm, 1998) in the typical mineralogy of Tenerife gabbroic cumulates (Neumann et al., 2000). Zirconium is compatible in amphibole (D = 1.2) and biotite (2.5) in an alkali basalt environment. In comparison with Zr, Sr is slightly less incompatible in clinopyroxene (0.16 - 0.785) and very compatible in

plagioclase (2.7 - 10) (Shimizu, 1980; Wood & Trigila, 2001; Matsui et al., 1977; Villemant et al., 1981). In turn, Sr is less compatible or incompatible in amphibole (0.3 - 1.02) and biotite (0.7) (Matsui et al., 1977; Villemant et al., 1981). From the photomicrograph shown in Neumann et al. (2000), we assumed mineral percentages of 30% plagioclase, 30% hornblende, 20% clinopyroxene and 15% oxides plus 5% minor phases as a typical example of a Tenerife gabbroic cumulate. Mass balance calculations replicated the average of cumulate analyses from Neumann et al. (2000) within 2 wt.% for each oxide. These percentages yielded ranges of average D values of between 0.50 - 0.57 for Zr and 0.86 - 3.19 for Sr when both pristine and recharge melt crystallise. This leads to an enrichment of Sr in cumulate rocks whereas Zr with its bulk partition coefficient of less than 1 will be enriched in the residual melt. We further used a D_{Nd} of 0.8 to account for the presence of apatite as as REE-incorporating mineral and a relatively low D_{Ni} of 3 for lack of olivine in the cumulate gabbro.

Using the parameters summarised in Table 3.7 yielded the following results. Mass of anatectic melt generated M_a^*: 0.39, mass of produced cumulate M_c: 0.338, mass of produced enclaves M_{en}: 0.127. This equals a total mass of produced solids of 0.465 versus a mass of anatectic melt of 0.39.

Trace elements reproduced the range of the high-Sr/high-Zr lava: Sr increased to 1148 ppm, Zr increased to 314 ppm, Nd increased to 92 ppm and Ni decreased to 75 ppm (Fig. 3.15).
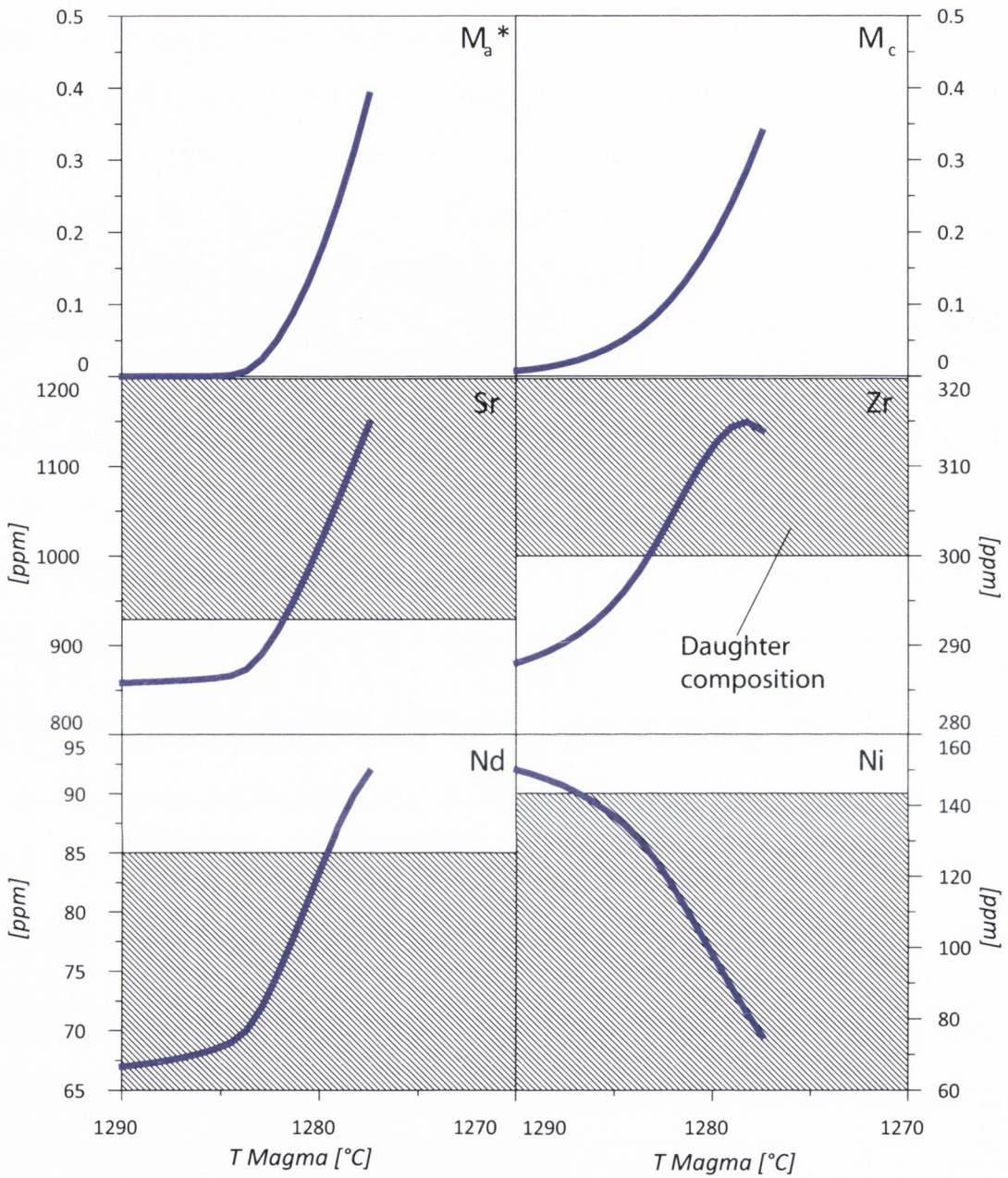
Fig. 3.15: The evolution of melt compositions from EC-RAχFC modelling. X-axis is magma temperature, the system thermally equilibrates itself from higher to lower temperatures (left to right). All parameters comply with the composition of the high-Sr/high-Zr primitive lavas.

Modelling was very sensitive to changes in the equilibration temperature, because the solidus and liquidus were closely spaced together (50 °C). Relatively small changes in equilibration temperature (~10 °C) therefore covered large distances in phase diagram space and allowed for a restricted combination of liquidus and initial temperatures.

The model was tested by including Ni, a compatible element that tends to be fractionated

largely into olivine and clinopyroxene in the most mafic melts. It was impossible to model Ni successfully when using lower than average concentrations of the low-Sr/low-Zr lavas for the 'pristine' melt. In turn, Sr and Zr were much more robust when adjusting starting concentrations in the model. This may be due to the natural variations within the samples. The cumulate Ni concentrations range between 6 and 265 ppm; a similar range is observed in the lavas, while Sr and Zr each are more constant. Compatible elements are mainly controlled by fractionation - once they enter a mineral they are difficult to extract unless high degrees of melting are at work. This implies that fractionation of minerals that incorporate Ni, like olivine, amphibole or clinopyroxene, may occur in widely differing amounts, while Sr and Zr are not affected by this variability.

The isotopic ratios of both Sr and Nd are too narrowly spaced to provide further conclusions, except that the whole range of observed ratios may be reproduced in the resulting magma. This is consistent with the observation that Tenerife Sr ratios rarely leave this narrow interval. The study in Chapter 4, in turn, implies that elevated Sr ratios originate instead from partial melting of country rock which may have been enriched in radiogenic Sr selectively in high Rb/Sr phases. Over time, these Tenerife rocks may exceed this "baseline" $^{87}Sr/^{86}Sr$ by enhanced radiogenic ingrowth. However, these elevated Sr ratios are never found in primitive lavas, implying that high Rb/Sr phases do not originate at deep levels. Constant magmatic reworking of the lower crustal material (including auto-genetic cumulate) precludes ingrowth of radiogenic Sr in high Rb/Sr phases for an extended period of time. Hence, magma batches cannot evolve towards high $^{87}Sr/^{86}Sr$ ratios at depth. At shallower levels, in turn, rocks may be left "untouched" for longer intervals, and therefore develop high $^{87}Sr/^{86}Sr$ ratios in high Rb/Sr phases.

This implies that Sr ratios of primitive lavas may be broadly consistent with real mantle values (at least in Tenerife). However, the constantly on-going auto-recycling at depth is likely responsible for the observed, small variations in $^{87}Sr/^{86}Sr$ ratios. A single isotopic ratio would therefore only approximate the mantle ratio with large uncertainties and the whole range of isotope ratios in one regional setting may instead constitute the diffuse signal of a specific mantle source, instead of recording a variable source composition.

Overall, the EC-RAχFC code allows modelling of the trace element concentrations of the high-Sr/high-Zr group of primitive lavas by closely following pre-existing compositional and thermal constraints. This shows that the combined mechanisms of assimilation and fractional crystallisation are most likely responsible for the two observed groups of primitive lavas. Low-Sr/low-Zr lavas, in turn, seem to have experienced rather little modifications within magma chambers. They either remain unaffected by RAFC processes (either short stays in magma chambers or by passing the magma chamber completely), or they represent an earlier stage of differentiation.

The results indicate the importance of auto-recycling throughout the Tenerife magmatic plumbing system. In his ground-breaking publication, O'Hara (1998) numerically modelled an ocean island plumbing system from its "birth" to eventual subaerial emplacement of lavas and found that the consumption of wall-rock is an essential mechanism for the inital emplacement of a plumbing system. Morevoer, auto-assimilation of previously or simultaneously fractionated mineral phases could account for increased amounts of incompatible trace elements in primitive lavas. In line with the "space problem" invoked by O'Hara (1998), the EC-RAχFC model required relatively equal amounts of the mass of crystallised solids and the mass of anatectic melt (i.e. the magma chamber keeps a balance between input and output). Only this approach achieved a resulting melt that approximated the natural high-Sr/high-Zr lavas. Our results therefore corroborate the theoretical study of O'Hara (1998) with the example of a natural plumbing system that has been modelled using multiple thermodynamical and chemical constraints.

It is probably appropriate to note that Hawaii, in comparison, constitutes an extreme case where a high buoyancy flux (Sleep, 1990) would literally dilute a comparable AFC signal, while fast plate displacement (Clague & Dalrymple, 1987) may account for a rapidly changing and therefore less "uniform" tectonic environment. Putirka et al. (1997), for example, constrained part of the Hawaiian plumbing system to range from shallow depths and extending to mantle regions.

5. CONCLUSIONS

- Using the obtained microanalytical data to model pre-eruptive melt compositions by employing the empirical equations from Blundy & Wood (1991), Bindeman et al. (1998) and Bédard (2006) allowed to constrain the thermal history of the Tenerife primitive lavas and define two groups of lavas that are compositionally distinct.

- Subsequent EC-RAχFC modelling (Spera & Bohrson, 2004 and references therein), applied these constraints obtained from the melt modelling. This allowed the geochemical and model data to be placed into an energy-constrained framework and showed that the two types of primitive magma that are erupted follow distinct paths of differentiation. One (the high-Sr/high-Zr type) experiences an extended period of residence within one or multiple magma chambers, the other (the low-Sr/low-Zr type) passes by this stage or experiences magma chamber residence at only short intervals.

- Strontium trace element patterns in feldspars and their host whole-rocks indicate that multiple feldspar populations may occur within one lava flow. Mixing of two compositionally distinct types of magma may therefore be common. This is consistent with some calculated crystallisation temperatures that indicate that plagioclase crystallises at temperatures too high to have been formed within some of the more evolved felsic melts. The amount of xenocrystic material in the erupted lavas may therefore be even greater than that indicated by phenocryst textures, which largely indicate equilibrium crystallisation.

- The Sr isotopic composition of Tenerife plagioclase lies within the interval of 0.7031 to 0.7034. Elevated Sr ratios cannot be excluded, but may be restricted to alkali feldspars in phonolites of high $^{87}Sr/^{86}Sr$ ratios (cf. Chapter 4).

BIMODALITY OF LAVAS IN THE POST-ICOD-COLLAPSE SUCCESSION IN TENERIFE - A CRUSTAL MELTING ORIGIN FOR THE TEIDE-PICO VIEJO PHONOLITES?

1. INTRODUCTION

The origin of abundant felsic volcanism in oceanic islands has long been a matter of debate. In a setting devoid of large regional tectonic influences and, for most ocean islands, large sedimentary sequences, it has long been proposed that crystal fractionation must be the dominant driver of differentiation to form magmatic bimodality (e.g. Chayes, 1963; Cann, 1968; Schmincke, 1969; Clague, 1978; Garcia et al., 1986; Ablay et al., 1998; Thompson et al., 2001).

Early investigations on the compositional bimodality of volcanic matter (called the "Bunsen-Daly Gap", from Bunsen (1851) and Daly (1925) and later expanded by Barth et al., 1939) were largely concerned with the discussion whether or not the Bunsen-Daly gap actually exists (e.g. Chayes, 1963, Baker, 1968; Cann, 1968). This manifested itself in an argument on potential sample bias (e.g. Baker, 1968; Cann, 1968) and suggestions for more detailed geological work (Harris, 1963).

Schmincke (1969) confirmed the presence of a Bunsen-Daly gap on Gran Canaria, while Ridley (1970) supported the view of a bimodality of erupted compositions in Tenerife. Fúster (1975), although conversely claiming that this feature is not too well developed on either Gran Canaria or Tenerife, suggested it had occurred on Fuerteventura, La Gomera, El Hierro and Lanzarote.

Those who acknowledged the existence of the Daly gap, mainly held fractional crystallisation responsible (e.g. Chayes, 1963; Cann, 1968; Clague, 1978; Garcia et al, 1986; Thompson et al., 2001), but also potential influences of partial melting were

mentioned (Chayes, 1977). Models for bimodality started to diversify considerably, with models of large crystal loads that restrain convection and induce a bimodality in erupted compositions (Marsh, 1981; Brophy, 1991). Bailey (1987) suggested an upper mantle or lower lithospheric origin of trachytic melts, while Bonnefoi et al. (1995) invoked a model of critical cooling dynamics to be responsible for observed compositional relationships. More recently, the idea of assimilation of country rock affecting magma composition in oceanic islands gained importance (e.g. Eiler et al., 1996; Thirlwall et al., 1997; Bohrson & Reid, 1998; Garcia et al., 1998; O'Hara, 1998; Harris et al., 2000; Troll & Schmincke, 2002).

In Tenerife, too, fractional crystallisation was long considered the main differentiation process for highly evolved lavas (Wolff, 1983; Wolff & Storey, 1984; Ablay et al., 1998) and it was not until Wolff et al. (2000) invoked recycling (i.e. partial or bulk melting) of island core to help produce the Diego Hernández Formation in Tenerife. We expand on this topic by investigating the most recent volcanic rocks from Tenerife (<200ka), for which we compiled a detailed isotopic dataset combined with existing major and trace element compositional data. To avoid overrepresentation of individual units, one sample per lava flow was analysed only. We demonstrate that the compositional bimodality in Tenerife does exist and that it probably originates from the combined effects of assimilation and fractional crystallisation. Considerable volumes of melted country rock may be involved in the generation of the most extreme compositions of the highly differentiated magmas.

2. METHODOLOGY

2.1. *Isotopic analyses of groundmass samples*

We analysed groundmass separates of 61 samples for their Pb, Sr and Nd isotopic composition. Apart from several duplicate analyses, only one sample per lava flow was analysed to avoid overrepresentation of any particular unit (Table 4.1). Only three of the eight Montaña Blanca phases were included.

We chose to perform groundmass analyses (instead of whole-rock) as a direct consequence of the microanalytical results on feldspar phenocrysts, presented in Chapter 3. Abundant glomerocrysts and disequilibrium-phenocrysts in the post-Icod-collapse lavas made this approach the most feasible. Indeed, more vigorous eruptive fluxes have been found to account for higher amounts of remobilised crystal cumulates (i.e. material that is not strictly native to a given batch of melt), which potentially alters the bulk composition (e.g. Murata & Richter, 1966; Marsh, 2004; Kinman et al., 2009). Fresh groundmass, in contrast, represents the very last melt composition and is, when properly separated, completely unaffected by any masking effects due to pheno-/xenocrysts. It thus allows melt processes to be constrained reliably.

Forty primitive lavas plus four duplicates were analysed. These comprise foidites, basanites, tephrites and phonotephrites. Ten transitional samples plus two duplicates were analysed. These are tephriphonolites, trachyandesites, trachytes and phonolites. Eleven evolved lavas plus one duplicate were analysed, comprising trachytes and phonolites with a high silica content (~ 60 wt.%). Moreover, five sedimentary rocks of the exhumed pre-island seafloor from Fuerteventura were analysed to serve as potential end-members for the isotopic composition of non-magmatic rocks that may be trapped underneath or within the islands (Fúster et al., 1968; Stillman et al., 1975; Hobson et al., 1998; Hansteen & Troll, 2003). A total of 69 $^{206}Pb/^{204}Pb$, $^{207}Pb/^{204}Pb$ and $^{208}Pb/^{204}Pb$, 53 $^{87}Sr/^{86}Sr$ and 30 $^{143}Nd/^{144}Nd$ analyses of groundmass are presented. Results for all three sets of radiogenic isotope systems are reported with 2SD errors (Table 4.1).

All groundmass isotopic analyses, including the necessary clean laboratory procedures, were carried out at the Isotope Geosciences Unit of the Scottish Universities Environmental Research Centre (SUERC), East Kilbride, Scotland. Samples for Pb, Sr and Nd were handled in a cleanbox (located within a cleanlab) and were digested using the following sequence of acids: 1. ultrapure 16M HNO_3 + HF, 2. ultrapure 16M HNO_3 and 3. ultrapure 6M HCl. Throughout the procedure, each sample stayed in the same 15ml Savillex Teflon beaker and was kept on a hotplate to dissolve the sample and to dry off the acid.

2.1.1. *Pb–Pb analysis*

The procedure for Pb analysis follows that of Ellam (2006). After digestion, the sample was put through columns made from ultraclean pipette tips and Eichrom Sr-Spec resin to separate Pb from other ions. Of nine columns per separation, eight were samples, while the remaining column served as a separation blank. Undesired fractions were eluted with 2M HCl. Lead was then eluted with 6M HCl. After drying off the HCl, the sample was conditioned with concentrated HNO_3 and finally diluted to 50 ppb in a mixture of 5% HNO_3 + 5 ppb Tl. The total procedure Pb blank was below 1 ng.

Samples were analysed on a MC-ICP-MS with Tl-doping to account for Pb mass bias (Belshaw et al., 1998; Rehkämper & Haliday, 1998; White et al., 2000). A Micromass IsoProbe MC-ICP-MS using a 50µl/min PFA nebuliser fitted to an Elemental Scientific© Apex nebuliser with an ACM desolvation unit was utilised for measurements of Pb isotopes. Beam intensities of ^{208}Pb ranged around 1V (1×10^{-11} A), and analyses were conducted in 5 blocks of 20 ratios with 5 s integrations in static multi-collection mode.

Mass bias was accounted for with doped Tl. An exponential law with a $^{205}Tl/^{203}Tl$ ratio of 2.3871 was chosen. Baselines were measured on-peak for 45 s in 5% HNO_3. During the course of a several hour analytical session, Pb memory build-up was accounted for by introducing a solution of 5% HNO_3/2% HF into the ICP-MS for 2 minutes between sample runs. Uncorrected NIST SRM981 standard runs gave $^{206}Pb/^{204}Pb$ = 16.941 ± 24, $^{207}Pb/^{204}Pb$ = 15.501 ± 22 and $^{208}Pb/^{204}Pb$ = 36.721 ± 58 (all 2 SD, N=15).

2.1.2. *Sr and Nd isotope measurements*

Samples were weighed and placed into PFA teflon screw-top beakers (Savillex®) and were then dissolved using ultra-pure reagents in a $HF-HNO_3-HCl$ acid digestion. Sr was separated in 2.5 N HCl using Bio-Rad AG50W X8 200-400 mesh cation exchange resin. A rare earth element (REE) concentrate was collected by elution of 3N HNO_3. Neodymium was separated in a "cocktail" of acetic acid (CH_3COOH), methanol (CH_3OH) and nitric acid (HNO_3) using Bio-Rad AG1x8 200-400 mesh anion exchange resin. Total procedure blanks for Sr and Nd were less than 0.5 ng.

Samples for Sr isotope analysis were loaded onto single Ta filaments with 1N phosphoric

acid and Nd samples were loaded directly onto triple Ta-Re-Ta filaments. Sr samples were analysed on a VG Sector 54-30 multiple collector mass spectrometer. A ^{88}Sr intensity of 1V (1 x 10^{-11}A) ± 10% was maintained. The ^{87}Sr/^{86}Sr ratio was corrected for mass fractionation using ^{86}Sr/^{88}Sr = 0.1194 and an exponential law. The mass spectrometer was operated in the peak-jumping mode with data collected as 15 blocks of 10 ratios. The NBS987 standard yielded a ^{87}Sr/^{86}Sr value of 0.710252 ± 26 (2 SD, n =49).

Samples for Nd isotope analysis samples were analysed on the VG Sector 54-30 instrument. ^{143}Nd/^{144}Nd ratios were measured with a ^{144}Nd beam of 1V (1 x 10^{-11}A). 12 blocks of 10 ratios were collected in peak jumping mode and corrected for mass fractionation using an exponential law and ^{146}Nd/^{144}Nd = 0.7219. Repeat analyses of the internal laboratory standard (JM) yielded a ^{143}Nd/^{144}Nd ratio of 0.511517 ± 21 (2 SD, n = 25).

Table 4.1: Radiogenic isotope ratios in groundmasses and whole-rock trace elements of Teide-Pico Viejo complex and rift zone eruptions

Sample	$^{206}Pb/^{204}Pb$	$^{207}Pb/^{204}Pb$	$^{208}Pb/^{204}Pb$	$^{87}Sr/^{86}Sr$	$^{143}Nd/^{144}Nd$	Pb [ppm]*	Sr [ppm]*	Nd [ppm]*	Comment
ABQ-47	19.5050 (22)	15.5919 (22)	39.4490 (68)	0.703118 (22)		2.77	953	60.4	Primitive
ARA-01	19.7002 (25)	15.6181 (25)	39.5117 (73)	0.703101 (19)	0.512921 (7)	2.97	875	48.0	Primitive
ARE-13	19.8133 (23)	15.6248 (23)	39.6045 (69)	0.703116 (26)	0.512940 (9)	2.70	796	51.7	Primitive
ARE-13 rerun				0.703121 (17)		2.70	796	51.7	Primitive
BAN-53	19.6773 (23)	15.5929 (21)	39.4962 (64)	0.703138 (26)	0.512905 (22)	2.69	871	45.3	Primitive
BAN-53 rerun				0.703095 (17)		2.69	871	45.3	Primitive
BIL-36	19.8142 (23)	15.6350 (21)	39.6282 (65)	0.703072 (19)	0.512991 (25)	2.91	911	48.8	Primitive
BOT-28	19.7723 (32)	15.6286 (30)	39.6036 (82)	0.703088 (19)	0.512907 (8)	5.84	1116	74.7	Primitive
CA1-21	19.6737 (24)	15.6040 (23)	39.4959 (64)	0.703099 (22)	0.512916 (9)	3.05	861	48.0	Primitive
CA2-20	19.7340 (23)	15.6163 (21)	39.5365 (52)	0.703063 (17)	0.512934 (7)	6.50	1124	69.7	Primitive
CA3-22	19.6932 (25)	15.6114 (23)	39.5215 (63)	0.703115 (17)	0.512913 (14)	3.08	879	48.4	Primitive
CAN-05	19.7172 (26)	15.6155 (24)	39.5304 (68)	0.703109 (19)	0.512914 (8)	6.06	1101	68.6	Primitive
CHA-03	19.7388 (26)	15.6139 (25)	39.5570 (69)	0.703119 (19)	0.512931 (7)	7.20	1026	66.8	Primitive
CHI-01	19.7316 (23)	15.6440 (23)	39.5984 (70)	0.703083 (16)	0.512930 (7)	3.12	1079	56.5	Primitive
CIO-77	19.7604 (25)	15.6045 (24)	39.5497 (72)	0.703088 (24)	0.512926 (11)	8.29	1011	68.8	Primitive
CIO-77 rerun	19.7599 (26)	15.6157 (22)	39.5613 (69)			8.29	1011	68.8	Primitive
COL-15	19.6643 (26)	15.6115 (25)	39.5123 (69)			3.64	863	46.8	Primitive
CRU-39	19.7625 (23)	15.6128 (23)	39.5644 (69)	0.703071 (19)	0.512964 (7)	5.21	1205	67.5	Primitive
EST-41	19.7362 (24)	15.6213 (23)	39.5638 (68)	0.703109 (20)	0.512901 (28)	4.09	718	44.7	Primitive
FAS-02	19.7057 (32)	15.6154 (4)	39.5200 (93)	0.703080 (24)		2.86	907	49.0	Primitive
GAR-04	19.7663 (23)	15.6231 (22)	39.5824 (65)	0.703116 (20)		2.52	743	43.0	Primitive
GUA-17	19.6664 (33)	15.6114 (31)	39.5041 (90)	0.703115 (23)		4.24	1046	60.7	Primitive
HOR-17	19.7365 (26)	15.6191 (27)	39.5454 (72)	0.703082 (20)		5.03	1117	70.7	Primitive
JEV-03	19.7476 (24)	15.6217 (25)	39.5597 (72)	0.703088 (24)		5.23	1186	72.8	Primitive
MAR-31	19.7718 (29)	15.6197 (26)	39.5835 (75)	0.703108 (20)	0.512948 (7)	9.44	940	67.1	Primitive
MNE-33	19.7658 (29)	15.6210 (27)	39.5888 (73)	0.703155 (26)		3.63	949	53.9	Primitive
MOS-11	19.7340 (18)	15.6245 (17)	39.5222 (51)	0.703173 (26)		3.15	748	45.7	Primitive
NEG-51	19.6379 (21)	15.6047 (20)	39.5218 (61)	0.703154 (24)		3.02	791	42.1	Primitive
PAL-56	19.6265 (21)	15.6057 (22)	39.5147 (62)	0.703119 (19)		3.42	1258	73.0	Primitive
PT-ANT-16	19.7616 (20)	15.6191 (19)	39.5884 (59)	0.703182 (20)		4.98	1268	77.3	Primitive
PT-EAR-15	19.6987 (19)	15.6082 (18)	39.5218 (54)		0.512919 (9)	4.53	1150	67.8	Primitive
PV-EAR-13	19.7627 (34)	15.6100 (30)	39.5533 (80)	0.703229 (19)	0.512902 (21)	5.80	1057	60.4	Primitive
PV-EVO-06	19.8014 (27)	15.6299 (23)	39.6296 (65)	0.703096 (23)	0.512924 (8)	5.44	1031	63.2	Primitive
PV-INT-09	19.7713 (24)	15.6180 (21)	39.5685 (65)	0.703115 (19)	0.512930 (7)	8.26	1041	69.4	Primitive
PV-INT-09 rerun	19.7692 (24)	15.6144 (25)	39.5611 (73)			8.26	1041	69.4	Primitive
RAT-44	19.7696 (24)	15.6149 (25)	39.5648 (71)	0.703105 (23)		6.42	1100	73.2	Primitive
REV-87	19.7173 (26)	15.6218 (26)	39.5534 (73)	0.703105 (19)	0.512921 (7)	6.11	1112	68.5	Primitive

Table 4.1 continued: Radiogenic isotope ratios in groundmasses and whole-rock trace elements of Teide-Pico Viejo complex and rift zone eruptions

Sample	$^{206}Pb/^{204}Pb$	$^{207}Pb/^{204}Pb$	$^{208}Pb/^{204}Pb$	$^{87}Sr/^{86}Sr$	$^{143}Nd/^{144}Nd$	Pb [ppm]*	Sr [ppm]*	Nd [ppm]*	Comment
SAM-27	19.7740 (26)	15.6457 (24)	39.6289 (68)	0.703040 (22)		4.74	1146	71.22	Primitive
SIL-60	19.8001 (22)	15.6187 (23)	39.6371 (68)	0.703146 (20)		4.2	1074	69.39	Primitive
TAC-59	19.7306 (24)	15.6164 (24)	39.6035 (70)			6.03	1343	83.52	Primitive
TOM-14	19.7179 (21)	15.6085 (20)	39.5177 (57)			7.74	1118	66.83	Primitive
TOP-55	19.6828 (24)	15.6049 (23)	39.5265 (67)			2.56	927	46.51	Primitive
TRI-61	19.7570 (24)	15.6179 (24)	39.5624 (75)	0.703128 (20)		4.47	907	68.31	Primitive
VON-13	19.7888 (35)	15.6152 (29)	39.5828 (80)			6.21	1106	72.91	Primitive
CIE-18	19.7504 (24)	15.6208 (24)	39.5734 (65)	0.703115 (24)		10.1	419	51.5	Transitional
CIE-18 rerun				0.703136 (17)		10.1	419	51.5	Transitional
COR-05	19.7494 (27)	15.6233 (26)	39.5780 (78)	0.703127 (22)	0.512951 (11)	13.2	864	57.88	Transitional
CUE-14	19.7793 (27)	15.6221 (25)	39.5752 (77)	0.703120 (19)	0.512916 (8)	15.96	767	58.48	Transitional
CUE-14 rerun	19.7669 (28)	15.6102 (24)	39.5537 (71)			15.96	767	58.48	Transitional
LEN-15	19.7744 (24)	15.6226 (24)	39.5917 (69)	0.703107 (17)	0.512956 (14)	13.09	323	49.22	Transitional
PO1-06	19.7705 (31)	15.6208 (28)	39.5933 (82)	0.703094 (20)		13.2	862	57.3	Transitional
PO2-09	19.7586 (20)	15.6184 (21)	39.5762 (61)	0.703095 (19)		n/a	n/a	n/a	Transitional
PT-INE-11	19.7609 (25)	15.6120 (22)	39.5633 (62)	0.703178 (17)	0.512923 (6)	14.7	261	38.4	Transitional
PV-LAT-01	19.7612 (25)	15.6160 (21)	39.5654 (61)	0.703399 (23)	0.512924 (45)	14.98	360	58.21	Transitional
REV-85	19.7688 (25)	15.6186 (24)	39.5776 (67)			14.73	184	47.66	Transitional
VER-32	19.7667 (29)	15.6337 (28)	39.6068 (80)	0.703135 (17)		11.8	302	51.7	Transitional
ABA-36	19.7618 (26)	15.6095 (24)	39.5630 (64)			19.3	5.5	56	Evolved
ABB-19	19.7648 (22)	15.6143 (23)	39.5713 (65)			19.2	7.2	57.5	Evolved
BOQ-13	19.7623 (26)	15.6047 (25)	39.5316 (73)	0.704083 (20)		19.8	3.3	55.3	Evolved
BOQ-13 rerun				0.704083 (20)		19.8	3.3	55.3	Evolved
CAB-27	19.7635 (26)	15.6084 (24)	39.5549 (69)	0.703395 (23)	0.512938 (8)	17.6	34.2	44.1	Evolved
MAJ-17	19.7680 (29)	15.6175 (27)	39.5838 (75)	0.703321 (19)		17.64	34.94	53.89	Evolved
MB5-05	19.7660 (25)	15.6141 (20)	39.5713 (67)			18.97	9.63	57.22	Evolved
MB7-08	19.7817 (25)	15.5289 (23)	39.6002 (69)	0.704900 (16)		20.95	8.22	56.84	Evolved
MB8-06	19.7578 (26)	15.6056 (25)	39.5474 (73)		0.512945 (23)	21.45	2.41	61.93	Evolved
PT-LAE-04	19.7541 (29)	15.6064 (25)	39.5379 (65)	0.703091 (2)	0.512940 (6)	16.1	117	50	Evolved
RBL-01	19.7585 (28)	15.6171 (24)	39.5645 (69)	0.703275 (17)	0.512926 (8)	19.2	3.8	57.4	Evolved
PT-SUM-01	19.7657 (30)	15.6130 (28)	39.5758 (79)		0.512950 (17)	n/a	n/a	n/a	Evolved
FU-Msed-PtoP II-1	19.7448 (3)	15.6269 (28)	39.6810 (84)			n/a	n/a	n/a	Sediment
FU-Msed-PtoP II-5	19.4369 (28)	15.6516 (25)	39.4798 (76)			n/a	n/a	n/a	Sediment
FU-Msed-I-1	18.8000 (27)	15.6713 (27)	39.0664 (79)			n/a	n/a	n/a	Sediment
FV-Msed-D1-PtoP	19.0767 (31)	15.6767 (30)	39.4150 (86)			n/a	n/a	n/a	Sediment
FU-PLK-PtoP-II	18.5307 (63)	15.6263 (54)	38.2679 (141)			n/a	n/a	n/a	Sediment

Table 4.1.: Results from groundmass isotope analyses. All errors are 2 SD. Classification of samples according to trace element geochemistry in right hand column. *Whole-rock trace element data from Rodríguez-Badiola et al. (2008).

2.2. Oxygen isotope analysis

Feldspar separates from 15 lava flows were analysed for their $\delta^{18}O$ composition. Six of these 15 units were also analysed for the $\delta^{18}O$ composition of their groundmass. Samples were freed from weathered surfaces and run through a jaw crusher. The resulting chips were hand-picked under a stereo-microscope to exclude crystalline material, weathered parts or xenoliths. The chips were then ground by hand using an agate mortar and pestle (Table 4.2). The feldspar and groundmass separates were then picked under a stereo-microscope.

Analyses were performed in the stable isotope laboratory at the University of Oregon (Bindeman, 2008). Plagioclase phenocrysts were analysed by laser fluorination to determine $\delta^{18}O$ values using 1-2 mg of unaltered phenocrysts (1 to 3 individual crystals for each analysis). After laser extraction with a 35W Newwave CO_2 laser in a BrF_5 atmosphere, each sample was purified from traces of fluorine gas by boiling mercury and converted to CO_2. A yield of close to 95 % CO_2 indicated limited reaction of samples with BrF_5 at room temperature. The laser fluorination line was coupled to a Finnigan MAT 253 mass spectrometer and normalized to garnet standard GMG = 5.75 ‰ values. Standards measured during the experiment runs were 5.61 ±0.06 ‰ (1 stdev; n = 12). Due to daily variations, our standards were converted to the SMOW scale by adding between 0.10-0.23‰ to the measured values on the unknowns. Based on repeated analyses of standards, the maximum analytical uncertainties on $\delta^{18}O$ measurements are estimated at 0.1‰. The "melt" values were calculated using the equation: $\delta^{18}O_{melt} = \delta^{18}O_{plag} + (0.027 \times SiO_2[wt.\%] - 1.45)$ using a method which estimates mineral-melt fractionation (Bindeman et al., 2004).

Table 4.2: Oxygen isotope composition of feldspar and groundmass from Teide-Pico Viejo-complex and rift zone eruptions

	$\delta^{18}O$ feldspar	Error feldspar	$\delta^{18}O$ groundmass	Error groundmass	$\Delta\delta^{18}O_{fsp-gm}$	Comments
	[‰, SMOW]	[± ‰]	[‰, SMOW]	[± ‰]	[‰]	
Primitive						
CA1-23	5.43	0.11				
CIO-77	5.84	0.02				average
MAR-37	5.83	0.11	5.59	0.11	0.24	
PV-EAR-15	5.815	0.17				average
PV-INT-08	5.78	0.11				average
RAT-84	5.75	0.11	5.73	0.11	0.02	
Transitional						
CUE-14	5.875	0.03				average
LAJ-23	5.46	0.11				
LEN-15	5.88	0.11	6.80	0.11	-0.92	
PT-INE-17	5.86	0.11	6.00	0.11	-0.14	
PV-LAT-04	5.82	0.09				average
PV-LAT-66	5.82	0.09				average
Evolved						
MAJ-17	5.88	0.11	6.23	0.11	-0.35	
PT-LAE-02	5.99	0.11				
RBL-02	5.98	0.11	5.81	0.11	0.17	

Table 4.2.: Oxygen isotope values of feldspar and corresponding groundmass separates grouped according to trace element chemistry. Several feldspars have been analysed twice, and an average is given in these cases.

2.3. *Statistical analysis of major element correlation*

To characterise the primitive, transitional and evolved lavas and statistically quantify the processes that underlie their behaviour, the major element concentration data of the three groups were tested for tightness of fit to a regression line.

In statistical terms, the residual mean squares ($\overline{\sigma}^2$) derived from the regression trends yields an average value of deviation of the sample points from the regression trend of each major element for each compositional group. This reflects the quality of a trend, whereas R^2 values, for instance, serve better to distinguish whether or not a correlation between two variables exists. In other words, the lower the value of $\overline{\sigma}^2$ parameter, the tighter the fit of the sample points to the regression trend. Comparing the tightness of fit allows assessing if significant differences between trends persist.

This method was employed to detect if major element correlations behave significantly differently between compositional groups. We used an f-test to verify significant changes in $\overline{\sigma}^2$. Thresholds of significance for this test are derived from F distribution tables (http://

www.statsoft.com/textbook/sttable.html#f) where the degrees of freedom are defined as number of samples minus one: primitive = 49 - 1 = 48; transitional = 17 - 1 = 16; evolved = 17 - 1 = 16 (the number of samples differ from the number of samples analysed in this study because the dataset from Rodríguez-Badiola et al. (2008) is used). For instance, comparing primitive and evolved lavas yields a value of $F_{(.025, 48, 16)}$ = 2.1819 from the F distribution tables. Is the *ratio* of the $\bar{\sigma}^2$ values of primitive and evolved lavas higher than this F value, a significant change in tightness of fit can be read from that and shows a potential change in behaviour. We used an α of 0.025 to yield a 95% confidence interval.

3. RESULTS

3.1. *Isotope ratios in groundmass samples*

3.1.1. *Strontium isotope composition in groundmass samples*

Thirty-four primitive, nine transitional and six evolved samples (plus four duplicate analyses) were measured for the $^{87}Sr/^{86}Sr$ composition of their groundmass. Primitive and transitional lavas overlap considerably in $^{87}Sr/^{86}Sr$ ratios (primitive: 0.703040(21) to 0.703229(18); transitional: 0.703094(20) to 0.703332(17)). Only one transitional sample exceeds the range of the primitive group with a $^{87}Sr/^{86}Sr$ ratio of 0.703332(17). This phonolite from Montaña Reventada is part of a composite eruption of basanite and phonolite, with abundant mixing textures within the phonolite (Araña et al., 1994) and is studied in detail in chapter 4.

In contrast, the $^{87}Sr/^{86}Sr$ ratios of the evolved lavas yield values from 0.703091(2) up to 0.704900(16), significantly higher than in primitive and transitional lavas. Although all compositional groups share a common lower end of $^{87}Sr/^{86}Sr$ ratios of 0.703040(21) to 0.703094(20), Sr isotope ratios increase with higher degrees of differentiation (Fig. 4.1).

Two Fuerteventura sediment samples were analysed and yield Sr isotope ratios of 0.703473(21) and 0.707684(21).
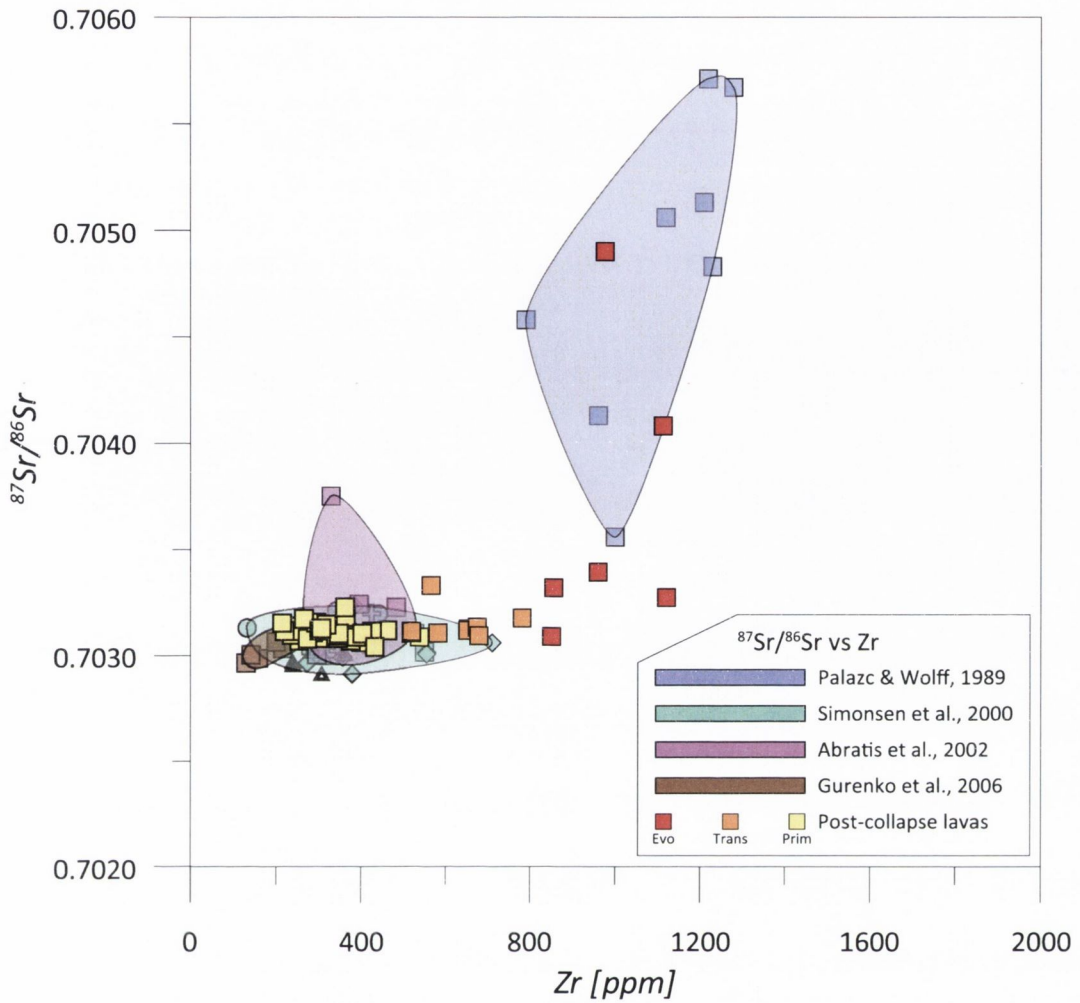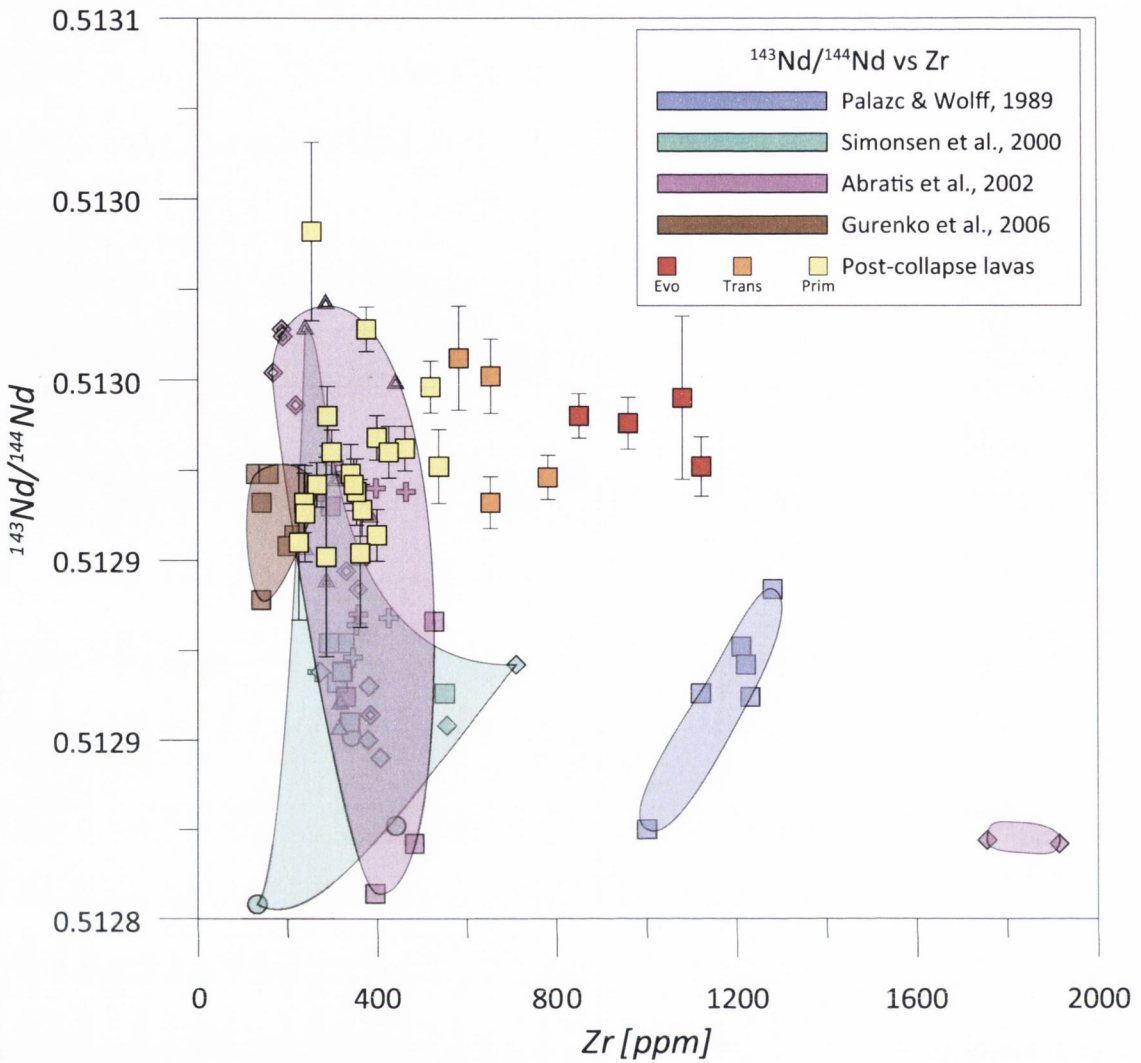
Fig. 4.1: Sr isotope ratios of Tenerife post-collapse lavas, using Zr concentration as differentiation index, compared to literature data (blue: Palacz & Wolff, 1989; green: Simonsen et al., 2000; purple: Abratis et al., 2002; brown: Gurenko et al., 2006). Errors are 2SD and included in symbols when not visible. The majority of samples possess a $^{87}Sr/^{86}Sr$ ratio of around 0.7031. Samples from Abratis et al. (2002) are dredged from the slopes of Tenerife and some of them may thus be elevated in Sr isotopes due to seawater alteration. In turn, high $^{87}Sr/^{86}Sr$ ratios from subaerial lavas and ignimbrites appear to be restricted to highly evolved compositions.

3.1.2. Neodymium isotope composition in groundmass samples

Analyses of $^{143}Nd/^{144}Nd$ on groundmass were undertaken on 20 primitive, four transitional and six evolved samples. Primitive lavas yielded $^{143}Nd/^{144}Nd$ ratios of 0.519201 to 0.512991 (± 6-45). Transitional samples are constrained to a smaller interval of $^{143}Nd/^{144}Nd$ between 0.512916 to 0.512956, and evolved samples plot in an even tighter range of 0.512924 to 0.512950. Nd-isotope ratios are consistent with existing data at low levels of differentiation (<400 ppm Zr), but exceed published data for transitional and evolved samples (Fig. 4.2).

Fig. 4.2: Nd isotope ratios of Tenerife post-collapse lavas using Zr concentration as differentiation index, compared to literature data (blue: Palacz & Wolff, 1989; green: Simonsen et al., 2000; purple: Abratis et al., 2002; brown: Gurenko et al., 2006). Errors are 2SD. Nd ratios below 400 ppm Zr overlap with existing data, but appear to be higher than published data in samples with Zr concentrations above 400 ppm.

3.1.3. Pb–Pb systematics in groundmass samples

Altogether 69 samples have been analysed for their $^{206}Pb/^{204}Pb$, $^{207}Pb/^{204}Pb$ and $^{208}Pb/^{204}Pb$ isotopic ratios. Among these samples were 61 from lava flows, plus three duplicate analyses to test data reproducibility. Moreover, five sediment samples from Fuerteventura were analysed. Grouped after their degree of differentiation, lavas yielded the following ratios, reported with 2SD in brackets:

- Forty primitive samples plus two duplicates: $^{206}Pb/^{204}Pb$ ratios range from 19.5050(22) to 19.8142(22), $^{207}Pb/^{204}Pb$ from 15.5919(22) to 15.6456(24) and $^{208}Pb/^{204}Pb$ from

39.4490(68) to 39.6371(68),

- Ten transitional samples plus one duplicate: ^{206}Pb/^{204}Pb ratios range from 19.7493(26) to 19.7743(26), ^{207}Pb/^{204}Pb from 15.6102(24) to 15.6337(28) and ^{208}Pb/^{204}Pb from 39.5536(70) to 39.6067(80),

- Eleven evolved samples: ^{206}Pb/^{204}Pb ratios range from 19.7541(28) to 19.7816(24), ^{207}Pb/^{204}Pb from 15.5288(22) to 15.6174(26) and ^{208}Pb/^{204}Pb from 39.5316(72) to 39.6001(68) (Fig. 4.3).
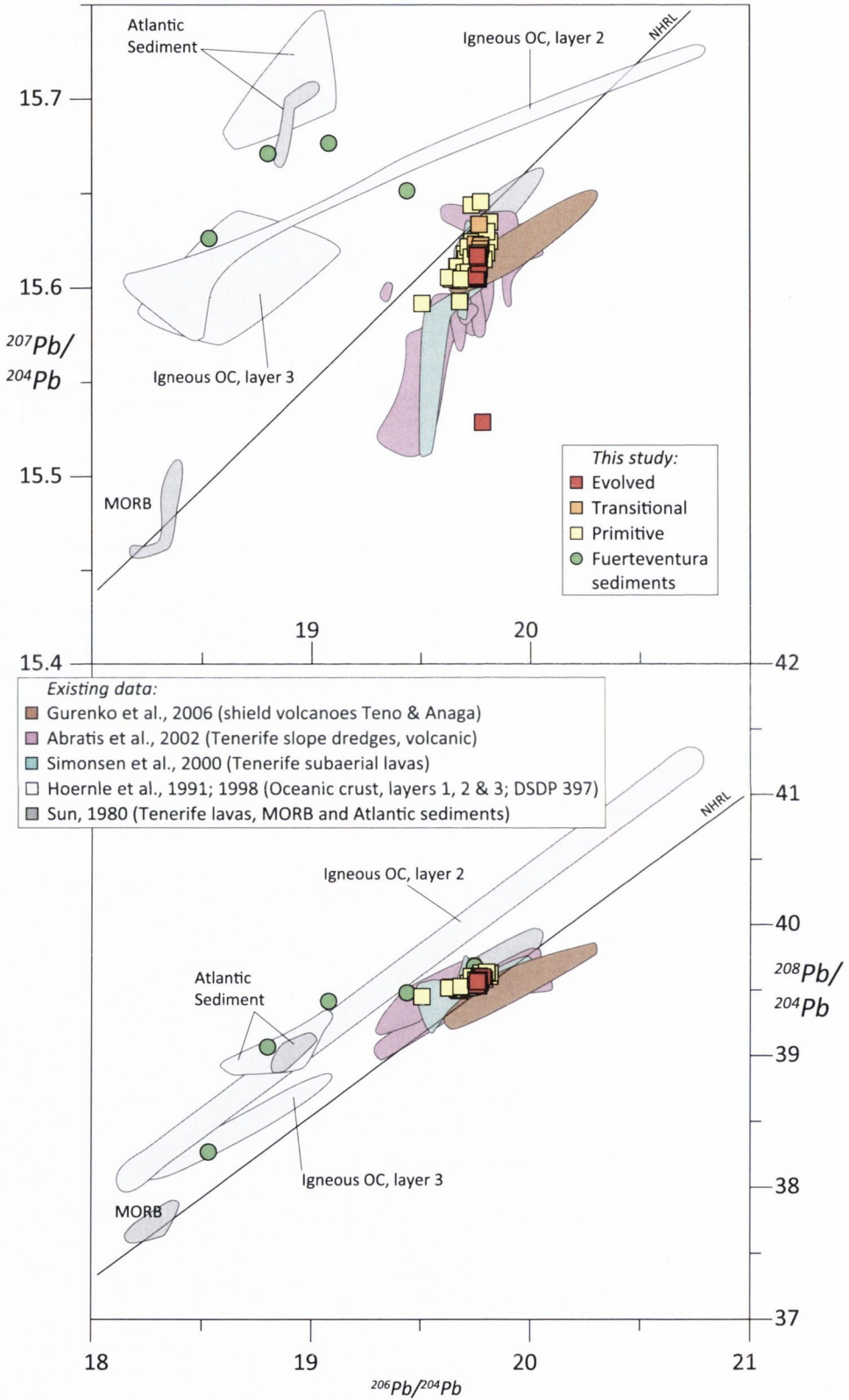
Fig. 4.3: Pb isotope analysis of Tenerife post-collapse lavas (points) compared to literature data (fields). All errors are 2σ standard deviation and are all smaller than the symbol. Northern Hemisphere Reference Line (NHRL) after Hart (1984). and with oceanic crust/MORB data (Sun, 1980; Hoernle et al., 1991, 1998) Note confinement of transitional and evolved lavas to a narrow range of ^{206}Pb/^{204}Pb ratios.

Our results broadly agree with existing data on Tenerife (Palacz & Wolff, 1989; Simonsen et al., 2000; Abratis et al., 2002; Gurenko et al., 2006). Sample MB7, with the lowest $^{207}Pb/^{204}Pb$ detected, is well within the range of available Pb-Pb-data for Tenerife (Fig. 4.3). Higher $^{207}Pb/^{204}Pb$ ratios (15.614 to 15.64) were obtained for historical lavas when compared to those of Simonsen et al. (2000) (15.586 to 15.59).

More differentiated lavas are strongly confined in their $^{206}Pb/^{204}Pb$ ratio. The primitive lavas trend alongside the Northern Hemisphere Reference Line (NHRL) on a plot of $^{206}Pb/^{204}Pb$ versus $^{207}Pb/^{204}Pb$, with a variation $\Delta^{206}Pb/^{204}Pb_{max-min} = 0.3048$. The transitional and evolved lavas, in turn, are confined to a $\Delta^{206}Pb/^{204}Pb_{max-min}$ of 0.0250 and a $\Delta^{206}Pb/^{204}Pb_{max-min}$ of 0.0275, or 8.2% and 9% of the primitive range, respectively (Table 4.3).

Table 4.3: Values of ΔPb-$Pb_{max-min}$ for compositional groups

	$\Delta^{206}Pb/^{204}Pb_{max-min}$	$\Delta^{207}Pb/^{204}Pb_{max-min}$	$\Delta^{208}Pb/^{204}Pb_{max-min}$
Primitive	0.3092 (12)	0.0538 (12)	0.1881 (34)
Transitional	0.0250 (13)	0.0235 (14)	0.0531 (40)
Evolved	0.0275 (14)	0.0886 (13)	0.0685 (36)

Table 4.3.: $\Delta^{20X}Pb/^{204}Pb_{max-min}$ values for all three compositional groups, calculated following: $(\Delta^{20X}Pb/^{204}Pb_{max}) - (\Delta^{20X}Pb/^{204}Pb_{min})$. The larger error of the maximum and minimum Pb isotope values is given in brackets. Compared to primitive lavas, transitional and evolved lavas show a strong confinement in $^{206}Pb/^{204}Pb$ (low $\Delta^{206}Pb/^{204}Pb$ value).

3.2. Oxygen isotope composition of groundmass and feldspars

Fifteen $\delta^{18}O$ measurements have been performed on feldspar. Feldspar data increase in oxygen ratio from 5.43 to 5.99 ‰ (±0.03 - 0.29 ‰) with decreasing whole-rock MgO concentration except for one outlier at 5.46 ‰.

Broken down into compositional groups, feldspars from primitive lavas show an increase from 5.43 ±0.11 ‰ to 5.84 ±0.02 ‰ from 8 to 2.5 wt.% MgO. This covers three rift zone eruptions, one radial vent of the central complex and two early Pico Viejo lavas. Feldspars from transitional lavas are similar, with values between 5.82 ±0.29 ‰ to 5.88 ±0.11 ‰, with the exception of the above mentioned outlier at 5.46 ±0.11 ‰ (Montaña Las Lajas,

LAJ). The evolved lavas are confined to below 0.5 wt.% MgO, with feldspars that range from 5.88 ±0.11 ‰ to 5.99 ±0.11 ‰.
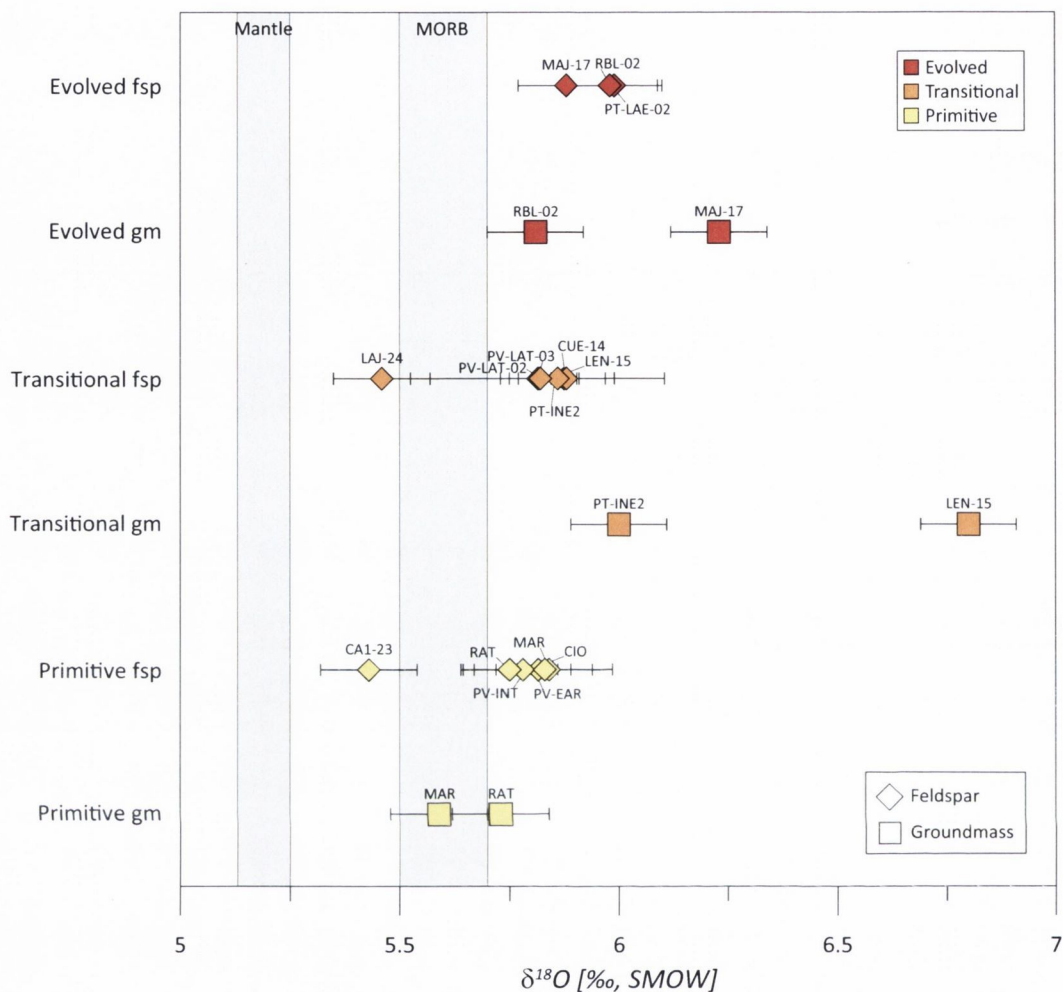

Fig. 4.4: Comparison of feldspar and groundmass $\delta^{18}O$ values for the three main stages of evolution. Squares are groundmass, diamonds are feldspar data. Note overall increase of oxygen values with degree of differentiation and the large discrepancy between groundmass and feldspars in the transitional group, which may indicate a large amount of xenocrysts and/or post-crystallisation change of melt in oxygen composition.

We carried out six $\delta^{18}O$ analyses of groundmass that have a corresponding feldspar analysis. Groundmass samples show higher values from 5.59 to 6.80 ‰ and loosely increase with decreasing MgO. Two groundmass analyses on primitive lavas resulted in ratios of 5.59 ±0.11 ‰ and 5.73 ±0.11 ‰. Two transitional groundmass samples yielded $\delta^{18}O$ values of 6.00 ±0.11 ‰ and 6.80 ±0.11 ‰., while two groundmass analyses of evolved lavas resulted in values of 5.81 ±0.11 ‰ and 6.23 ±0.11 ‰ (Fig. 4.4).

In two of the resulting six pairs of feldspar and groundmass data, the feldspar crystals show a lower $\delta^{18}O$ ratio than their host groundmass (samples: transitional LEN and evolved MAJ), in one a higher (primitive MAR) and in three the errors overlap (primitive

RAT, transitional PT-INE and evolved RBL).

When calculating the theoretical equilibrium values of groundmass (melt) $\delta^{18}O$ from the feldspar ratio after Bindeman et al. (2004), five out of six pairs of feldspar and host groundmass data appear to be out of equilibrium. Only in sample PT-INE does the calculated melt composition overlap with the error of the groundmass analysis, indicating an equilibrium between feldspar and groundmass (Fig. 4.5).
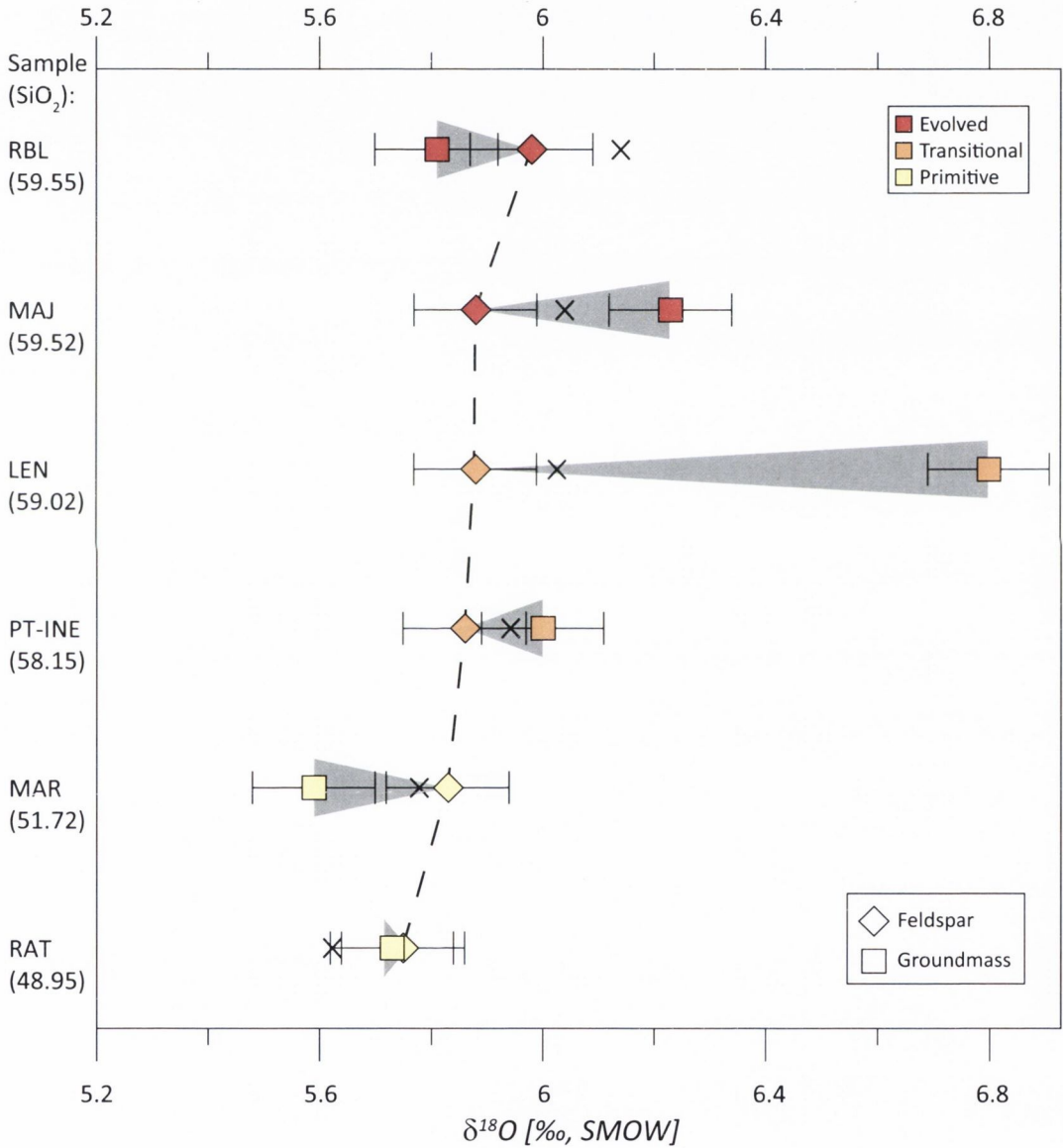

Fig. 4.5: Pairs of feldspar and groundmass $\delta^{18}O$ values for six eruptions (increasing SiO$_2$ from bottom to top). Squares are groundmass and diamonds feldspar data, crosses indicate expected melt values calculated from plagioclase values (Bindeman et al., 2004). Feldspar values (dashed line) rise continuously with silica concentration whereas groundmasses scatter widely. All pairs except for PT-INE are out of equilibrium as indicated by the discrepancy between the calculated and measured melt values.

3.3. *Whole-rock composition keyed by trace element characteristics*

The transitional and evolved lavas cluster together in the TAS diagram. To "disentangle" them, we used whole-rock Zr concentration as a differentiation index on the abscissa, following the example of Wolff et al. (2000). As an incompatible element, Zr is enriched with ongoing differentiation, until it is incorporated in accessory phases such as zircon. We did not find zircon in our samples and, indeed, zircon is considered absent even in the most evolved Tenerife lavas (Watson, 1979; Wolff, 1987; Wolff & Toney, 1993; Bryan et al., 2002). Zirconium concentrations of several thousand ppm have been reported from late crystallising, interstitial pyroxenes and amphiboles, indicating the parent liquid must have been highly enriched in Zr. Texture and chemistry indicated that these pockets of melt were residual quenched liquids and were thought to bear no volumetric significance (Wolff, 1987). For our purpose, however, Zr is a suitable indicator for the level of differentiation of these lavas.

In plots of major elements versus Zr concentration, primitive lavas rise in Al_2O_3, Na_2O, K_2O, decline in MgO, Fe_2O_3, CaO and TiO_2 and show a distinct spike in P_2O_5. The MnO concentrations are barely above detection limit (all described from low to high Zr content). Transitional lavas tend to broadly continue this trend. However, in all major elements, their trend is less well defined with a slightly shallower slope and a wider scatter than the primitive lavas. The evolved lavas, in contrast, show almost no variation in major elements and tend to form arrays that are sub-parallel to the x-axis (Fig. 4.6).

The three compositional groups can be characterised by their tightness of fit to a regression line. The dashed lines in Fig. 4.6 indicate this tightness of fit ($\bar{\sigma}^2$) for each compositional group. The closer spaced the dashed lines are for each trend, the better the fit, i.e. the better the real data reproduce the regression equation.
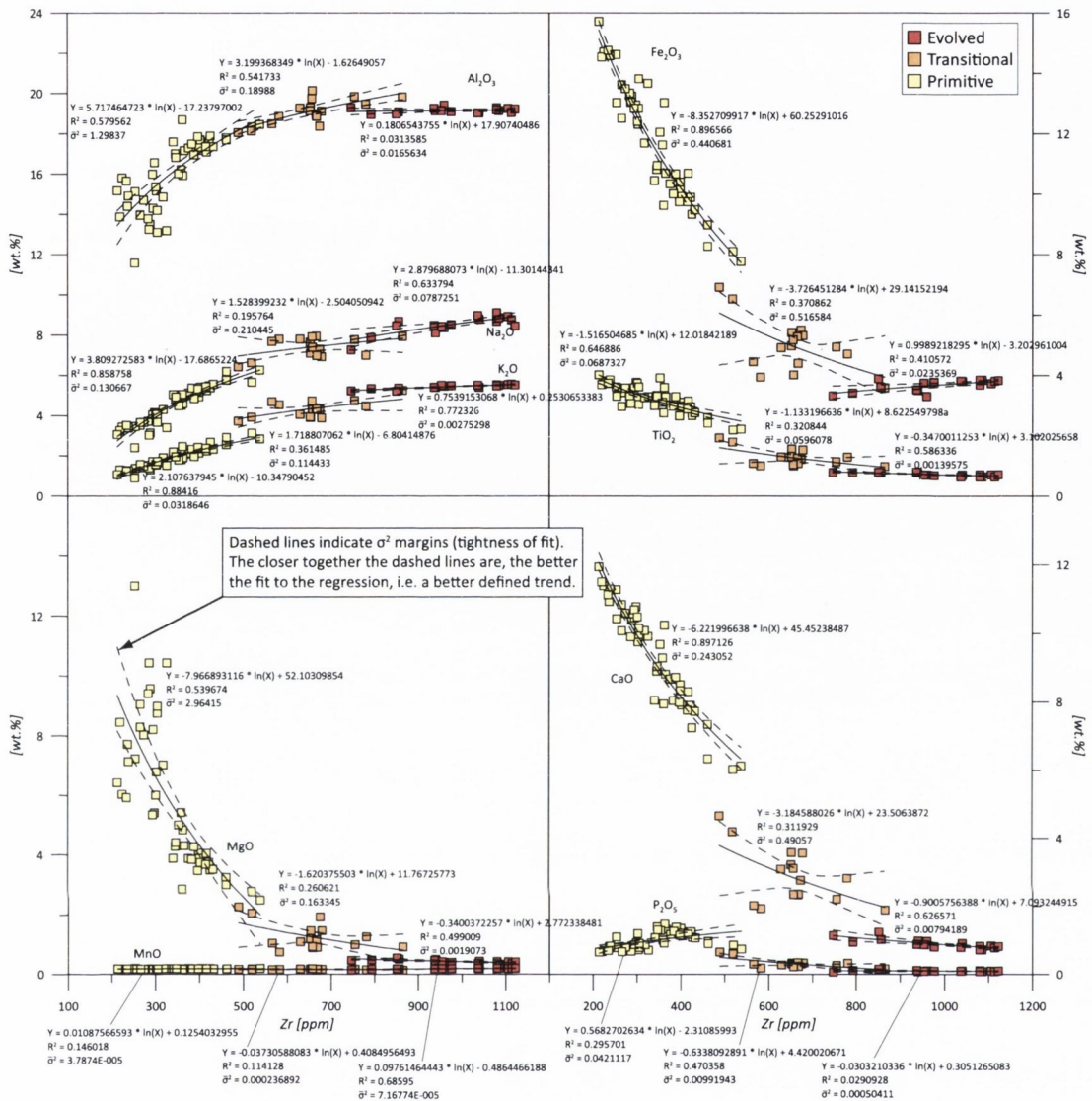
Fig. 4.6: **Wholerock major elements plotted versus Zr content on the x-axis.** Note sub-linear arrays of primitive and evolved lavas whereas transitional lavas have a more random distribution of major element contents. Solid lines are log fit regression trends ($Y = B \times \ln(x) + A$), dashed lines are 2σ confidence intervals. A log fit best describes the average development of the primitive sections and the same type of fit was used for the other groups. Some of the evolved group's sub-horizontal trends yield low R^2 values because the variables effectively do *not* correlate, therefore $\overline{\sigma}^2$ was a more suitable parameter for testing the robustness of trends.

Statistical analysis shows that all groups behave differently relative to each other.

i) Primitive versus transitional lavas: The primitive lavas show a significantly tighter fit in MnO, CaO and K_2O, whereas transitional lavas have a tighter fit in Al_2O_3, MgO and P_2O_5. The TiO_2, Fe_2O_3 and Na_2O fits do not change significantly between the two groups.

ii) Primitive versus evolved lavas: In the primitive versus the evolved lavas, all elements except MnO show a tighter fit for the evolved group. Changes in MnO and Na_2O fits are not significant, whereas F values for TiO_2, Al_2O_3, Fe_2O_3, CaO, K_2O and P_2O_5 are in the

double-digit range and F_{MgO} has the largest deviation of fit with 1554.11.

iii) Transitional versus evolved lavas: Between the transitional and the evolved lavas, we find a continuous pattern of $\bar{\sigma}^2$ deviation. The transitional group values are always larger than the evolved group, and the variation in fit is significant. The F values between these two groups are mostly double-digit figures, which indicates a very different behaviour between the two groups (Table 4.4).

Table 4.4: F-test results for wholerock major elements

Species		Primitive vs Transitional			Primitive vs Evolved			Transitional vs Evolved	
Degrees of freedom: (nearest value in table)		49 (40) vs 15 (15)			49 (40) vs 16 (15)			15 (15) vs 16 (15)	
Species		Threshold	F value*		Threshold	F value*		Threshold	F value*
TiO_2	$\sigma_{prim} < \sigma_{trans}$	2.509	1.15	$\sigma_{prim} > \sigma_{evo}$	2.1819	**49.24**	$\sigma_{trans} > \sigma_{evo}$	2.7875	**42.71**
Al_2O_3	$\sigma_{prim} > \sigma_{trans}$	2.1819	**6.84**	$\sigma_{prim} > \sigma_{evo}$	2.1819	**78.39**	$\sigma_{trans} > \sigma_{evo}$	2.7875	**11.46**
Fe_2O_3	$\sigma_{prim} < \sigma_{trans}$	2.509	1.17	$\sigma_{prim} > \sigma_{evo}$	2.1819	**18.72**	$\sigma_{trans} > \sigma_{evo}$	2.7875	**21.95**
MnO	$\sigma_{prim} < \sigma_{trans}$	2.509	**6.25**	$\sigma_{prim} < \sigma_{evo}$	2.509	1.89	$\sigma_{trans} > \sigma_{evo}$	2.7875	**3.30**
MgO	$\sigma_{prim} > \sigma_{trans}$	2.1819	**18.15**	$\sigma_{prim} > \sigma_{evo}$	2.1819	**1554.11**	$\sigma_{trans} > \sigma_{evo}$	2.7875	**85.64**
CaO	$\sigma_{prim} < \sigma_{trans}$	2.509	**2.02**	$\sigma_{prim} > \sigma_{evo}$	2.1819	**30.60**	$\sigma_{trans} > \sigma_{evo}$	2.7875	**61.77**
Na_2O	$\sigma_{prim} < \sigma_{trans}$	2.509	1.61	$\sigma_{prim} > \sigma_{evo}$	2.1819	1.66	$\sigma_{trans} > \sigma_{evo}$	2.7875	**2.67**
K_2O	$\sigma_{prim} < \sigma_{trans}$	2.509	**3.59**	$\sigma_{prim} > \sigma_{evo}$	2.1819	**11.57**	$\sigma_{trans} > \sigma_{evo}$	2.7875	**41.57**
P_2O_5	$\sigma_{prim} > \sigma_{trans}$	2.1819	**4.25**	$\sigma_{prim} > \sigma_{evo}$	2.1819	**83.54**	$\sigma_{trans} > \sigma_{evo}$	2.7875	**19.68**
Result		**No distinct difference**			**Evolved lavas significantly tighter**			**Evolved lavas significantly tighter**	

Table 4.4.: Statistical analysis of wholerock data. In each column, the $\bar{\sigma}^2$ values (tightness of fit) of two compositional groups are compared. The threshold values are derived from standard F-distribution tables (http://www.statsoft.com/textbook/sttable.html#f). Bold F values are larger than the threshold value and indicate that the difference between the groups is significant. For instance, a very loose and scattered trend in the transitional group is always followed by a very tight and well-defined trend in the evolved group. This indicates a potential change in the processes responsible for petrogenesis.

In summary, the primitive lavas show variable fits among the major elements, whereas transitional lavas show looser fits in all elements, i.e. badly defined trends. In turn, the evolved lavas consistently show the tightest fits in all major elements (i.e. the best-defined trends).

4. DISCUSSION

Here, we firstly interpret all the data that were generated from our work, in this case data on the composition of the radiogenic isotopes in our samples. We then test these results by using whole-rock and trace element data, obtained from the literature (Rodríguez-Badiola et al., 2008) and our own oxygen isotope data. An AFC model, using the spreadsheet from Erson & Helvaci (2009) complements the discussion.

4.1. Pb isotopes

In the evolved and transitional group, the samples show a very narrow range in $^{206}Pb/^{204}Pb$ (19.75 to 19.78). This coincides with a peak distribution of number of primitive samples in this narrow interval of $^{206}Pb/^{204}Pb$ (Fig. 4.7a). The samples also show peak distributions in $^{207}Pb/^{204}Pb$ ratio, in which, however, evolved samples are offset from primitive samples. In numbers, $^{207}Pb/^{204}Pb$ ratios are 15.53 to 15.62 for evolved, compared to 15.61 to 15.64 for primitive samples (Fig. 4.7b).

It is likely that this dominant Pb isotope composition in primitive lavas indicates the potential mantle source composition. Samples that possess this "dominant" Pb isotope signature may largely be derived from a parental magma by fractional crystallisation. In contrast, samples that deviate from this Pb isotope signature within the primitive group are potentially affected by open-system processes that may considerably alter the isotopic composition of a magma.

In the evolved lavas, the combined Pb isotope signatures differ significantly from those that are found in the primitive lavas. Although, both $^{206}Pb/^{204}Pb$ and $^{207}Pb/^{204}Pb$ ratios in evolved lavas are consistent with the ranges of Pb isotope data that have been found in Tenerife, the combination of this "dominant" $^{206}Pb/^{204}Pb$ signal and a very low $^{207}Pb/^{204}Pb$ ratio in the evolved lavas is new. As such, although the primitive and evolved lavas overlap to some extent in their $^{207}Pb/^{204}Pb$ ratio, the two groups are distinct from each other in the range of values displayed for this ratio, however (Fig. 4.7b). This means that the majority of evolved lavas cannot have been derived directly by closed-system fractional crystallisation from a primitive parental magma and an open system is required to account

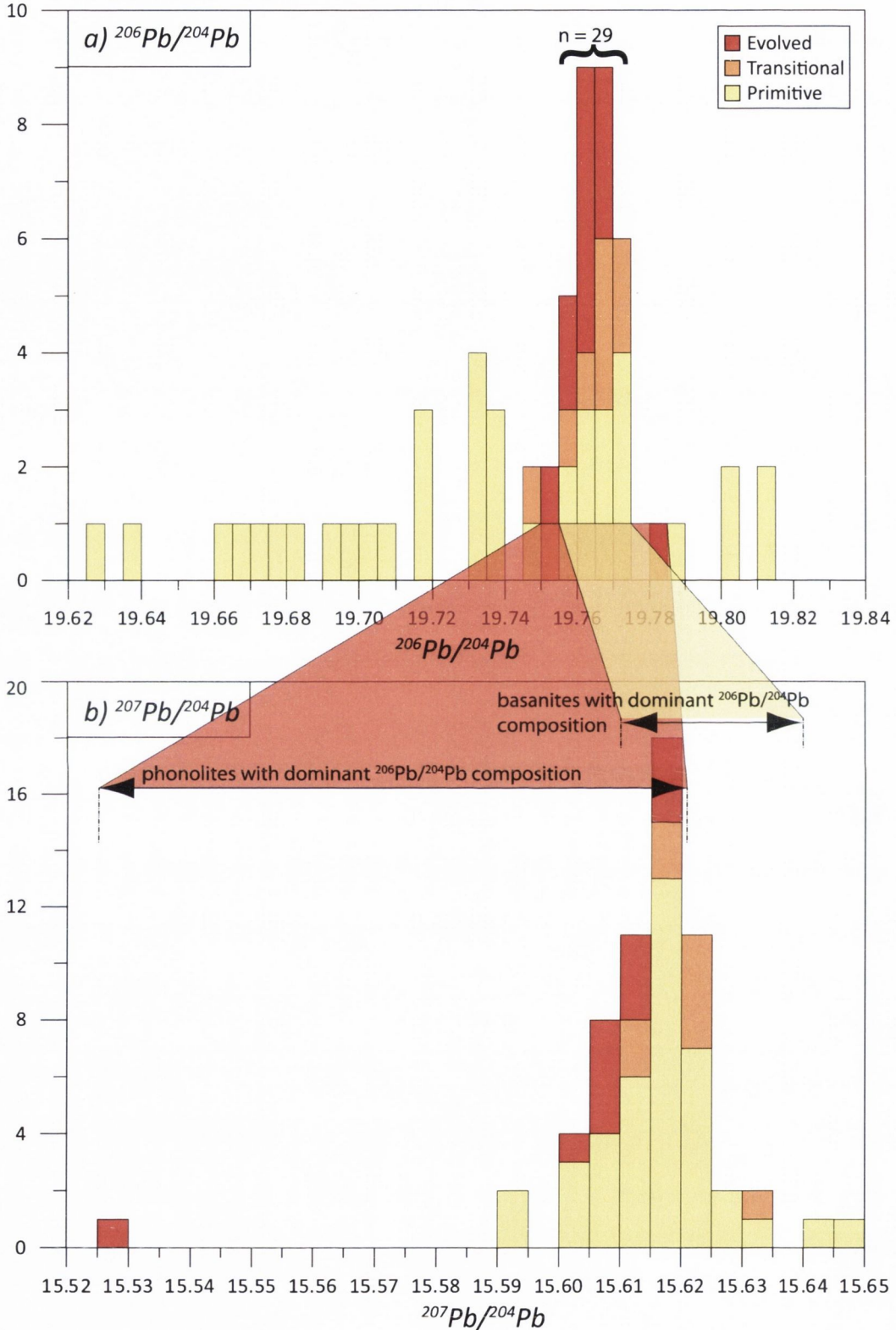for the petrogenesis of the evolved lavas in Tenerife.

Fig. 4.7: a) Histogram of $^{206}Pb/^{204}Pb$ ratios in Tenerife postcollapse lavas. Primitive lavas show a peak in $^{206}Pb/^{204}Pb$ ratio distribution at around 19.76, complemented by transitional and evolved lavas which also group around this Pb isotope composition. A second peak in primitive lavas is discernible at around 19.73. b) Histogram of $^{207}Pb/^{204}Pb$ ratios in Tenerife postcollapse lavas. Lavas of peak $^{206}Pb/^{204}Pb$ composition are indicated by arrows. Primitive lavas show a peak in $^{207}Pb/^{204}Pb$ ratio distribution at around 15.62. The bulk of transitional and evolved lavas also group around this Pb isotope composition, but also reach lower ratios overall.

In an open-system scenario. such as e.g. assimilation and fractional crystallisation, a primitive magma of the "dominant" $^{206}Pb/^{204}Pb$ composition could produce a phonolite magma of similar $^{206}Pb/^{204}Pb$, but lower $^{207}Pb/^{204}Pb$ composition through assimilation of a distinct component that leaves the $^{206}Pb/^{204}Pb$ undisturbed but lowers the $^{207}Pb/^{204}Pb$ of the magma.

As an end-member that is potentially present during the magmatic ascent, Atlantic sediments (Sun, 1980; Hoernle et al., 1991) and uplifted sediments from Fuerteventura (this study) generally plot at lower $^{206}Pb/^{204}Pb$, but much higher $^{207}Pb/^{204}Pb$ compositions, and are thus unlikely to be responsible for the observed variations in Pb compositions in the post-Icod-collapse lavas. So far, the primitive lavas from the Diego Hernández Formation and the Las Cañadas Volcano sequence are the only rocks that have been found in Tenerife to meet the requirements of low $^{207}Pb/^{204}Pb$ ratios and similar $^{206}Pb/^{204}Pb$ composition (Simonsen et al., 2000). Sample MB7 possesses a yet lower $^{207}Pb/^{204}Pb$ value and can thus not be explained on grounds of Pb isotope data through any mixing or assimilation relationship with existing end-member data (Fig. 4.8). Consequently, a different end-member that has not been discovered so far is required for this low $^{207}Pb/^{204}Pb$ ratio.

The Pb isotope ratios therefore allow arguing for open system magmatic differentiation of the post-Icod-collapse lava sequence in Tenerife. As the transitional and evolved lavas form a linear and subvertical array on a plot of $^{207}Pb/^{204}Pb$ versus $^{206}Pb/^{204}Pb$, a component (or a mixture of components) is required that possesses the same narrow $^{206}Pb/^{204}Pb$ and a lower $^{207}Pb/^{204}Pb$ than observed in the primitive lavas.
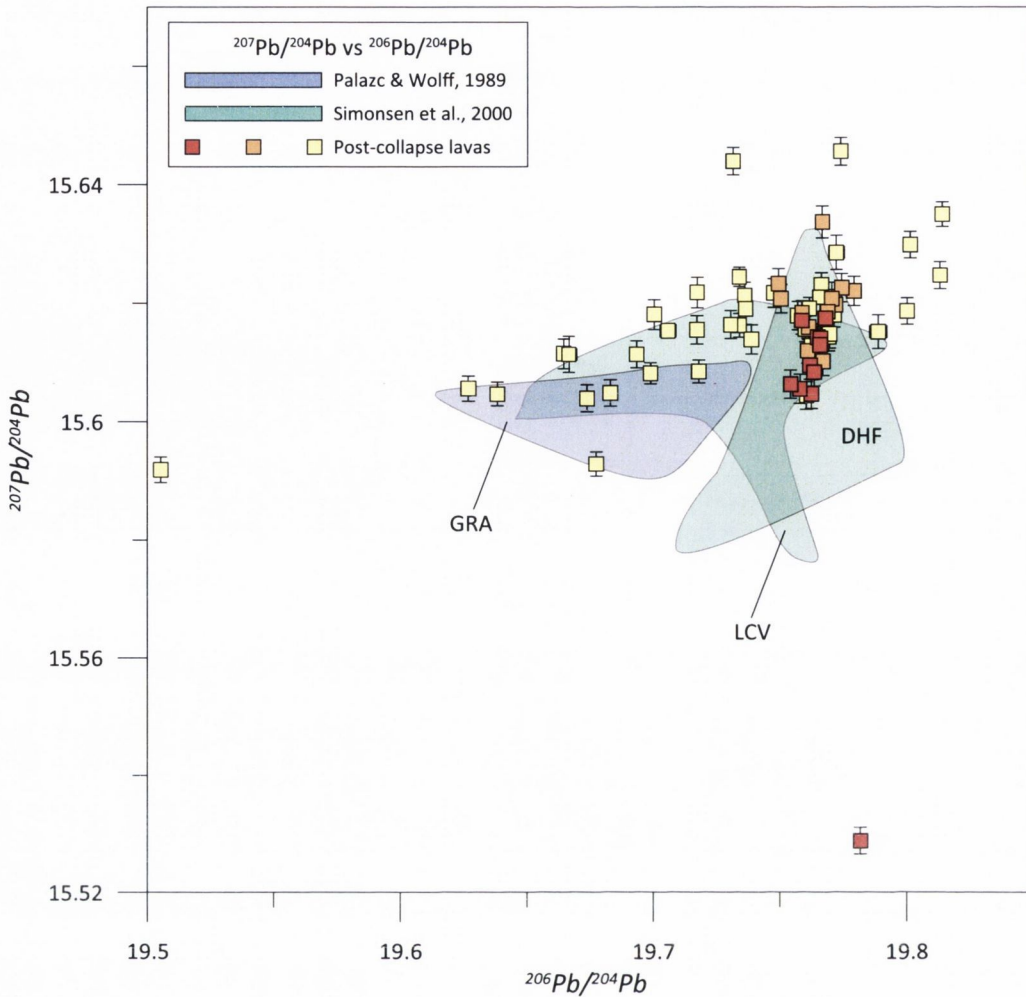
Fig. 4.8: Pb-Pb isotope systematics of Tenerife post-collapse lavas, 2σ errors included in symbol when not visible. Fields after Palazc & Wolff (1989) and Simonsen et al. (2000). LCV = Las Cañadas Volcano (not specified in more detail). GRA = Granadilla Formation (600 ka) and DHF = Diego Hernandez Formation (pre- or syn-collapse ignimbrite), both part of the Las Cañadas Volcano stratigraphy.

4.2. Sr and Nd isotope systematics

The confinement of Nd ratios to narrower intervals in more evolved groups may, in similar fashion to the $^{206}Pb/^{204}Pb$ isotope ratios, indicate a "dominant" signal in the magmatic source of these lavas, or point towards reworking of crustal material, where the ratios would indicate an increasingly stronger influence of an assimilant that possesses a distinct $^{143}Nd/^{144}Nd$ ratio. Either possibility is conceivable, and as pure closed-system differentiation of these lavas is not an exclusive process on the basis of the Pb isotope systematics, it implies that any assimilant that is incorporated during the magmatic evolution is either subordinate in Nd concentration or of very similar Nd isotope

composition (and increasingly dominant with differentiation).

The samples BOQ and MB7 show the highest Sr isotope ratios in this study and are thus important to consider, because they potentially experienced the largest degree of influx of isotopically distinct material. Unfortunately, Nd isotope data are unavailable for these samples. However, the observed narrowing in $^{143}Nd/^{144}Nd$ ratios with increasing differentiation in the post-Icod-collapse lavas indicates that these two lavas most probably possess very similar $^{143}Nd/^{144}Nd$ signatures relative to the lavas that were analysed. The arithmetic mean of the analysed evolved lavas in this study was therefore assumed to be a potential $^{143}Nd/^{144}Nd$ ratio for these two phonolites, i.e. BOQ and MB7 (0.512937, n=6). This allows for a complete picture in a plot of $^{143}Nd/^{144}Nd$ versus $^{87}Sr/^{86}Sr$ (Fig. 4.9). For comparison, the mean of all measured $^{143}Nd/^{144}Nd$ ratios (primitive, transitional and evolved lavas) is only marginally lower at 0.512930, compared to 0.512937 for the evolved lavas, and would therefore have equally suited.
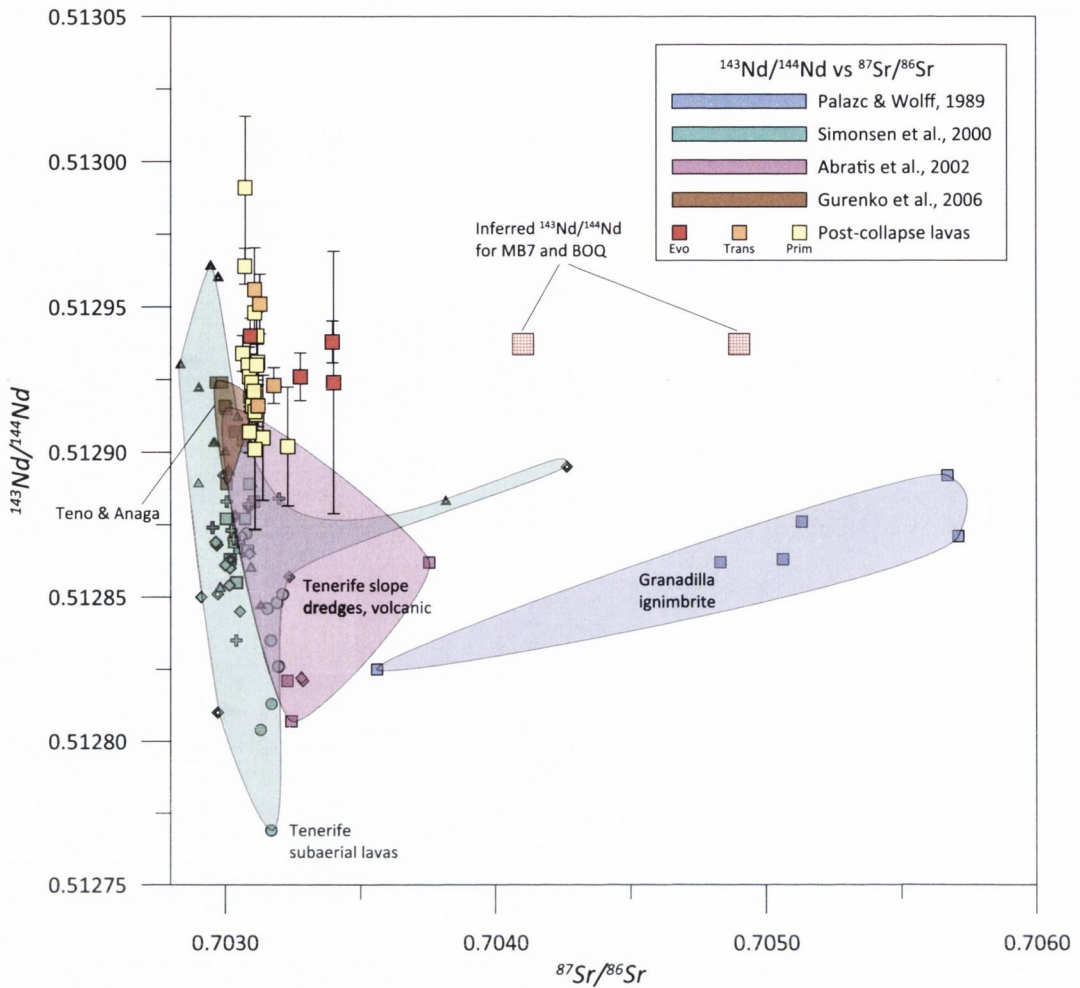
Fig. 4.9: $^{87}Sr/^{86}Sr$ versus $^{143}Nd/^{144}Nd$ of Tenerife post-Icod-collapse lavas. Coloured fields represent data from Palazc & Wolff, 1989, Simonsen et al., 2000; Abratis et al., 2002 (Tenerife data only) and Gurenko et al., 2006. Note that for the samples with the highest $^{87}Sr/^{86}Sr$ there are no $^{143}Nd/^{144}Nd$ data available; the mean of the Nd ratios of evolved lavas has been used as inferred Nd ratio for these (cross-hatched squares).

The $^{87}Sr/^{86}Sr$ ratios stay at a common level of 0.7031 through 0.7033, except for several lavas of the evolved group that reach up to 0.7049. Principally, elevated Sr isotope ratios can form in magmas by radiogenic in-growth ("aging") within a closed system or by taking up an assimilant that possesses a higher Sr isotope ratio. Radiogenic in-growth of ^{87}Sr in a given magma depends, among the Rb/Sr ratio of the magma, on the timescales from primary formation to eventual solidification. In Tenerife, Hawkesworth et al. (2000) suggested that a hypothetical closed-system fractional crystallisation scenario would take a maximum of ~300 ka (including the error) for basanite magma to develop to residual phonolite. These maximum estimates are far too short to create such an elevated $^{87}Sr/^{86}Sr$ ratio by means of radioactive decay alone. Therefore, assimilation of a high $^{87}Sr/^{86}Sr$

component must have given rise to the high Sr ratios measured. This is consistent with the findings from Pb isotope systematics. The only existing data from Tenerife with such high $^{87}Sr/^{86}Sr$ ratios are on the Granadilla ignimbrite (Palacz & Wolff, 1989). These data were therefore used as potential end-member for elevated Sr isotope ratios in the evolved lavas of the post-Icod-collapse succession.

The Granadilla ignimbrite represents the erupted deposits of a caldera-forming event within the Guajara cycle of the Upper Group in the central Las Cañadas edifice (Martí et al., 1994, 1997; Bryan et al., 1998; Wolff et al., 2000). Palacz & Wolff (1989) analysed six whole-rock samples of large pumice clasts from the Granadilla ignimbrite for both, Sr and Nd isotopes. All six were used to model mixing hyperbolas in plots of $^{143}Nd/^{144}Nd$ versus $^{87}Sr/^{86}Sr$. A mixture was calculated between each of these six Granadilla samples and five samples from the evolved group to test whether high $^{87}Sr/^{86}Sr$ evolved lavas can be explained as mixture of end-member and other evolved lavas (Fig. 4.10). Primitive and transitional lavas were not used as end-member during this step, because their Sr/Nd ratios are higher than the ones found in the Granadilla ignimbrite (3.86-19.92 versus 0.18-0.50). Mixing primitive lavas with Granadilla samples therefore creates downward convex mixing hyperbolas, which are insufficient to explain the pattern that the evolved lavas produce.
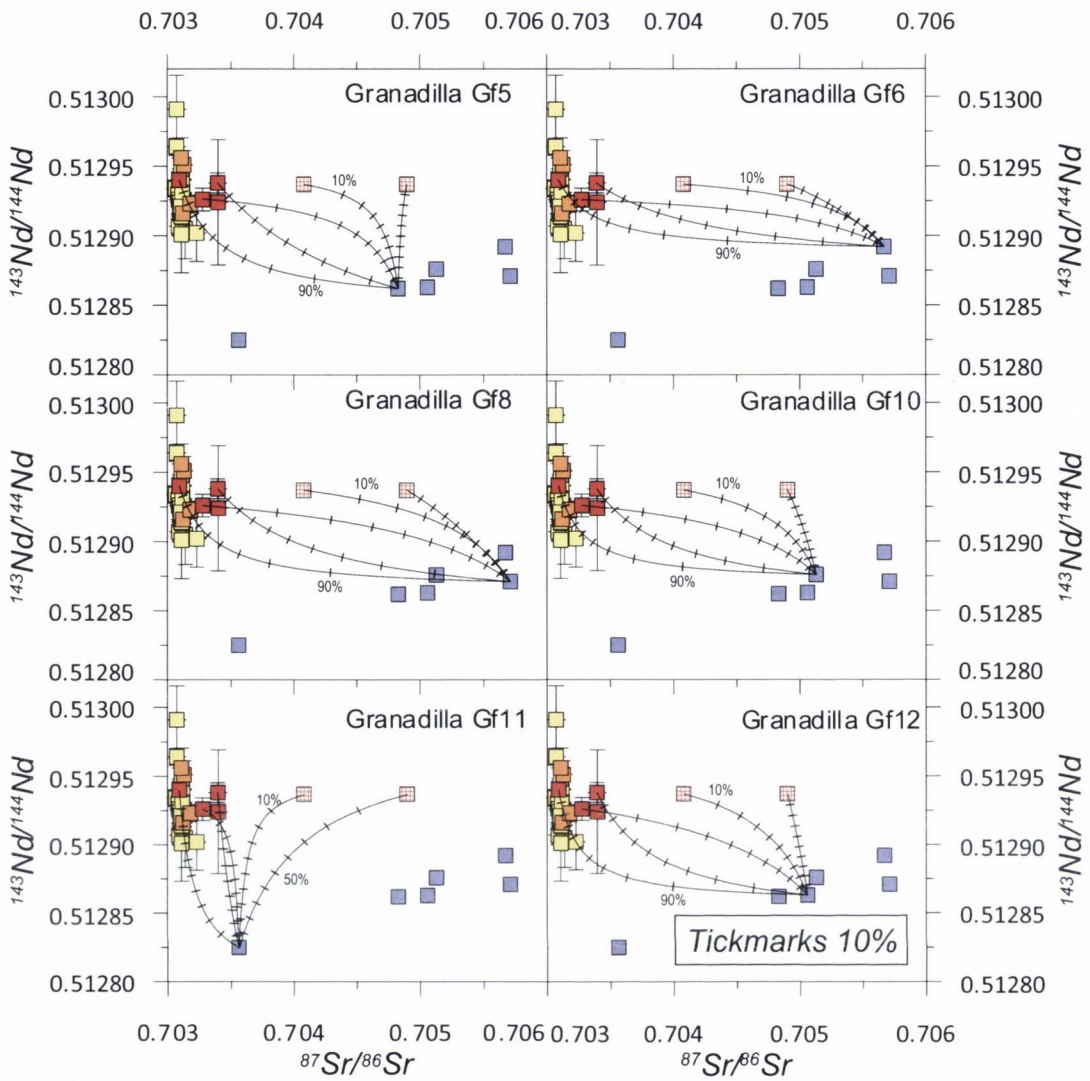
Fig. 4.10: $^{87}Sr/^{86}Sr$ versus $^{143}Nd/^{144}Nd$ of post-collapse lavas (<200 ka) compared to data of Palazc & Wolff, 1989 (Granadilla ignimbrite, blue squares). Mixing hyperbolas are calculated for each of the six Granadilla samples, paired with low Sr/Nd samples from this study. Tick marks represent 10% mixing intervals, percentage values indicate the amount of Granadilla ignimbrite incorporated in a potential mixture. Note that for the samples with the highest $^{87}Sr/^{86}Sr$ (checkered-pattern-symbols) there are no $^{143}Nd/^{144}Nd$ data available, hence, the arithmetic mean of available evolved lava $^{143}Nd/^{144}Nd$ ratios was used. While theoretical mixing curves can be calculated for each individual evolved sample, the mixing hyperbolas conflict a continuous mixing relationship for the succession basanite-phonolite-assimilant or the succession phonolite-assimilant.

When calculating the mixing curves with the Granadilla ignimbrite end-member, mixing models largely deviate from the pattern defined by the composition of the evolved lavas. One curve that results from modelling with the Granadilla sample Gf6 approaches the pattern that the evolved lavas define, albeit at lower $^{143}Nd/^{144}Nd$ values. This means that a very peculiar combination of samples is needed to find a single solution. In turn, the majority of melt-contaminant combinations fail to reproduce the observed phonolite pattern. The evolved succession and the high $^{87}Sr/^{86}Sr$ ratios that occur in some of these lavas cannot be explained by simple mixing of a low $^{87}Sr/^{86}Sr$ component and the

Granadilla ignimbrite (Fig. 4.10).

To achieve a plot of $^{87}Sr/^{86}Sr$ versus $1/^{86}Sr$ in which mixing relationships plots as straight arrays, the concentration of ^{86}Sr were calculated in each sample as follows:

(Equation 2.1)

$$^{86}Sr = c(Sr) * \frac{\dfrac{^{86}Sr}{^{88}Sr}}{\dfrac{^{84}Sr}{^{88}Sr} + \dfrac{^{86}Sr}{^{88}Sr} + \dfrac{^{87}Sr}{^{88}Sr} + \dfrac{^{88}Sr}{^{88}Sr}}$$

The ratios $^{87}Sr/^{88}Sr$ and $^{88}Sr/^{88}Sr$ can be expressed as:

(Equation 2.2)

$$\frac{^{88}Sr}{^{88}Sr} = 1$$

(Equation 2.3)

$$\frac{^{87}Sr}{^{88}Sr} = \frac{^{87}Sr}{^{86}Sr} * \frac{^{86}Sr}{^{88}Sr}$$

The resulting equation allows ^{86}Sr to be calculated by using the measured concentration of Sr and the measured ratio of $^{87}Sr/^{86}Sr$ as variables for each sample. The ratios $^{84}Sr/^{88}Sr$ and $^{86}Sr/^{88}Sr$ were assumed to be constant at 0.00676 and 0.1194, respectively.

(Equation 2.4)

$$^{86}Sr = c(Sr) * \frac{\dfrac{^{86}Sr}{^{88}Sr}}{\dfrac{^{84}Sr}{^{88}Sr} + \dfrac{^{86}Sr}{^{88}Sr} + \left(\dfrac{^{87}Sr}{^{86}Sr} * \dfrac{^{86}Sr}{^{88}Sr} \right) + 1}$$

In the resulting plot, all primitive and most transitional lavas are located near the origin and very closely spaced. All evolved lavas and one transitional lava (REV-85) deviate from this, either due to high $^{87}Sr/^{86}Sr$ ratios, lower ^{86}Sr concentrations (i.e. a higher $1/^{86}Sr$) or a combination of both. Together with primitive and transitional samples, the evolved

samples PT-LAE-02, MAJ-17, CAB and MB7 open up a linear array, whereas evolved samples RBL-02 and BOQ plot outside at higher $1/^{86}Sr$ values (Fig. 4.11). The samples BOQ and RBL-02 appear to have been affected by an end-member that is much lower in ^{86}Sr concentration.

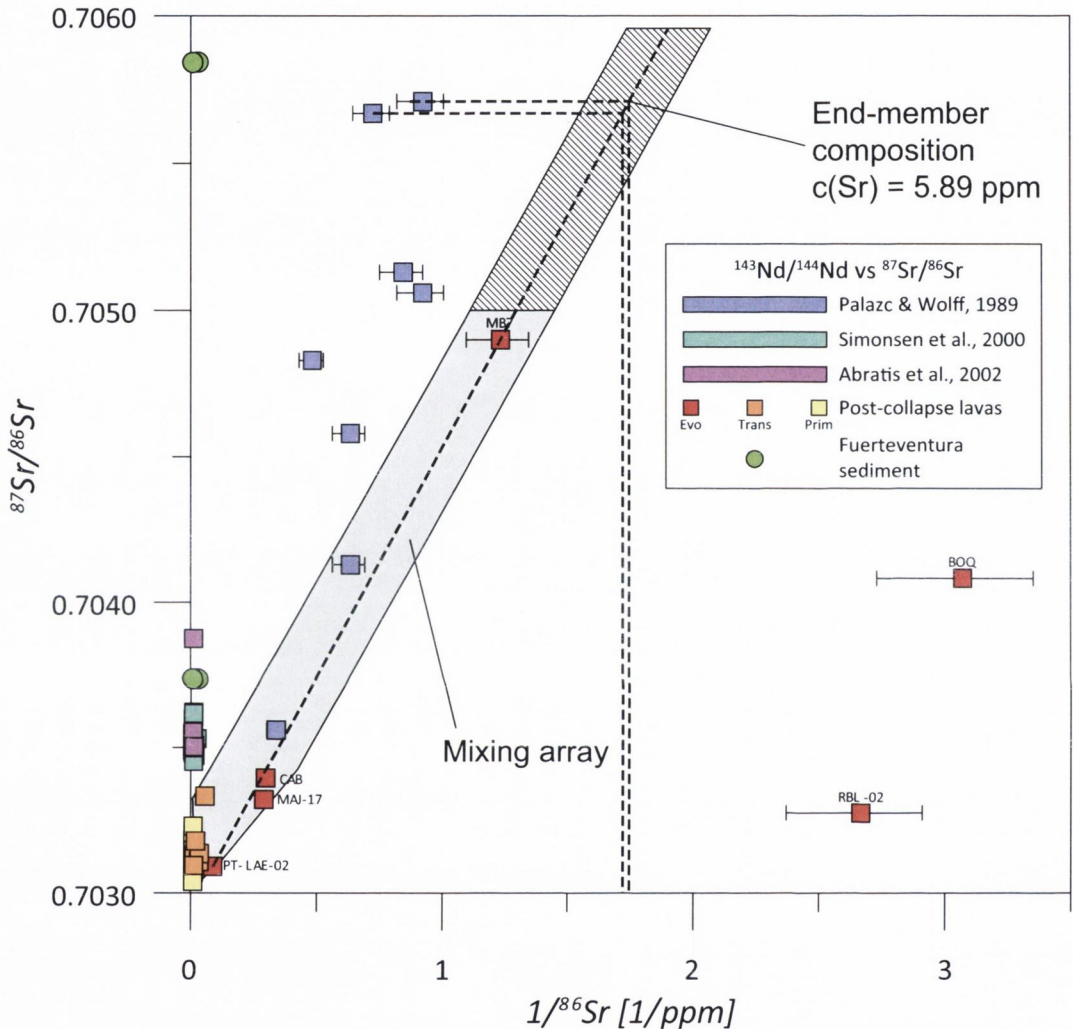Fig. 4.11: Groundmass $^{87}Sr/^{86}Sr$ versus $1/^{86}Sr$ of Tenerife post-collapse lavas. The concentration of ^{86}Sr has been calculated depending on the measured $^{87}Sr/^{86}Sr$ ratio and Sr concentration. Data from literature of Palacz & Wolff, (1989), Simonsen et al. (2000) and Abratis et al. (2002) were likewise recalculated to concentrations of $1/^{86}Sr$. Errors (2SD) are contained within symbols when invisible. Sr concentrations of Fuerteventura sediments are from Deegan (unpubl.data). Samples BOQ and RBL-02 plot at low ^{86}Sr concentrations and may have been affected by a different end-member than the bulk of the evolved lavas. This majority of evolved lavas, PT-LAE-02, MAJ-17, CAB and MB7, open a straight array interpreted to stem from mixing with a higher radiogenic component. The Granadilla ignimbrite samples deviate from this mixing array, but allow to infer how the "true" end-member must have looked like. The Sr concentration of this "true" end-member was calculated to be 5.89 ppm.

Existing data on basalt lavas and samples dredged from the submarine slopes of Tenerife show high ^{86}Sr concentrations and plot in similar fashion to what is observed in primitive lavas from this study (Simonsen et al., 2000; Abratis et al., 2002). Although having

somewhat elevated $^{87}Sr/^{86}Sr$ ratios, the rocks analysed in these two studies remain well outside the observed mixing array of evolved lavas and thus probably played no role during assimilation events that influenced the evolved magmas.

Likewise, the Fuerteventura sediments plot outside the potential mixing array defined by the evolved lavas. The Sr concentrations of these hydrothermally altered sediments from Fuerteventura have been measured in a tandem study to range between 377 to 1505 ppm (Deegan et al., in prep.), which leads to very low $1/^{86}Sr$ values. Similar to the Pb isotope systematics, this allows to exclude these sediment samples as a potential contaminant for the recent postcollapse lavas in Tenerife.

The Granadilla ignimbrite samples, in turn, are the closest of all analysed Tenerife rocks to a potential end-member. However, their ^{86}Sr concentrations are slightly higher than needed (lower $1/^{86}Sr$ values), indicating that the Granadilla ignimbrite can ultimately not be the end-member that was exclusively responsible for the high $^{87}Sr/^{86}Sr$ ratios in the postcollapse evolved lavas. Granadilla ignimbrite samples are also too low in $^{206}Pb/^{204}Pb$ ratios to fully explain the origin of the evolved lavas.

Although the Granadilla ignimbrite possesses ^{86}Sr concentrations too high to explain the mixing array defined by the evolved samples MB7, CAB, MAJ-17 and PT-LAE-02 in full, the Granadilla formations is very close and as such demonstrates the characteristics the "true" end-member would need to have had. This would be $^{143}Nd/^{144}Nd$ values similar to the evolved lavas, elevated $^{87}Sr/^{86}Sr$ ratios of higher than 0.705, a low Sr concentration of 5.89 ppm (calculated with a $^{87}Sr/^{86}Sr$ ratio of 0.70571), a distinct $^{206}Pb/^{204}Pb$ composition similar to the observed "dominant" ratio that may reflect a source signal and a $^{207}Pb/^{204}Pb$ ratio lower than or similar to the lowest one observed (sample MB7).

However, the search for the real isotopic end-member is hampered by the thin database of isotope ratios on evolved rocks in the Las Cañadas edifice, on top of which the post-Icod-collapse sequence is built. Simonsen et al. (2000) focussed on the basaltic members in the Las Cañadas Volcano, only, while the Granadilla ignimbrite, analysed by Palacz & Wolff (1989), has $^{143}Nd/^{144}Nd$ and $^{206}Pb/^{204}Pb$ ratios that are too low. However, all the necessary characteristics can be observed each in several distinct deposits, including

the ones studied here: suitable Pb isotope ratios are found in the centrally located Diego Hernández Formation basalts, the rocks from this study and basaltic rocks in Tenerife (Simonsen et al., 2000) possess fitting $^{143}Nd/^{144}Nd$ values and high Sr isotope ratios, albeit rare, do occur in Tenerife. Hence, it is realistic to assume that a suitable end-member (or a mixture of these) exists underneath Teide-Pico Viejo complex.

The key feature of this enigmatic end-member(s) seems to be a high Sr isotope ratio, which can only be found in highly differentiated rocks in Tenerife. The Granadilla ignimbrite provides the highest observed bulkrock $^{87}Sr/^{86}Sr$ ratio in Tenerife, along with Sr and Nd concentrations that are typical for this type of rock in this island and thus represent the best fit. In a plot of $^{143}Nd/^{144}Nd$ versus $^{87}Sr/^{86}Sr$, the Granadilla ignimbrite data from Palacz & Wolff (1989) was therefore slightly modified to "construct" a hypothetical contaminant. The original data was combined with a higher $^{143}Nd/^{144}Nd$ ratio than what was measured by Palacz & Wolff (1989): the arithmetic mean of the $^{143}Nd/^{144}Nd$ ratios of the evolved lavas was applied that was also used for the samples BOQ and MB7. Mixing was modelled between all lavas as melt compositions and this hypothetical contaminant (Fig. 4.12).

The resulting mixing hyperbolas not only encompass all evolved lavas within one mixing relationship, but also allow various solutions to include the transitional and primitive lavas, i.e. the complete differentiation sequence from primitive to evolved. Transitional lavas are typically reproduced by mixing ~33 to 77% of contaminant into a primitive melt. Evolved lavas can be expressed as mixtures that contain between 77 and 99.78% contaminant, regardless of using a primitive, transitional or low $^{87}Sr/^{86}Sr$ evolved lava as melt composition (Table 4.5).
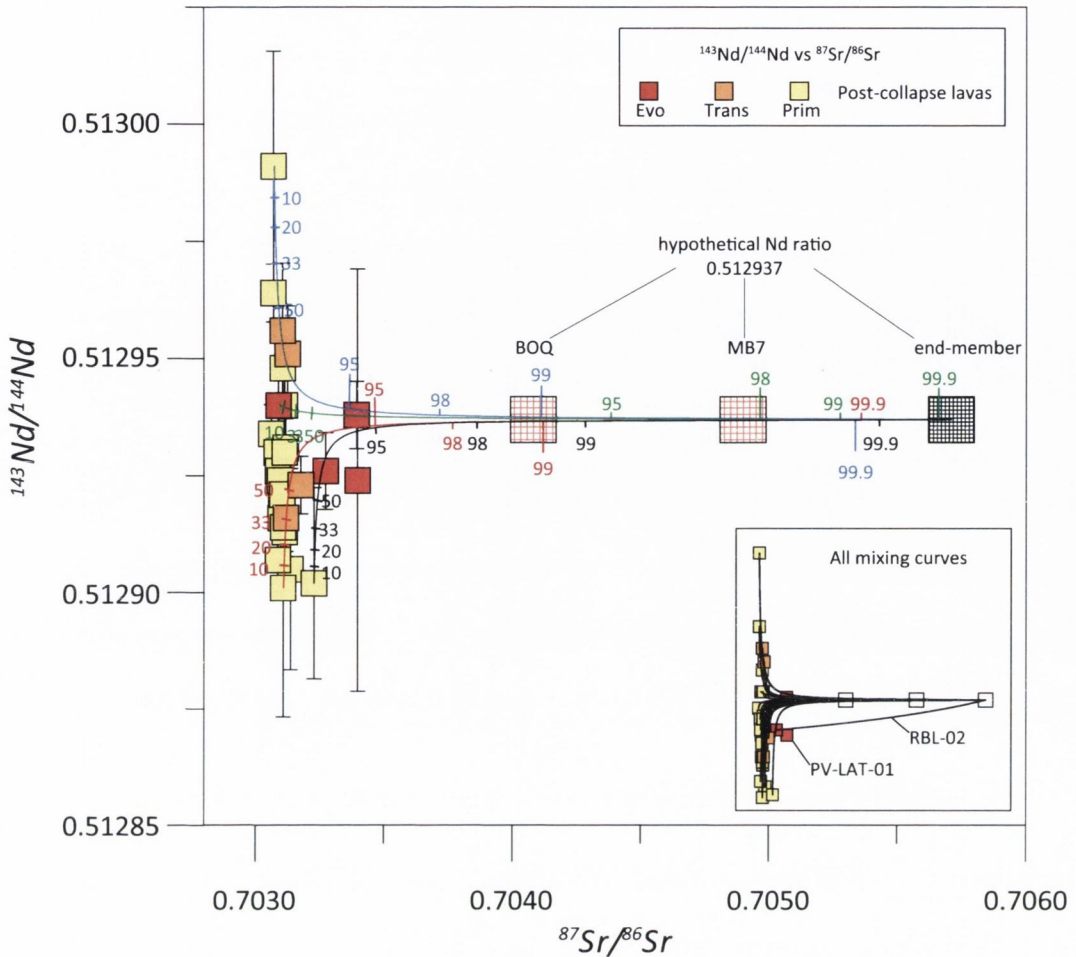
Fig. 4.12: ^{87}Sr/^{86}Sr versus ^{143}Nd/^{144}Nd of post-collapse lavas (<200 ka). A hypothetical contaminant has been constructed using the composition of the Granadilla ignimbrite sample with the highest ^{87}Sr/^{86}Sr ratio (Palacz & Wolff, 1989) combined with the arithmetic mean of the ^{143}Nd/^{144}Nd ratios of evolved lavas. Four representative mixing hyperbolas are presented between the hypothetical contaminant and three primitive lavas (curves: red, black and blue) and one evolved lava (green curve). Hyperbolas of all calculations are shown in the inset; for sample PV-LAT-01 there was no compositional data available. The curve between RBL-02 and the contaminat deviates from the general pattern observed. Instead of representing a suitable melt composition, this sample is better explained as mixture of more primitive magma and the contaminant. Numbers indicate percentage of hypothetical end-member involved in the mixture. Note: to successfully model the sample MB7 with the highest ^{87}Sr/^{86}Sr ratio, 97 to 99.5 % of end-member are required.

The two-component bulk mixing model mathematically describes the combined isotopic compositions of Sr and Nd in the final magma. Usually, this allows to detect if there is a genetic relationship in the systematics observed. However, it does not describe the real, physical process of differentiation, i.e. it is unlikely that the whole differentiation sequence represents a binary mixing system of a primitive magma and a highly differentiated contaminant. In the Canaries, primitive lavas that reached the surface show main crystallisation levels at Moho depths or slightly shallower at ~8km (e.g. Klügel et al., 2005; Galipp et al., 2006; Longpré et al., 2008; Stroncik et al., 2009). This type of lavas

is commonly interpreted to ascend swiftly from these depths, exploiting the pathways provided by dyke complexes that exist at depth within the rift zones. Most likely, the primitive lavas differentiated to intermediate levels, rather unaffected by this particular highly differentiated contaminant.

In the transitional lavas, a significantly narrower range of ^{143}Nd/^{144}Nd ratios can be observed, an indication that a contaminant with a distinct Nd isotope composition has been incorporated to significant amounts. Magma mixing and/or assimilation is therefore an important process during the formation of transitional lavas, as has been demonstrated in Chapter 2 in the case of the transitional lava of Montaña Reventada.

The same holds true for the evolved lavas, where an even narrower range of ^{143}Nd/^{144}Nd ratios is observed, along with extremely variable ^{87}Sr/^{86}Sr ratios. Using primitive lavas as melt composition yields at least 77% of contamination in all evolved lavas. When using the evolved lava PT-LAE-02 as melt composition, between 60 and 97.8% of contaminant are necessary, depending on the ^{87}Sr/^{86}Sr ratio of the sample that is being modelled (Table 4.5). It is of interest that for the two evolved lavas with the highest ^{87}Sr/^{86}Sr ratio, BOQ and MB7, the calculated mixtures yield an end-member percentage of 92.4 and 97.8%, i.e. the magma that gave rise to these two lavas appears to have consisted dominantly of a re-melted, highly differentiated country rock. All lavas from this study have been tested as magmatic end-member, yet, this high percentage of contaminant is observed at melt compositions down to 117 ppm of Sr (PT-LAE-02). The results were tested, using an artificially high ^{87}Sr/^{86}Sr ratio of 0.708 in the contaminant (never observed in Tenerife), but even then remain at 83.4% (BOQ) and 92.1% (MB7), i.e. a largely dominant influence of highly differentiated contaminant in these two samples.

Table 4.5: Results of isotope mixing calculations

Melt	Rocktype	Sr [ppm]	$^{87}Sr/^{86}Sr$	Nd [ppm]	$^{143}Nd/^{144}Nd$	End-member 1 [%] MB7	BOQ	End-member 2 [%] MB7	BOQ
MB7	Evolved	8.22	0.7049	56.84	0.512937	0	n/a	0	n/a
BOQ	Evolved	3.3	0.704083	55.3	0.512937	36	0	12.9	0
RBL-02	Evolved	3.8	0.703275	57.4	0.512926	56.5	24.5	25.3	11.8
CAB	Evolved	34.2	0.703395	44.1	0.512938	91.5	71	73.8	51
PT-LAE-02	Evolved	117	0.703091	50	0.51294	97.8	92.4	92.1	83.4
COR-04	Transitional	864.3	0.703127	57.88	0.512951	99.69	98.86	98.83	97.3
CUE-14	Transitional	767.1	0.70312	58.48	0.512916	99.65	98.72	98.68	96.95
LEN-15	Transitional	323.1	0.703107	49.22	0.512956	99.18	97.07	96.95	93.2
PT-INE2	Transitional	528	0.703178	49.1	0.512923	99.48	98.03	98.04	95.4
ARA-01	Primitive	875.1	0.703101	48	0.512921	99.7	98.9	98.86	97.39
ARE	Primitive	795.8	0.703116	51.67	0.51294	99.67	98.7	98.73	97.1
BAN	Primitive	871	0.703138	45.3	0.512905	99.68	98.85	98.83	97.28
BIL-34	Primitive	910.5	0.703072	48.84	0.512991	99.73	98.97	98.92	97.57
CA1-23	Primitive	861.4	0.703099	48.02	0.512916	99.7	98.9	98.84	97.35
CA2-20	Primitive	1124	0.703063	69.74	0.512934	99.77	99.18	99.13	98.03
CA3-24	Primitive	879.1	0.703115	48.45	0.512913	99.7	98.9	98.85	97.37
CAN-06	Primitive	1101	0.703109	68.55	0.512914	99.76	99.13	99.09	97.9
CHA-03	Primitive	1026	0.703119	66.78	0.512931	99.74	99.05	99.02	97.72
CHI-01	Primitive	1079	0.703083	56.52	0.51293	99.76	99.12	99.08	97.92
EST-40	Primitive	717.9	0.703109	44.68	0.512901	99.63	98.67	98.6	96.82
PV-EVO-05	Primitive	1031	0.703096	63.2	0.512924	99.75	99.07	99.03	97.8
REV bas	Primitive	1112	0.703105	68.51	0.512921	99.76	99.13	99.1	97.95
BOT-28	Primitive	1116	0.703088	74.72	0.512907	99.76	99.14	99.11	97.96
CIO	Primitive	1011	0.703088	68.8	0.512926	99.76	99.13	99.1	97.95
CRU-39	Primitive	1205	0.703071	67.54	0.512964	99.78	99.24	99.18	98.15
MAR	Primitive	939.9	0.703108	67.14	0.512948	99.72	98.96	98.93	97.57
PV-EAR	Primitive	1057	0.703229	60.4	0.512902	99.73	98.95	98.98	97.51
PV-INT	Primitive	1041	0.703115	69.4	0.51293	99.74	99.06	99.03	97.77

Contaminants

End-member 1		5.89	0.70571	53	0.512937	Granadilla ign., adjusted $^{143}Nd/^{144}Nd$			
End-member 2		5.89	0.708	53	0.512937	Artifically high $^{87}Sr/^{86}Sr$			

Table 4.5.: Results of modelling, using Sr and Nd isotope ratios to calculate mixtures of post-Icod-collapse lavas (column "melt") and two hypothetical contaminants. In the results section to the right, the percentages of contaminant are given that are necessary to reproduce the two phonolite samples with high $^{87}Sr/^{86}Sr$, MB7 and BOQ. End-member 1 is the Granadilla ignimbrite, whose $^{143}Nd/^{144}Nd$ ratio has been adjusted to a higher value. End-member 2 uses an artificially high $^{87}Sr/^{86}Sr$ ratio, but does not yield significantly lower mixing percentages. When using transitional or primitive lavas as melt compositions, the amount of contaminant involved in the mixture stays usually stays above 97%. The evolved sample PT-LAE-02 shows a similar $^{87}Sr/^{86}Sr$ ratio to the primitive and transitional samples and yields 92.4 - 97.8% of the "realistic" end-member 1. The remaining evolved lavas RBL-02 and CAB yield lower percentages, but have higher $^{87}Sr/^{86}Sr$ ratios and are probably themselves strongly affected by contamination and are therefore unlikely to be a real melt end-member.

4.3. Trace element modelling

The whole-rock data of Rodríguez-Badiola et al. (2008) was applied in a two-component bulk mixing model to test if the mixing percentages derived for melt-contaminant combinations in isotope modelling are consistent with the incompatible trace element concentrations in these samples. As contaminant, we used the trace element data on the highly differentiated rocks from the Diego Hernández Formation, the last major magmatic cycle of the central Las Cañadas succession prior to the Icod collapse and the construction of Teide (Wolff et al., 2000). In addition to the data on whole-rock samples of

this formation, Wolff et al. (2000) reported abundant nepheline syenite blocks, both fresh and hydrothermally altered, contained within these ignimbrites, which they included in their list of analyses. In the following discussion, these trace element data are applied to test if highly differentiated rocks (fresh or altered) of similar trace element composition to the ones found in the Diego Hernández Formation can serve as contaminant in mixing calculations that use the percentages derived from the isotope modelling in this study.

The following parameters were used for the two-component bulk trace element modelling: the four end-member compositions BIL-34, EST-40, PV-EAR and PT-LAE-02 of post-Icod-collapse lavas that have been used for the four mixing hyperbolas in Fig. 4.12. Of these, BIL-34, EST-40 and PV-EAR have a primitive composition, while PT-LAE-02 possesses an evolved character. Each of these four curves yields a certain mixture for a given target isotopic composition. To reproduce the samples BOQ and MB7 that show the highest $^{87}Sr/^{86}Sr$ ratios, we used eight percentages, ranging from 92.25 to 99.73%, in order to test if the trace element compositions of these samples can be modelled by mixing of primitive lavas and a highly differentiated contaminant. Each combination of these four end-member compositions and eight percentages were then mixed with the trace element data of 25 samples from Wolff et al. (2000).

These 25 Diego Hernández whole-rock samples are both, depleted and enriched in most trace elements compared to the Teide evolved lavas, with the exception of Ba and Sr that are equal or more enriched in the Diego Hernández samples. Nepheline syenite blocks found within the Abrigo member of the Diego Hernández formation have been interpreted to be co-genetic with the erupted Diego Hernández pumice, based on whole-rock and mineral chemistry, with the intrusive nepheline syenite blocks representing a higher overall degree of differentiation (Wolff, 1987; Wolff et al., 2000). Fresh nepheline syenite is overall more enriched than the Teide evolved lavas, but shows less pronounced Ba and Sr anomalies. Altered nepheline syenite is mostly similar to the Diego Hernández samples apart from higher concentrations in U, Th, Zr and Hf. Barium is less enriched than in the Teide evolved lavas, while the Sr anomaly appears of similar magnitude (Fig. 4.13b).

According to the values derived from isotope modelling, there are high percentages of differentiated end-member rock involved in these mixtures. The modelled trace element mixtures are a "spitting image" of the trace element signatures of the nepheline syenite blocks and their host rock, the Diego Hernández Formation (Fig. 4.13c). These results produce a considerable overlap with the evolved lavas, indicating that the percentages derived from isotope modelling can sufficiently explain the origin of the most extreme $^{87}Sr/^{86}Sr$ lavas (n=2) by a mixture that dominantly consists of a highly differentiated end-member, similar to the Diego Hernández Formation, with variable contents of juvenile material (Fig. 4.13d).

a) The evolved lavas

All data normalised to the minimum
concentrations of the evolved lavas

Cs Ba U Ta Ce Pb Sr Zr Eu Tb Y Er Lu
Rb Th Nb La Pr Nd Sm Hf Gd Dy Ho Yb

b) Diego Hernández Formation and
nepheline syenites

Fresh nepheline syenite
Altered nepheline syenite
Diego Hernandez Formation whole-rock

Cs Ba U Ta Ce Pb Sr Zr Eu Tb Y Er Lu
Rb Th Nb La Pr Nd Sm Hf Gd Dy Ho Yb

c) Mixtures of trace elements
based on isotope modelling

Cs Ba U Ta Ce Pb Sr Zr Eu Tb Y Er Lu
Rb Th Nb La Pr Nd Sm Hf Gd Dy Ho Yb

d) Overlap of evolved lavas and modelled
compositions

Cs Ba U Ta Ce Pb Sr Zr Eu Tb Y Er Lu
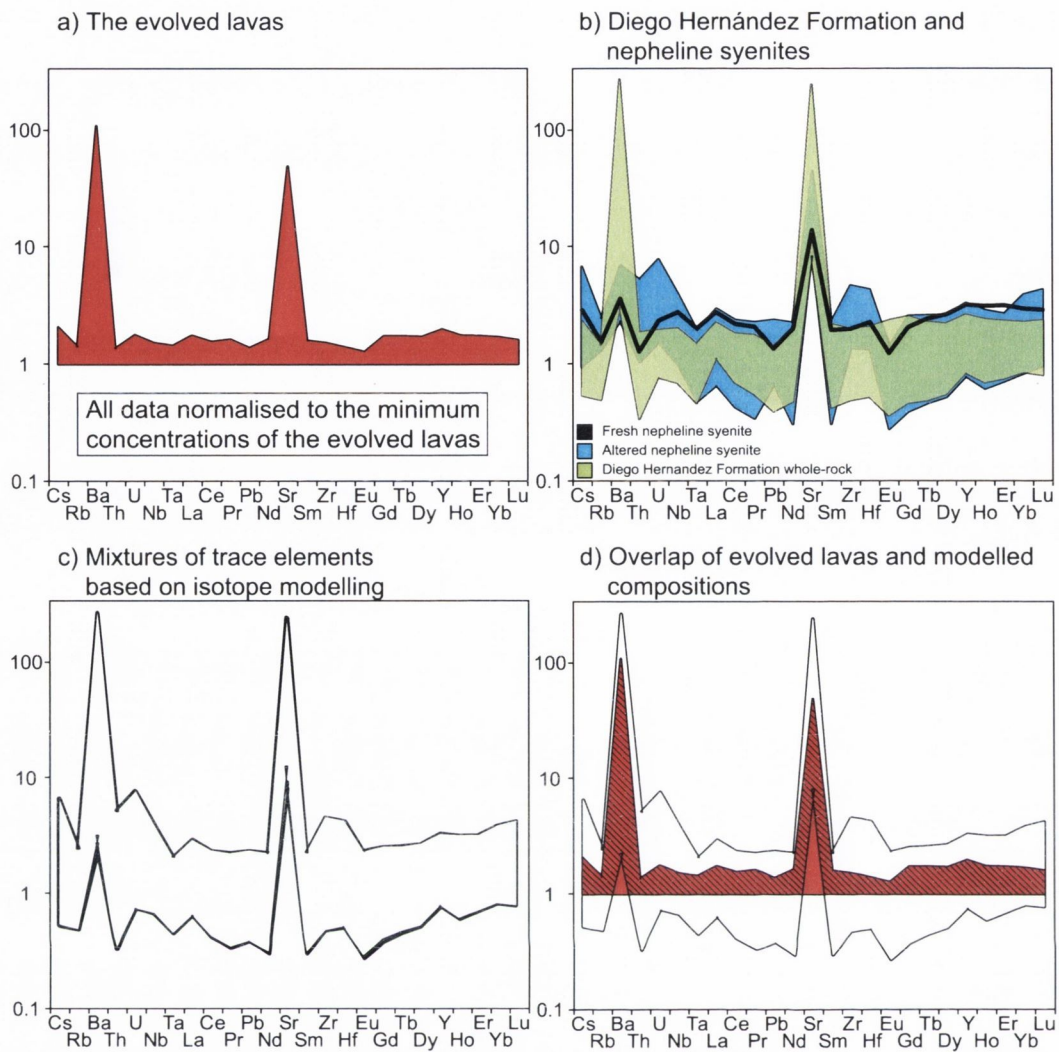Rb Th Nb La Pr Nd Sm Hf Gd Dy Ho Yb

Fig. 4.13: Results of trace element modelling, using the mixing percentages derived from isotope modelling. All data are normalised to the minimum concentrations of the evolved lavas. a) The evolved lavas for reference. Normal trace element enrichment among samples between factor 2 and 3, Ba and Sr can be enriched up to factor 100. b) Trace element data from Wolff et al. (2000) on the Diego Hernández Formation whole-rock samples and the nepheline syenite xenoliths (green and black) contained in this formation. c) Mixtures have been calculated for the samples BOQ and MB7 (the samples with the highest $^{87}Sr/^{86}Sr$ ratios), using the percentages derived from the isotope modelling in Fig. 2.15 and the Diego Hernández Formation whole-rock samples and its nepheline syenite xenoliths as contaminant. The resulting four fields are indistinguishable from each other due to the high percentages of highly differentiated rock involved. d) The overlap between the Teide evolved lavas and the modelling results are consistent with the trace element concentrations of the evolved lavas indicating a high percentage of differentiated country rock that has been melted.

Can the contaminant be a partial melt of the country rock?

Batch melting of Diego Hernández Formation rock compositions was calculated to constrain if a partial melt of these rocks can represent a contaminant in the two-component bulk mixing model. Batch partial melts of varying degrees were then mathematically "mixed" with the same melt compositions as in the previous two-component bulk mixing models. Bulk K_d values have been calculated using partition coefficients from comparable

rocks (Larsen, 1979; Wörner et al, 1983; Nash and Crecraft, 1985; Ewart & Griffin, 1994; Stimac & Hickmott, 1994; Marks et al., 2004) and modal abundances from Tenerife ignimbrites (Wolff, 1987).

Small variations in the compatibility of REE allow distinguishing the influence of partial melting, as the generally less compatible LREE tend to move into the melt phase preferentially when a rock is partially melted. In a plot of Gd/Yb versus La/Sm, this is expressed by higher La/Sm and Gd/Yb ratios for lower degrees of melt fraction.

When bulk melts of rocks from the Diego Hernández Formation (DHF) are mixed with melt compositions from the post-Icod-collapse succession, three DHF samples allow to reproduce the evolved lava compositions (Fig. 4.14). In turn, when using partial melts of DHF as contaminant, the mixing model fails to reproduce Teide-Pico Viejo phonolites below a melt fraction of F=0.95. In the two-component bulk mixing model, bulk crustal melts of Diego Hernández Formation country rock are therefore needed to successfully model the compositions of the most extreme evolved Teide lavas.
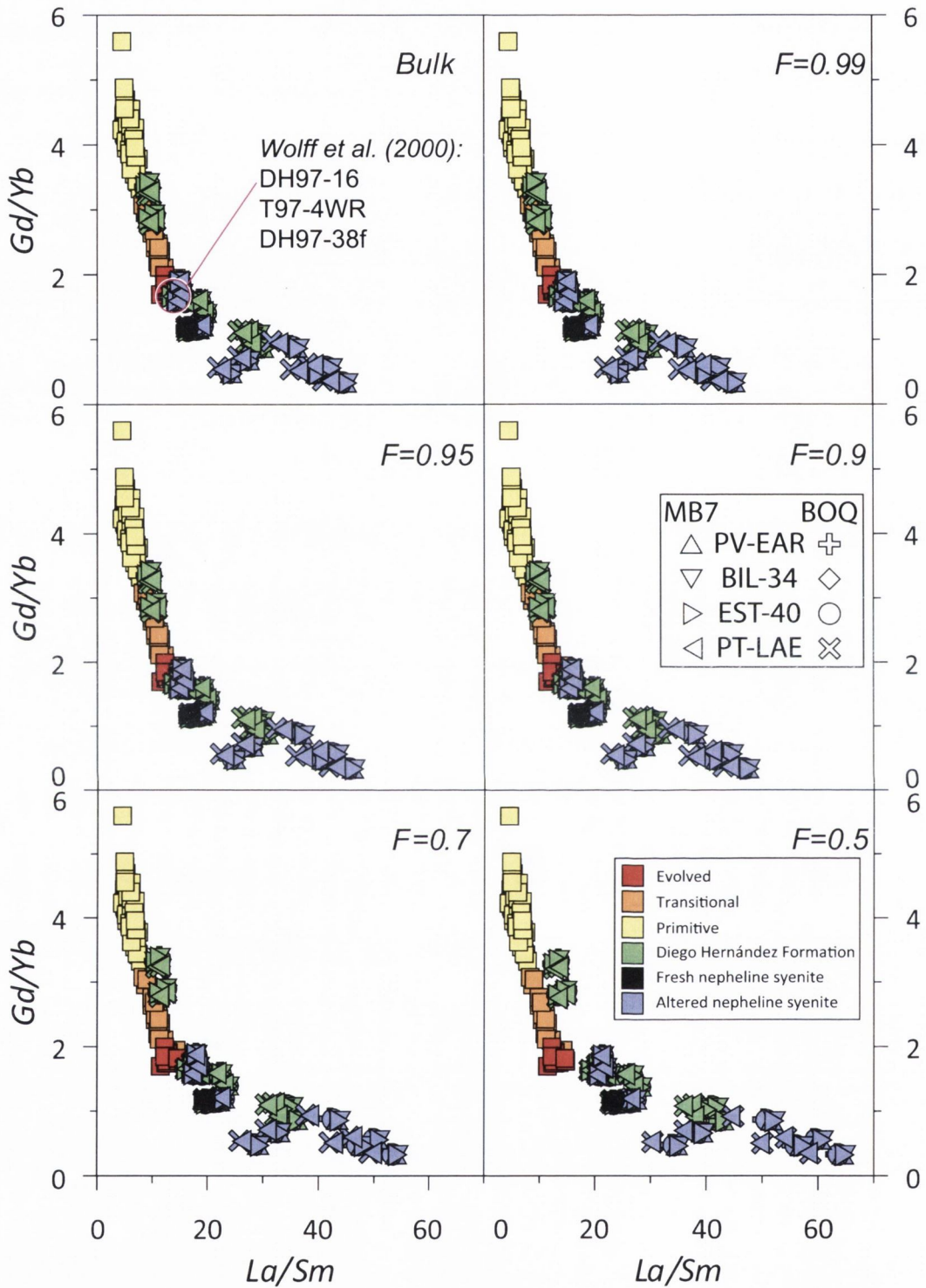
Fig. 4.14: Mixtures of four representative post-Icod-collapse lavas and 29 batch partial melts of Diego Hernán-
dez Formation whole-rock compositions (Wolff et al., 2000) to reproduce the two evolved samples BOQ and
MB7. Degree of partial melt given in right hand, upper corner of each graph. The Diego Hernández Formation
whole-rock samples are used as contaminants in green squares, the nepheline syenite xenoliths contained in this
formation in blue and black squares. The two-component mixing model works best, when using bulk melts of
the DHF samples that are indicated by the circle in the upper left hand. Lower degrees of partial melting (<0.95)
shift the resulting mixtures towards higher La/Sm ratios, offset from the measured compositions of the evolved
lavas.

4.4. Oxygen isotopes

The non-equilibrium state of the majority of feldspar-groundmass pairs indicates that either the feldspars analysed are mainly xenocrysts and bear no direct genetic relationship with the magma they are found in. Alternatively, a change in $\delta^{18}O$ ratio has occurred within these magmas after feldspar crystallisation, possibly upon or just prior to eruption and dependent on the type of country rock assimilated during eruption. A hydrothermally altered, low-$\delta^{18}O$ country rock (e.g. Hansteen & Troll, 2003) or meteoric waters from shallow level aquifers would, when assimilated during ascent of the magma, lower the $\delta^{18}O$ ratio of a magma whereas the uptake of a low-temperature altered country rock (cf. Donoghue et al., 2008) or magmatic water (Taylor, 1986) rises the oxygen isotope ratio.

It needs to be mentioned, though, that groundmass also tends to be prone to post-eruptive alteration due to its finer-crystalline structure compared to phenocrysts. Therefore, the influence of secondary alteration may be more pronounced (cf. Cousens et al., 1993), rendering the feldspar data as potentially more reliable.

The feldspar hosted in primitive lavas range from just below the MORB array (Taylor & Sheppard, 1986) up to 6 ‰ and form a linear increasing trend for $\delta^{18}O$ with decreasing MgO concentrations. One feldspar sample plots outside this trend (LAJ-24, Montaña Las Lajas) (Fig. 4.15).

In a contrasting scenario, Nicholson et al. (1991) found a *decrease* in $\delta^{18}O$ with MgO for the Krafla volcanic complex (Iceland) and interpret this as result of assimilation of partial melts of hydrothermally altered (low $\delta^{18}O$) country rock. In Tenerife, Wolff et al. (2000) determined a component of assimilated island core in the pre-Las Cañadas-collapse Diego Hernández Formation, and furthermore detected a low $\delta^{18}O$ component. Such a low $\delta^{18}O$ component is indiscernible within our sample suite, however, the possibility remains that a low $\delta^{18}O$ contaminant had an influence that is now masked.

The $\delta^{18}O$ ratios in feldspar crystals from the post-Icod-collapse succession therefore indicate a "magmatic" origin for this sequence. Potentially some minor influence of hydrothermally altered material is present, but indistinguishable with the available data. One outlying feldspar at a low MgO concentration may represent a xenocryst, as its $\delta^{18}O$
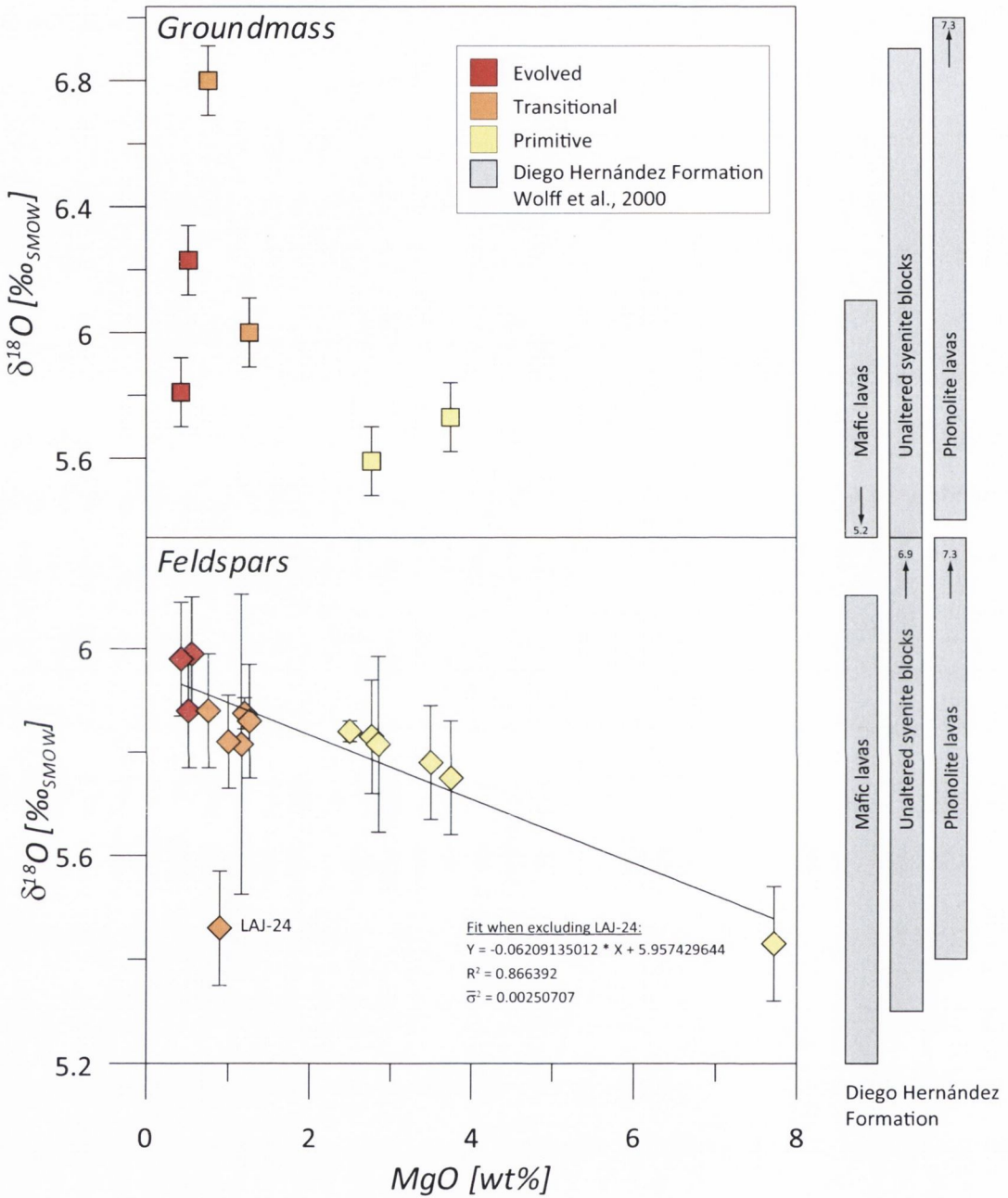
value is within the total range observed.

Fig. 4.15: Oxygen isotope ratios versus whole-rock MgO. Square symbols are groundmass, diamonds represent feldspars. Feldspar values increase with decreasing MgO, except for the altered outlier LAJ-24. Grey bars are data from Wolff et al. (2000) from the Diego Hernández Formation deposits. Continuous rise of feldspar data indicates a magmatic origin. Note overlap with the Diego Hernández deposits.

According to the results obtained from trace element modelling, the evolved rocks of the Diego Hernández Formation may be similar to the highly differentiated country rock that had been assimilated during formation of the evolved magma. As the data on the Diego Hernández Formation of Wolff et al. (2000) are the only existing oxygen data on

differentiated rocks in Tenerife, they are worth to be compared to the $\delta^{18}O$ ratios from this study. The $\delta^{18}O$ ratios from the differentiated rocks and the fresh nepheline syenite blocks contained within the Diego Hernández Formation overlap the values found for the post-Icod-collapse succession completely (Fig. 4.15). Such a type of rock, if assimilated to large degrees, can reproduce $\delta^{18}O$ ratios in the resulting magma that are still of "magmatic" origin.

Although the Diego Hernández rocks themselves may not be the true or complete end-member(s) to the evolved Teide lavas, they show that highly differentiated country rock exists and may contain comparable $\delta^{18}O$ signatures. When country rock and juvenile material bear a similar $\delta^{18}O$ value, any mixture of melted country rock with juvenile material will be indistinguishable on grounds of oxygen data from purely juvenile magma that evolved in a closed-system.

4.5. Whole-rock data

Statistical analysis of 80 whole-rock samples indicates that, for each of the three compositional groups, a distinct combination of differentiation processes is at work. In the primitive lavas, it is suggested that the larger $\bar{\sigma}^2$ values, that yield a less well-defined trend, stem from polybaric fractional crystallisation of varying amounts of phases such as olivine and clinopyroxene (based on the MgO data), or of a single phase of changing composition (solid solution plagioclase for Al_2O_3 or olivine for MgO) and the onset of fractionation at slightly more evolved compositions (e.g. apatite for P_2O_5). Fe_2O_3 may not reflect these trends due to ongoing magnetite or ilmenite fractionation when entering the transitional regime. TiO_2 and Na_2O trends are not significantly different to those of the transitional group, and may suggest similar processes at work for both groups with respect to these elements. In contrast, the differing, but internally consistent, behaviour of the evolved group is an indication of a separate set of processes. The evolved lavas define very tight and sub-horizontal trends (Fig. 4.6), when compared to the classic liquid-line-of-descent trends of the primitive lavas and the discontinuous and scattered trends of the transitional lavas. This is corroborated statistically through the significantly tighter fit of

the evolved lavas, compared to the primitive lavas in all but Na_2O and MnO, and to the transitional group in all major elements.

These results compare well with the patterns produced in the TAS diagram. In this diagram, the primitive lavas appear to trend towards a single focal point at about 53 wt.% SiO_2. Assuming a similar composition for all juvenile material, which needs to pass through a similar decrease of pressure conditions, thereby inducing crystallisation, this may indicate a pre-dominance of fractional crystallisation as differentiation process (Fig. 4.16). The paucity of samples in-between 53 and 57 wt.% SiO_2 is consistent with a Bunsen-Daly gap scenario. The pattern that the transitional lavas produce then widens with increasing SiO_2 concentration, which may indicate the introduction of magma mixing as important differentiation process. Finally, the evolved lavas plot at a steep angle to the trend normally defined by a continuous fractional crystallisation sequence in a TAS diagram. Traditionally, such trends are interpreted as partial melting being the pre-dominant influence to generate this pattern (cf. Mollo et al., 2010). Indeed, the evolved lavas overlay the field defined by rocks from the Diego Hernández Formation and the Granadilla ignimbrite, the type of highly differentiated rock that could be a potential end-member for the generation of the evolved lavas by partial or whole re-melting. The whole-rock data of Rodríguez-Badiola et al. (2008) are thus consistent with the formation of highly differentiated magmas by re-melting of country rock of broadly phonolitic composition.
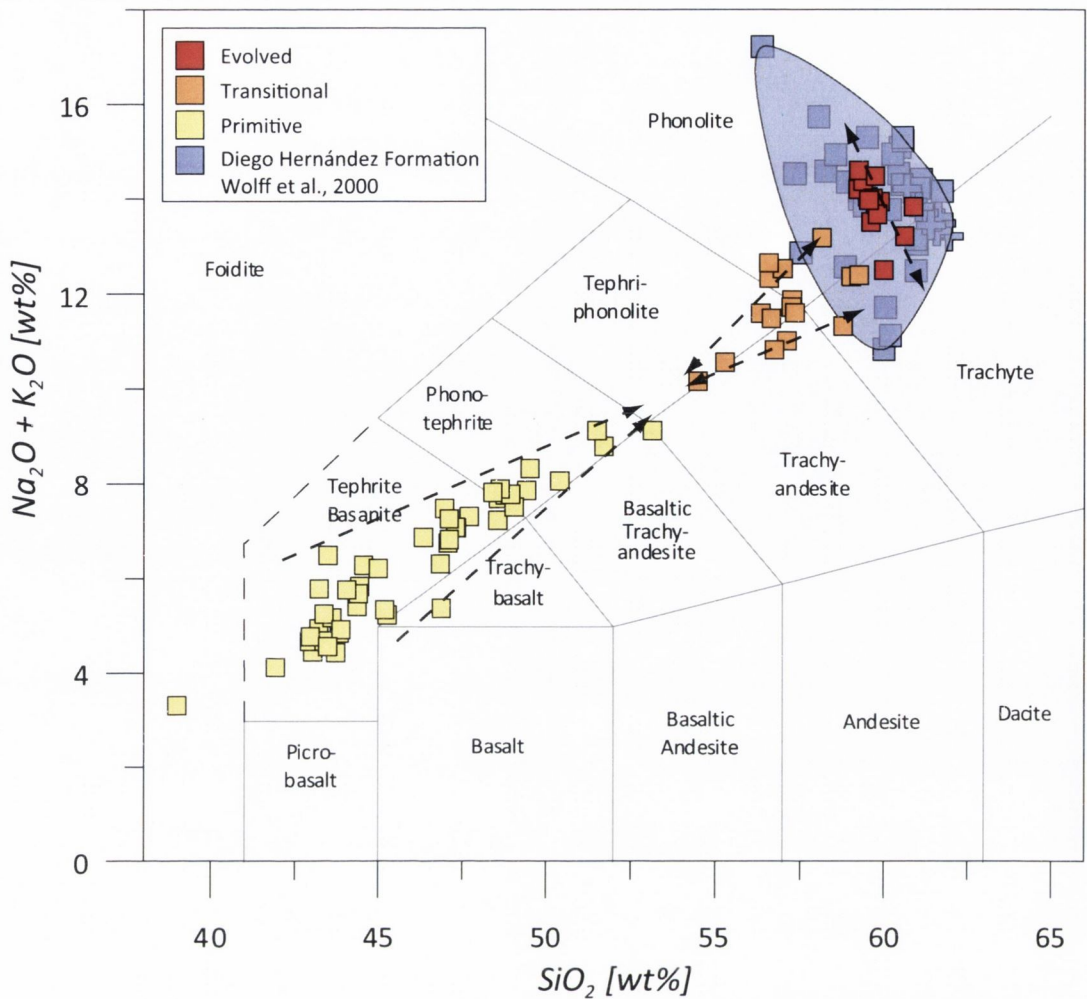
Fig. 4.16: Whole-rock data of the post-Icod-collapse succession compared to data from the Diego Hernández Formation (blue squares, Wolff et al., 2000) and the Granadilla ignimbrite (blue crosses, Palacz & Wolff, 1989). The primitive lavas define a narrowing pattern with differentiation, as if being distilled to a focal point by undergoing broadly similar P-T conditions during ascent. The pattern of transitional lavas widens again, indicating the increased importance of magma mixing at higher differentiation levels. The evolved lavas overlay the highly differentiated rocks from the Las Cañadas succession (blue) and define a sub-vertical trend resembling partial melting trends.

4.6. AFC modelling

Because the isotope data point towards an open system for the post-Icod-collapse succession, a contaminant (or a combination of several end-members that together yield an average composition) was needed that was "mixed" into various melt compositions. The model derived therefore mathematically represents a two-component bulk mixing model.

However, the model of two-component bulk mixing describes the end-result of magmatic differentiation, but not the very process how distinct combinations of trace element concentrations came to be.

To shed further light on the combination of differentiation processes at work, we attempted AFC modelling after DePaolo (1981) using the spreadsheet from Ersoy &

151

Helvaci (2009). In this spreadsheet, three sets of partition coefficients are available for "basic" (mafic), "intermediate" and "acidic" (felsic) magma compositions. To account for varying partition coefficients when moving within a differentiation sequence from mafic to felsic compositions, we modelled assimilation & fractional crystallisation within three compositional groups: *(i)* from the most primitive composition to a composition located at the tephrite/phonotephrite border in the TAS diagram, *(ii)* from the tephrite/phonotephrite border to the tephriphonolite/phonolite border, *(iii)* and from the tephriphonolite/phonolite to the highest differentiated composition observed.

A compilation of the relevant parameters used in the AFC modelling can be found in Table 4.6.

Table 4.6: AFC modelling parameters

	Mafic	Intermediate	Felsic
Parent	NEG/GAR-04	SAM/VON/TOM/RAT	CUE-15/LAJ-24/MON/REVtph
Daughter	SAM/VON/TOM/RAT	CUE-15/LAJ-24/MON	-
Contaminant	DH97-38f	T97-3WR	T97-4WR
r-value	0.1	0.4	0.9
F [%]	0.55	0.64	0.91
Olivine	41.9	-	-
Clinopyroxene	35.6	26.8	5.7
Plagioclase	6.9	29.1	-
K-feldspar	-	24.3	70.8
Magnetite	5.0	15.0	5.7
Ilmenite	6.8	-	-
Apatite	3.8	4.7	1.7
Biotite	-	-	15.1
Sphene	-	0.1	0.2
Amphibole	-	-	1.0

Table 4.6.: Best fit parameters obtained from AFC modelling. Several combinations of parent and daughter compositions are needed to cover the variability of compositions in the post-Icod-collapse succession. Contaminants are are from the Diego Hernández Formation (Wolff et al., 2000). The F value describes the fraction of melt remaining. Note increasing values for both, F and r-values, for higher differentiated rocks, indicating an increasing importance of assimilation.

Endmember: Throughout the differentiation sequence in the post-Icod-collapse succession, MREE are fractionated or LREE and HREE are enriched, which results in increasing La/Sm and decreasing Gd/Yb ratios. Pure fractional crystallisation is able to reproduce this pattern only up to intermediate rock compositions and with crystallisation of 99%. The REE systematics therefore require a contaminant that has a high La/Sm and a low Gd/Yb ratio. The Diego Hernández Formation rocks fulfill these requirements and have the additional advantage of being relatively variable in Sr and Ba throughout the succession, which was necessary to successfully model the post-Icod-collapse differentiation sequence. Several rock compositions from this sequence were used to model each compositional group.

Partition coefficients: To compensate for TiO_2 fractionation into ilmenite an arbitrary partition coefficient of 15 has been used for Ti. The K_d values from Watson & Green (1981) have been used for REE partitioning into apatite within a primitive alkaline melt. The compilation of partition coefficients in the "acidic" regime that is provided by Ersoy & Helvaci (2009) is best-suited for sub-alkaline, high-silica rocks many times, but not for the alkaline series of this study. For intermediate and felsic compositions, the partition coefficents from Wörner et al. (1983) were used and, when needed, complemented by published values on the alkaline series, taken from the GERM partition coefficient database (http://earthref.org/). Please see the FC-AFC-FCA spreadsheets in the electronic appendix for detailed references of partition coefficients.

Mafic: In the mafic group, fractional crystallisation of 45% and an r-value of 0.1 allow to model the variations observed within this group convincingly. The low percentage used for plagioclase fractionation is in accordance with the observed mineral abundances in this group of lavas and accounts for the increasing Sr and Ba concentrations with increasing differentiation. The Ba concentrations of the lavas Tierra del Trigo (TRI), Montaña de Taco (TAC) and Volcán de los Silos (SIL) are not reproduced by the AFC model. As these three lavas are located next to each other at a coastal platform in Teno in Northwestern Tenerife, it seems likely that interaction with seawater may have altered the Ba composition in the lavas themselves or in the contaminant that was involved. The REE patterns observed within this group are reproduced. The near constant $^{87}Sr/^{86}Sr$ ratios in this group are shown to be not affected by low degree assimilation of a high $^{87}Sr/^{86}Sr$ contaminant with low Sr concentration. Fractional crystallisation can thus be deemed the dominant process of magmatic differentiation within the mafic group. Slight amounts of assimilation may or may not occur (Fig. 4.17).
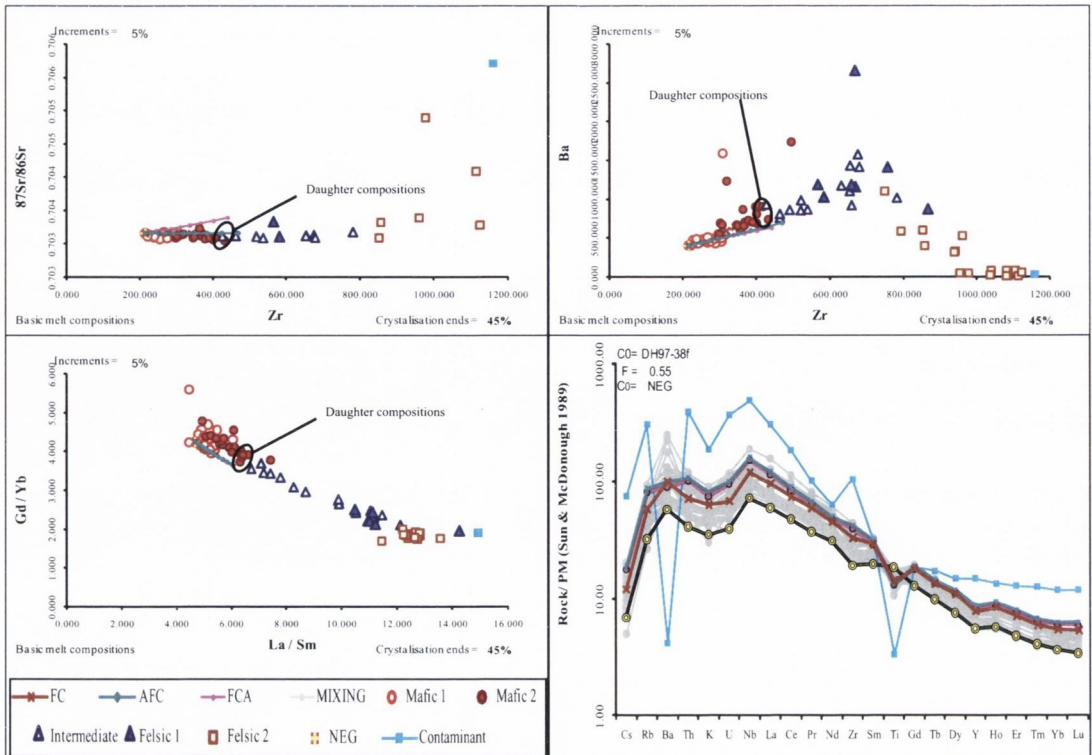
Fig. 4.17: Representative graphs of AFC modelling of mafic lavas. The names of sample groups Mafic 1, Mafic 2, Felsic 1 and Felsic 2 are due to the structure of the spreadsheet and bear no deeper meaning. The partition coefficient compilation for "basic" (mafic) melt compositions was used. Modelling increments are 5%. Contaminant compositions were taken from Wolff et al. (2000). FC, AFC and FCA differentiation models explain the variations observed.

Intermediate: Successfully modelling the transitional lavas proved more difficult. A less evolved contaminant of high Ba concentration was required (sample T97-3WR). However, with this contaminant, Pb, Ta and Nb were not reproduced convincingly and it is thus likely that another contaminant or multiple contaminants were involved to form this type of magma. Fractional crystallisation of 36% and an r-value of 0.4 provide the best fit for the majority of elements, and allow to model the slight Sr isotope variations by FCA (Fig. 4.18).
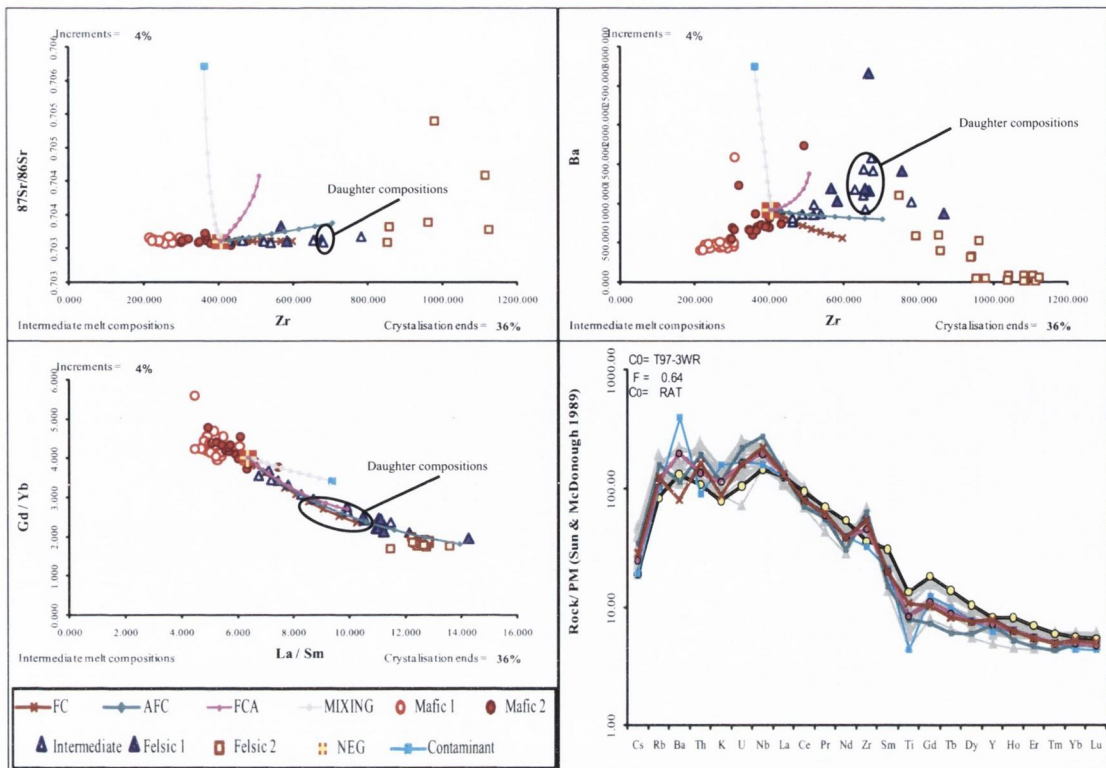
Fig. 4.18: Representative graphs of AFC modelling of intermediate lavas. The names of sample groups Mafic 1, Mafic 2, Felsic 1 and Felsic 2 are due to the structure of the spreadsheet and bear no deeper meaning. The partition coefficient compilation for intermediate melt compositions was used. Modelling increments are 4%. Contaminant compositions were taken from Wolff et al. (2000). Multiple parent-daughter combinations are necessary to cover the whole range of intermediate compositions. The AFC differentiation model explains the variations observed in incompatible trace elements best.

Felsic: A large variability in starting compositions characterises the AFC model of the felsic group. Combinations of low r-value and high degree of fractional crystallisation are possible for the remaining felsic samples, but exclude the sample MB7 that possesses the highest $^{87}Sr/^{86}Sr$ ratio from the model. This samples' highly variable Sr isotope ratios in the felsic lavas therefore dictate values for fractional crystallisation and r-value of 9% and 0.8, respectively, for a successful AFC model. More extreme combinations of r-value and F could not be tested due to the structure of the spreadsheet downloaded.

The incompatible trace element variations can be reproduced, albeit not for all elements. Selecting among several parent compositions was the most efficient way to account for the varying trace element concentrations in the felsic lavas that often cannot be reproduced by a single trend.

No single mathematical model of differentiation explains all variations sufficiently. The Sr isotope ratios require assimilation to play a role, for which reason closed system fractional crystallisation can be excluded in this sequence. The data on felsic lavas can be explained best by AFC, FCA, magma mixing and/or combinations between these (Fig. 4.19).
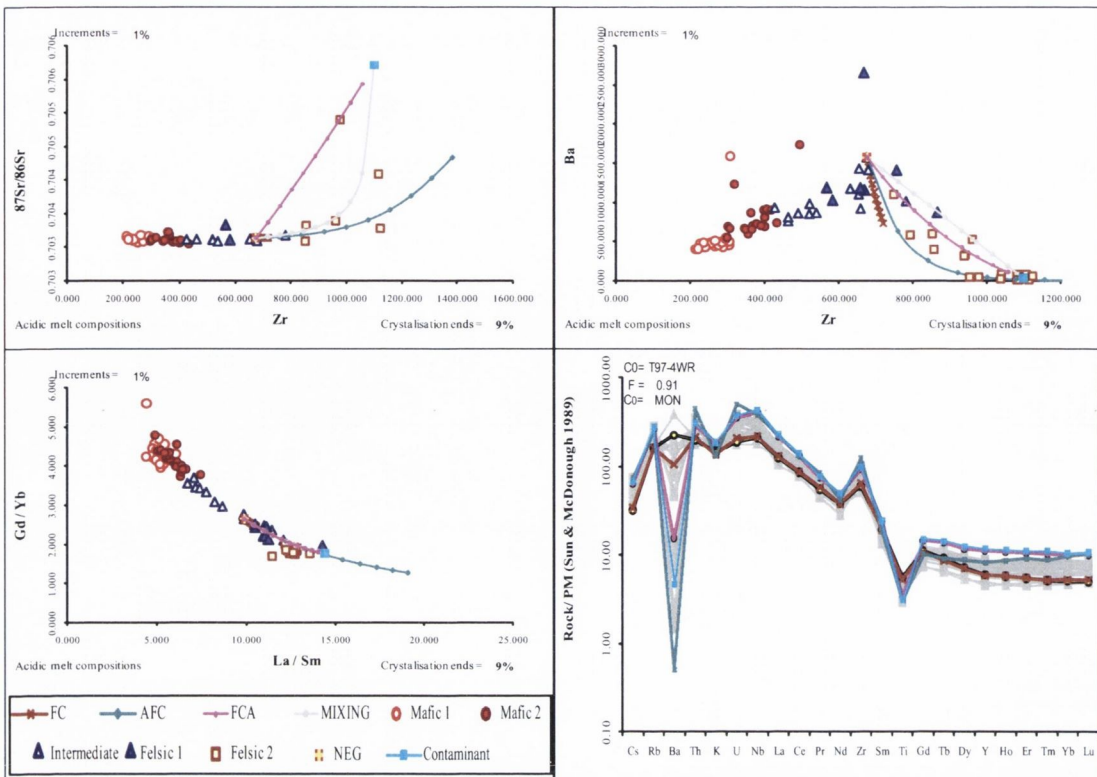
155

Fig. 4.19: Representative graphs of AFC modelling of felsic lavas. The names of sample groups Mafic 1, Mafic 2, Felsic 1 and Felsic 2 are due to the structure of the spreadsheet and bear no deeper meaning. The partition coefficient compilation for "acidic" (felsic) melt compositions was used. Modelling increments are 1%. Contaminant compositions were taken from Wolff et al. (2000). The Sr isotope ratio of Sample MB7 can only be explained by ;ow fractional crystallisation and a comparatively high r-value of 0.9. Multiple parent-daughter combinations are necessary to cover the whole range of felsic trace element compositions. AFC, FCA and magma mixing can explain the variations observed in incompatible trace elements.

The AFC model after DePaolo (1981) offers a wealth of combinations of starting compositions and contaminants when dealing with the complete series of differentiation of the Teide-Pico Viejo complex and the adjacent rift zones. The observed F and r-values model the sequence to a reasonable good degree, however, varying parent and contaminant compositions, along with combinations of differentiation processes (FC, AFC, FCA or magma mixing), are needed to fully explain all variations in incompatible trace elements. This, however, has to be expected within a regionally extensive succession and is a consequence of dealing with a natural system that may not be easily modelled with a single, mathematical solution.

Another characteristic of the AFC model is that it describes the combined effects of wall-rock assimilation and fractional crystallisation within a *single* magma chamber. By design, this model fails therefore, when envisaging a formation of crustal melts by heat transfer alone, i.e. when direct physical contact between parent magma (heat source) and daughter (crustal melt) does not occur (spatial decoupling). The two-component bulk

mixing model, in turn, convincingly explains the most extreme phonolites (n=2) as largely crustal melts, consistent with major and trace element and radiogenic and stable isotope data. Although a scenario of spatial decoupling of crustal melts cannot be reproduced by an AFC model, the r-values increase with increasing degree of differentiation of magma. This may indicate that crustal melting becomes increasingly significant in higher differentiated rocks in the post-Icod-collapse succession. Nevertheless, AFC modelling underlines the importance of fractional crystallisation for the bulk of the Teide-Pico Viejo succession.

4.7. Potential end-members

Common crystallisation depths for highly differentiated volcanic deposits in Tenerife appear to range around sea level (Wellman, 1970; Wolff & Storey, 1983; Wolff, 1987; Ablay et al., 1998; Neumann et al., 1999; Andújar et al., 2008). At this depth level, assimilation of country rock potentially occurs to an increased degree compared to sites which are relatively swiftly passed by the magma during ascent. However, extrusive rocks (lavas, ignimbrites, etc.) may be uncommon at such depths after an intrusive history in Tenerife of at least 12 Myr (Guillou et al., 2004b). The assimilated end-member country rock is thus likely of intrusive character.

The Las Cañadas succession which directly underlies the Teide-Pico Viejo complex provides a wealth of highly differentiated compositions throughout its stratigraphy of more than 3 Myr. The Quarternary Diego Hernández Formation (the terminal stage of Las Cañadas Volcano, ~180 - 600 ka, Martí et al., 1990; Wolff et al., 2000; Edgar et al., 2007) has been determined, among others, to have erupted from the region of the present-day Las Cañadas Caldera (e.g. Ancochea et al., 1999, Bryan et al., 2000; Edgar et al., 2007). The intrusive remnants of the Las Cañadas Volcano feeder system are likely to rest underneath the present Teide-Pico Viejo complex and any ascending Teide-Pico Viejo magma will have to pass these intrusive remnants. Low melting points that range from 680 to 770°C for the Tenerife nepheline syenites (Wolff, 1987; Edgar et al., 2007) imply that these rocks are susceptible to being melted by juvenile material that may be 1100 to

1200°C hot. These highly differentiated intrusive rocks thus represent a key component for country rocks that are being remelted.

Primary formation of high Sr isotope ratios within an oceanic island

High $^{87}Sr/^{86}Sr$ ratios have been documented in Tenerife rocks and are thus available for assimilation (Palacz & Wolff, 1989). Therefore, the question of their primary formation is of peripheral importance to this study, and can indeed not be satisfactorily resolved, using the data presented here. However, it seems apt to briefly outline the several mechanisms that can serve to introduce elevated $^{87}Sr/^{86}Sr$ ratios into a volcanic edifice like Tenerife, whose source is thought to be of low $^{87}Sr/^{86}Sr$ composition (Simonsen et al. 2000).

Upon first time penetration of the oceanic crust, magma will have had to pass thick sedimentary sequences that possess elevated $^{87}Sr/^{86}Sr$ ratios (Hoernle et al., 1991). It is not unlikely that some of this high $^{87}Sr/^{86}Sr$ material was consumed during ascent. Subsequent hydrothermal circulation may have leached the oceanic crust further and transported high $^{87}Sr/^{86}Sr$ fluids upwards through the stratigraphy.

High Sr isotope ratios may also be produced in relatively old, highly evolved and low-Sr bodies of rock that contain phases with a high Rb/Sr ratio and thus strongly accelerated ingrowth of ^{87}Sr. For example, a mineral phase with a Rb/Sr ratio of 50 such as biotite would need less than 1 Ma to evolve from a $^{87}Sr/^{86}Sr$ of 0.7031 to 0.705. Such rocks maintain their low Sr concentration, while rapidly increasing their bulk $^{87}Sr/^{86}Sr$ (cf. Halliday et al., 1989; Christensen & DePaolo, 1993). Melting these rocks (and their constituent phases) to different degrees most likely introduces strong isotopic heterogeneities between the partial melt produced and the restite left behind (cf. Hammouda et al., 1996; Duffield & Ruiz, 1998; Knesel & Davidson, 2002; Troll et al., 2005).

Seawater contamination of freshly erupted lavas has been found to occur under magmatic conditions at Axial Seamount, being nearly instantaneous upon contact of the lava with seawater (Schiffman et al., 2010). The seawater's compositional signature can be traced within the rim of these samples to ~1cm depth. Such seawater contamination may introduce significant compositional heterogeneities during the submarine growth of an oceanic island. The rocks contaminated by seawater during the seamount stage are either

still present or have been reworked by subsequent magmatic activity (cf. Hansteen & Troll, 2003). However, in one form or another the elevated Sr signature of these rocks may be kept within the system and may as such serve to introduce higher $^{87}Sr/^{86}Sr$ ratios in later erupted lavas, increasingly reflected in those that have assimilated more wall-rock.

In all these potential mechanisms, the generation of highly radiogenic Sr isotope ratios would occur at crustal levels. Source variation may not be responsible for this. It seems instead plausible that elevated Sr isotope signatures in Tenerife originate from early sediment incorporation, seamount-seawater interaction, hydrothermal element remobilisation or radiogenic ingrowth of phases like biotite with high Rb/Sr ratios or combinations of these. These heterogeneities may have been introduced into the system a long time ago and may only come to bear in rocks of low Sr concentration in which this elevated Sr isotope ratio cannot be diluted easily.

5. MODEL

The Sr, Nd, Pb and O systematics from the rocks in this study consistently exclude sediment contamination, despite all magma having to cross an approximately 2 km thick sequence of sedimentary oceanic crust, similar to the one observed underneath Gran Canaria (Hoernle et al., 1998; Ye et al., 1999; Krastel & Schmincke, 2002). This means pre-existing pathways are likely to be used time and again, resulting in a lack of "foreign" material within the recent magmatic plumbing system in Tenerife. Older lavas, in turn, may well have experienced a component of sediment assimilation, but the most recent volcanic events in Tenerife (<200 ka) appear to be free from that.

A brief petrological history may thus have evolved along the following lines: The initial, "old" Teide eruptions were basanitic (Rodriguez-Badiola et al., 2008). Evolved intrusive material corresponding to pre-Icod-collapse eruption cycles was not subjected to remelting at this stage. Accelerated ascent due to the unroofing of the Las Cañadas edifice by the Icod landslide may have impeded pooling of newly arriving magma batches at crustal levels (cf. Longpré et al, 2008; 2009). Hence, Teide started out as a chemically primitive

edifice (cf. Ablay et al., 1998; Rodríguez-Badiola et al., 2008).

The increasing portion of crustal melts within some of the most evolved lavas, which started to occur at around 10 ka, indicates that at some point during the history of Teide-Pico Viejo complex country rock began to be recycled. A potential explanation for this could be density filtering due to the increasing load exerted by the growing Teide-Pico Viejo edifice (Pinel & Jaupart, 2000). As the new edifice increased in volume, new batches of magma may have underplated this nested edifice to an increasing degree, inverting the geothermal gradient and so beginning to (super-) heat the country rock (Fig. 4.21, cf. Annen & Sparks, 2002). The transitional lavas first erupted at around 15 ka, i.e. *before* the first evolved lavas appeared (Carracedo et al., 2007), but can be expressed geochemically either as mixtures of evolved and primitive lavas or by AFC and FCA processes. Both options are conceivable, as shown by the work on Montaña Reventada (Chapter 2) and the AFC modelling conducted in this chapter.

However, in the evolved lavas that show the highest $^{87}Sr/^{86}Sr$ ratio (n=2), the amount of differentiated material in the mixtures modelled is predominant. This implies that the juvenile magma acted as the heat source at depth to melt the country rock and only had limited direct contact with the newly forming anatectic melt (Fig. 4.21). It appears plausible that the actively melting country rock formed new pockets of magma that remained largely autonomous. As the evolved lavas form a continuum in their isotopic characteristics, various amounts of juvenile magmas may be "mixed in" with a pure crustal end-member that is most strongly reflected in the lavas El Boquerón (BOQ) and Phase 7 of Montaña Blanca (MB7).
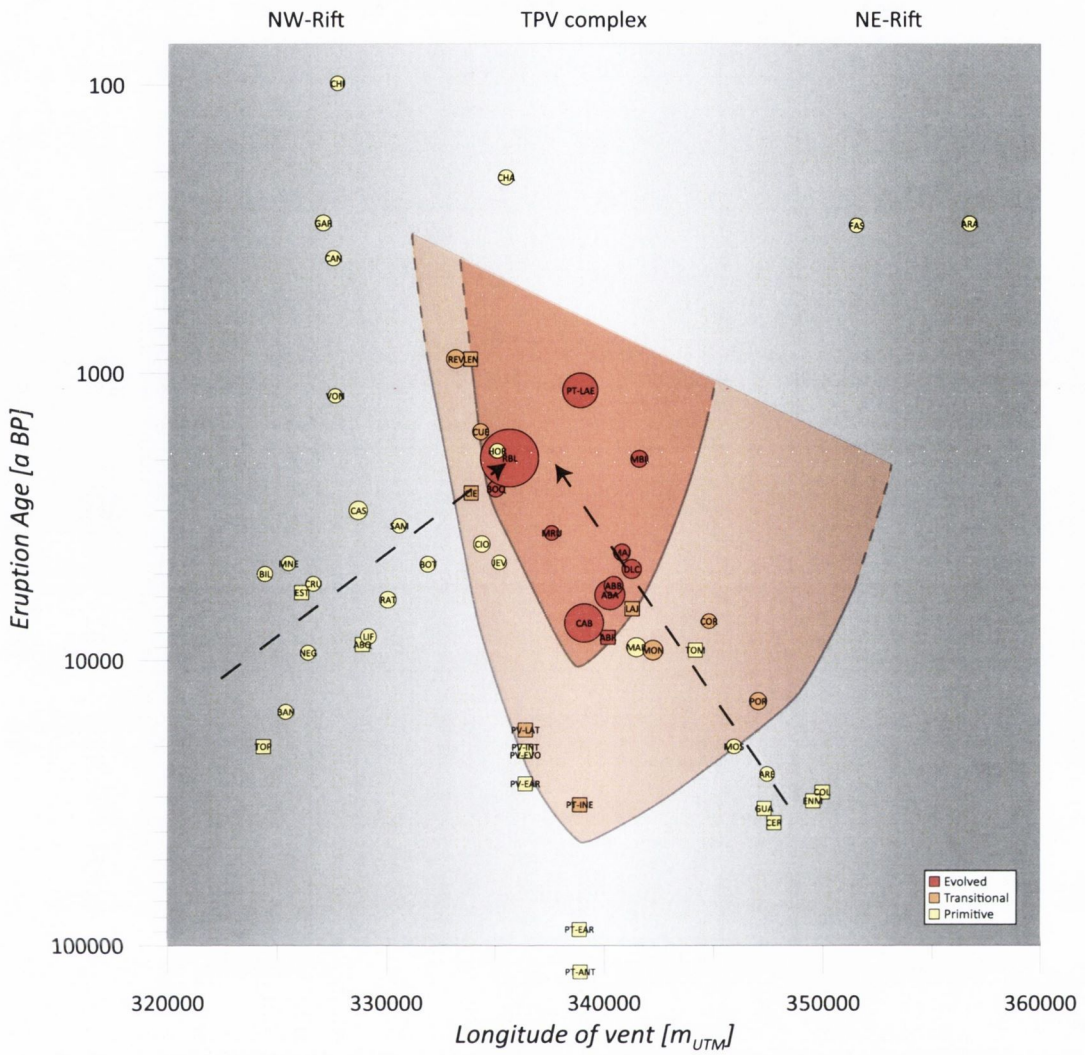
Fig. 4.20: Projected section of Teide-Pico Viejo and rift zones as seen from South (vent longitude on x-axis from W to E), eruption age on y-axis. Symbol size is proportional to eruption volume (Carracedo et al., 2008). The coloured fields show the extent of transitional and evolved lavas and how their vents spread out with time. Note how primitive eruptions have occurred simultaneously with the transitional and evolved ones, but were geographically separated. The arrows indicate the age progression from outside the rift zones towards the centre. Culminating phonolitic eruptions at 1000 - 2000 BP may have relaxed the system. After that, eruptions occurred again, but are widely dispersed on the rift zones. Future eruptions of primitive composition are expected from the Northwest rift, whereas evolved eruptions are expected from the central complex.

Future activity in Tenerife will most likely encompass small, mafic eruptions in the rift zones. Here, the historical activity (<500 BP) has deviated from the progressive convergence towards the central complex that can be observed before (Fig. 4.20, arrows). In a longer time-frame, large phonolitic eruptions up to renewed ignimbritic activity are not inconceivable, but will likely occur with periodicities beyond that of a human lifetime and, furthermore, with notable precursory activity (cf. Carracedo & Troll, 2006).
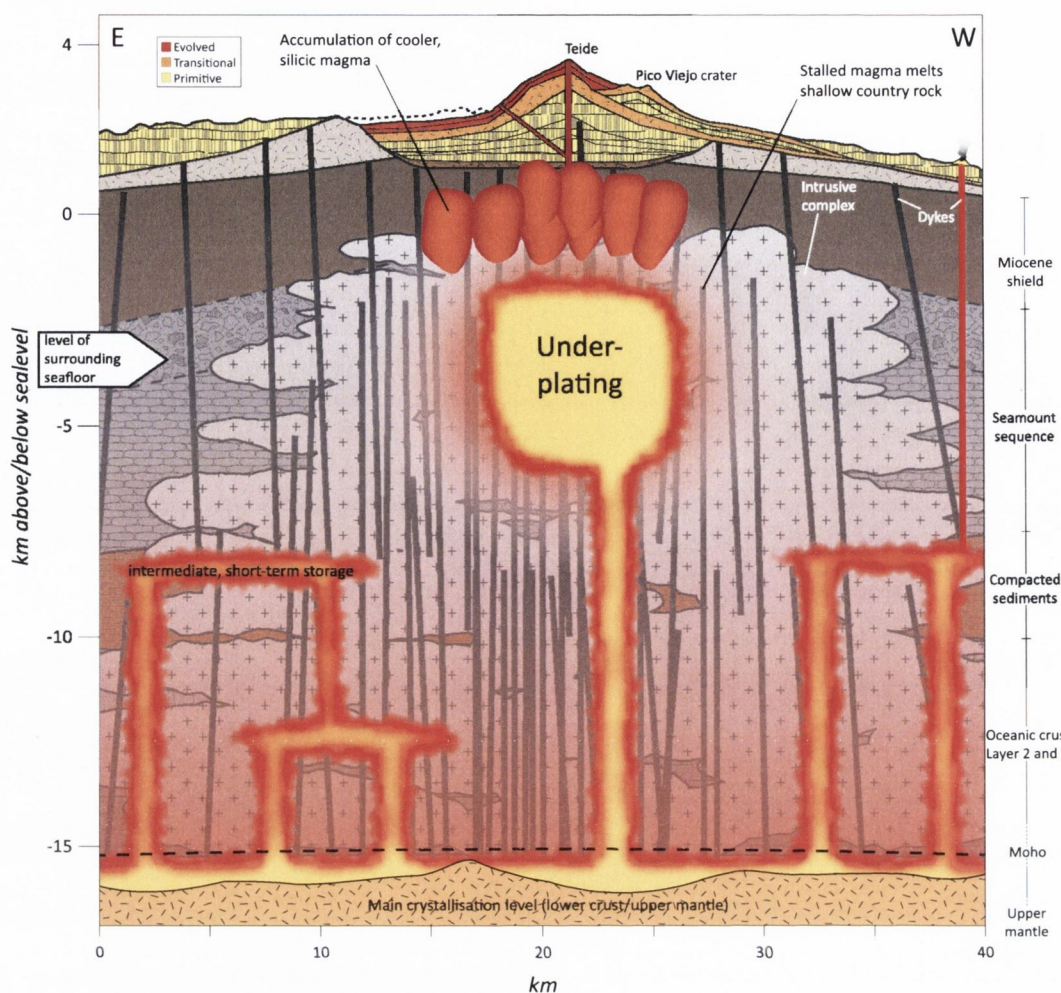
Fig. 4.21: E-W cross-section interpretation of the current plumbing system of Tenerife. Post-collapse deposits are colour-coded after compositional groups. 1.8× vertical exaggeration. Deep island core and ocean crust lithology are represented in this sketch for orientation but may in fact have been reworked largely by Tenerife's combined igneous activity since Miocene times. Included are information from the following publications: crustal structure, Krastel et al. (2002); seamount sequence, Staudigel & Schmincke (1984); Teide-Pico Viejo and underlying units, Carracedo et al. (2007); height of landslide breccia, Marquez et al. (2008); inverse geothermal gradient, Annen & Sparks (2002). Lower crustal/upper mantle as main crystallisation level has been invoked by multiple workers (e.g. Ablay et al., 1998; Hill et al., 2002; Spera & Bohrson, 2004). On the Canary Islands specifically, intermediate levels of short-term residence of magma were detected, inferred from the re-equilibration of CO_2-inclusions in mineral phases (Klügel et al., 2005; Galipp et al., 2006). Underplating of juvenile material underneath the central Teide-Pico Viejo complex may cause formation of anatectic melts. These anatectic melts may be decoupled from the heat-providing juvenile material.

Moreover, the vents of transitional and evolved eruptions can be observed to have spread out from the central complex with time. This may indicate that either the window of country rock melting that centered around Teide-Pico Viejo complex widened or that eruptions got increasingly deflected towards the margins of the central complex (see V-shaped distribution of eruptions in Fig. 4.20).

6. CONCLUSIONS

The Sr, Nd, Pb and $\delta^{18}O$ isotopic data allow devising a coherent model for the origin of the most recent high $^{87}Sr/^{86}Sr$ phonolite lavas in Tenerife.

1. Sr, Nd and Pb isotope data exclude significant sediment contamination of the recent succession of Teide/Pico Viejo complex and the rift zones.

2. Pb isotope data indicate an open system for the differentiation of the lavas within the post-Icod-collapse succession in Tenerife.

3. Sr and Nd isotope systematics indicate that an end-member with a high $^{87}Sr/^{86}Sr$ ratio must be present within the magmatic plumbing system. Such high $^{87}Sr/^{86}Sr$ ratios are rare and restricted to highly differentiated rocks in Tenerife.

4. Mixing hyperbolas modelled for the two highest $^{87}Sr/^{86}Sr$ phonolites, using Sr-Nd isotope ratios yield percentages in-between 92.25 and 99.73% of a potential highly differentiated, recycled end-member that has been remobilised.

5. Oxygen isotope data from feldspars are of "magmatic" origin, and do not preclude a two-component mixing where both components possess comparable magmatic $\delta^{18}O$ ratios. Highly differentiated rocks with magmatic $\delta^{18}O$ values clearly exist underneath Teide-Pico Viejo complex.

Crustal melting has been invoked in several tectonic settings as an origin for felsic magmas (e.g. Sorensen, 1988; Flagler & Spray, 1991; Sawyer, 1991; Troll et al., 2004, 2005; Ferla & Meli, 2006). For ocean islands, in particular, a number of workers have argued for this mode of felsic magma generation (e.g. Williams et al., 1995; Bohrson & Reid, 1998; Borg & Clynne, 1998; Troll & Schmincke, 2002). In a very similar case to Tenerife, Legendre et al. (2005) suggested a large variety of differentiation processes for the alkaline series of Ua Pou Island (French Polynesia), among these a crustal melt origin for the compositionally most extreme phonolites.

We therefore argue that crustal melts of evolved country rock are largely responsible for the generation of two of the most recent phonolitic eruptions in Tenerife. As a result of the observed contrast in differentiation processes between primitive and evolved lavas, the bimodality of erupted lavas in the Tenerife post-Icod-collapse succession may originate

by creating intermediate compositions from both of the extremes of the compositional range, although an AFC model is equally possible. The most primitive compositions seem to evolve towards intermediate levels mainly by means of fractional crystallisation and potentially varying, but small degrees of assimilation. Such highly differentiated rocks are then readily available to be remelted in later stages of island evolution and seem to become increasingly more recycled over the lifespan of an ocean island plumbing system.

CONCLUDING REMARKS

Magmatic differentiation was considerably revised for the generation of phonolitic melt in the post-Icod-collapse succession in Tenerife. Pre-existing whole-rock data allowed a "custom-made" classification of lava rocks, based on their trace element fingerprints. Grouping lavas this way helped to classify them according to their geochemical histories, instead of applying somewhat arbitrary TAS labels that may serve better to compare between regional settings. Merely looking at phonolites as defined by the TAS diagram would not have sufficed. Applying trace element fingerprints was key to distinguish between these suites of lavas that share common magmatic histories, and thus common differentiation processes.

Finally, based on this trace element fingerprinting, the combined use of 'work-horse' and 'cutting-edge' geochemical techniques in this study allowed to break down the magmatic plumbing system into three distinct differentiation regimes (primitive, intermediate and evolved). These regimes interplay to yield an apparently continuous series of differentiation at the surface. Many references in Chapters 2 and 4 to feldspar data in Chapter 3 are testimony to that, and both datasets, whole-sample and microanalytical, reinforce each other to yield a comprehensive picture, yielding an overall refined view of the recent magmatic plumbing system beneath Tenerife.

The main conclusions from this study are:

- The lavas with the highest Sr isotope ratios in the post-collapse succession in Tenerife are phonolites that appear to have primarily formed by crustal melting of country rock. Parent rock compositions are likely to be intrusive remnants of highly differentiated magmatic rocks, residues from earlier, abundant felsic eruptions in Tenerife. The Sr isotope systematics of earlier eruptive cycles, e.g. the Diego Hernández Formation and potentially the whole Las Cañadas volcano that is comprised of several of these cycles, are very similar to those of the post-Icod-collapse succession. As Sr isotopes were key to determine the crustal melt

character of the post-collapse phonolites and to exclude sediment contamination, this type of differentiation may well be applicable to the formation of felsic magma in older successions in Tenerife.

• The most primitive lavas, in turn, appear to follow assimilation and fractional crystallisation (AFC) systematics. Detailed microanalysis of all feldspar phenocryst compositions (apart from the ones with the highest Rb/Sr ratio) from the whole compositional range of their host lavas, together with a reconstruction of melt compositions at the time of feldspar crystallisation, yielded an energy constrained model of replenishment, assimilation and fractional crystallisation (EC-RAχFC) for upper mantle/lower crustal magma chambers below Tenerife. The EC-RAχFC model considered gabbroic xenoliths as assimilant, which are interpreted to have formed as cumulate in upper mantle/lower crustal magma chambers. Digesting the rocks that an earlier and similar batch of magma fractionated, allowed the magma to be modelled to reproduce the natural data of high-Sr/high-Zr lavas. These lavas therefore appear to have experienced prolonged residence times in the magma reservoirs for differentiation processes to achieve an observable effect. Low-Sr/ low-Zr lavas, in turn, seem to have been less affected by assimilation and fractional crystallisation, potentially implying a short upper mantle/lower crustal residence.

• One potential mechanism to generate intermediate magma in Tenerife was explored in the case of the Montaña Reventada composite lava flow, where magma mixing was observed in outcrop. Extensive field evidence indicated a close temporal relationship between basanite and phonolite. Textures of mafic inclusions and their contact relationships to the surrounding phonolite were suggestive of a brief contact only between basanite and phonolite prior to eruption. Mass balance calculations using a detailed dataset of major- and trace element concentrations as well as radiogenic and stable isotopes allowed to constrain the formation of enclaves of intermediate composition.

Page intentionally left blank

The last four years brought me from Bremen to Dublin and from there to many different places, a constant movement, restless, until I ended up in Tenerife, this place that always made me feel like walking on clouds.

Growth defined my inner journey instead. When I arrived, I knew literally nothing about volcanoes, coming from a degree in Oceanography in Bremen. And all was not easy in the beginning in Dublin. That this project turned out so well in the end, is my personal achievement. However, hardly anything in this world can be achieved as a lone rider. Were it not for the restless efforts of my supervisor Valentin R. Troll who initiated this project, constantly gave new ideas and was incredibly approachable literally anytime I needed him, I would not be where I am now.

I would like to thank Dave Chew. After Val had left to take his post in Uppsala, Dave selflessly took over as supervisor and helped me up to the last minute with corrections for this work.

Probably the most humbling experience during this time was arriving in Tenerife to spend the last year of this project there. When Juan Carlos Carracedo and Pauline Agnew welcomed me, I felt I was taken up into a family. The incredible generosity that I received from them, both on a personal and with Juan Carlos also on a professional level, shall be me an example for life. I wish them a long and healthy future, may you continue as the sincere minds that you are. This part of my life would not have come to such a fortunate end without you.

The office in 193 Pearse St. was a dark hole, but being filled with warm people, it was more than bearable. Thanks Audray Delcamp, Frances Deegan, Marc-Antoine Longpré, Graeme Nicoll, Fiona Meade and David Jordan. Not only them, but all VAMP members made life good, I was and still am glad to be a part of this troop of volcanologists. Here's to Jane Chadwick, Eleanor Donoghue, Paul Byrne, Eoghan Holohan, Brian O'Driscoll, Lucy Mathieu and Lara Blythe. Neil Kearney, Declan Burke, Maura Morgan and Francis Hendron were a lovely bunch of people and always helpful when needed.

The crew at Washington State University made for incredible stays in Pullman, WA, greets to John A. Wolff, Paul Olin, Scott Burroughs, Charles Knaack, Scotty Cornelius and Garret Hart. John, I need you to invite me to your house during the Worlds 2010, I've come to get used to your couch during the grand tournaments of the past four years. Maybe more so to your homebrew.

Thanks to Rob Ellam for his input on isotope anlyses. Anne Kelly, Vincent Gallagher and Paul Gorman at SUERC in lovely East Kilbride, Sco made for funny non-understandable conversations ("what happened, Paul, I was able to understand you before!" - "tha's because the ferrst too days we ma'e aneffrrt!"). They made me appreciate Scotsmen as one of the most relaxed breed of people on Earth. Ny borra! ...and not to forget the set-up for Celtic Park, incredible! (needless to say, I enjoyed working with you guys, thanks!)

I made many friends during my time in Dublin, too many to list them all here, but I would like to let you know that I think of you nevertheless. The closest were from doin' time in Braemor and Mountjoy: Laura Sudulich, Giuseppe Ruvio, Beatriz Tejerina Gonzalez and Lola Flores, Sergio Curto, Alexandra Kohn, Leonardo Baccini and Jill Connaughton. Shall all have a good daa-aay!

Das größte Danke ist jedoch für meine Eltern bestimmt. In dieser Zeit, die von großer Entfernung zu ihnen geprägt war, haben sie immer zu mir gehalten und mich, so wie es ihnen möglich war, mich unterstützt. Ohne Euch hätte es nicht geklappt!

21.6.2010, San Cristóbal de La Laguna

References

Abdel-Monem, A., Watkins, N. D. & Gast, P. W. (1971). Potassium-argon ages, volcanic stratigraphy, and geomagnetic polarity history of the Canary Islands; Lanzarote, Fuerteventura, Gran Canaria, and La Gomera. American Journal of Science 271, 490-521.

Abdel-Monem, A., Watkins, N. D. & Gast, P. W. (1972). Potassium-argon ages, volcanic stratigraphy, and geomagnetic polarity history of the Canary Islands; Tenerife, La Palma and Hierro. American Journal of Science 272, 805-825.

Ablay, G. J., Carroll, M. R., Palmer, M. R., Martí, J. & Sparks, R. S. J. (1998). Basanite-Phonolite Lineages of the Teide-Pico Viejo Volcanic Complex, Tenerife, Canary Islands. Journal of Petrology 39, 905-936.

Ablay, G. J., Ernst, G. G. J., Marti, J. & Sparks, R. S. J. (1995). The ~2ka subplinian eruption of Montana Blanca, Tenerife. Bulletin of Volcanology 57, 337-355.

Abratis, M., Schmincke, H. U. & Hansteen, T. (2002). Composition and evolution of submarine volcanic rocks from the central and western Canary Islands. International Journal of Earth Sciences 91, 562-582.

Albarède, F., Telouk, P., Blichert-Toft, J., Boyet, M., Agranier, A. & Nelson, B. (2004). Precise and accurate isotopic measurements using multiple-collector ICPMS. Geochimica et Cosmochimica Acta 68, 2725-2744.

Ancochea, E., Fuster, J., Ibarrola, E., Cendrero, A., Coello, J., Hernan, F., Cantagrel, J. M. & Jamond, C. (1990). Volcanic evolution of the island of Tenerife (Canary Islands) in the light of new K-Ar data. Journal of Volcanology and Geothermal Research 44, 231-249.

Ancochea, E., Huertas, M. J., Cantagrel, J. M., Coello, J., Fuster, J. M., Arnaud, N. & Ibarrola, E. (1999). Evolution of the Canadas edifice and its implications for the origin of the Canadas Caldera (Tenerife, Canary Islands). Journal of Volcanology and Geothermal Research 88, 177-199.

Andújar, J., Costa, F., Martí, J., Wolff, J. A. & Carroll, M. R. (2008). Experimental constraints on pre-eruptive conditions of phonolitic magma from the caldera-forming El Abrigo eruption, Tenerife (Canary Islands). Chemical Geology 257, 173-191.

Annen, C. & Sparks, R. S. J. (2002). Effects of repetitive emplacement of basaltic intrusions on thermal evolution and melt generation in the crust. Earth and Planetary Science Letters 203, 937-955.

Araña, V., Aparicio, A., Garcia Cacho, L. & Garcia Garcia, R. (1989). Mezcla de magmas en la región central de Tenerife. In: Araña, V. & Coello, J. (eds.) Los volcanes y la caldera del Parque Nacional del Teide (Tenerife, Islas Canarias): Ministerio de Agricultura Pesca

y Alimentación, 269-298.

Araña, V., Martí, J., Aparicio, A., García-Cacho, L. & García-García, R. (1994). Magma mixing in alkaline magmas: An example from Tenerife, Canary Islands. Lithos 32, 1-19.

Bailey, D. K. (1987). Mantle metasomatism--perspective and prospect. Geological Society Special Publication 30, 1-13.

Baker, I. (1968). Intermediate oceanic volcanic rocks and the 'Daly gap'. Earth and Planetary Science Letters 4, 103-106.

Baker, J., Peate, D., Waight, T. & Meyzen, C. (2004). Pb isotopic analysis of standards and samples using a 207Pb-204Pb double spike and thallium to correct for mass bias with a double-focusing MC-ICP-MS. Chemical Geology 211, 275-303.

Barth, T. F. W., Correns, C. W. & Eskola, P. (1939). Die Entstehung der Gesteine. Berlin: Springer Verlag.

Bédard, J. H. (2006). Trace element partitioning in plagioclase feldspar. Geochimica et Cosmochimica Acta 70, 3717-3742.

Belshaw, N. S., Freedman, P. A., O'Nions, R. K., Frank, M. & Guo, Y. (1998). A new variable dispersion double-focusing plasma mass spectrometer with performance illustrated for Pb isotopes. International Journal of Mass Spectrometry 181, 51-58.

Bence, A. E. & Albee, A. L. (1968). Empirical correction factors for the electron microanalysis of silicates and oxides. Journal of Geology 76, 382-403.

Berlo, K., Blundy, J., Turner, S. & Hawkesworth, C. (2007). Textural and chemical variation in plagioclase phenocrysts from the 1980 eruptions of Mount St. Helens, USA. Contributions to Mineralogy and Petrology 154, 291-308.

Bindeman, I., Gurenko, A., Sigmarsson, O. & Chaussidon, M. (2008). Oxygen isotope heterogeneity and disequilibria of olivine crystals in large volume Holocene basalts from Iceland: Evidence for magmatic digestion and erosion of Pleistocene hyaloclastites. Geochimica et Cosmochimica Acta 72, 4397-4420.

Bindeman, I., Ponomareva, V. V., Bailey, J. C. & Valley, J. W. (2004). Kamchatka Peninsula: a province with high-d18O magma sources and large scale 18O/16O depletion of the upper crust. Geochimica et Cosmochimica Acta 68, 841-865.

Bindeman, I. N. & Davis, A. M. (1999). Convection and redistribution of alkalis and trace elements during the mingling of basaltic and rhyolitic melts. Petrology 7, 91-101.

Bindeman, I. N., Davis, A. M. & Drake, M. J. (1998). Ion microprobe study of plagioclase-basalt partition experiments at natural concentration levels of trace elements. Geochimica et Cosmochimica Acta 62, 1175-1193.

Bindeman, I. N. & Perchuk, L. L. (1993). Experimental studies of magma mixing at high

pressures. International Geology Review 35, 721-733.

Blake, S. (1981a). Eruptions from zoned magma chambers. Journal of the Geological Society (London, United Kingdom) 138, 281-287.

Blake, S. & Ivey, G. N. (1986). Magma-mixing and the dynamics of withdrawal from stratified reservoirs. Journal of Volcanology and Geothermal Research 27, 153-178.

Blundy, J. & Wood, B. (1994). Prediction of crystalÂ–melt partition coefficients from elastic moduli. Nature 372, 452-454.

Blundy, J. D. & Shimizu, N. (1991). Trace element evidence for plagioclase recycling in calc-alkaline magmas. Earth and Planetary Science Letters 102, 178-197.

Blundy, J. D. & Wood, B. (1991). Crystal-chemical controls on the partitioning of Sr and Ba between plagioclase feldspar, silicate melts, and hydrothermal solutions. Geochimica et Cosmochimica Acta 55, 193-209.

Bohrson, W. A. & Reid, M. R. (1998). Genesis of Evolved Ocean Island Magmas by Deep- and Shallow-Level Basement Recycling, Socorro Island, Mexico: Constraints from Th and other Isotope Signatures. Journal of Petrology 39, 995-1008.

Bohrson, W. A. & Spera, F. J. (2001). Energy-Constrained Open-System Magmatic Processes II: Application of Energy-Constrained Assimilation-Fractional Crystallization (EC-AFC) Model to Magmatic Systems. Journal of Petrology 42, 1019-1041.

Bohrson, W. A. & Spera, F. J. (2003). Energy-constrained open-system magmatic processes IV: Geochemical, thermal and mass consequences of energy-constrained recharge, assimilation and fractional crystallization (EC-RAFC). Geochemistry, Geophysics, Geosystems 4.

Bonnefoi, C. C., Provost, A. & Albarède, F. (1995). The 'Daly gap' as a magmatic catastrophe. Nature 378, 270-272.

Borg, L. E. & Clynne, M. A. (1998). The Petrogenesis of Felsic Calc-alkaline Magmas from the Southernmost Cascades, California: Origin by Partial Melting of Basaltic Lower Crust. Journal of Petrology 39, 1197-1222.

Borghini, G., Fumagalli, P. & Rampone, E. (2009). The Stability of Plagioclase in the Upper Mantle: Subsolidus Experiments on Fertile and Depleted Lherzolite. Journal of Petrology egp079.

Brian, S., Geoffrey, T., Margaret, S. & John, N. L. (1980). Analysis of geologic materials using an automated x-ray fluorescence system. X-Ray Spectrometry 9, 198-205.

Brophy, J. G. (1991). Composition gaps, critical crystallinity, and fractional crystallization in orogenic (calc-alkaline) magmatic systems. Contributions to Mineralogy and Petrology 109, 173-182.

Brown, R. J., Barry, T. L., Branney, J. J., Pringle, M. S. & Bryan, S. E. (2003). The Quaternary pyroclastic succession of Southeast Tenerife, Canary Islands; explosive eruptions, related caldera subsidence, and sector collapse. Geological Magazine 140, 265-288.

Brown, R. J. & Branney, M. J. (2004). Event-stratigraphy of a caldera-forming ignimbrite eruption on Tenerife: the 273 ka Poris Formation. Bulletin of Volcanology 66, 392-416.

Browne, B. L., Eichelberger, J. C., Patino, L. C., Vogel, T. A., Uto, K. & Hoshizumi, H. (2006). Magma mingling as indicated by texture and Sr / Ba ratios of plagioclase phenocrysts from Unzen volcano, SW Japan. Journal of Volcanology and Geothermal Research 154, 103-116.

Bryan, S. E., Cas, R. A. F. & Marti, J. (2000). The 0.57 Ma plinian eruption of the Granadilla Member, Tenerife (Canary Islands): an example of complexity in eruption dynamics and evolution. Journal of Volcanology and Geothermal Research 103, 209-238.

Bryan, S. E., Marti, J. & Cas, R. A. F. (1998). Stratigraphy of the Bandas del Sur Formation: an extracaldera record of Quaternary phonolitic explosive eruptions from the Las Canadas edifice, Tenerife (Canary Islands). Geological Magazine 135, 605-636.

Bryan, S. E., Marti, J. & Leosson, M. (2002). Petrology and Geochemistry of the Bandas del Sur Formation, Las Canadas Edifice, Tenerife (Canary Islands). Journal of Petrology 43, 1815-1856.

Bunsen, R. (1851). Ueber die Processe der vulkanischen Gesteinsbildungen Islands. Annalen der Physik und Chemie 159, 197-272.

Cann, J. R. (1968). Bimodal distribution of rocks from volcanic islands. Earth and Planetary Science Letters 4, 479-480.

Carracedo, J. C. (1979). Paleomagnetismo y historia geológica de Tenerife. Santa Cruz de Tenerife: Aula Cultura Cabildo Insular de Tenerife.

Carracedo, J. C. (1994). The Canary Islands: An example of structural control on the growth of large oceanic-island volcanoes. Journal of Volcanology and Geothermal Research 60, 225.

Carracedo, J. C. (1996). Morphological and structural evolution of the western Canary Islands: hotspot-induced three-armed rifts or regional tectonic trends? Journal of Volcanology and Geothermal Research 72, 151-162.

Carracedo, J. C. (1999). Growth, structure, instability and collapse of Canarian volcanoes and comparisons with Hawaiian volcanoes. Journal of Volcanology and Geothermal Research 94, 1-19.

Carracedo, J. C., Guillou, H., Rodríguez-Badíola, E., Pérez Torrado, F. J., Rodríguez González, A., Paris, R., Troll, V. R., Wiesmaier, S., Delcamp, A. & Fernandez-Turiel, J. L. (2009). La dorsal NE de Tenerife: hacia un modelo del origen y evolución de los rifts

de islas oceánicas. Estudios Geologicos 65.

Carracedo, J. C., Rodríguez Badiola, E., Guillou, H., Paterne, M., Scaillet, S., Pérez Torrado, F. J., Paris, R., Fra-Paleo, U. & Hansen, A. (2007). Eruptive and Structural History of Teide Volcano and Rift Zones of Tenerife, Canary Islands. Geological Society of America Bulletin 119, 1027–1051.

Carracedo, J. C., Rodríguez Badiola, E., Guillou, H., Paterne, M., Scaillet, S., Pérez Torrado, F. J., Paris, R., Rodríguez González, A. & Socorro, S. (2008). El Volcán Teide - Volcanología, Interpretación de Pasajes y Iterinarios Comentados: Caja Generál de Ahorros de Canarias.

Carracedo, J. C. & Troll, V. R. (2006). Seismicity and gas emissions on Tenerife: a real cause for alarm? Geology Today 22, 138-141.

Cas, R. A. F. & Wright, J. V. (1987). Volcanic successions - modern and ancient. London: Allen & Unwin Ltd.

Chadwick, J. P., Troll, V. R., Ginibre, C., Morgan, D., Gertisser, R., Waight, T. E. & Davidson, J. P. (2007). Carbonate Assimilation at Merapi Volcano, Java, Indonesia: Insights from Crystal Isotope Stratigraphy. Journal of Petrology 48, 1793-1812.

Charlier, B. L. A., Ginibre, C., Morgan, D., Nowell, G. M., Pearson, D. G., Davidson, J. P. & Ottley, C. J. (2006). Methods for the microsampling and high-precision analysis of strontium and rubidium isotopes at single crystal scale for petrological and geochronological applications. Chemical Geology 232, 114-133.

Chayes, F. (1963). Relative abundance of intermediate members of the oceanic basalt-trachyte association. Journal of Geophysical Research 68, 1519.

Chayes, F. (1977). The oceanic basalt-trachyte relation in general and in the Canary Islands. American Mineralogist 62, 666-671.

Chertkoff, D. G., Morgan, D., Davidson, J. P., Pearson, D. G., Jerram, D. A. & Nowell, G. M. (2005a). In-situ Sr isotopic investigations of feldspar phenocrysts from the Teide-Pico Viejo stratovolcanic complex, Tenerife. European Geosciences Union. Geophysical Research Abstracts.

Chertkoff, D. G., Morgan, D., Mock, A., Jerram, D. A., Davidson, J. P., Pearson, D. G. & Nowell, G. M. (2005b). Textural and micro-Sr isotopic investigations of feldspar phenocrysts from the Teide-Pico Viejo stratovolcanic complex, Tenerife (Canary Islands). AGU 86(52), Fall Meet. Suppl. San Francisco.

Christensen, J. N. & DePaolo, D. J. (1993). Time scales of large volume silicic magma systems: Sr isotopic systematics of phenocrysts and glass from the Bishop Tuff, Long Valley, California. Contributions to Mineralogy and Petrology 113, 100-114.

Clague, D. & Dalrymple, G. B. (1987). The Hawaiian-Emperor volcanic chain. Part I: Geologic evolution. In: Decker, W., Wright, T. L. & Stauffer, P. H. (eds.) Volcanism in

Hawaii. Prof. Paper 1350: United States Geological Survey, 5-54.

Clague, D. A. (1978). The Oceanic Basalt-Trachyte Association: An Explanation of the Daly Gap. Journal of Geology 86, 739-743.

Coombs, M. L., Eichelberger, J. C. & Rutherford, M. J. (2003). Experimental and textural constraints on mafic enclave formation in volcanic rocks. Journal of Volcanology and Geothermal Research 119, 125-144.

Cousens, B. L., Spera, F. J. & Dobson, P. F. (1993). Post-eruptive alteration of silicic ignimbrites and lavas, Gran Canaria, Canary Islands: Strontium, neodymium, lead, and oxygen isotopic evidence. Geochimica et Cosmochimica Acta 57, 631-640.

Daly, R. A. (1925). The Geology of Ascension Island. Proceedings of the American Academy of Arts and Sciences 60, 3-80.

Davaille, A., Stutzmann, E., Silveira, G., Besse, J. & Courtillot, V. (2005). Convective patterns under the Indo-Atlantic « box ». Earth and Planetary Science Letters 239, 233-252.

Davidson, J., Tepley III., F., Palacz, Z. & Meffan-Main, S. (2001). Magma recharge, contamination and residence times revealed by in situ laser ablation isotopic analysis of feldspar in volcanic rocks. Earth and Planetary Science Letters 184, 427-442.

Davidson, J. P. & Tepley III, F. J. (1997). Recharge in Volcanic Systems: Evidence from Isotope Profiles of Phenocrysts. Science 275, 826-829.

Davies, D. R. & Davies, J. H. (2009). Thermally-driven mantle plumes reconcile multiple hot-spot observations. Earth and Planetary Science Letters 278, 50-54.

Deegan, F., Troll, V. R. & Freda, C. (in preparation). Partial melting in the Fuerteventura Betancúria massif.

DePaolo, D. J. (1981). Trace element and isotopic effects of combined wallrock assimilation and fractional crystallization. Earth and Planetary Science Letters 53, 189-202.

Donoghue, E., Troll, V. R., Harris, C., O'Halloran, A., Walter, T. R. & Pérez Torrado, F. J. (2008). Low-temperature hydrothermal alteration of intra-caldera tuffs, Miocene Tejeda caldera, Gran Canaria, Canary Islands. Journal of Volcanology and Geothermal Research 176, 551-564.

Duffield, W. A. & Ruiz, J. (1998). A model that helps explain Sr-isotope disequilibrium between feldspar phenocrysts and melt in large-volume silicic magma systems. Journal of Volcanology and Geothermal Research 87, 7-13.

Duncan, R. A. (1981). Hotspots in the southern oceans, an absolute frame of reference for the motion of the Gondwana continents. Tectonophysics 74, 29-42.

Edgar, C. J., Wolff, J. A., Olin, P. H., Nichols, H. J., Pittari, A., Cas, R. A. F., Reiners,

P. W., Spell, T. L. & Martí, J. (2007). The late Quaternary Diego Hernandez Formation, Tenerife: Volcanology of a complex cycle of voluminous explosive phonolitic eruptions. Journal of Volcanology and Geothermal Research 160, 59-85.

Eggins, S. M., Woodhead, J. D., Kinsley, L. P. J., Mortimer, G. E., Sylvester, P., McCulloch, M. T., Hergt, J. M. & Handler, M. R. (1997). A simple method for the precise determination of >= 40 trace elements in geological samples by ICPMS using enriched isotope internal standardisation. Chemical Geology 134, 311-326.

Eichelberger, J. C. (1980). Vesiculation of mafic magma during replenishment of silicic magma reservoirs. Nature 288, 446-450.

Eichelberger, J. C., Chertkoff, D. G., Dreher, S. T. & Nye, C. J. (2000). Magmas in collision: Rethinking chemical zonation in silicic magmas. Geology 28, 603-606.

Eiler, J. M., Farley, K. A., Valley, J. W., Hofmann, A. W. & Stolper, E. M. (1996). Oxygen isotope constraints on the sources of Hawaiian volcanism. Earth and Planetary Science Letters 144, 453-467.

Elburg, M., Vroon, P., van der Wagt, B. & Tchalikian, A. (2005). Sr and Pb isotopic composition of five USGS glasses (BHVO-2G, BIR-1G, BCR-2G, TB-1G, NKT-1G). Chemical Geology 223, 196-207.

Ellam, R. M. (2006). New constraints on the petrogenesis of the Nuanetsi picrite basalts from Pb and Hf isotope data. Earth and Planetary Science Letters 245, 153-161.

Ersoy, Y. & HelvacI, C. FC-AFC-FCA and mixing modeler: A Microsoft® Excel© spreadsheet program for modeling geochemical differentiation of magma by crystal fractionation, crustal assimilation and mixing. Computers & Geosciences 36, 383-390.

Ewart, A. & Griffin, W. L. (1994). Application of proton-microprobe data to trace-element partitioning in volcanic rocks. Chemical Geology 117, 251-284.

Fagereng, Å., Harris, C., La Grange, M. & Stevens, G. (2008). Stable isotope study of the Archaean rocks of the Vredefort impact structure, central Kaapvaal Craton, South Africa. Contributions to Mineralogy and Petrology 155, 63-78.

Ferla, P. & Meli, C. (2006). Evidence of Magma Mixing in the 'Daly Gap' of Alkaline Suites: a Case Study from the Enclaves of Pantelleria (Italy). Journal of Petrology 47, 1467-1507.

Flagler, P. A. & Spray, J. G. (1991). Generation of plagiogranite by amphibolite anatexis in oceanic shear zones. Geology 19, 70-73.

Fowler, S. J., Bohrson, W. A. & Spera, F. J. (2004). Magmatic Evolution of the Skye Igneous Centre, Western Scotland: Modelling of Assimilation, Recharge and Fractional Crystallization. Journal of Petrology 45, 2481-2505.

Freundt, A. & Schmincke, H.-U. (1992). Mixing of rhyolite, trachyte and basalt magma

erupted from a vertically and laterally zoned reservoir, composite flow P1, Gran Canaria. Contributions to Mineralogy and Petrology 112, 1-19.

Fujimaki, H., Tatsumoto, M. & Aoki, K.-I. (1984). Partition coefficients of Hf, Zr, and REE between phenocrysts and groundmasses. Journal of Geophysical Research 89, 662-672.

Fúster, J. M. (1975). Las Islas Canarias: un ejemplo de evolución espacial y temporal del vulcanismo oceanico. Estudios Geologicos 31, 439-463.

Fúster, J. M., Cendrero, A., Gastesi, P., Ibarrola, E. & López Ruiz, J. (1968). Geology and Volcanology of the Canary Islands, Fuerteventura. Madrid: Instituto Lucas Mallada.

Gagnevin, D., Daly, J. S., Poli, G. & Morgan, D. (2005). Microchemical and Sr Isotopic Investigation of Zoned K-feldspar Megacrysts: Insights into the Petrogenesis of a Granitic System and Disequilibrium Crystal Growth. Journal of Petrology 46, 1689-1724.

Gagnevin, D., Waight, T. E., Daly, J. S., Poli, G. & Conticelli, S. (2007). Insights into magmatic evolution and recharge history in Capraia Volcano (Italy) from chemical and isotopic zoning in plagioclase phenocrysts. Journal of Volcanology and Geothermal Research 168, 28-54.

Galipp, K., Klügel, A. & Hansteen, T. H. (2006). Changing depths of magma fractionation and stagnation during the evolution of an oceanic island volcano: La Palma (Canary Islands). Journal of Volcanology and Geothermal Research 155, 285-306.

Gamble, J. A. (1979). Some relationships between coexisting granitic and basaltic magmas and the genesis of hybrid rocks in the Tertiary central complex of Slieve Gullion, Northeast Ireland. Journal of Volcanology and Geothermal Research 5, 297-316.

Garcia, M. O., Frey, F. A. & Grooms, D. G. (1986). Petrology of volcanic rocks from Kaula Island, Hawaii. Contributions to Mineralogy and Petrology 94, 461-471.

Garcia, M. O., Ito, E., Eiler, J. M. & Pietruszka, A. J. (1998). Crustal Contamination of Kilauea Volcano Magmas Revealed by Oxygen Isotope Analyses of Glass and Olivine fromPuu Oo Eruption Lavas. Journal of Petrology 39, 803-817.

Geldmacher, J., Haase, K. M., Devey, C. W. & Garbe-Schönberg, C. D. (1998). The petrogenesis of Tertiary cone-sheets in Ardnamurchan, NW Scotland: petrological and geochemical constraints on crustal contamination and partial melting. Contributions to Mineralogy and Petrology 131, 196-209.

Ginibré, C., Kronz, A. & Wörner, G. (2002a). High-resolution quantitative imaging of plagioclase composition using accumulated backscattered electron images: new constraints on oscillatory zoning. Contributions to Mineralogy and Petrology 142, 436-448.

Ginibré, C., Wörner, G. & Kronz, A. (2002b). Minor- and trace-element zoning in plagioclase: implications for magma chamber processes at Parinacota volcano, northern Chile. Contributions to Mineralogy and Petrology 143, 300-315.

Guillou, H., Carracedo, J. C., Paris, R. & Perez Torrado, F. J. (2004b). Implications for the early shield-stage evolution of Tenerife from K/Ar ages and magnetic stratigraphy. Earth and Planetary Science Letters 222, 599.

Gurenko, A. A., Hoernle, K. A., Hauff, F., Schmincke, H. U., Han, D., Miura, Y. N. & Kaneoka, I. (2006). Major, trace element and Nd-Sr-Pb-O-He-Ar isotope signatures of shield stage lavas from the central and western Canary Islands: Insights into mantle and crustal processes. Chemical Geology 233, 75-112.

Halliday, A. N., Mahood, G. A., Holden, P., Metz, J. M., Dempster, T. J. & Davidson, J. P. (1989). Evidence for long residence times of rhyolitic magma in the Long Valley magmatic system: the isotopic record in precaldera lavas of Glass Mountain. Earth and Planetary Science Letters 94, 274-290.

Hammer, J. E., Cashman, K. V. & Voight, B. (2000). Magmatic processes revealed by textural and compositional trends in Merapi dome lavas. Journal of Volcanology and Geothermal Research 100, 165-192.

Hammouda, T., Pichavant, M. & Chaussidon, M. (1996). Isotopic equilibration during partial melting: an experimental test of the behaviour of Sr. Earth and Planetary Science Letters 144, 109-121.

Hansteen, T. H., Klügel, A. & Schmincke, H.-U. (1998). Multi-stage magma ascent beneath the Canary Islands: evidence from fluid inclusions. Contributions to Mineralogy and Petrology 132, 48-64.

Hansteen, T. H. & Troll, V. R. (2003). Oxygen isotope composition of xenoliths from the oceanic crust and volcanic edifice beneath Gran Canaria (Canary Islands): consequences for crustal contamination of ascending magmas. Chemical Geology 193, 181-193.

Harris, C., Smith, H. S. & le Roex, A. P. (2000). Oxygen isotope composition of phenocrysts from Tristan da Cunha and Gough Island lavas: variation with fractional crystallization and evidence for assimilation. Contributions to Mineralogy and Petrology 138, 164-175.

Harris, P. G. (1963). Comments on a paper by F. Chayes, "Relative abundance of intermediate members of the oceanic basalt-trachyte association". Journal of Geophysical Research 68, 5103-5107.

Hart, S. R. (1984). A large-scale isotope anomaly in the Southern Hemisphere mantle. Nature 309, 753-757.

Harvey, P. K., Taylor, D. M., Hendry, R. D. & Bancroft, F. (1973). An accurate fusion method for the analysis of rocks and chemically related materials by X-ray fluorescence spectrometry. X-Ray Spectrometry 2, 33-44.

Hawkesworth, C. J., Blake, S., Evans, P., Hughes, R., Macdonald, R., Thomas, L. E., Turner, S. P. & Zellmer, G. (2000). Time Scales of Crystal Fractionation in Magma Chambers--Integrating Physical, Isotopic and Geochemical Perspectives. Journal of

Petrology 41, 991-1006.

Hibbard, M. J. (1995). Petrography to Petrogenesis. Englewood Cliffs: Prentice Hall.

Hill, D. P., Pollitz, F. & Newhall, C. (2002). Earthquake-volcano interactions. Physics Today Novemebr 2002, 41-47.

Hobson, A., Bussy, F. & Hernandez, J. (1998). Shallow-Level Migmatization of Gabbros in a Metamorphic Contact Aureole, Fuerteventura Basal Complex, Canary Islands. Journal of Petrology 39, 1025-1037.

Hoernle, K. (1998). Geochemistry of Jurassic Oceanic Crust beneath Gran Canaria (Canary Islands): Implications for Crustal Recycling and Assimilation. Journal of Petrology 39, 859-880.

Hoernle, K., Schmincke, H. U. (1993). The role of partial melting in the 15-Ma geochemical evolution of Gran Canaria: a blob model for the Canarian hotspot. Journal of Petrology 34, 599-626.

Hoernle, K., Tilton, G. & Schmincke, H.-U. (1991a). Sr-Nd-Pb isotopic evolution of Gran Canaria: evidence for shallow enriched mantle beneath the Canary Islands. Earth and Planetary Science Letters 106, 44-63.

Hoernle, K., Tilton, G. & Schmincke, H.-U. (1991b). SrNdPb isotopic evolution of Gran Canaria: Evidence for shallow enriched mantle beneath the Canary Islands. Earth and Planetary Science Letters 106, 44-63.

Huppert, H. E., Turner, J. S., Stephen, R. & Sparks, J. (1982). Replenished magma chambers: effects of compositional zonation and input rates. Earth and Planetary Science Letters 57, 345-357.

Izbekov, P. E., Eichelberger, J. C. & Ivanov, B. V. (2004). The 1996 Eruption of Karymsky Volcano, Kamchatka: Historical Record of Basaltic Replenishment of an Andesite Reservoir. Journal of Petrology 45, 2325-2345.

Jackson, S., Pearson, N. & Griffin, W. L. (2001). In situ isotope determination using laser ablation (LA)-magnetic sector-ICPMS: Mineralogical Association of Canada, Short Course.

King, S. D. & Anderson, D. L. (1998). Edge-driven convection. Earth and Planetary Science Letters 160, 289-296.

King, S. D. & Ritsema, J. (2000). African Hot Spot Volcanism: Small-Scale Convection in the Upper Mantle Beneath Cratons. Science 290, 1137-1140.

Kinman, W. S., Neal, C. R., Davidson, J. P. & Font, L. (2009). The dynamics of Kerguelen Plateau magma evolution: New insights from major element, trace element and Sr isotope microanalysis of plagioclase hosted in Elan Bank basalts. Chemical Geology 264, 247-265.

Klitgord, K. D. & Schouten, H. (1986). Plate kinematics of the Central Atlantic. The Geology of North America: the Western Atlantic Region, 351-378.

Klügel, A., Hansteen, T. H. & Galipp, K. (2005). Magma storage and underplating beneath Cumbre Vieja volcano, La Palma (Canary Islands). Earth and Planetary Science Letters 236, 211-226.

Klügel, A., Hoernle, K. A., Schmincke, H.-U. & White, J. D. L. (2000). The chemically zoned 1949 eruption on La Palma (Canary Islands): Petrologic evolution and magma supply dynamics of a rift zone eruption. Journal of Geophysical Research 105.

Knesel, K. M. & Davidson, J. P. (1999). Sr isotope systematics during melt generation by intrusion of basalt into continental crust. Contributions to Mineralogy and Petrology 136, 285-295.

Knesel, K. M. & Davidson, J. P. (2002). Insights into Collisional Magmatism from Isotopic Fingerprints of Melting Reactions. Science 296, 2206-2208.

Kouchi, A. & Sunagawa, I. (1985). A model for mixing basaltic and dacitic magmas as deduced from experimental data. Contributions to Mineralogy and Petrology 89, 17-23.

Koyaguchi, T. (1989). Chemical gradient at diffusive interfaces in magma chambers. Contributions to Mineralogy and Petrology 103, 143-152.

Krastel, S. & Schmincke, H.-U. (2002a). The channel between Gran Canaria and Tenerife: constructive processes and destructive events during the evolution of volcanic islands. International Journal of Earth Sciences 91, 629-641.

Krastel, S. & Schmincke, H.-U. (2002b). Crustal structure of northern Gran Canaria, Canary Islands, deduced from active seismic tomography. Journal of Volcanology and Geothermal Research 115, 153-177.

Kuritani, T. (2001). Replenishment of a mafic magma in a zoned felsic magma chamber beneath Rishiri Volcano, Japan. Bulletin of Volcanology 62, 533-548.

Larsen, L. M. (1979). Distribution of REE and other trace elements between phenocrysts and peralkaline undersaturated magmas, exemplified by rocks from the Gardar igneous province, south Greenland. Lithos 12, 303-315.

Le Bas, M. J., Maitre, R. W. L., Streckeisen, A., Zanettin, B. & Rocks, I. S. o. t. S. o. I. (1986). A Chemical Classification of Volcanic Rocks Based on the Total Alkali-Silica Diagram. Journal of Petrology 27, 745-750.

Le Bas, M. J. & Streckeisen, A. L. (1991). The IUGS systematics of igneous rocks. Journal of the Geological Society (London, United Kingdom) 148, 825-833.

Legendre, C., Maury, R. C., Caroff, M., Guillou, H., Cotten, J., Chauvel, C., Bollinger, C., Hemond, C., Guille, G., Blais, S., Rossi, P. & Savanier, D. (2005). Origin of Exceptionally Abundant Phonolites on Ua Pou Island (Marquesas, French Polynesia):

Partial Melting of Basanites Followed by Crustal Contamination. Journal of Petrology 46, 1925-1962.

Lesher, C. E. (1986). Effects of silicate liquid composition in mineral-liquid element partitioning from Soret diffusion studies. Journal of Geophysical Research 91, 6123-6141.

Lesher, C. E. & Walker, D. (1986). Solution properties of silicate liquids from thermal diffusion experiments. Geochimica et Cosmochimica Acta 50, 1397-1411.

Longpré, M.-A., Troll, V. R. & Hansteen, T. H. (2008). Upper mantle magma storage and transport under a Canarian shield-volcano, Teno, Tenerife (Spain). Journal of Geophysical Research 113.

Longpré, M.-A., Troll, V. R., Walter, T. R. & Hansteen, T. H. (2009). Volcanic and geochemical evolution of the Teno massif, Tenerife, Canary Islands: Some repercussions of giant landslides on ocean island magmatism. Geochemistry, Geophysics, Geosystems 10, Q12017.

Luais, B., Telouk, P. & Albaréde, F. (1997). Precise and accurate neodymium isotopic measurements by plasma-source mass spectrometry. Geochimica et Cosmochimica Acta 61, 4847-4854.

Marks, M., Halama, R., Wenzel, T. & Markl, G. (2004). Trace element variations in clinopyroxene and amphibole from alkaline to peralkaline syenites and granites: implications for mineral-melt trace-element partitioning. Chemical Geology 211, 185-215.

Márquez, A., López, I., Herrera, R., Martín-González, F., Izquierdo, T. & Carreño, F. (2008). Spreading and potential instability of Teide volcano, Tenerife, Canary Islands. Geophysical Research Letters 35.

Marsh, B. D. (1981). On the crystallinity, probability of occurrence, and rheology of lava and magma. Contributions to Mineralogy and Petrology 78, 85-98.

Marsh, B. D. (2004). A Magmatic Mush Column Rosetta Stone: The McMurdo Dry Valleys of Antarctica. EOS Trans. American Geophysical Union 85, 497-508.

Martí, J. & Gudmundsson, A. (2000). The Las Canadas caldera (Tenerife, Canary Islands): an overlapping collapse caldera generated by magma-chamber migration. Journal of Volcanology and Geothermal Research 103, 161-173.

Martí, J., Hurlimann, M., Ablay, G. & Gudmundsson, A. (1997a). Vertical and lateral collapses on Tenerife (Canary Islands) and other volcanic ocean islands. Geology 25, 879-882.

Martí, J., Hurlimann, M., Ablay, G. J. & Gudmundsson, A. (1997b). Vertical and lateral collapses on Tenerife (Canary Islands) and other volcanic ocean islands. Geology 25, 879-882.

Martí, J., Mitjavila, J. & Araña, V. (1994). Stratigraphy, structure and geochronology of the Las Cañadas caldera (Tenerife, Canary Islands). Geological Magazine 131, 715-727.

Martí, J., Mitjavila, J. & Villa, I. M. (1990). Stratigraphy and K-Ar ages of the Diego Hernández wall and their significance on the Las Cañadas Caldera formation (Tenerife, Canary Islands). Terra Nova 2, 148-153.

Matsui, Y., Onuma, N., Nagasawa, H., Higuchi, H. & Banno, S. (1977). Crystal structure control in trace element partition between crystal and magma. Tectonics 100, 315-324.

McDonough, W. F. & Sun, S. s. (1995). The composition of the Earth. Chemical Geology 120, 223-253.

Meade, F. C., Chew, D. M., Troll, V. R., Ellam, R. M. & Page, L. M. (in press). Magma ascent along a major terrane boundary: crustal contamination and magma mixing at the Drumadoon Intrusive Complex, Isle of Arran, Scotland. Journal of Petrology.

Mollo, S., Gaeta, M., Freda, C., Di Rocco, T., Misiti, V. & Scarlato, P. Carbonate assimilation in magmas: A reappraisal based on experimental petrology. Lithos 114, 503-514.

Morgan, W. J. (1983). Hotspot tracks and the early rifting of the Atlantic. Tectonophysics 94, 123-139.

Morse, S. A. (1984). Cation Diffusion in Plagioclase Feldspar. Science 225, 504-505.

Murata, K. J. & Richter, D. H. (1966). The settling of olivine in Kilauean magma as shown by lavas of the 1959 eruption. American Journal of Science 264, 194-203.

Nash, W. P. & Crecraft, H. R. (1985). Partition coefficients for trace elements in silicic magmas. Geochimica et Cosmochimica Acta 49, 2309-2322.

Nekvasil, H., Simon, A. & Lindsley, D. H. (2000). Crystal Fractionation and the Evolution of Intra-plate hy-normative Igneous Suites: Insights from their Feldspars. Journal of Petrology 41, 1743-1757.

Nelson, S. T. & Montana, A. (1992). Sieve-textured plagioclase in volcanic rocks produced by rapid decompression. American Mineralogist 77, 1242-1249.

Neumann, E.-R., Vannucci, R. & Tiepolo, M. (2005). N-MORB crust beneath Fuerteventura in the easternmost part of the Canary Islands: evidence from gabbroic xenoliths. Contributions to Mineralogy and Petrology 150, 156-173.

Neumann, E. R., Sorensen, V. B., Simonsen, S. L. & Johnsen, K. (2000). Gabbroic xenoliths from La Palma, Tenerife and Lanzarote, Canary Islands: evidence for reactions between mafic alkaline Canary Islands melts and old oceanic crust. Journal of Volcanology and Geothermal Research 103, 313-342.

Neumann, E. R., Wulff-Pedersen, E., Pearson, N. J. & Spencer, E. A. (2002). Mantle

Xenoliths from Tenerife (Canary Islands): Evidence for Reactions between Mantle Peridotites and Silicic Carbonatite Melts inducing Ca Metasomatism. Journal of Petrology 43, 825-857.

Neumann, E. R., Wulff-Pedersen, E., Simonsen, S. L., Pearson, N. J., Marti, J. & Mitjavila, J. (1999). Evidence for Fractional Crystallization of Periodically Refilled Magma Chambers in Tenerife, Canary Islands. Journal of Petrology 40, 1089-1123.

Nicholson, H., Condomines, M., Fitton, J. G., Fallick, A. E., Gronvold, K. & Rogers, G. (1991). Geochemical and isotopic evidence for crustal assimilation beneath Krafla, Iceland. Journal of Petrology 32, 1005-1020.

Norrish, K. & Hutton, J. T. (1969). An accurate X-ray spectrographic method for the analysis of a wide range of geological samples. Geochimica et Cosmochimica Acta 33, 431-453.

O'Hara, M. J. (1998). Volcanic Plumbing and the Space Problem-Thermal and Geochemical Consequences of Large-Scale Assimilation in Ocean Island Development. Journal of Petrology 39, 1077-1089.

Olin, P. & Wolff, J. (2010). Rare earth and high field strength element partitioning between iron-rich clinopyroxenes and felsic liquids. Contributions to Mineralogy and Petrology

Palacz, Z. A. & Wolff, J. A. (1989). Strontium, neodymium and lead isotope characteristics of the Granadilla Pumice, Tenerife: a study of the causes of strontium isotope disequilibrium in felsic pyroclastic deposits. Geological Society Special Publication 42, 147-159.

Paris, R., Guillou, H., Carracedo, J. C. & Torrado, F. J. P. (2005). Volcanic and morphological evolution of La Gomera (Canary Islands), based on new K-Ar ages and magnetic stratigraphy: implications for oceanic island evolution. Journal of the Geological Society (London, United Kingdom) 162, 501-512.

Pinel, V. & Jaupart, C. (2000). The effect of edifice load on magma ascent beneath a volcano. Phil. Trans. R. Soc. Lond. 358, 1515-1532.

Putirka, K. (1997). Magma transport at Hawaii: Inferences based on igneous thermobarometry. Geology 25, 69-72.

Ramos, F. C., Wolff, J. A. & Tollstrup, D. L. (2004). Measuring 87Sr/86Sr variations in minerals and groundmass from basalts using LA-MC-ICPMS. Chemical Geology 211, 135-158.

Ramos, F. C., Wolff, J. A. & Tollstrup, D. L. (2005). Sr isotope disequilibrium in Columbia River Flood basalts: evidence for rapid shallow-level open-system processes. Geology 33, 457-460.

Ranero, C. R., Torne, M. & Banda, E. (1995). Gravity and multichannel seismic reflection constraints on the lithospheric structure of the Canary Swell. Marine Geophysical

Researches 17, 519-534.

Rehkämper, M. & Halliday, A. N. (1998). Accuracy and long-term reproducibility of lead isotopic measurements by multiple-collector inductively coupled plasma mass spectrometry using an external method for correction of mass discrimination. International Journal of Mass Spectrometry 181, 123-133.

Ridley, W. (1970). The abundance of rock types on tenerife, canary islands, and its petrogenetic significance. Bulletin of Volcanology 34, 196-204.

Rihm, R., Jacobs, C. L., Krastel, S., Schmincke, H.-U. & Alibes, B. (1998). Las Hijas Seamounts - the next Canary Islands? Terra Nova 10, 121-125.

Rodríguez-Badíola, E., Pérez-Torrado, F. J., Carracedo, J. C. & Guillou, H. (2008). Petrografía y Geoquímica del edificio volcánico Teide-Pico Viejo y las dorsales noreste y noroeste de Tenerife. In: Carracedo, J. C. (ed.) Los volcanes del Parque Nacional del Teide / El Teide, Pico Viejo y las dorsales activas de Tenerife. Madrid: Organismo Autónomo Parques Nacionales Ministerio De Medio Ambiente, 129-186

Roeser, H. A. (1982). Magnetic anomalies in the magnetic quiet zone of Morocco. In: Von Rad, U., Hinz, K., Sarnthein, M. & Seibold, E. (eds.) Geology of the Northwest African Continental Margin. Berlin: Springer, 60-68.

Roest, W. R., Dañobeitia, J. J., Verhoef, J. & Collette, B. J. (1992). Magnetic anomalies in the Canary Basin and the Mesozoic evolution of the Central North Atlantic. Marine Geophysical Research 14, 1-24.

Roy, J. & Neufeld, L. (2004). Laser ablation solid sampling for plasma spectrochemistry. Spectroscopy 19, 16-28.

Salisbury, M. J., Bohrson, W. A., Clynne, M. A., Ramos, F. C. & Hoskin, P. (2008). Multiple Plagioclase Crystal Populations Identified by Crystal Size Distribution and in situ Chemical Data: Implications for Timescales of Magma Chamber Processes Associated with the 1915 Eruption of Lassen Peak, CA. Journal of Petrology 49, 1755-1780.

Sawyer, E. W. (1991). Disequilibrium Melting and the Rate of Melt-Residuum Separation During Migmatization of Mafic Rocks from the Grenville Front, Quebec. Journal of Petrology 32, 701-738.

Schiffman, P., Zierenberg, R., Chadwick, W. W., Jr., Clague, D. A. & Lowenstern, J. Contamination of basaltic lava by seawater: Evidence found in a lava pillar from Axial Seamount, Juan de Fuca Ridge. Geochemistry, Geophysics, Geosystems 11, Q04004.

Schmincke, H.-U., Klügel, A., Hansteen, T. H., Hoernle, K. & van den Bogaard, P. (1998). Samples from the Jurassic ocean crust beneath Gran Canaria, La Palma and Lanzarote (Canary Islands). Earth and Planetary Science Letters 163, 343-360.

Schmincke, H.-U. & Rihm, R. (1994). Ozeanvulkan 1993, Cruise No. 24, 15 April - 9 May 1993. Hamburg: University Hamburg.

Schmincke, H. (1969). Ignimbrite sequence on Gran Canaria. Bulletin of Volcanology 33, 1199-1219.

Shimizu, H. (1980). Experimental study on rare-earth element partitioning in minerals formed at 20 and 30kb for basaltic systems. Geochemical Journal 14, 185-202.

Simonsen, S. L., Neumann, E. R. & Seim, K. (2000). Sr-Nd-Pb isotope and trace-element geochemistry evidence for a young HIMU source and assimilation at Tenerife (Canary Island). Journal of Volcanology and Geothermal Research 103, 299-312.

Sleep, N. H. (1990). Hotspots and Mantle Plumes: Some Phenomenology. Journal of Geophysical Research 95.

Sorensen, S. S. (1988). Petrology of amphibolite-facies mafic and ultramafic rocks from the Catalina Schist, southern California: metasomatism and migmatization in a subduction zone metamorphic setting. Journal of Metamorphic Geology 6, 405-435.

Sparks, R. S. J. & Huppert, H. E. (1984). Density changes during the fractional crystallization of basaltic magmas: fluid dynamic implications. Contributions to Mineralogy and Petrology 85, 300-309.

Sparks, S. R. J., Sigurdsson, H. & Wilson, L. (1977). Magma mixing: a mechanism for triggering acid explosive eruptions. Nature 267, 315-318.

Spera, F. J. & Bohrson, W. A. (2001). Energy-Constrained Open-System Magmatic Processes I: General Model and Energy-Constrained Assimilation and Fractional Crystallization (EC-AFC) Formulation. Journal of Petrology 42, 999-1018.

Spera, F. J. & Bohrson, W. A. (2002). Energy-constrained open-system magmatic processes 3. Energy-Constrained Recharge, Assimilation, and Fractional Crystallization (EC-RAFC). Geochemistry, Geophysics, Geosystems 3.

Spera, F. J. & Bohrson, W. A. (2004). Open-System Magma Chamber Evolution: an Energy-constrained Geochemical Model Incorporating the Effects of Concurrent Eruption, Recharge, Variable Assimilation and Fractional Crystallization (EC-E'RA{chi} FC). Journal of Petrology 45, 2459-2480.

Staudigel, H. & Schmincke, H.-U. (1984). The Pliocene Seamount Series of La Palma/ Canary Islands. Journal of Geophysical Research 89.

Stewart, M. L. & Pearce, T. H. (2004). Sieve-textured plagioclase in dacitic magma: Interference imaging results. American Mineralogist 89, 348-351.

Stillman, C. J., Fúster, J. M., Bennell Baker, M. J., Muñoz, M., Smewing, J. D. & Sagredo, J. (1975). Basal complex of Fuerteventura (Canary Islands) is an oceanic intrusive complex with rift-system affinities. Nature 257, 469-471.

Stimac, J. & Hickmott, D. (1994). Trace-element partition coefficients for ilmenite, orthopyroxene and pyrrhotite in rhyolite determined by micro-PIXE analysis. Chemical

Geology 117, 313-330.

Stroncik, N., Klügel, A. & Hansteen, T. (2009). The magmatic plumbing system beneath El Hierro (Canary Islands): constraints from phenocrysts and naturally quenched basaltic glasses in submarine rocks. Contributions to Mineralogy and Petrology 157, 593-607.

Sun, S. S. (1980). Lead Isotopic Study of Young Volcanic Rocks from Mid-Ocean Ridges, Ocean Islands and Island Arcs. Philosophical Transactions of the Royal Society of London, Series A: Mathematical, Physical and Engineering Sciences 297, 409-445.

Taylor, B. E. (1986). Magmatic volatiles; isotopic variation of C, H, and S. Reviews in Mineralogy and Geochemistry 16, 185-225.

Taylor, H. P. J. & Sheppard, S. M. F. (1986). I. Processes of isotopic fractionation and isotope systematics. Reviews in Mineralogy and Geochemistry 16, 227-272.

Tepley, F. J. & Davidson, J. P. (2003). Mineral-scale Sr-isotope constraints on magma evolution and chamber dynamics in the Rum layered intrusion, Scotland. Contributions to Mineralogy and Petrology 145, 628-641.

Tepley, F. J., III, Davidson, J. P., Tilling, R. I. & Arth, J. G. (2000). Magma Mixing, Recharge and Eruption Histories Recorded in Plagioclase Phenocrysts from El Chichon Volcano, Mexico. Journal of Petrology 41, 1397-1411.

Tepley III, F. J., Davidson, J. P. & Clynne, M. A. (1999). Magmatic Interactions as Recorded in Plagioclase Phenocrysts of Chaos Crags, Lassen Volcanic Center, California. Journal of Petrology 40, 787-806.

Thirlwall, M. F., Jenkins, C., Vroon, P. Z. & Mattey, D. P. (1997). Crustal interaction during construction of ocean islands: Pb---Sr---Nd---O isotope geochemistry of the shield basalts of Gran Canaria, Canary Islands. Chemical Geology 135, 233-262.

Thirlwall, M. F., Singer, B. S. & Marriner, G. F. (2000). 39Ar-40Ar ages and geochemistry of the basaltic shield stage of Tenerife, Canary Islands, Spain. Journal of Volcanology and Geothermal Research 103, 247-297.

Thompson, Thompson, G., Smith, Smith, I., Malpas & Malpas, J. (2001). Origin of oceanic phonolites by crystal fractionation and the problem of the Daly gap: an example from Rarotonga. Contributions to Mineralogy and Petrology 142, 336-346.

Thompson, R. N., Morrison, M. A., Hendry, G. L., Parry, S. J., Simpson, P. R., Hutchison, R. & O'Hara, M. J. (1984). An Assessment of the Relative Roles of Crust and Mantle in Magma Genesis: An Elemental Approach [and Discussion]. Philosophical Transactions of the Royal Society of London, Series A: Mathematical, Physical and Engineering Sciences 310, 549-590.

Triebold, S., Kronz, A. & Wörner, G. (2006). Anorthite-calibrated backscattered electron profiles, trace elements, and growth textures in feldspars from the Teide-Pico Viejo volcanic complex (Tenerife). Journal of Volcanology and Geothermal Research 154,

117-130.

Troll, V., Sachs, P., Schmincke, H.-U. & Sumita, M. (2003). The REE-Ti mineral chevkinite in comenditic magmas from Gran Canaria, Spain: a SYXRF-probe study. Contributions to Mineralogy and Petrology 145, 730-741.

Troll, V. R., Chadwick, J. P., Ellam, R. M., McDonnell, S., Emeleus, C. H. & Meighan, I. G. (2005). Sr and Nd isotope evidence for successive crustal contamination of Slieve Gullion ring-dyke magmas, Co. Armagh, Ireland. Geological Magazine 142, 659-668.

Troll, V. R., Donaldson, C. H. & Emeleus, C. H. (2004). Pre-eruptive magma mixing in ash-flow deposits of the Tertiary Rum Igneous Centre, Scotland. Contributions to Mineralogy and Petrology 147, 722-739.

Troll, V. R. & Schmincke, H. U. (2002). Magma Mixing and Crustal Recycling Recorded in Ternary Feldspar from Compositionally Zoned Peralkaline Ignimbrite 'A', Gran Canaria, Canary Islands. Journal of Petrology 43, 243-270.

Troll, V. R., Walter, T. R. & Schmincke, H. U. (2002). Cyclic caldera collapse: Piston or piecemeal subsidence? Field and experimental evidence. Geology 30, 135-138.

Turner, J. S. (1980). A fluid-dynamical model of differentiation and layering in magma chambers. Nature 285, 213-215.

Turner, J. S. & Campbell, I. H. (1986). Convection and mixing in magma chambers. Earth-Science Reviews 23, 255-352.

Verhoef, J., Collette, B. J., Dañobeitia, J. J., Roeser, H. A. & Roest, W. R. (1991). Magnetic anomalies off West-Africa (20–38° N). Marine Geophysical Researches 13, 81-103.

Villemant, B., Jaffrezic, H., Joron, J.-L. & Treuil, M. (1981). Distribution coefficients of major and trace elements; fractional crystallization in the alkali basalt series of Chaîne des Puys (Massif Central, France). Geochimica et Cosmochimica Acta 45, 1997-2016.

Waight, T., Baker, J. & Peate, D. (2002). Sr isotope ratio measurements by double-focusing MC-ICPMS: techniques, observations and pitfalls. International Journal of Mass Spectrometry 221, 229-244.

Walker, D. & DeLong, S. E. (1982). Soret separation of mid-ocean ridge basalt magma. Contributions to Mineralogy and Petrology 79, 231-240.

Walker, D., Lesher, C. E. & Hays, J. F. (1981). Soret separation of lunar liquids. Lunar and Planetary Science XII, 991-999.

Walter, T. R. & Troll, V. R. (2003). Experiments on rift zone evolution in unstable volcanic edifices. Journal of Volcanology and Geothermal Research 127, 107-120.

Walter, T. R., Troll, V. R., Cailleau, B., Belousov, A., Schmincke, H. U., Amelung, F. & Bogaard, P. v. d. (2005). Rift zone reorganization through flank instability in ocean

island volcanoes: an example from Tenerife, Canary Islands. Bulletin of Volcanology 67, 281-291.

Watson, E. B. (1979). Zircon saturation in felsic liquids: Experimental results and applications to trace element geochemistry. Contributions to Mineralogy and Petrology 70, 407-419.

Watson, E. B. (1982). Basalt contamination by continental crust: Some experiments and models. Contributions to Mineralogy and Petrology 80, 73-87.

Watson, E. B. & Baker, D. R. (1991). Chemical diffusion in Magmas: An overview of experimental results and geochemical applications. In: Perchuk, L. L. & Kushiro, I. (eds.) Advances in Physical Geochemistry. New York: Springer, 120-151.

Watson, E. B. & Baxter, E. F. (2007). Diffusion in solid-Earth systems. Earth and Planetary Science Letters 253, 307-327.

Watson, E. B. & Green, T. H. (1981). Apatite/liquid partition coefficients for the rare earth elements and strontium. Earth and Planetary Science Letters 56, 405-421.

Watts, A. B., Masson, D. G. (1995). A giant landslide on the northflank of Tenerife, Canary Islands. Journal of Geophysical Research 100, 24487-24498.

Wellman, T. R. (1970). The Stability of Sodalite in a Synthetic Syenite plus Aqueous Chloride Fluid System. Journal of Petrology 11, 49-72.

White, W. M., Albarède, F. & Télouk, P. (2000). High-precision analysis of Pb isotope ratios by multi-collector ICP-MS. Chemical Geology 167, 257-270.

Wilcox, R. E. (1999). The Idea of Magma Mixing: History of a Struggle for Acceptance. Journal of Geology 107, 421-432.

Williams, M. L., Hanmer, S., Kopf, C. & Darrach, M. (1995). Syntectonic generation and segregation of tonalitic melts from amphibolite dikes in the lower crust, Striding-Athabasca mylonite zone, northern Saskatchewan. Journal of Geophysical Research 100.

Wolff, J. A. (1983). Petrology of Quaternary pyroclastic deposits from Tenerife, Canary Islands. London: University of London, 542.

Wolff, J. A. (1987). Crystallisation of nepheline syenite in a subvolcanic magma system: Tenerife, Canary islands. Lithos 20, 207-223.

Wolff, J. A., Grandy, J. S. & Larson, P. B. (2000). Interaction of mantle-derived magma with island crust? Trace element and oxygen isotope data from the Diego Hernandez Formation, Las Canadas, Tenerife. Journal of Volcanology and Geothermal Research 103, 343-366.

Wolff, J. A. & Palacz, Z. A. (1989). Lead isotope and trace element variation in Tenerife pumices - Evidence for recycling within an ocean island volcano. Mineralogical Magazine

53, 519-525.

Wolff, J. A., Ramos, F. C. & Davidson, J. P. (1999). Sr isotope disequilibrium during differentiation of the Bandelier Tuff: Constraints on the crystallization of a large rhyolitic magma chamber. Geology 27, 495-498.

Wolff, J. A. & Storey, M. (1983). The volatile component of some pumice-forming alkaline magmas from the Azores and Canary Islands. Contributions to Mineralogy and Petrology 82, 66-74.

Wolff, J. A. & Storey, M. (1984). Zoning in highly alkaline magma bodies. Geological Magazine 121, 563-575.

Wolff, J. A. & Toney, J. B. (1993). Trapped liquid from a nepheline syenite: a re-evaluation of Na-, Zr-, F-rich interstitial glass in a xenolith from Tenerife, Canary Islands. Lithos 29, 285-293.

Wood, B. J. & Trigila, R. (2001). Experimental determination of aluminous clinopyroxene-melt partition coefficients for potassic liquids, with application to the evolution of the Roman province potassic magmas. Chemical Geology 172, 213-223.

Wörner, G., Beusen, J. M., Duchateau, N., Gijbels, R. & Schmincke, H. U. (1983). Trace element abundances and mineral/melt distribution coefficients in phonolites from the Laacher See volcano (Germany). Contributions to Mineralogy and Petrology 84, 152-173.

Ye, S., Canales, J. P., Rihm, R., Dañobeitia, J. J. & Gallart, J. (1999). A crustal transect through the northern and northeastern part of the volcanic edifice of Gran Canaria, Canary Islands. Journal of Geodynamics 28, 3-26.

Zack, T. & Brumm, R. (1998). Ilmenite/liquid partition coefficients of 26 trace elements determined through ilmenite/clinopyroxene partitioning in garnet pyroxene. Cape Town: Red Roof Design.

Zhang, Y.-S. & Tanimoto, T. (1992). Ridges, hotspots and their interaction as observed in seismic velocity maps. Nature 355, 45-49.